Semiannual Technical Report

Interface Properties of Wide Bandgap Semiconductor Structures

Supported under Grant #N00014-92-J-1477
Office of the Chief of Naval Research
Report for the period 6/1/95–12/31/95

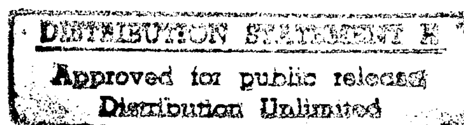

R. F. Davis, S. Bedair*, J. Bernholc†, R. J. Nemanich†, and Z. Sitar
c/o Materials Science and Engineering Department,
*Electrical and Computer Engineering Department
and †Department of Physics
North Carolina State University
Campus Box 7907
Raleigh, NC 27695-7907

19960226 126

December, 1995

DTIC QUALITY INSPECTED 1

REPORT DOCUMENTATION PAGE

Form Approved
OMB No. 0704-0188

Public reporting burden for this collection of information is estimated to average 1 hour per response, including the time for reviewing instructions, searching existing data sources, gathering and maintaining the data needed, and completing and reviewing the collection of information. Send comments regarding this burden estimate or any other aspect of this collection of information, including suggestions for reducing this burden to Washington Headquarters Services, Directorate for Information Operations and Reports, 1215 Jefferson Davis Highway, Suite 1204, Arlington, VA 22202-4302, and to the Office of Management and Budget Paperwork Reduction Project (0704-0188), Washington, DC 20503.

1. AGENCY USE ONLY *(Leave blank)*

2. REPORT DATE
December, 1995

3. REPORT TYPE AND DATES COVERED
Semiannual Technical 7/1/95–12/31/95

4. TITLE AND SUBTITLE
Interface Properties of Wide Bandgap Semiconductor Structures

5. FUNDING NUMBERS
uri41114a-01
1114SS
N00179
N66005
4B855

6. AUTHOR(S)
Robert F. Davis and R. J. Nemanich

7. PERFORMING ORGANIZATION NAME(S) AND ADDRESS(ES)
North Carolina State University
Hillsborough Street
Raleigh, NC 27695

8. PERFORMING ORGANIZATION REPORT NUMBER
N00014-92-J-1477

9. SPONSORING/MONITORING AGENCY NAMES(S) AND ADDRESS(ES)
Sponsoring: ONR, 800 N. Quincy, Arlington, VA 22217-5660
Monitoring: Administrative Contracting Officer, Office of Naval Research
Regional Office Atlanta, 101 Marietta Tower, Suite 2805
101 Marietta Street
Atlanta, GA 30323-6145

10. SPONSORING/MONITORING AGENCY REPORT NUMBER

11. SUPPLEMENTARY NOTES

12a. DISTRIBUTION/AVAILABILITY STATEMENT
Approved for Public Release; Distribution Unlimited

12b. DISTRIBUTION CODE

13. ABSTRACT *(Maximum 200 words)* **Page 1 of 2**

A surface analytical study of bias enhanced nucleation of diamond on TiC(111) indicated that C vacancies form at the substrate and that the procedure may result in enhanced surface diffusion. Oriented diamond growth has been achieved on both (100) and (111) Ni substrates. A key aspect of the process is the formation of a molten Ni-C-H surface layer that promotes the nucleation of oriented particles. Experiments have been initiated to explore transmutation doping of B-doped homoepitaxial diamond by conversion of B to Li through neutron irradiation. Theoretical studies indicate that alternating exposure of hydrocarbon and fluorocarbon precursors may be suitable for ALE growth on diamond (110) surfaces. Field emission from diamond-coated, needle-shaped emitters demonstrated a significant enhancement of the total emission current and improved stability of the tip. A series of different *ex situ* chemical-based techniques have been explored for cleaning of 6H-SiC surfaces. Results indicated that O bonded to C on the surface was not easily removed. The impurity concentrations were measured for epitaxial SiC films on 6H-SiC(0001) and 3C-SiC(111) that were prepared by gas source MBE using SiH_4 and C_2H_2. MIS diodes of Al/AlN/SiC were prepared by gas source MBE and characterized with C-V measurements. Ohmic contacts on p-type SiC were obtained using Ni/NiAl and annealing to 1000°C. AlGaN films were grown directly on 6H-SiC, and the films were characterized with TEM, XRD, and cathodoluminescence.

14. SUBJECT TERMS
diamond, nucleation, molecular beam epitaxy, MBE, atomic hydrogen, Ni_4C, molecular dynamics, atomic layer epitaxy, SiC, surface cleaning, Schottky barrier height, MIS diodes, GaN, gallium nitride powder, gallium nitride, GaN, aluminum nitride, AlN, $Al_xGa_{1-x}N$, InGaN, indium gallium nitride, organometallic vapor phase epitaxy, OMVPE, nickel substrates, α(6H)-SiC(0001) substrates, surface states, surface

15. NUMBER OF PAGES
260

16. PRICE CODE

17. SECURITY CLASSIFICATION OF REPORT	18. SECURITY CLASSIFICATION OF THIS PAGE	19. SECURITY CLASSIFICATION OF ABSTRACT	20. LIMITATION OF ABSTRACT
UNCLAS	UNCLAS	UNCLAS	SAR

Table of Contents

I. Introduction 1

Carbon-based Materials

II. Surface Analytical Study of the Bias-enhanced Nucleation of Diamond on Titanium Carbide(111) 3
M. T. McClure and Z. Sitar

III. Nucleation and Growth of Oriented Diamond Films in the Ni-C-H System 11
C. Wolden and Z. Sitar

IV. Donor Doping of Diamond Using Nuclear Transmutation 29
S. P. Bozeman, R. J. Nemanich and R. F. Davis

V. Negative Electron Affinity Surfaces of Aluminum Nitride and Diamond 34
R. J. Nemanich, P. K. Baumann, M. C. Benjamin, S. W. King, J. van der Weide and R. F. Davis

VI. Field Emission Characteristics of Diamond Coated Silicon Field Emitters 47
M. McClure and Z. Sitar

VII. *Ex Situ* Cleaning Techniques for 6H-SiC Surfaces 56
S. King and R. F. Davis

VIII. Electrical Characterization of SiC Grown by Gas-source Molecular Beam Epitaxy 75
S. Kern and R. F. Davis

IX. Fabrication and Characterization of Al/AlN/SiC MIS Diodes Grown by Gas-source Molecular Beam Epitaxy 82
S. Kern and R. F. Davis

X. Rectifying and Ohmic Contacts for P-type Alpha (6H) Silicon Carbide 90
L. Porter, S. Fleming and R. F. Davis

Nitrogen-based Materials

XI. Growth and Doping of $Al_xGa_{1-x}N$ Deposited Directly on α(6H)-SiC(0001) Substrates Via Organometallic Vapor Phase Epitaxy 99
M. D. Bremser, W. G. Perry, T. Zheleva and R. F. Davis

XII. Structural Characterization of III-Nitride Films and Interfaces by TEM and XRD 110
T. Zheleva and R. F. Davis

XIII. Luminescence Studies of GaN 119
W. G. Perry and R. F. Davis

XIV. Measurement of the Electron Flux from Diamond and III-V Nitride Surfaces 130
B. L. Ward and R. J. Nemanich

XV. (Negative) Electron Affinity of AlN and AlGaN Alloys — 136
R. J. Nemanich, M. C. Benjamin, S. P. Bozeman, M. D. Bremser, S. W. King, B. L. Ward, R. F. Davis, B. Chen, Z. Zhang, and J. Bernholc

XVI. UV Photoemission Study of Heteroepitaxial AlGaN Films Grown on 6H-SiC — 151
M. C. Benjamin, M. D. Bremser, T. W. Weeks, Jr., S. W. King, R. F. Davis and R. J. Nemanich

XVII. High Quality InGaN Films by Atomic Layer Epitaxy — 159
K. S. Boutros, F. G. McIntosh, J. C. Roberts, S. M. Bedair, E. L. Piner and N. A. El-Masry

XVIII. Growth and Characterization of AlInGaN Quaternary Alloys — 167
K. S. Boutros, F. G. McIntosh, J. C. Roberts, S. M. Bedair, E. L. Piner and N. A. El-Masry

XIX. Raman Spectroscopy for Characterization of Hard, Wide Band Gap Semiconductors: Diamond, GaN, GaAlN, AlN, BN — 175
L. Bergman and R. F. Nemanich

XX. Synthesis Routes and Characterization of High Purity, Single Phase GaN Powders — 202
C. Balkas and R. F. Davis

XXI. Hot Pressing of III-V Nitrides — 211
S. Taylor-Kern and R. F. Davis

XXII. Towards the Identification of the Dominant Donor in GaN — 215
J. Bernholc

XXIII. Dry Etching of Gallium Nitride — 227
S. Smith and R. F. Davis

XXIV. Photoassisted Dry Etching of GaN — 233
R. T. Leonard and S. M. Bedair

XXV. Contact Formation on n-type and p-type GaN — 239
L. Smith and R. F. Davis

XXVI. III-V Nitrides for Use in Semiconductor Microelectronic Device Applications — 257
R. Therrien and R. F. Davis

XXVII. Distribution List — 260

I. Introduction

Heteroepitaxy is the growth of a crystal (or a film) on a foreign crystalline substrate that determines its orientation. Such oriented growth requires that lattice planes in both materials have similar structure. In general, an epitaxial relationship is probable whenever the orientation of the substrate and overgrowth produces an interface with a highly coincident atomic structure having low interfacial energy relative to a random arrangement.

During the past decade, nonequilibrium techniques have been developed for the growth of epitaxial semiconductors, superconductors, insulators and metals which have led to new classes of artificially structured materials. In many cases, the films were deposited on substrates having a different chemistry from that of the film, and heteroepitaxy was achieved. Moreover, layered structures with a periodicity of a few atomic layers have also been produced by the sequential heteroepitaxial deposition of a film of one type on another. Metastable structures can be generated which possess important properties not present in equilibrium systems. A consideration of the materials under consideration for next generation electronic and optoelectronic devices, e.g., the III-V nitrides show that only a few of them can currently be grown in bulk, single crystal form having a cross-sectional area of $>3cm^2$. Thus other, commercially available substrates must be used. This introduces a new set of challenges for the successful growth of device quality films which are not present in homoepitaxial growth and which must be surmounted if these materials are to be utilized in device structures.

In addition to providing structures which do not exist in nature, applications of advanced heteroepitaxial techniques permit the growth of extremely high quality heterostructures involving semiconductors, metals, and insulators. These heterostructures offer the opportunity to study relationships between the atomic structure and the electrical properties of both the film itself and the interface between the two dissimilar materials. They also allow the study of epitaxial growth between materials exhibiting very different types (ionic, covalent, or metallic) of bonding.

While the potential of heteroepitaxial deposition has been demonstrated, significant advances in theoretical understanding, experimental growth and control of this growth, and characterization are required to exploit the capabilities of this process route. It is particularly important to understand and control the principal processes which control heteroepitaxy at the atomic level. It is this type of research, as well as the chemistry of dry etching via laser and plasma processing, which forms the basis of the research in this grant.

The materials of concern in this report are classified as wide bandgap semiconductors and include diamond, SiC and the III-V nitrides of Al, Ga, and In and their alloys. The extremes in electronic and thermal properties of diamond and SiC allow the types and numbers of current and conceivable applications of these materials to be substantial. However, a principal driving force for the interest in the III–V nitrides is their potential for solid-state optoelectronic devices

for light emission and detection from the visible through the far ultraviolet range of the spectrum.

The principal objectives of the research program are the determination of (1) the fundamental physical and chemical processes ongoing at the substrate surface and substrate/film interface during the heteroepitaxial deposition of both monocrystalline films of the materials noted above, as well as metal contacts on these materials, (2) the mode of nucleation and growth of the materials noted in (1) on selected substrates and on each other in the fabrication of multilayer heterostructures, (3) the resulting properties of the individual films and the layered structures and the effect of interfacial defects on these properties, (4) the development and use of theoretical concepts relevant to the research in objectives (1–3) to assist in the fabrication of improved films and structures and (5) the determination of process chemistry which leads to the laser assisted and plasma etching of these wide bandgap compound semiconductors.

This is the seventh bi-annual report since the initiation of the project. The following sections introduce each topic, detail the experimental approaches, report the latest results and provide a discussion and conclusion for each subject. Each major section is self-contained with its own figures, tables and references.

Carbon-based Materials

II. Surface Analytical Study of the Bias-enhanced Nucleation of Diamond on Titanium Carbide(111)

A. Introduction

Epitaxial diamond films have been grown on both cBN and diamond [1-3]; however, these materials are expensive and large area substrates are not available. There has been past research to suggest that diamond heteroepitaxy may be achieved on other non-diamond or related substrates. The recent deposition on ß-SiC, Si, and Ni have shown the most dramatic results [4-10]. In the case of the work conducted on ß-SiC and Si, bias-enhanced nucleation (BEN) was used for the formation of these epitaxial diamond crystals [11]. The term highly oriented diamond (HOD) has been used to describe the partial alignment of individual grains. The individual particles may be epitaxial with respect to the substrate, however, tilting in both azimuthal and transverse directions results in the formation of low-angle grain boundaries [12]. The origin of this misalignment is believed to be a result of an approximately 22% mismatch at the diamond/SiC interface [9]. Recently, the use of the BEN procedure on TiC(111) has resulted in the deposition of oriented diamond particles [13].

Despite the number of substrates that have resulted in oriented diamond deposition, understanding the nucleation mechanism remains elusive. To gain further understanding, a surface analytical (XPS and LEED) investigation of TiC(111) after sequential exposures to the BEN procedure was undertaken. The structural and chemical information these two techniques can provide are exceptionally useful to describe surface changes during the bias-enhanced nucleation process.

B. Experimental Procedure

Upon receiving the samples from Advanced Technology Materials, Inc., the samples were polished using progressively finer media. The polishing scheme started with 600 grit SiC, then 30µm diamond and progressing through 6µm, 1µm, and 0.1µm diamond and finishing with one hour of 0.05µm Al_2O_3 powder to remove any residual diamond detritus that may have been embedded in the TiC surface. Then the samples were cleaned using acetone, methanol, and isopropanol. After polishing and characterization of the substrate surface, the sample was loaded into the deposition chamber and subjected to a H_2 plasma cleaning to remove any advantitious hydrocarbon adsorbates. Table I summarizes the system parameters that resulted in the deposition of oriented diamond particles [13]. For the analytical series, the same BEN conditions were used for 5 minute intervals and the sample was transferred *in vacuo* to the surface analytical system.

Table I. Summary of MPCVD System Parameters
Used to Deposit Oriented Diamond Particles

System Parameter	H_2 Plasma Cleaning	BEN	Growth
Power (W)	600	600	600
Pressure (Torr)	25	15	40
CH4:H2 ratio	...	5%	0.2%
Bias current (mA)	...	120	...
Bias current (Vdc)	...	225±10	...
Temperature (°C)	660±20	785±20	900
Duration	30 min	10-15 min	8 h

C. Results of Surface Analytical Examination

Results of LEED Analysis. After the H_2 plasma cleaning, the sample was transferred into the surface analytical chamber and a LEED pattern was observed. The pattern was consistent with a {111}-(1×1) structure expected for the TiC(111) face. A LEED pattern was obtained only after the H_2 plasma cleaning stage and not at any other time of experiment. The formation of islands or loss of symmetry on the surface by amorphization or polycrystallization would have resulted in the loss of a LEED pattern.

Results of XPS Analysis. Low energy electron diffraction was used to determine the structure of the surface but could not provide information about the chemical nature of the surface. To gain chemical identification and bonding information about the species on the surface x-ray photoelectron spectroscopy (XPS) was also performed after each period of the BEN series. XPS provided elemental identification of surface and sub-surface species and, by detecting any shift from the elemental peak position, XPS also supplied information about the bonding nature of the elements detected. Examination of the peak intensities as a function of time provided information about structure of an overlayer that is being deposited. Detailed explanation of each aspect of XPS analysis is provided in the relevant sections.

Peak Identification. Initially a low resolution scan, termed a "survey scan," of the surface was performed for elemental identification. Examination of this spectrum indicated that oxygen, titanium, and carbon were present on the surface. To gain bonding information a higher resolution scan over the particular peak energies were performed. The XPS spectra for each energy region and step in the temporal series are shown Fig. 1(a-c). The peak centers and area intensities were determined by fitting the spectra to Voigt peaks, which are a combination of Gaussian and Lorentzian peaks, using the IGOR Pro software from Wavemetrics, Inc. In all stages some residual oxygen was detected, but the photoelectron peak was broad indicating that the oxygen was only weakly bound to the surface and may have adsorbed during transfer between chambers. Importantly, peaks that would indicate oxygen bonding with titanium were

absent. The high binding energy features in some of the C1s spectra were due to some of the residual oxygen binding to carbon species to form a C-O complex. The feature appeared again only in the spectrum taken after 25 minutes of biasing and may have formed while the substrate cooled after the plasma was extinguished. The other features in the C1s spectra were characteristic of C-C bonding (285 eV) and C-Ti (282 eV) bonding. In the Ti2p region only those features indicative of Ti-C (455 eV) bonding were present [14, 15].

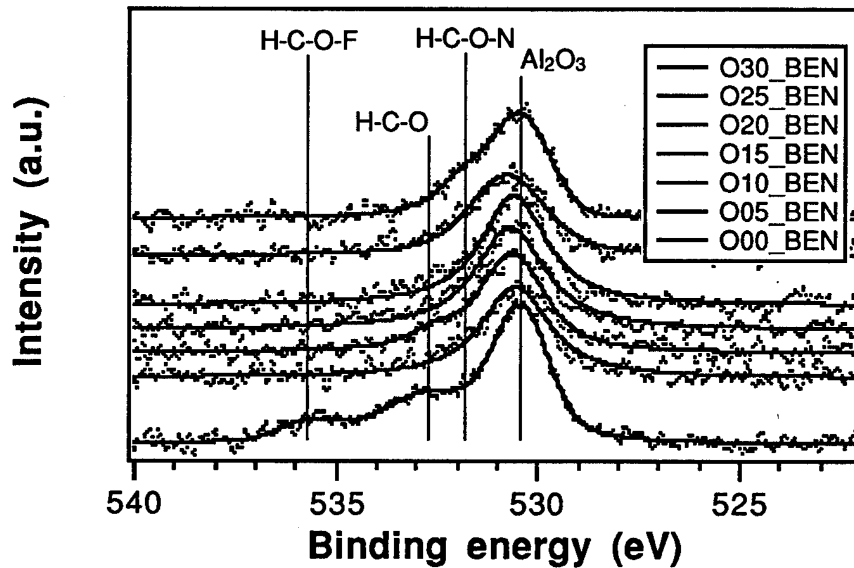

Figure 1(a). XPS spectra for the O1s photoelectron energy. Energy positions for relevant species are shown.

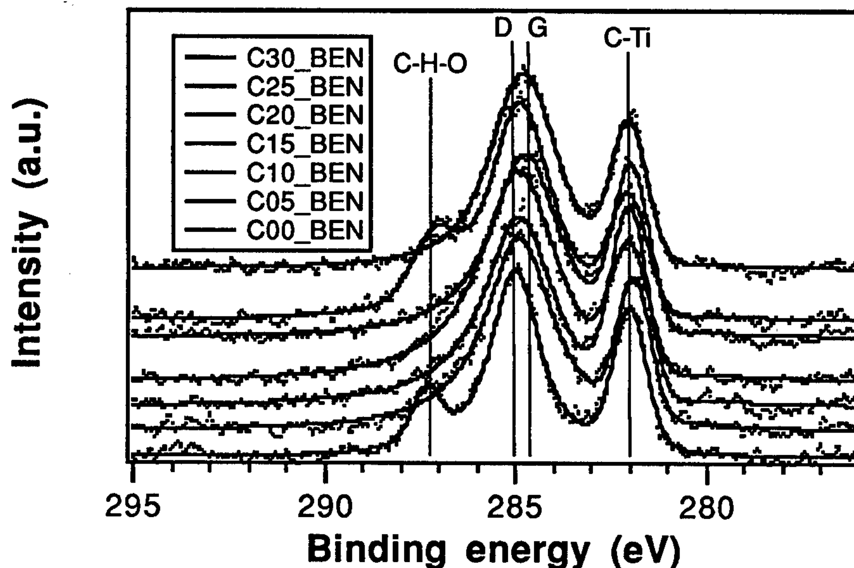

Figure 1(b). XPS spectra for the C1s photoelectron energy. Energy positions for relevant species are shown.

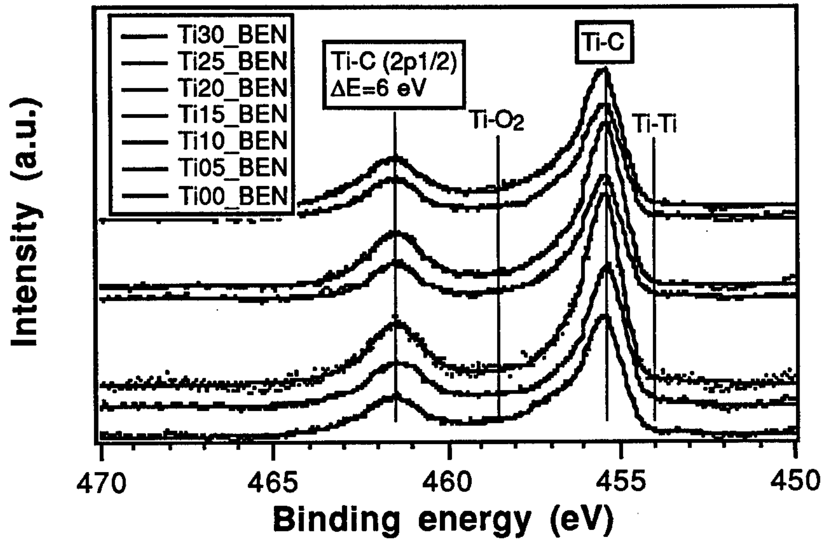

Figure 1(c). XPS spectra for the Ti2p photoelectron energy. Energy positions for relevant species are shown.

Compositional Analysis. Compositional and overlayer thickness calculations were made given the peak area intensities determined by curve fitting the XPS spectra. By comparing the area intensity of the C-Ti (282 eV) peak to the Ti-C (455.5 eV) peak the composition of the surface was determined (Fig. 2). Equation 1 was used to calculate the C:Ti ratio for each time step examined and the results are shown in Fig. 3. After 5 minutes of the BEN procedure, the C:Ti ratio decreased dramatically and leveled off after 15 minutes of biasing [14].

$$n_C / n_{Ti} = \left(I_C / I_{Ti} \right) \sigma_{Ti} / \sigma_C \qquad (1)$$

where n_{Ti} and n_C are the concentrations of Ti and C, respectively,
I_C and I_{Ti} are the peak areas of the C1s and Ti2p peaks, respectively, and
σ_{Ti} and σ_C are the photoionization cross sections of Ti and C, respectively.

The decay of the C:Ti ratio with BEN duration suggested that the composition of the substrate in the near surface region became carbon deficient. Because the peak intensity of the Ti-C peak (455 eV) did not increase with time, the data did not suggest that the near surface region became Ti abundant rather the C-Ti peak (282 eV) decrease with time suggested carbon deficiency. One explanation for the decrease in the C:Ti ratio was the formation of carbon vacancies by ion bombardment as a result of the applied negative substrate potential. The displaced carbon atoms could have been knocked into interstitial positions where they remained or migrated to the surface. This data provided clues to the BEN mechanism but no clear answers.

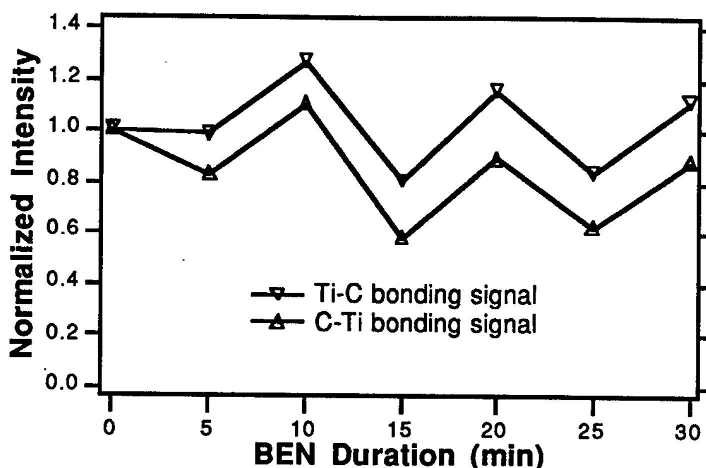

Figure 2. The normalized photoelectron intensity for the C-Ti and Ti-C bonding as a function of BEN duration.

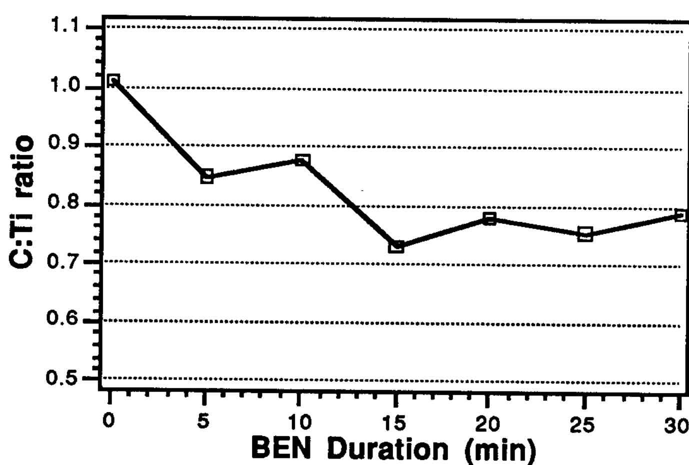

Figure 3. C:Ti ratio as a function of BEN duration. The ratio was calculated using Eq. 1.

Overlayer Information. The decay in intensity of the photoelectrons can be used to determine the growth of the overlayer. The attenuation is due to the exponential probability of electrons escaping the surface without suffering inelastic collisions with atoms in the overlayer. The shape of the attenuation curve supplies information for determining the growth mode. If the growth mode is "layer-by-layer" then the intensity of the substrate photoelectron peak can be written as:

$$I_S/I_{So} = (1-x)\exp[-nl/\lambda] + x\exp[-(n+1)l/\lambda] \quad (2)$$

where I_S and I_{So} are the peak intensities for the substrate with an overlayer present and for the clean substrate, respectively,

l is the monolayer thickness,

λ is the inelastic mean free path of the photoelectron,

(1-x) is the fraction of the surface covered with n layers, and

x is the fraction of the surface covered with (n+1) layers.

If the growth mode is "islanding," the attenuation curve is not a simple exponential because some of substrate will always be exposed to eject electrons and the substrate signal will persist for significant amounts of material deposited. To correctly interpret an electron yield curve in this case would require an accurate knowledge of the surface coverage of the islands and knowledge of the mean free path of the electrons. An intermediate case occurs when islands form after a few initial layers have deposited in a "layer-by-layer" fashion. This growth mode is termed "layer-plus-islanding." In this case the attenuation curve follows an exponential decay as long as the deposition is "layer-by-layer," but afterwards the signal from the substrate persists. The equation below illustrates this type of attenuation for the case where islands two monolayers high cover 50% of the surface after the initial monolayer has deposited uniformly.

$$I_S/I_{So} = (1-x)\exp[-l/\lambda] + x\exp[-3l/\lambda], \qquad 0 \le x \le 0.5, \qquad (3)$$

where all variables have the same meaning as in Eq. 2.

The attenuation curves for all three growth modes are illustrated in Figure 4(a). Curves for the intensity increase overlayer can also be modeled and they have similar shapes according to the growth mode but increase with the form of $1\text{-}e^x$ (Fig. 4(b)) [14].

The non-zero value of the C-C signal after the H_2 plasma cleaning and the apparent saturation of the signal from BEN times 15 - 30 minutes allowed two different analyses. First, the C-C signal intensity has been normalized to show the increase in the signal after the H_2 plasma cleaning. The shape of this curve was indicative of a "islanding" deposition mode. Second, the C-C intensity was normalized assuming the signal from 15 to 30 minutes was a maximum signal and has a relative value of 1. Using this method, the thickness of the carbon layer after the H_2 plasma cleaning was calculated according to Eq. 2, assuming the remaining C-C signal comes from an equivalent uniform thickness. Combining these two analysis methods, the C-C signal indicated that the carbon layer was equivalent to one monolayer of TiC (i.e., the TiC(111) plane was carbon terminated) and the deposited carbon islands covered 55% of the substrate surface.

D. Summary

The proof-of-concept deposition on the TiC(111) substrate proved successful with the observation of oriented diamond particles and a characteristic Raman spectra. A surface analysis series was performed after 5 minute periods of the biasing procedure. Analysis of the

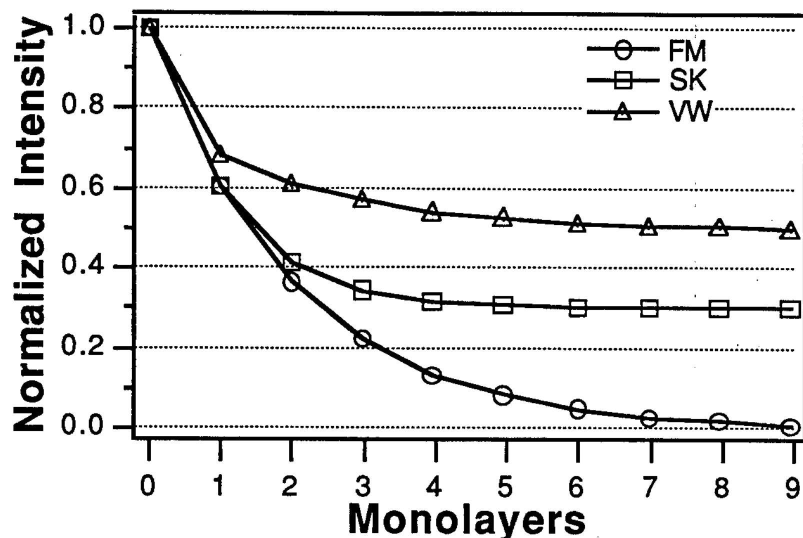

(a)

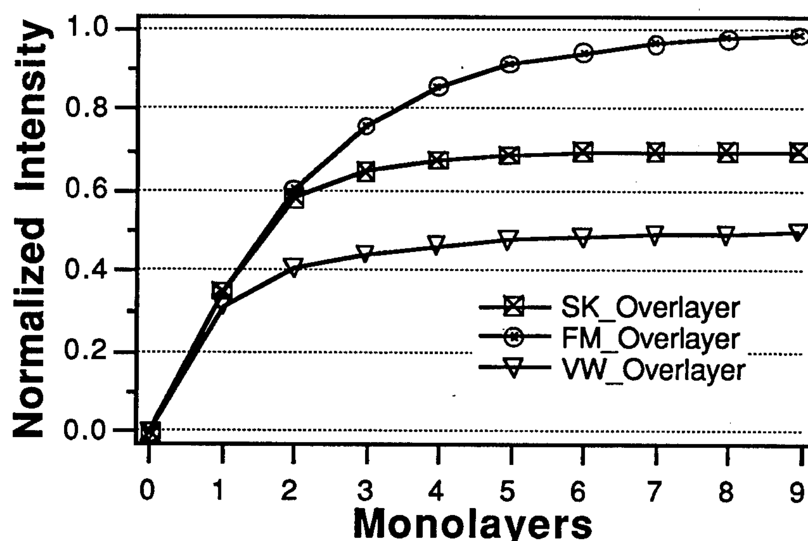

(b)

Figure 4. Attenuation curves for (a) substrate and (b) overlayer photoelectrons as a function of average coverage of an overlayer. In these examples the mean free path is taken as 2 monolayers and the islands cover 50% of the surface.

C1s photoelectron spectra revealed three important results: i) the substrate (TiC(111) plane) was carbon terminated, ii) the BEN process caused carbon vacancies on TiC as noted from the decay of C-Ti photoelectron signal, and iii) the resultant carbon was deposited in a "island-like" growth mode. These results suggested the BEN process formed vacancies similar to an ion implantation technique and may have increased the surface mobility of C atoms so they can migrate to form islands.

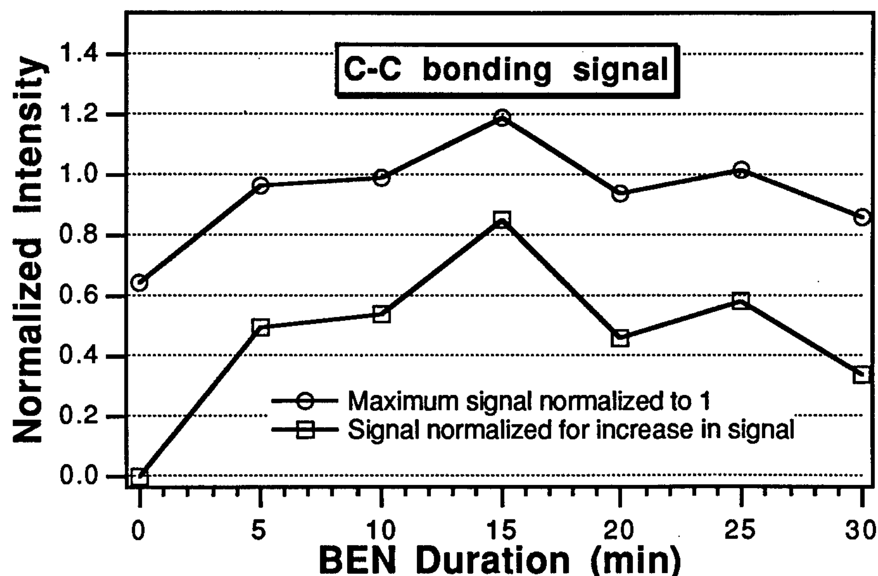

Figure 5. The normalized photoelectron intensity for C-C bonding as a function of BEN duration.

E. References

1. H. Meada, S. Masuda, K. Kusakabe and S. Morooka, Dia. Rel. Mat. **3**, 398 (1994).
2. S. Koizumi, T. Murakami, T. Inuzuka and K. Suzuki, Applied Physical Letters **57** (6), 563 (1990).
3. M. Kamo, H. Yurimoto and Y. Sato, "Epitaxial growth of diamond on diamond substrate by plasma assisted CVD" in *Proceedings of Proceedings of the Fourth International Conference on Solid Films and Surfaces (ICSFS-4),* Aug 23-27 1987, Hamamatsu, Jpn., edited by p. 553-560.
4. B. R. Stoner, G. H. Ma, S. D. Wolter, W. Zhu, Y.-C. Wang, R. F. Davis and J. T. Glass, Dia. Rel. Mat. **2**, 142 (1993).
5. B. R. Stoner, "Bias Enhanced Nucleation and Heteroepitaxial Growth of Diamond by Microwave Plasma Chemical Vapor Deposition," Doctor of Philosophy thesis, North Carolina State University, 1992.
6. P. C. Yang, W. Zhu and J. T. Glass, Journal of Materials Research **8** (8), 1773 (1993).
7. S. D. Wolter, B. R. Stoner, J. T. Glass, P. J. Ellis, D. S. Buhaenko, C. E. Jenkins and P. Southworth, Appl. Phys. Lett. **62** (11), 1215 (1993).
8. Y. Sato, I. Yashima, H. Fujita, T. Ando and M. Kamo, "Epitaxial Growth of Diamond from the Gas Phase" in *Proceedings of New Diamond Science and Technology,* Washington, D.C., September 23-27, 1990, edited by R. Messier, J. T. Glass, J. E. Bulter and R. Roy, (Materials Research Society, Pittsburgh, PA, 1991) p. 371.
9. X. Jiang, C.-P. Klages, R. Zachai, M. Hartweg and H.-J. Füsser, Appl. Phys. Lett. **62** (26), 3438 (1993).
10. C. Wild, R. Kohl, N. Herres, W. Müller-Sebert and P. Koidl, Dia. Rel. Mat. **3**, 373 (1994).
11. B. R. Stoner and J. T. Glass, Appl. Phys. Lett. **60** (6), 698 (1992).
12. W. Zhu, X. H. Wang, B. R. Stoner, G. H. M. Ma, H. S. Kong, M. W. H. Braun and J. T. Glass, Phys. Rev. B **47** (11), 6529 (1993).
13. S. D. Wolter, M. T. McClure, J. T. Glass and B. R. Stoner, Appl. Phys. Lett. **66** (21), 2810 (1995).
14. L. C. Feldman and J. W. Mayer, *Fundamentals of Surface and Thin Film Analysis,* (Elsevier, New York, 1986), p. 352.

III. Nucleation and Growth of Oriented Diamond Films in the Ni-C-H System

A. Introduction

The growth of highly oriented heteroepitaxial films represents an important step toward the attainment of large-area, device-quality diamond [1-3]. It has been known for decades that Ni and other transition metals are effective solvent-catalyst metals for diamond crystallization under high pressure and high temperature (HPHT) conditions [4]. The properties of diamond and the transition metals are shown in Table I. Nickel was chosen as a substrate material in this research because of its close lattice match (1.13%).

Table I. The Properties of Diamond and the Transition Metals.

Mater.	Electron Configur.	Crystal Structure	Lattice Const. (20°C, Å)	Density (20°C, g/cm^3)	Melt. Point (°C)	Coeff. Thermal Expansion (20°C, 10^{-6}/°C)	Electrical Resistivity (20°C, /mohm·cm)	Hydrogen Solubility (1 atm., ppm)	Me-C Eutectic M.P. (°C, wt.%C)	Carbides	Hydrides
Diam.	[He]$2p^2 2s^2$	fcc	3.56	3.52	3830	0.8	10^{14-16}	—	—	—	—
Ni	[Ar]$3d^8 4s^2$	fcc	3.52	8.91	1453	13.3	6.8	200 (420°C) 500 (900°C)	1326 (2.2%)	Ni_3C	NiH
Co	[Ar]$3d^7 4s^2$	hcp (α-Co) <417°C fcc (β-Co) >417°C	a=2.51 c=4.07 3.55	8.92	1495	12.5	6.2	65 (700°C) 134 (900°C)	1320 (2.6%)	Co_3C Co_2C	CoH CoH_2
Fe	[Ar]$3d^6 4s^2$	bcc (α-Fe) <912°C fcc (γ-Fe) >912°C	2.87 3.65	7.87	1536	12.6	9.7	120 (800°C) 250 (1000°C)	1147 (4.3%)	Fe_3C	x
Mn	[Ar]$3d^5 4s^2$	bcc(α-Mn) <727°C cub(β-Mn) >727°C	8.89 6.29	7.43	1245	22.8	185	600 (400°C) 1400 (800°C)	1231 (min. M.P. at 0.3%)	$Mn_{23}C_6$ Mn_3C Mn_5C_2 Mn_7C_3	MnH
Cr	[Ar]$3d^5 4s^1$	bcc	2.88	7.19	1875	6.2	12.9	13 (400°C) 44 (800°C)	1534 (3.6%)	$Cr_{23}C_6$ Cr_7C_3 Cr_3C_2	CrH CrH_2

The strong catalytic effect of Ni on hydrocarbon decomposition and subsequent graphite formation at low pressures have prevented CVD diamond nucleation on the Ni surface without the deposition of an intermediate graphite layer [5]. A graphite interlayer generally forms immediately when Ni substrates are placed in a methane-hydrogen CVD environment [6].

However, Badzian and Badzian [7] found that graphite formation is inhibited when Ni first forms a nickel hydride. In addition, Sato *et al.* and Fujita *et al.* [8] reported that both <111> and <100> oriented diamond nuclei could be grown on Ni substrates. However, the amount of orientation was rather limited, and no details were given about the deposition process.

Work that has led to the achievement of oriented diamond growth on Ni in the Ni-C-H system is reported here. We describe the process, characterize the deposited films, and develop a model to explain the nucleation mechanism. In addition, the results of diamond growth from the liquid phase are reported. Current investigations and plans for future work are reviewed.

B. Experimental

Oriented Diamond Growth. The experiments were carried out in both hot-filament and microwave CVD systems. Both (100) and (111) single crystal Ni and polycrystalline Ni were used as substrates. Substrates were polished using standard metal polishing techniques, the final polish being accomplished with a 1 μm diamond aerosol. Samples were then cleaned with trichloroethylene, acetone, and DI water. For subsequent seeding, the substrates were simply immersed in a diamond /acetone suspension, and a layer of diamond powders (<2 mm) was left on the Ni surfaces when the samples were removed.

The nucleation and growth was conducted through a three-step process including: deoxidation (step 1); high temperature annealing (step 2); and a standard diamond growth conditions (step 3) as shown in Fig. 1. Step 1 involved annealing the seeded substrates at a temperature of 900 °C in a hydrogen atmosphere for 10-30 minutes to remove oxides from the substrate surface.

In the hot filament CVD system, the substrates were heated by radiative heating from the tungsten filaments without an external heater. All cited temperatures were calibrated by the melting points of Ge and Ni-Cu alloys, as well as thermocouples attached to the substrate surface.

For step 2, the substrate temperature was raised to about 1100°C while the tungsten filament was held at a temperature of approximately 2300°C. At this high temperature and in the presence of atomic hydrogen the diamond seeds started to dissolve rapidly into the Ni lattice. The high temperature annealing time varied depending on the degree of seeding and the exact surface temperature. It is believed that the annealing time must be long enough to permit sufficient reaction between the nickel, diamond seeds, and hydrogen to form a Ni-C-H intermediate layer which suppresses graphite formation and promotes diamond nucleation. After the high temperature anneal, the substrate temperature was lowered to about 900°C and CH_4 gas flow at 0.5% was started to begin diamond growth. The experimental conditions of the multi-step process are summarized in Table II.

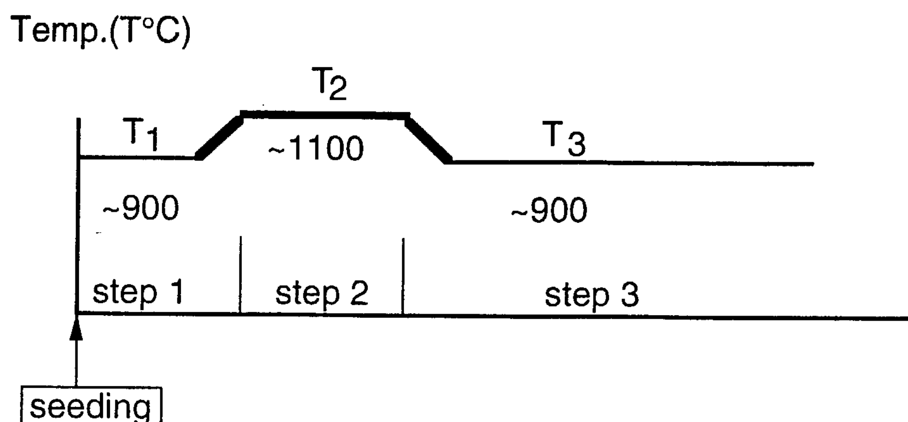

step1: de-oxidation
step2: high temperature annealing to form Ni-C-H surface phases
step3: nucleation and growth

Figure 1. The schematic diagram of the seeding and multi-step process.

Table II. Experimental Conditions of the Multi-step Process

	Substrate Temperature [°C]	CH_4/H_2 Flow Rate [sccm]	Duration Time
Step 1 Deoxidation	900	0/400	10-30 minutes
Step 2 High Temp Anneal	1100	0/400	10-60 minutes
Step 3 Regular Growth	900	2/400	4-20 hours

*P = 30 torr at all times

In practice, the duration of the anneal was effectively controlled by the visual appearance of the seeded substrates. The surface would change from dark gray in the initial annealing stage to reflective or "shiny" when the desirable Ni-C-H surface layer was formed. Laser reflection measurements were used to detect the surface reflectivity changes during the multi-step process. A HeNe laser beam was directed at the substrate and the reflection intensity was monitored. Figure 2 shows a typical intensity curve during the multi-step process. Initially the reflective light intensity is very low, because the light was scattered by the carbon seeds on the surface.

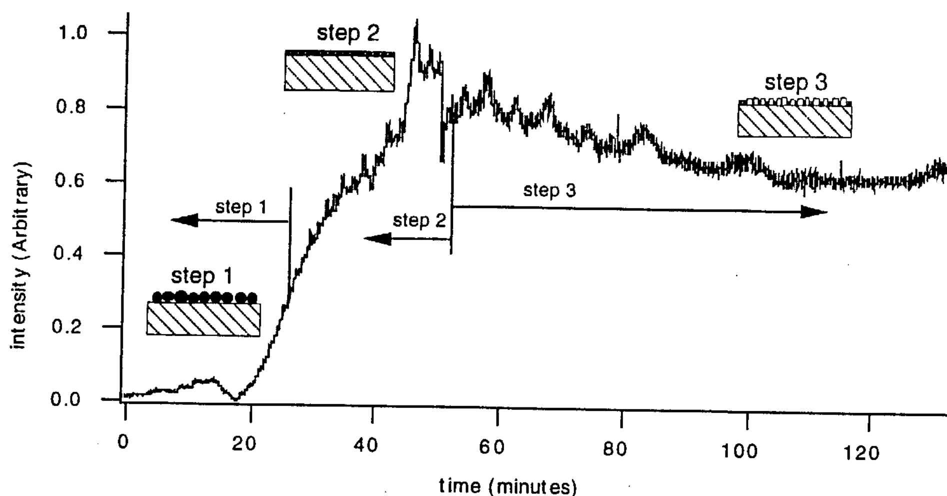

Figure 2. Laser reflection monitoring of the seeding and multi-step process.

The reflected light intensity increased rapidly when the substrate temperature was raised to about 1100°C where it approached a saturated value, possibly indicating the formation of a molten surface layer.

TEM Analysis of Oriented Growth Mechanism. To provide insight into the mechanism of diamond orientation on Ni plan-view and cross-section TEM samples of the oriented diamond on Ni were made. The plan-view samples were prepared by the standard method. For cross-section samples difficulties were encountered since diamond is hardest material known, and Ni is very soft. The following technique was developed to overcome some of the difficulties. Two samples are glued together with diamond particles sides face to face. Then the sample is placed into copper or molybdenum tube and cut into slices about 400 μm thick. The slice is first flatted, dimpled, and polished to 60 μm on one side. Then the sample is turned over and further ground and polished to the minimum thickness possible. Finally, the sample is ion milled by using "sector rotation speed control," which rotates the specimen slowly when the ion beam is perpendicular to the layer in the specimen and rapidly through the remaining sectors. Although time-consuming, this procedure was found to successfully yield TEM samples from which high quality micrographs were obtained.

Liquid Phase Diamond Growth. A liquid phase diamond growth method has been developed to grow diamond from a Ni-C solution in an atomic hydrogen environment at low pressures. The experiment was conducted in a HFCVD system, as shown in Fig. 3. Nickel and graphite (2.3 wt%) powders are mixed and put into an alumina crucible. As a reference, at 2.2 wt% nickel and carbon form a eutectic at 1327°C at atmospheric pressure. The crucible is then placed under a tungsten filament which is maintained at a temperature of 2300°C. The Ni and C powders are heated to a molten state and kept there for about 3 hours in a hydrogen ambient. The molten Ni-C solution is cooled down to room temperature. The resulting solid

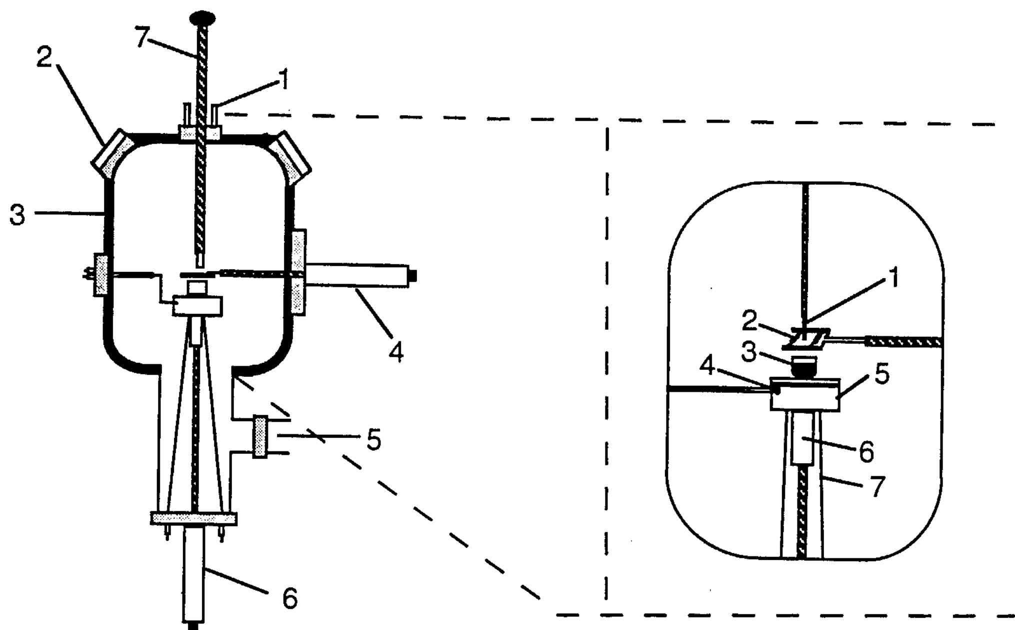

1--Gas Inlet
2--Viewports
3--Water Cooling
4--Linear Transfer for filament
5--to Pump
6--Sample Manipulator
7--Seed Holder

1--Seed
2--Filaments for creating atomic H
3--Crucible
4--Thermocouple for controlling growth temperature
5--h-BN heater
6--h-BN support
7--Heater wires

Figure 3. System for diamond growth.

assumes a ball-like shape due to surface tension. During the cool down process supersaturated carbon precipitates on the surface in the form of diamond particles.

C. Results

Oriented Diamond Growth. The oriented diamond films grown on Ni substrates using diamond seeding were first investigated by scanning electron microscopy (SEM). Figures 4 and 5 show SEM micrographs of oriented diamond films deposited by HFCVD on single-crystal (111) and (100) Ni, respectively. Micro-Raman was performed by focusing an argon laser, at a wavelength of 514.5 μm, on the diamond surface with a spot size of approximately 5 μm. A representative Raman spectrum is shown in Fig. 6, confirming the high-quality of the diamond. A very small amount of graphite (no amorphous sp^2C) is observed on the substrate areas not covered by the diamond nuclei.

X-ray diffraction has been utilized to probe the formation of an interfacial carbide phase [9]. A high nucleation density diamond film was prepared using the multi-step process on a single-crystal {100} Ni substrate. A micrograph of the high density film is presented in

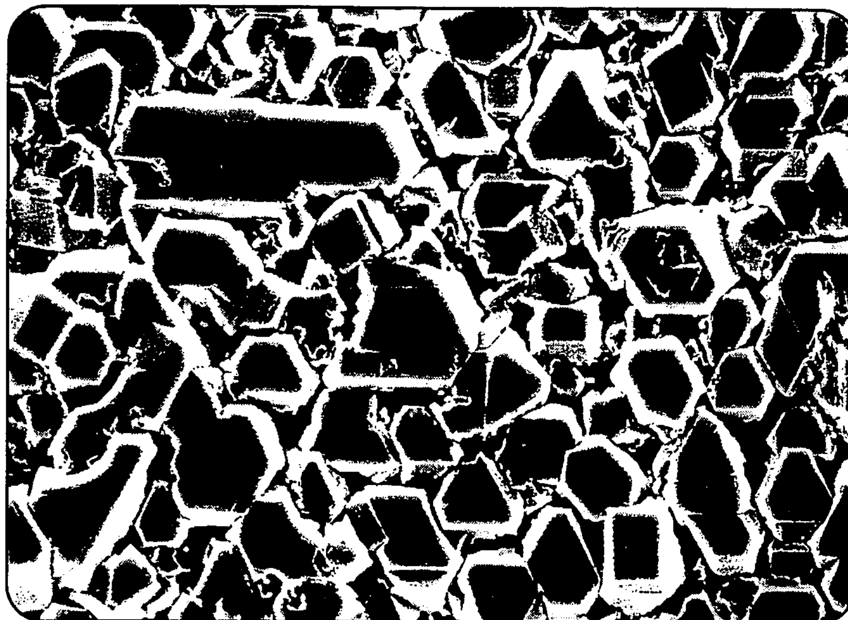

(a) —5 μm

(b) — 2.5μm

Figure 4. SEM micrographs of diamond films grown on a (111) oriented single crystal Ni surface. (a) An overview at low magnification and (b) a high magnification image.

Figure 5. The 45° tilted SEM micrograph of a (100) oriented diamond film on a Ni substrate.

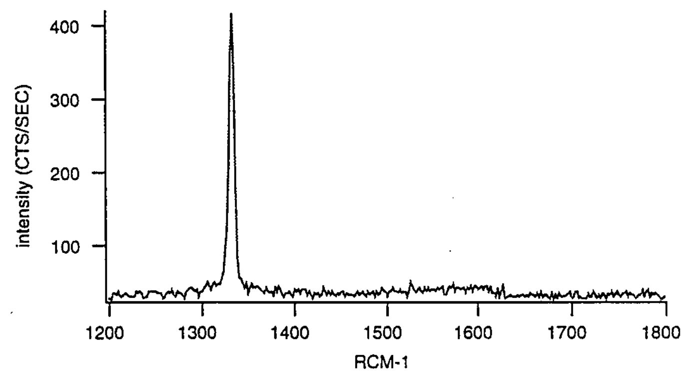

a

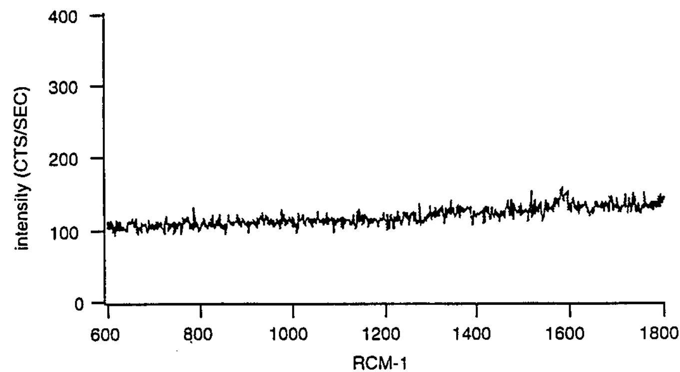

b

Figure 6. (a) A typical Raman spectrum from the diamond nuclei and (b) Raman spectrum from the substrate not covered by the diamond nuclei.

Fig. 7, which clearly shows coalescence of the (100) oriented diamond particles. Phase identification by X-ray diffraction (XRD) was undertaken using the wide-film Debye-Scherrer X-ray technique developed by Read. The XRD photograph from the diamond on nickel sample is shown in Fig. 8. Generally speaking, the observed diffraction pattern consists of two components: (i) a set of strong diffraction spots from the single crystal Ni substrate; and (ii) weaker diffraction lines from the thin film growth. The latter component may be further divided into lines of two types: (a) a set of "grainy" lines from a phase or phases exhibiting a large grain (°5 μm) structure; and, (b) a set of smooth lines from a phase or phases exhibiting a small grain structure (<5 μm). The XRD data is summarized in Table III.

Table III. X-ray Diffraction Data from a (100) Oriented Diamond Film on Ni

Actual Data	d (Å)	structure (hkl) [intensity in brackets]
5.19	3.593	
5.52	3.273	3.348 (002) [100] graphite
7.96 (S+G)	2.022	2.039 (111) [100] Ni_4C
same	same	2.027 (101) [15] graphite
same	same	2.06 (111) [100s] diamond
9.10 (S)	1.744	1.765 (200) [80] Ni_4C
13.34 (G)	1.259	1.261 (220) [25] diamond
13.64 (S)	1.243	1.259 (022) [60] Ni_4C

In particular, "grainy" lines are observed at d spacings of 2.03 Å and 1.26 Å which is attributable to diffraction from diamond crystallites [d=2.06 Å for the {111} diamond and d=1.26 Å for {220} diamond]. This interpretation is bolstered by SEM images that show identifiable diamond crystallites with grain sizes on the order of 5 μm (see Fig. 7). Furthermore, smooth lines are found in similar positions: 3.32; 2.03-04, 1.75 and 1,24 Å, essentially coincident with the "grain" diamond lines.

It appears that small graphite crystallites contribute to the lines at 3.32 Å [d=3.35 Å for {100} graphite] and 2.03-2.04 Å [d=2.03 Å for {101} graphite]. Small grains of cubic Ni_4C phase may be associated with the smooth lines at 2.03-2.04 Å [d=2.04 Å for {111} Ni_4C], 1.75 Å [d=1.75 Å for {200} Ni_4C], and 1.24 Å [d=1.26 Å for {022} Ni_4C].

The X-ray scattering results indicate the presence of three phases in the thin film deposition. Diffraction from diamond crystallites with relatively large grain sizes dominates, but weaker and smoother lines from graphite and Ni_4C crystallites with relatively small grain sizes are readily detected. The presence of the graphitic phase is not particularly surprising

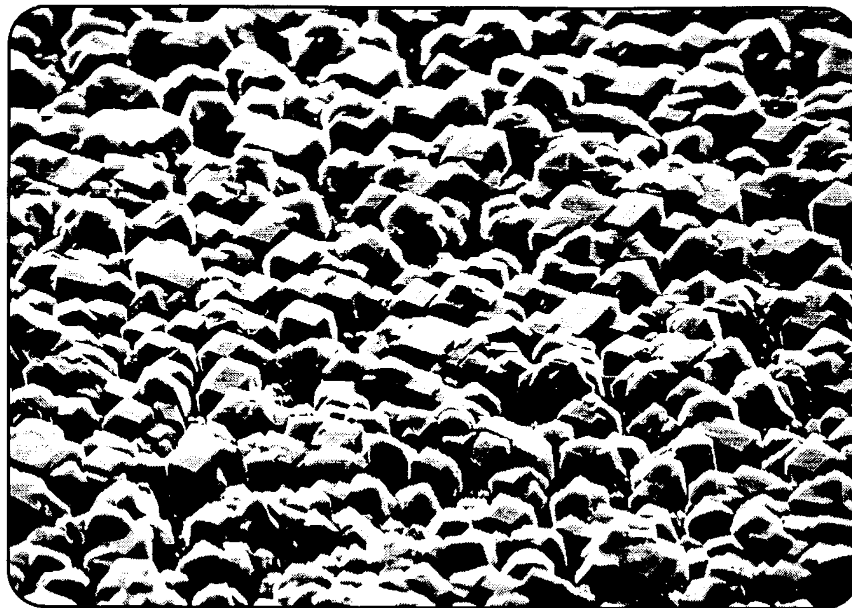

Figure 7. SEM micrograph of high density (100) oriented diamond film on a Ni substrate which is used in the x-ray diffraction analysis.

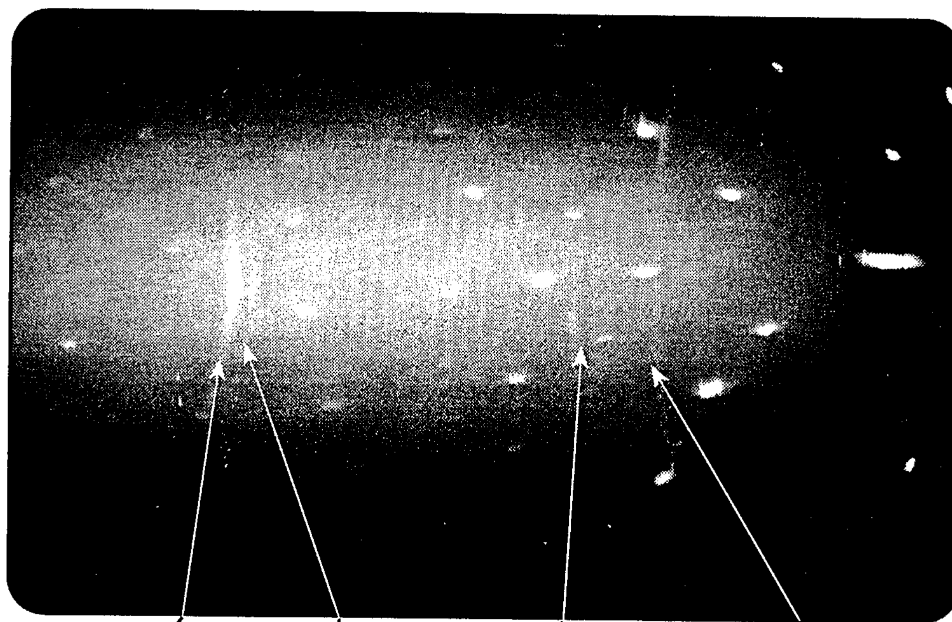

Figure 8. X-ray diffraction photograph of the high density (100) oriented diamond film on the (100) single crystal Ni substrate.

because the deposition conditions are not entirely uniform across the whole substrate. More importantly the X-ray diffraction lines are consistent with the presence of a metastable Ni_4C phase which is normally very difficult to detect due to the broad overlap of polycrystalline X-ray patterns for Ni, diamond, and Ni_4C. The observed separation of the scattering vectors from these three components is somewhat fortuitous, and is attributed to the single-crystal nature of the Ni substrate and the difference in the grain sizes of the diamond and Ni_4C phases.

It can be seen that the {022} and {200} Ni_4C lines are relatively strong compared to the {111} lines of diamond. This suggests that the C/Ni ratio is at least 25% [10,11]. The Ni_4C is in a NaCl structure with carbon atoms in the octahedral interstitial sites.

TEM Analysis of Oriented Growth Mechanism. A cross-section TEM specimen was prepared from a sample of oriented diamond on Ni after 4 hours of growth. Figure 9 shows a TEM micrograph of two oriented diamond particles which was attained after the sample preparation discussed above. There are three distinct regions in Fig. 9: (i) the diamond crystal, (ii) the Ni substrate, and (iii) an irregular interlayer of Ni_4C approximately 0.5 mm thick. SAD analysis (photographs also shown in Fig. 9) clearly identifies each phase.

The (200) ring is the special diffraction line which shows the presence of the Ni_4C phase. From the ring pattern, it can be concluded that the fine grain polycrystalline Ni_4C phase was formed between diamond and Ni substrate. For diamond the (200) reflection is forbidden,

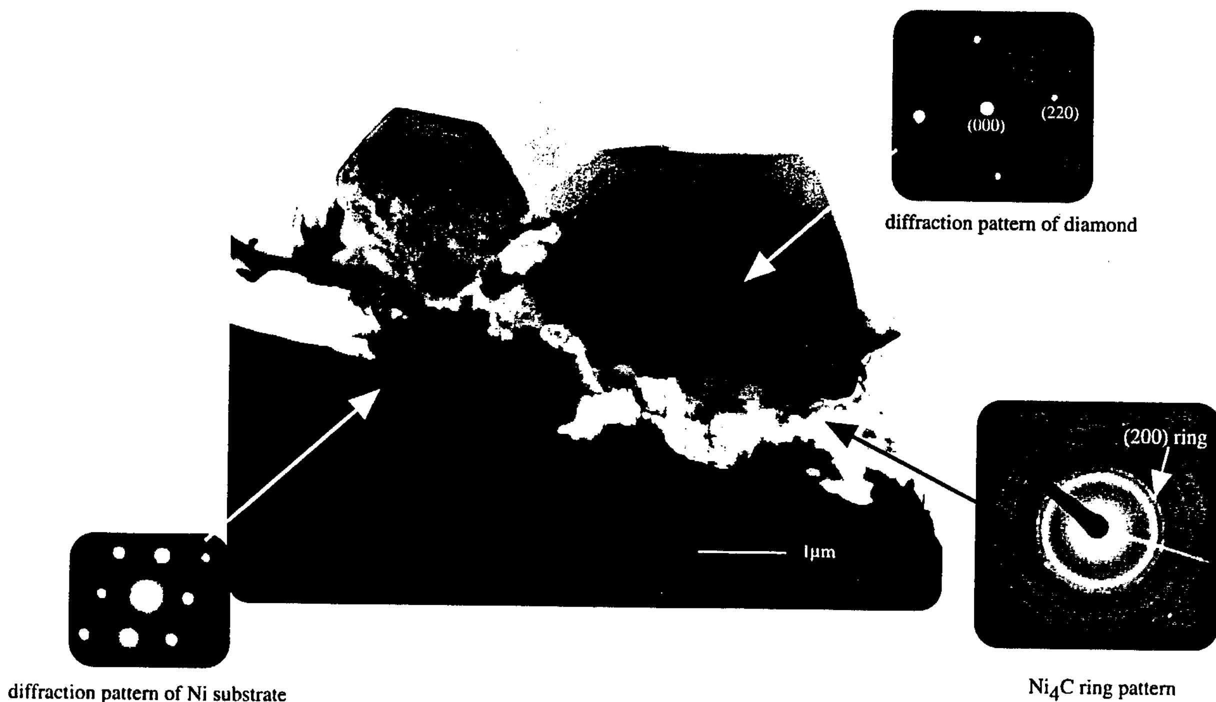

Figure 9. Cross-section TEM analysis of the interfacial Ni_4C phase involved in the nucleation and growth of oriented diamond on Ni.

although it may be allowed if the particles are either defective or too small. However, the SEM micrographs show relatively large (°5 mm) crystallites and there are no signs of twinning or other macroscale defects. The [100] zone axis diffraction pattern can be used to identify the diamond as shown in Fig. 9.

Liquid Phase Diamond Growth. Figure 10 shows the SEM micrographs of diamond particles grown on the surface of the molten Ni-C ball. Figure 11 shows the Micro-Raman spectrum obtained from these diamond particles. As only hydrogen gas was present, the results demonstrate that the carbon is supplied from the liquid phase, not the vapor phase. The melting point of the Ni-C solution is reduced appreciably by atomic H to about 1100°C. Also, it is speculated that the solubility of C in Ni may be enhanced by the presence of atomic hydrogen. The experimental results show that diamond can be grown from a liquid phase.

D. Discussion

Oriented Diamond Growth. Based on experimental evidence from the multi-step deposition process, the model shown schematically in Fig. 12, was proposed to understand the mechanism of oriented nucleation and growth of diamond on nickel substrates. In the first step a single crystal nickel substrate is seeded with carbon powders, either diamond or graphite. When the seeded substrate is heated to about 1100°C in a hydrogen atmosphere reactions among nickel, carbon, and atomic hydrogen occur and eventually lead to the formation of a molten, Ni-C-H eutectic compound on the surface. These two steps can also be accomplished by saturating the nickel surface with gaseous carbon species at 1100°C.

During the subsequent cooling to a substrate temperature of 900-950°C diamond nucleation is initiated from the molten eutectic compound at the surface, which is now anticipated to be supersaturated with carbon. The diamond nuclei grow with an epitaxial relationship to the substrate which has a very close lattice constant to that of diamond. Finally, diamond grows out from the nuclei and forms oriented diamond particles using normal CVD diamond growth conditions.

This model emphasizes the importance of forming a molten Ni-C-H surface layer during the high temperature anneal in hydrogen. Evidence for this can be seen in the area surrounding oriented diamond particles on nickel, where flow patterns have been observed on the substrate using contrast microscopy, as shown in Fig. 13. The step increase in the reflection intensity shown in Fig. 2 is also consistent with surface melting.

For the observed surface melting to occur at 1100°C or below, atomic hydrogen must play an important role in the depression of the eutectic melting point. Badzian has also reported the melting of Ni at 1150°C when annealed in a hydrogen plasma [7], much below the melting point of Ni at 1450°C.

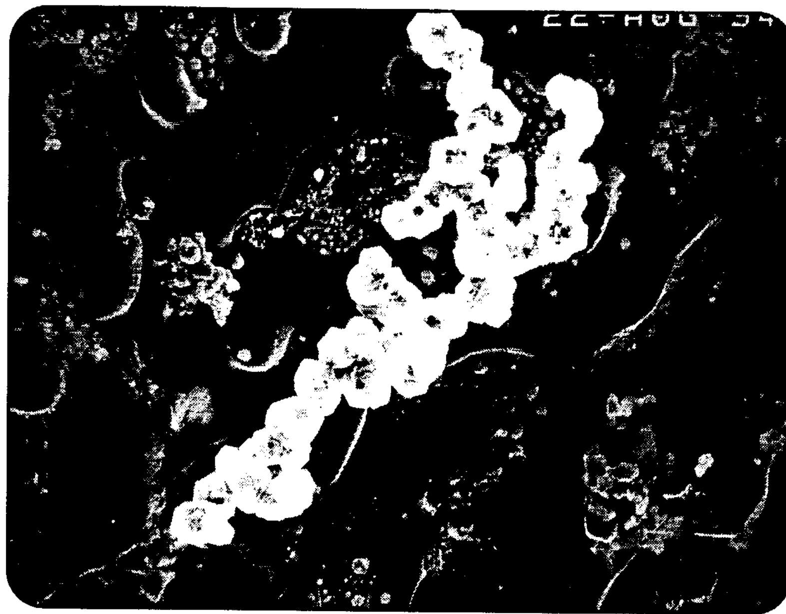

10μm

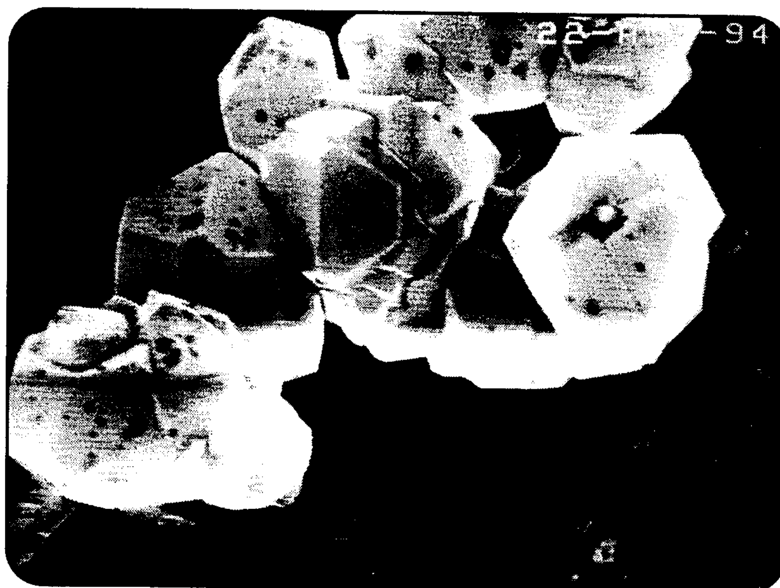

3μm

Figure 10. Diamond particles on the surface of molten Ni-C ball.

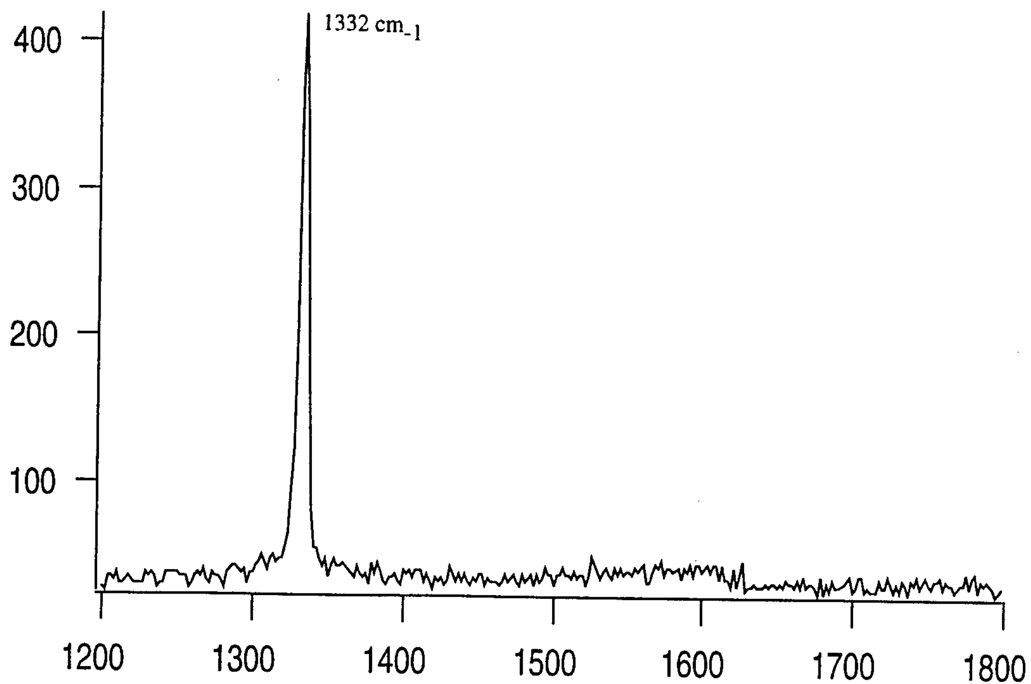

Figure 11. Micro-Raman spectrum on the diamond particles.

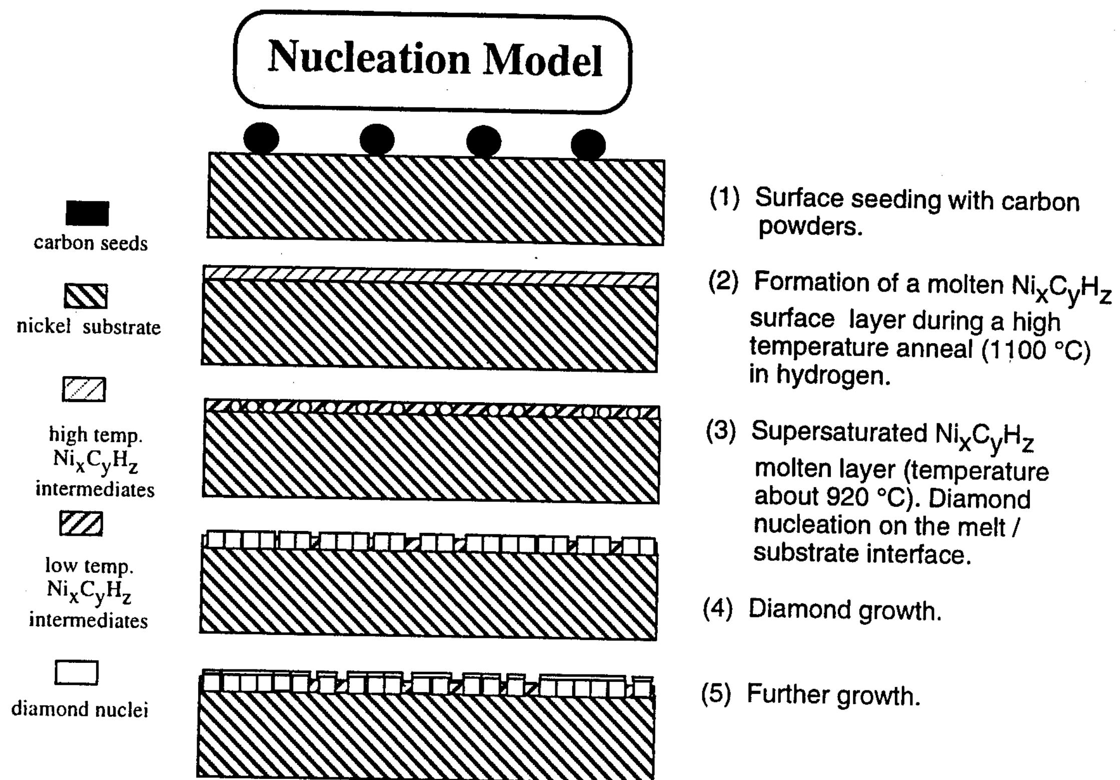

Figure 12. Nucleation model of the seeding and multi-step deposition process.

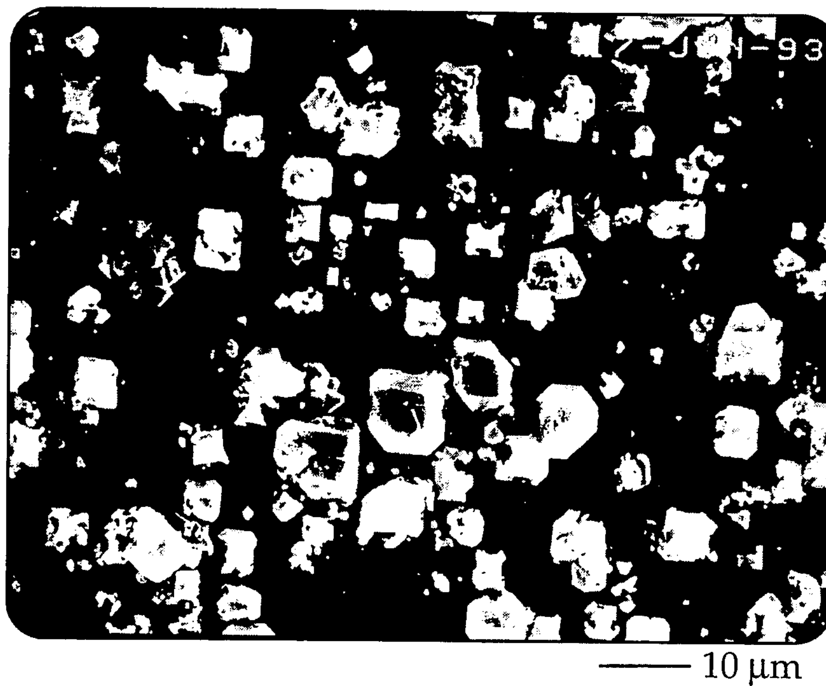

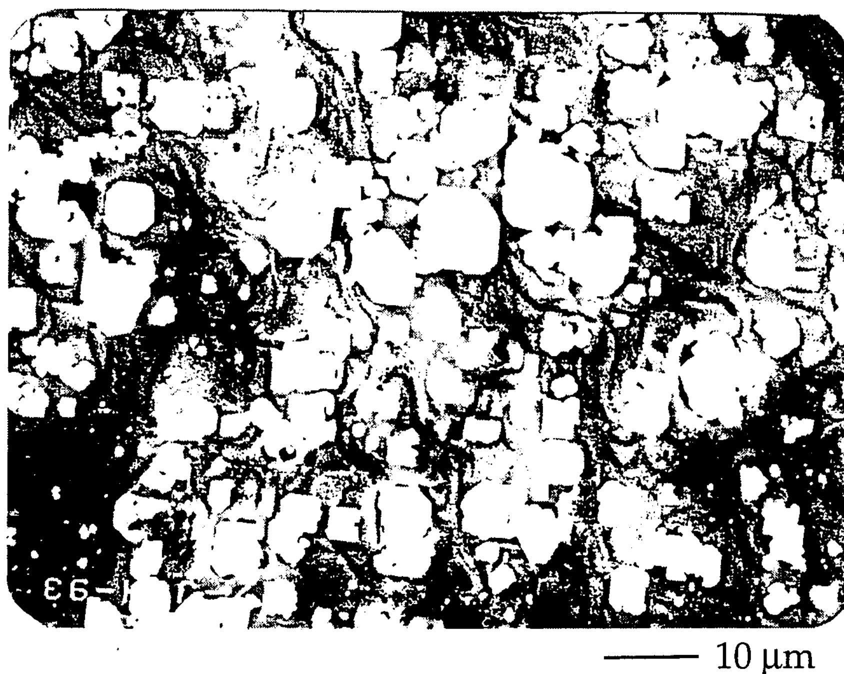

Figure 13. SEM micrographs of the (100) oriented diamond films on the Ni substrate with a different contrast in order to illustrate the evidence of surface melting and flow patterns.

The basic findings here are analogous to diamond formation using Ni by the HPHT process [12]. The free energy difference between non-diamond carbon and diamond at the high synthesis pressure and temperature results in graphite being more soluble than diamond in the same solvents. If the catalytic effects operate, diamond will crystallize from the solution. The nickel-carbon phase diagram at 57 kbars as worked out by Strong and Hanneman [13] shows that diamond crystallizes near the eutectic point from supersaturated C due to the solubility difference between diamond and graphite in Ni in the hypereutectic region. The temperature interval between the liquidus and the eutectic in this region is about 60°C. A similar mechanism is thought to exist in the multi-step process. However, the required energy is now supplied by atomic hydrogen instead of excessive pressures.

TEM Analysis of Oriented Growth Mechanism. The TEM and X-ray diffraction analysis shows the presence of the Ni_4C interlayer. The metastable Ni_4C carbide phase can be characterized as a NaCl-type structure with Ni occupying the fcc lattice positions of Na, and carbon occupies statistically some of the lattice positions of Cl, i.e. the octahedral interstitial sites of Ni lattice. Figure 14 depicts the (111) planes of Ni and carbon atoms in Ni_4C. The top layer is Ni and carbon atoms sit in the 3-fold interstitial position 1.04 Å beneath the surface Ni layer. In the figure the bold triangle shows an area where 6 nickel atoms lie on the surface and one carbon atom resides in the octahedral interstitial position. If a group of carbon atoms is now placed on top of each hollow position of this triangle, the effect of the interstitial C atom No. 1 on the No. 2 atom is different from that on the No. 3, 4, and 5 atoms. Under the influence of atomic hydrogen the interstitial carbon atom changes the electronic configuration of the Ni atoms. This difference affects the influence of interstitial carbon atoms on the alternate network and will tend to pucker the graphite plane network such that the sp^2 C is not stable. Therefore, an sp^3 C precursor could be formed. The same consideration can be applied to the case where the carbon atoms No. 3, 4, and 5 are on the tetrahedral position directly on top of the Ni atoms.

Yang and Whitten *et al.* [14] calculated the effects of subsurface Na, H and C on the bonding of carbon to nickel surfaces and conclude that tetrahedral CH_3 binds strongly to Ni(111) when an interstitial Na or H atom is present. The hydrogen calculation is in good agreement with the present experiments. Atomic H in the lattice appears to play a very important role in stabilizing the tetrahedral carbon bonding formation.

It is likely that the seeded carbon atoms dissolve into the surface Ni-C-H liquid as free atoms, and the intermediate Ni_4C phase will be formed under the influence of atomic hydrogen and catalytic properties of Ni. This Ni_4C structure will favor formation of a tetrahedral sp^3 C precursor and maintain the orientational relationship between diamond and Ni.

Liquid Phase Diamond Growth. The arguments of the previous two subsections apply to the liquid phase growth. The presence of atomic hydrogen facilitates the formation of a low temperature Ni-C-H eutectic. Upon cooling the carbon become supersaturated and precipitates

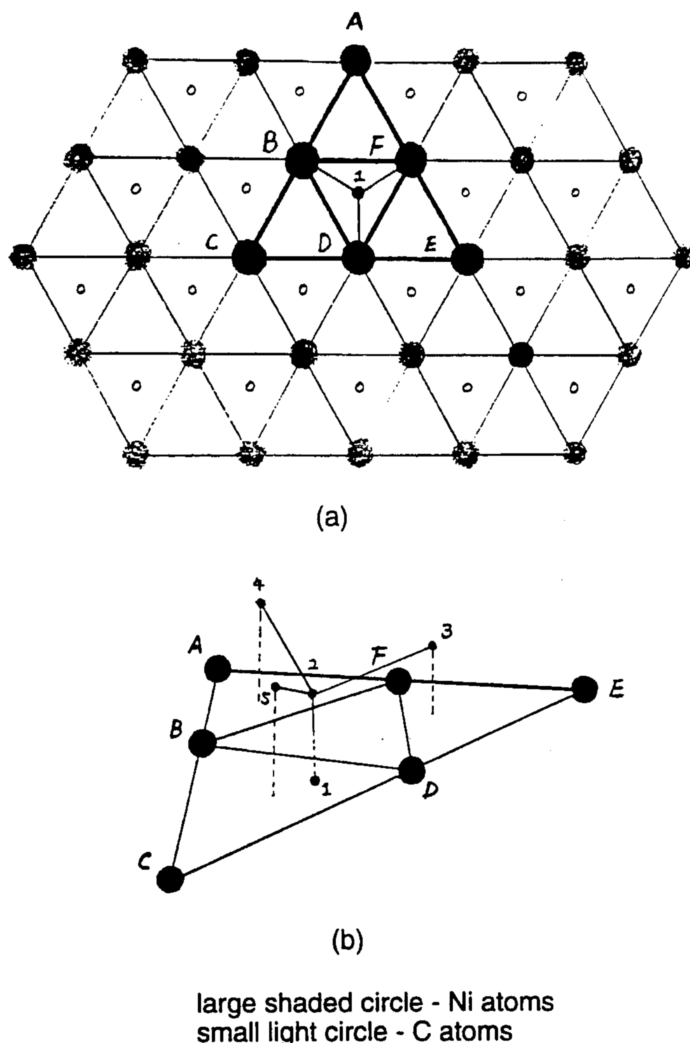

Figure 14. (a) Ni (111) planes with the carbon atoms in the interstitial sites 1.04Å beneath the Ni layer; (b) sp^3 C precursor originated from the Ni_4C structure.

on the surface as diamond. In fact, the success of the liquid phase experiments is further support for the existence of a molten surface phase. One would expect that a similar Ni_4C structure is formed prior to diamond precipitation, although that has not been investigated. One difference is that since the entire bulk is liquid, the orientation of the diamond particles is random.

E. Conclusions

Oriented diamond films have been achieved on both (100) and (111) single crystal Ni substrates using a multi-step method. *In-situ* laser reflectometry is used to monitor and control the process. Cross-sectional TEM and X-ray diffraction demonstrate the formation of a polycrystalline Ni_4C interlayer. A model is proposed to explain the nucleation mechanism, and structure arguments show why sp^3C precursors are stabilized on Ni_4C. The key to the process

involves a molten surface layer of Ni-C-H. The presence of atomic hydrogen dramatically reduces the melting temperature of this phase and facilitates the dissolution of seeded C into the Ni. Similarly, diamond growth has been demonstrated from liquid phase Ni-C in the presence of atomic hydrogen.

F. Future Research Plans and Goals

Oriented Diamond Growth. The focus of current work is directed at a better understanding of the surface molten phase. Specifically, the differential thermal analysis (DTA) is being used to determine the exact melting temperature as a function of composition. In addition, studies are planned using a microbalance to provide *in-situ* monitoring of mass changes. The reactor has been modified to allow for precise temperature control, and the process will be optimized with respect to the duration of the annealing stage (step 2), and the rate of cooling between step 2 and step 3.

In addition, future research work will concentrate on obtaining continuous, single crystal diamond films on Ni substrates. Because of the high solubility of C in Ni, a high growth rate is very important for getting highly oriented diamond facets to grow together (coalesce) after the nucleation stage by the seeding and multi-step process. We have demonstrated the growth of highly oriented <100> diamond films on Si substrates in a combustion growth system using pre-nucleated substrates prepared in a microwave bias enhanced growth system [15]. Similarly we plan to grow oriented films on samples that have been nucleated using the multi-step process. The growth rate of the combustion system is at least 10 μm/hour, which should favor growing out the oriented diamond nuclei to coalescence to form single crystal diamond films.

TEM Analysis of Oriented Growth Mechanism. The reactor has been modified to allow for rapid ($>70° s^{-1}$) quenching of samples. Quenched samples will be obtained from different stages of the multi-step process and subsequent SEM and TEM analysis will be performed to monitor microstructure evolution. In addition, chemical analysis is planned to ascertain the composition of the Ni-C-H phase.

Liquid Phase Diamond Growth. Having achieved diamond precipitation from the melt, the next step is controlling the precipitation and achieving it on a diamond or non-diamond seed. First of all, a top-seeded technique, will be used to grow diamond on a diamond seed or non-diamond seeds (such as Mo, W, and Al_2O_3). The critical parameters such as temperature control and viscosity of the solution need to be optimized. The seed will be chosen for lattice-match with diamond, chemical properties and physical shape, which are key factors for liquid phase growth. It is also very important to optimize the conditions to create enough atomic H to form the Ni-C-H intermediate state. By precise control of the degree of carbon supersaturation in the solution, the diamond can be precipitated from the Ni-C-H intermediate state and nucleated on the seed and then grown.

G. References

1. B. R. Stoner, D. M. Malta, A. J. Tessmer, J. Holmes, D. L. Dreifus, R. C. Glass, A. Sowers, and R. J. Nemanich, "Highly Oriented Diamond Films on Si: Growth, Characterization and Devices," in Proceedings of Diamond-Film Semiconductors, SPIE-The International Society for Optical Engineering, Los Angeles, California, (by the Society of Photo-Optical Instrumentation Engineers, (1994) p. 147.
2. P. C. Yang, W. Zhu, and J. T. Glass, Journal of Materials Research **8**, 1773 (1993).
3. C. Wild, R. Kohl, N. Herres, W. Müller-Sebert, and P. Koidl, Diamond and Related Materials **3**, 373 (1994).
4. H. P. Bovenkerk, F. P. Bundy, H. T. Hall, and H. M. Strong, Nature **184** (1959).
5. D. E. Ramaker, "CEELS as a Probe of the Carbide ite Transformation on Ni," in *Proceedings of New Diamond Science and Technology*, Washington, DC, Eds., J. T. G. Russell Messier, James E. Butler and Rustum Roy (Materials Research Society, 1991) p. 379.
6. D. N. Belton and S. J. Schmieg, Journal of Applied Physics **66**, 4223 (1989).
7. A. Badzian and T. Badzian, "Routes to diamond heteroepitaxy," in *Proceedings of Chemical Vapor Deposition of Refractory Metals and Ceramics II*, Boston, Massachusetts, Eds., T. M. Besmann, B. M. Gallois, and J. W. Warren (Materials Research Society, 1992) p. 339.
8. Y. Sato, H. Fujita, T. Ando, T. Tanaka, and M. Kamo, *Philosophical Transactions of the Royal Society of London* A **342**, 225 (1993).
9. T. J. Kistenmacher, Private Communication
10. R. Bernier, Ann. Chim. **6**, 104 (1951).
11. A. R. Badzian and A. Klokocki, Journal of Crystal Growth **52**, 843 (1981).
12. R. H. Wentorf, The Journal of Physical Chemistry **75**, 1833 (1971).
13. H. M. Strong, Acta Metallurgica **12**, 1411 (1964).
14. H. Yang, J. L. Whitten, and R. J. Markunas, Applied Surface Science **75** (1993) 12.
15. S. D. Trent, J. T. Glass, B. R. Stoner, and J. T. Prater, "Growth of Oriented Diamond Films via Ox-Acetylene Combustion," in *Proceedings of 5th Annual Diamond Technology Workshop*, Troy, MI, 1994) p. 65.

IV. Donor Doping of Diamond Using Nuclear Transmutation

A. Introduction

Nuclear transmutation has been proposed for donor doping of diamond [1]. The goal of this process is to convert boron incorporated during growth to interstitial lithium through the reaction $^{10}B(n,\alpha)^{7}Li$. Calculations indicate that interstitial Li in diamond produces a shallow acceptor state [2]. This doping mechanism is of interest in diamond because of difficulties encountered in attempts to incorporate Li by more conventional means such as diffusion or incorporation during CVD. A similar transmutation process has been used for low and uniform doping of Si with P for high power applications through the conversion $^{30}Si(n,\gamma)^{31}Si$ which then decays to ^{31}P. Some important differences between the two processes are the nature of the atom to be converted and the effect of radiation damage on the lattice. First, for the case of boron in diamond, one is converting a acceptor dopant to a donor dopant. As a result, a large majority, probably greater than 90%, of the boron must be converted to avoid compensation, requiring a large neutron dose. Secondly, the diamond lattice can be irreversibly converted to graphite if the radiation damage is too great.

Previous work in this area has included neutron irradiation of ^{10}B doped polycrystalline films and annealing studies of the resulting damage. These studies indicated that damage from doses as large as 2.6×10^{20} n/cm^{-2} could be recovered by annealing [3]. However, electrical measurements have not been reported.

There are several technical and scientific challenges that must be overcome in evaluating the transmutation of boron in diamond. A suitable source of isotopically pure ^{10}B must be identified. A high neutron flux must be available, as a dose of 5×10^{20} n/cm^{2} is estimated to be necessary to convert a large fraction of the ^{10}B and avoid compensation. Evaluation of electrical measurements made after irradiation must be done with care, as irradiation damage can lead to defect conduction. In addition, grain boundaries can alter both conduction and diffusion processes if polycrystalline films are used [4]. Furthermore, the possibility of lithium diffusion through the lattice after conversion must be considered.

In response to these challenges, our approach has been to investigate transmutation in well characterized homoepitaxial films grown by established techniques. Growth and electrical measurements have been performed at Kobe Steel USA by researchers with extensive experience in electrical measurements on homoepitaxial and polycrystalline diamond film. Our isotopically pure boron source is diborane, one of the most common doping sources of boron for CVD diamond growth. The carrier concentration and mobility have been measured as a function of temperature prior to irradiation. In addition, our experiments include control samples with no boron and with the natural abundance of boron to separate the effects of irradiation damage from the effects of Li production. We are also in contact with a group at Oak

Ridge National Laboratory which can provide a neutron flux of 2×10^{15} n/cm^{2}s which can produce the desired dose in 3 days of continuous irradiation.

Table I. Samples and target boron content. All films are grown on (100) oriented type 2a natural diamond substrates. The natural isotopic abundance of boron is 19% ^{10}B and 81% ^{11}B.

Sample	Boron Content (Target value, cm^{-3})	Isotopic Composition
1	10^{18}	natural abundance
2	10^{20}	natural abundance
3	10^{18}	^{10}B enriched
4	10^{20}	^{10}B enriched
5	10^{20}	^{10}B enriched

B. Experimental Procedure

Homoepitaxial boron doped films have been grown using microwave CVD with diborane as to dopant source. Growth conditions were similar to previously reported work by researchers at Kobe Steel USA [5]. Table I shows the target boron concentrations for each of the five films. All films are grown on (100) oriented type 2a natural diamond substrates and range from 3 to 8 microns in thickness. The films were grown over a 3×3mm^2 area on the 4×4mm^2 substrates to isolate the films from the edges of the wafers. The edges of natural diamond wafers have a higher conductivity which has lead to anomalous results in the past. This selected area deposition also facilitates measurement of the film thickness. Films with the natural abundance of the two boron isotopes are included to aid in separating the effects of Li production from the effects of damage. The natural isotopic abundance of boron is 19% ^{10}B and 81% ^{11}B, so the maximum possible conversion of the natural abundance samples (#1 and #2) is 19%. Samples 4 and 5 have the same boron content to provide a duplicate experiment. In addition, measurements can be made of the back surfaces of the diamond wafers to analyze the effects of neutron irradiation on diamond which is free of boron.

Metal contacts consisting of Ti and Au were applied. The carrier concentration and mobility were measured at several temperatures from 300 to 600 K using the Hall effect in a van der Pauw geometry. Descriptions of the metallization process and Hall measurements can be found in publications by researchers at Kobe Steel [5].

C. Results and Discussion

The measured room temperature values of resistivity, mobility, and carrier concentration for the five films are given in Table II. These quantities are plotted as a function of temperature

in Fig. 1 (resistivity), Fig. 2 (mobility), and Fig. 3 (carrier concentration). The two samples with lower boron concentrations yield similar results in the electrical measurements, as do the more heavily doped samples. Mobility values are lower for the more highly doped samples, as would be expected. Samples 4 and 5 with the same target boron concentration vary in carrier concentration be nearly a factor of 10. This variation could be caused by different doping levels or by different percentage activation. The true boron concentration will be measured via SIMS after the irradiation experiments are completed. SIMS measurements have been deferred to avoid possible damage to the samples.

Table II. Room Temperature Values of Resistivity, Mobility, and Carrier Concentration for Homoepitaxial Boron-doped Films Which Will be Irradiated.

Sample	Boron content (Target, cm^{-3})	Thickness (μm)	Resistivity (Ω-cm)	Mobility (cm^2/Vs)	Carrier Concentration (cm^{-3})
1	10^{18}	6.2	19	933	3.49×10^{14}
2	10^{20}	5	8	53	1.50×10^{16}
3	10^{18}	8	20	1160	2.70×10^{14}
4	10^{20}	5.5	10	62	9.91×10^{15}
5	10^{20}	3.3	2	32	1.13×10^{17}

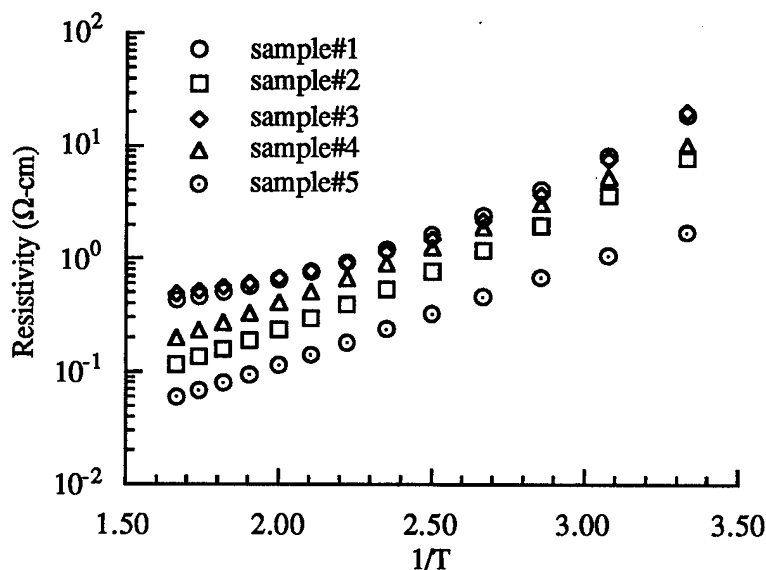

Figure 1. Resistivity as a function of 1/T for the five homoepitaxial films which will be irradiated.

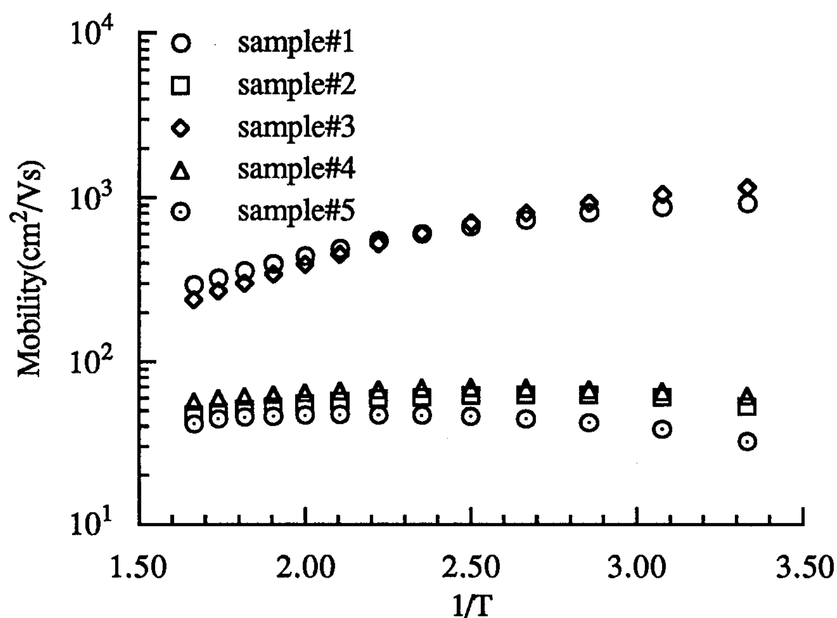

Figure 2. Hole mobility as a function of 1/T for the five homoepitaxial films which will be irradiated.

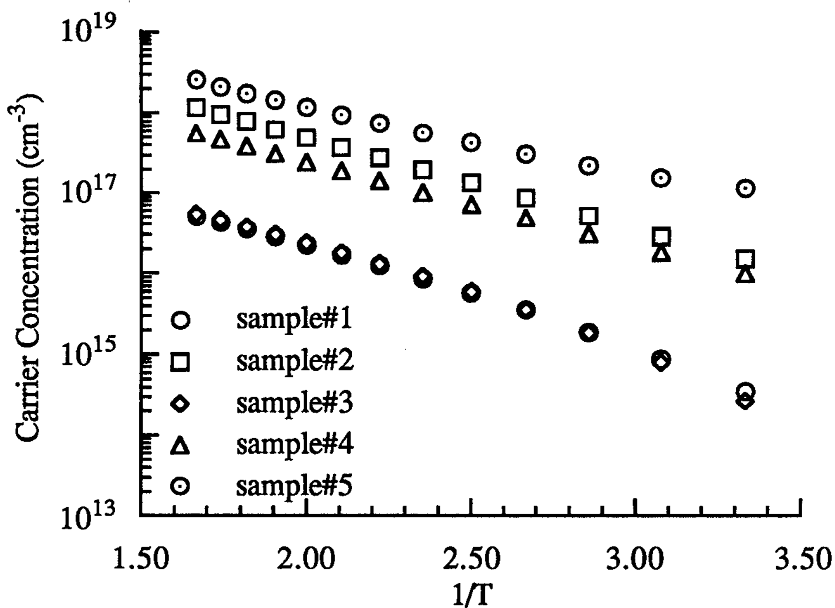

Figure 3. Carrier concentration (p-type) as a function of 1/T for the five homoepitaxial films which will be irradiated.

D. Conclusions

In summary, nuclear transmutation is being investigated as a means for donor doping of diamond. To date samples have been prepared for irradiation and baseline electrical measurements have been performed.

E. Future Research Plans and Goals

The next steps in the project are (1) completion of pre-irradiation characterization, (2) neutron irradiation, (3) characterization and annealing studies post irradiation. The complexity of the post irradiation studies will be determined by the amount of damage produced in the irradiation process. Post irradiation studies will begin with optical assessment of the damage via Raman and Photoluminescence spectroscopy. Electrical characterization via I-V measurements and Hall effects measurements will then be performed. If the carrier type is changed by the irradiation process, different contact materials may be necessary. Following the electrical measurements SIMS can be used to measure the percentage of boron converted to lithium. Finally, if the electrical measurements are promising, RBS-channeling may be used to determine the lattice location of the lithium.

F. References

1. B. Spitsyn, G. Popovici and M. A. Prelas, *Second International Conference on the Applications of Diamond Films and Related Materials*, edited by M. Yoshikawa, M. Murakawa, Y. Tzeng and W. A. Yarbrough, Tokyo, Japan, 1993, 57-64.
2. S. A. Kajihara, A. Antonelli, J. Bernholc and R. Car, Physical Review Letters **66**, 2010 (1991).
3. S. A. Khasawinah, G. Popovici and H. White, Journal of Materials Research **10**, 2523 (1995).
4. J. Y. W. Seto, Journal of Applied Physics **46**, 5247 (1975).
5. D. M. Malta, J. A. v. Windheim, H. A. Wynands and B. A. Fox, Journal of Applied Physics **77**, 1536 (1995).

V. Negative Electron Affinity Surfaces of Aluminum Nitride and Diamond

R. J. Nemanich, P. K. Baumann, M. C. Benjamin, S. W. King, J. van der Weide, and R. F. Davis

Department of Physics and Department of Materials Science and Engineering
North Carolina State University
Raleigh, NC 27695-8202

Abstract

The electron affinity of diamond and AlGaN surfaces are studied by UV photoemission spectroscopy. It is shown that H terminated diamond surfaces exhibit a negative electron affinity while oxide terminated surfaces exhibit a positive electron affinity. In addition, thin metal layers can also induce a NEA on both (100) and (111) surfaces of diamond. Photoemission results of AlGaN alloy films grown on 6H-SiC indicate a negative electron affinity for as-prepared and air exposed surfaces with high Al concentrations.

To be published in the Proceedings of Diamond Films '95

Introduction

Wide bandgap semiconductors have the potential of exhibiting a negative electron affinity (NEA). These materials could be key elements of cold cathode electron emitters which could be used in applications that include flat panel displays, high frequency amplifiers, and vacuum microelectronics. The surface conditions are shown to be of critical importance in obtaining a negative electron affinity. In this paper, angle resolved UV-photoemission spectroscopy (ARUPS) is used to explore the effect for diamond and AlGaN surfaces. The value of UV photoemission in characterizing electron emission is that the technique emphasizes effects of the emission process. To fully characterize electron emission properties it is necessary to also employ additional measurements such as distance dependence of field emission, and secondary electron emission. These measurements have recently been compared for properties of CVD diamond films [1].

The electron affinity of a semiconductor is defined as the energy required to remove an electron from the conduction band minimum to a distance macroscopically far from the semiconductor (i.e. away from image charge effects.). At the surface this energy can be shown schematically as the difference between the vacuum level and the conduction band minimum. The electron affinity is not, in general, dependent on the Fermi level of the semiconductor. Thus while doping can change the Fermi level in the semiconductor and the work function will change accordingly, the electron affinity is unaffected by these changes. An alternative view is that the electron affinity is a measure of the heterojunction band offset between the vacuum and a semiconductor of interest. For most semiconductors, the conduction band minimum is below the vacuum level and electrons in the conduction band are bound to the semiconductor by an energy equal to the electron affinity. In some cases, surface conditions can be obtained in which the conduction band minimum is above the vacuum level. In that case the first conduction electron would not be bound to the sample but could escape with a kinetic energy equal to the difference in energy of the conduction band minimum and the vacuum level. This situation is termed a negative electron affinity. (Note that the electron is still bound to the vicinity of the sample by coulomb forces.)

The electron affinity or work function of a material is usually ascribed to two aspects of the material (1) the origin of the atomic levels, and (2) the surface dipole due to the surface termination [2]. These effects are shown schematically in Fig. 1. The atomic levels are more or less intrinsic to a material and cannot be changed. This is not the case for the surface dipole. The surface dipole can be substantially affected by surface reconstructions and surface adsorbates. As a simple example to illustrate the magnitude of this effect consider a surface with hydrogen termination, and assume that the average nuclear and electronic charges are point charges separated by 0.5Å. Then for a surface density of 1×10^{15} cm^{-2} we would find a ~9eV effect due to the surface dipole. (Certainly complete charge transfer is never a reasonable

possibility, but this simple calculation demonstrates the significance of the surface dipole.) Because of the large effect of the surface dipole, it is essentially impossible to determine if a material is "intrinsically NEA." Thus the surface termination is critical in describing the electron affinity (or NEA) properties of a material.

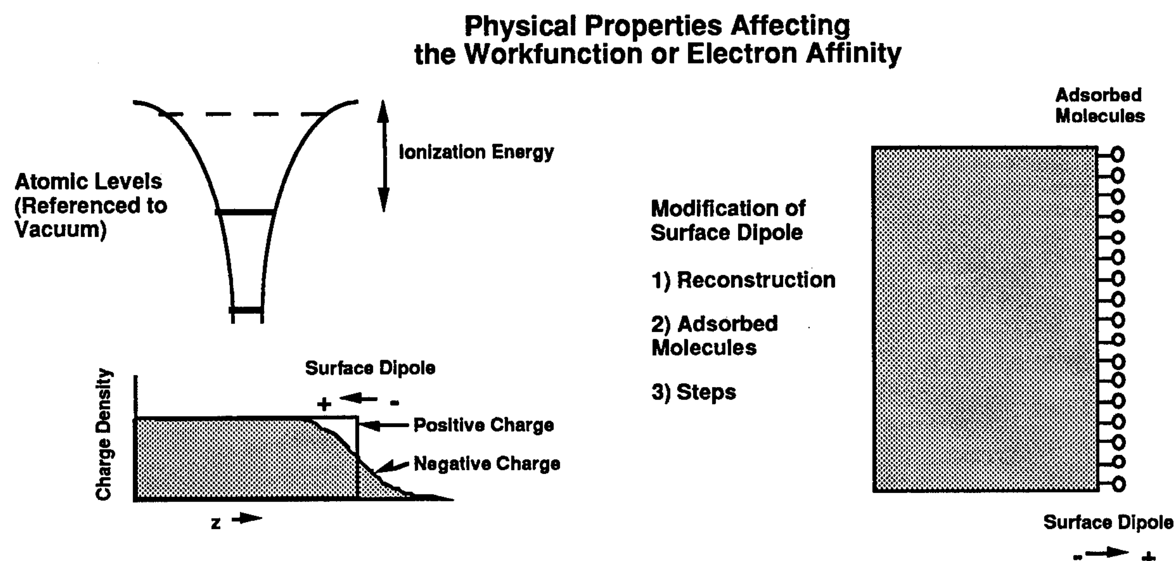

Figure 1. A representation of the effects which contribute to the workfunction (or electron affinity) of any material. While the atomic levels are an intrinsic property of the material, changes in the surface bonding can substantially affect the workfunction or electron affinity.

One method to measure the electron affinity of a semiconductor is UV-photoemission [3,4]. The changes in the spectra due to NEA are indicated in Fig. 2. [5] The electrons from the valence band are excited into the conduction band. In transiting towards the surface, electron scattering occurs and a large number of secondary electrons accumulate at the valence band minimum. For materials with a positive electron affinity these electrons cannot escape, while for a NEA the electrons can be emitted directly and will be observed with a low kinetic energy. Thus the two effects which signify a NEA are an extension of the spectral range to lower energy and the appearance of a sharp peak at low kinetic energy. This feature will appear at the largest (negative) binding energy in typical presentations of UPS spectra.

In addition to the sharp feature that is often evident in the spectra of a NEA semiconductor, the width of the photoemission spectrum (W) can be related to the electron affinity. The spectral width is obtained from a linear extrapolation of the emission onset edge to zero intensity at both the low kinetic energy cutoff and at the high kinetic energy end (reflecting the valence band maximum). From Fig 2. it is evident that we can write the following relations:

$\chi = h\nu - E_g - W$ for a positive electron affinity

$0 = h\nu - E_g - W$ for a negative electron affinity

where E_g is the bandgap and hν is the excitation energy. We stress that the photoemission measurements cannot be used to determine the energy position of the electron affinity for the NEA surface. Careful measurements of the width of the spectra are helpful in distinguishing whether the effect is direct emission of the electrons from conduction band states or whether excitons are involved in the emission process. The effects of excitons have recently been reported by Pate and co-workers [6].

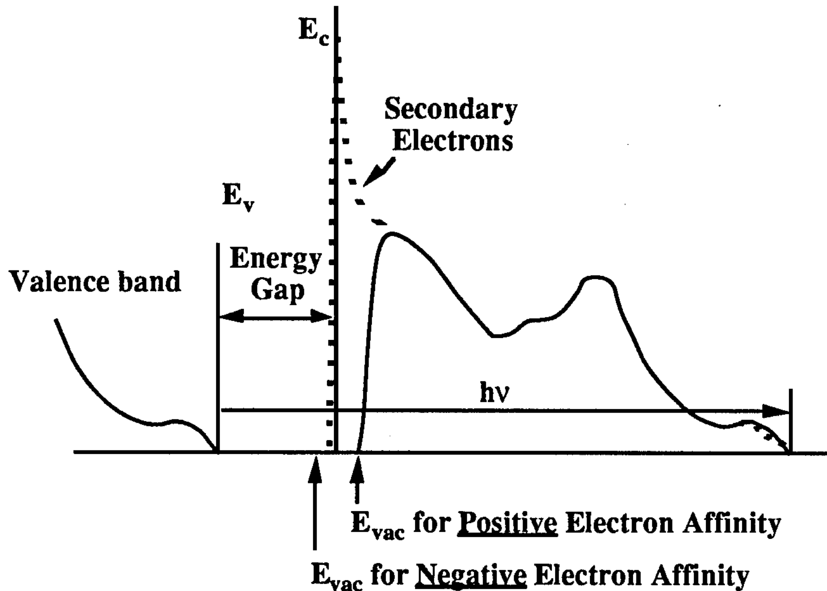

Figure 2. A schematic of how NEA affects the photoemission spectra. For a NEA surface the spectra is broadened to lower kinetic energy and a peak due to quasi thermalized electrons is detected also at the lowest kinetic energy.

In addition to measurement of the electron affinity, the position of the surface Fermi level can be obtained. For a grounded sample, the Fermi level of the sample will be the same as that of the metal holder. The Fermi level of the metal can easily be determined, and the energy difference of the valence band maximum and the metal Fermi level gives the position of the surface Fermi level of the semiconductor.

Experimental Procedure

The experiments described in this summary paper were carried out in an integrated UHV system with surface preparation, film growth and surface characterization capabilities. The system consists of eight chambers interconnected by a linear sample transfer mechanism. The overall length of the sample transfer chamber is ~35ft. A portion of the system is shown schematically in Fig. 3. This figure shows the relations of the UV photoemission system, the plasma surface processing system, the LEED/Auger systems, and the MBE chamber. In the

experiments described here, the UV-photoemission measurements were made with HeI (21.21eV) radiation and the electrons were analyzed with a VSW HAC50 50mm mean radius hemispherical electron analyzer. The spectra were collected at normal emission with a collection angle of ~2°. The sample was biased with ~1 to 3V so that the low energy electrons can overcome the work function of the analyzer. While higher sample bias can be employed, the low bias used here is to minimize spectral distortions that occur due to changes in the effective collection angle for the higher sample bias.

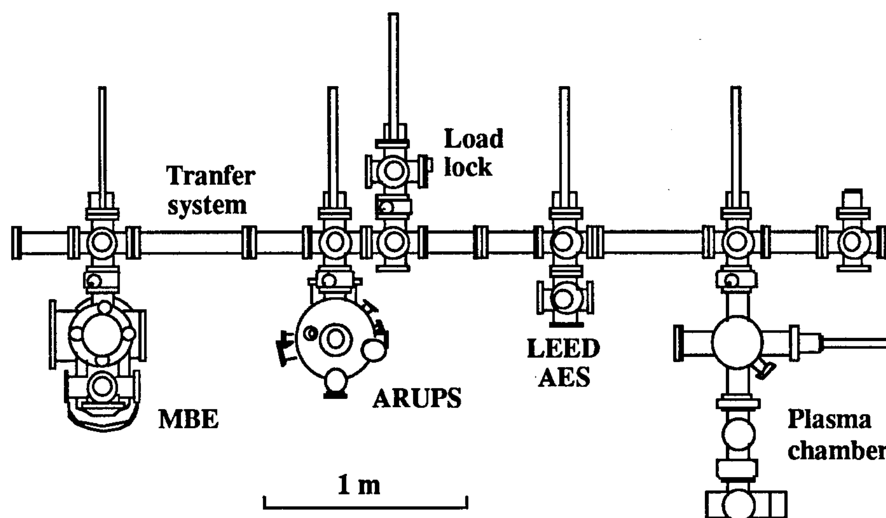

Figure 3. A schematic of a portion of the integrated surface processing and characterization system used in the studies described here.

In the studies of diamond, H plasma, Ar plasma exposures and anneals in UHV have been employed to process the diamond (100) and (111) surfaces. Following each surface preparation step the surfaces were characterized with UPS, LEED and AES. The effects of metals on the surfaces were also considered. In these measurements thin layers of Ni, Ti, Cu and Co have been deposited on diamond (100) and (111) surfaces. The metals were deposited on substrates terminated by oxygen, hydrogen or free of adsorbates. The Schottky barrier height Φ_B can be measured by means of UPS. For a p-type semiconductor the Schottky barrier height is determined by the difference between the valence band edge and the Fermi level. For metal film thicknesses less than or equal to the electron mean free path ($\leq$ 5Å) both the Fermi level of the metal as well as the valence band edge of the diamond can be observed by photoemission spectroscopy.

To avoid charging and to obtain high quality epitaxy, the AlGaN films were grown on (0001) 6H-SiC substrates. The substrates were supplied by Cree Research, Inc. [1] The SiC wafers were n-type with doping concentrations of 10^{16} to $10^{18}/cm^3$. The AlGaN alloy samples

were grown by CVD (OMVPE) in a remote location and transported in ambient to the analysis system. Clean, as-grown surfaces of AlN and GaN were prepared in the integrated UHV transfer system (described above) by gas source molecular beam epitaxy (GSMBE), and transferred directly to the UPS system. The Al concentration of the alloy samples was estimated from respective cathodoluminescence measurements.

Electron Affinity of Diamond Surfaces

As-loaded diamond (100) samples exhibit oxygen surface contaminants as evidenced by AES and a 1×1 unreconstructed LEED pattern, and a positive electron affinity is observed by photoemission spectroscopy. Following a 900°C–1050°C anneal in UHV, the oxygen is removed from the surface. The annealing temperatures vary depending on the chemical pre treatment of the diamond samples prior to loading into UHV [7-10]. The oxygen is removed at 900°C for samples cleaned by an electrochemical etch and at 1050°C for those treated with a chromic acid clean. However in both cases the removal of oxygen from the diamond (100) surface coincides with a 2×1 reconstructed LEED pattern and with the appearance of a sharp low-energy peak indicative of a NEA in the UPS spectra. This feature is positioned 15.7eV below the energy of the valence band maximum in the spectrum. This value corresponds to the width of a spectrum from a NEA diamond surface (i.e. 0=21.2eV-5.5eV-15.7eV). Subsequent to a hydrogen plasma exposure the intensity of the NEA peak is found to be doubled. And upon heating the samples to 1150°C the UPS spectra are indicative of a positive electron affinity. However the NEA can be induced again by another H plasma exposure. Following both the H plasma cleans and the 1150°C anneal the surface remained 2×1 reconstructed and the AES spectra did not change. It is suggested that a H plasma clean results in a uniform monohydride-terminated surface. From the intensity differences of the NEA emission it is estimated that approximately half the surface is covered by a monohydride subsequent to an anneal at the lowest temperature when oxygen is no longer observable by AES. A 1150°C anneal is thought to remove the hydrogen from the surface leading to a positive electron affinity. In addition ab initio calculations for the 2×1 reconstructed surface suggest a NEA for the monohydride-terminated surface and a positive electron affinity for the clean surface [8].

Similarly a NEA can be induced on the diamond (111) surface by employing a H plasma [11]. The NEA can be removed from the surface either by means of an anneal to 950°C or alternatively by an Ar plasma exposure. A second exposure to a H plasma leads to a NEA again. The NEA is associated with a hydrogen terminated surface. Whereas the 950°C anneal and the Ar plasma clean remove the hydrogen from the surface. Either one of these processes leads to a clean surface which exhibits a positive electron affinity. A number of UPS spectra on both diamond (100) and (111) surfaces are shown in Fig. 4.

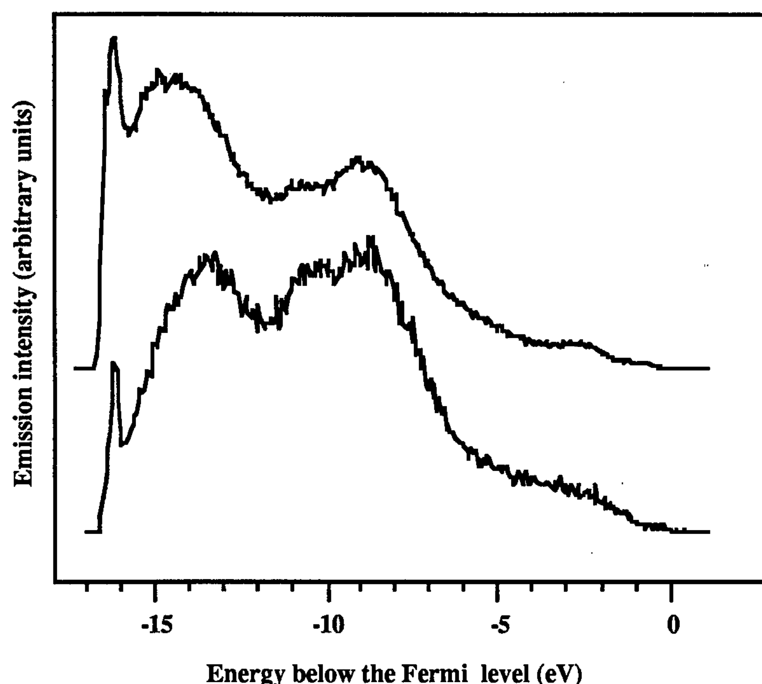

Figure 4. UV photoemission spectra of monohydride terminated diamond (100) and (111) surface. Both surfaces exhibit a NEA.

The first demonstration of a negative electron affinity of semiconductors was most likely Cs coated GaAs. Here we consider the effects of metals deposited on diamond substrates. A Schottky barrier of Φ_B = 0.5 eV and a metal induced NEA are determined for Ni on the clean diamond (111) face. However depositing Ni on a monohydride terminated (111) surface leads to a value of Φ_B = 1.0 eV and a positive electron affinity [12]. For Ti on the adsorbate free diamond (111) face, a Schottky barrier of 1.0 eV and a NEA are obtained [13]. Similarly Cu grown on the clean C(100) surface results in Φ_B = 1.0 eV and a NEA [7]. For Co deposited on the clean C(100) surface a Schottky barrier of 0.35 eV and a NEA are obtained. In contrast, for Co on the oxygen terminated C(100) face, Φ_B = 1.45 eV and a positive electron affinity is found. Results from photoemission measurements of metals on diamond are summarized in Fig. 5.

Erwin and Pickett [14–17] and Pickett, Pederson and Erwin [18] performed theoretical studies of the Ni–diamond interface. A Schottky barrier height of less than 0.1 eV was calculated for the most stable configurations on the clean diamond (100) and (111) surfaces. For copper on diamond (111) surfaces the Schottky barrier height was calculated depending on the interface structure by Lambrecht [19]. A Schottky barrier of less than 0.1 eV was determined for the adsorbate free surface and ≥ 1.0 eV for the hydrogen terminated surface. Similar values for both Ni and Cu on clean surfaces are obtained. And these results indicate that the Schottky barrier depends on the interface termination.

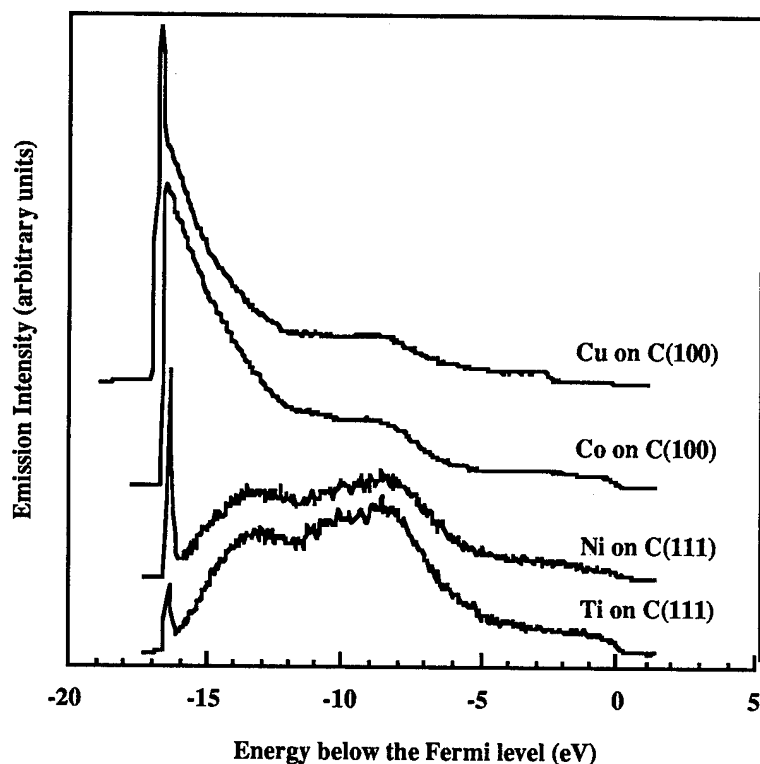

Figure 5. UV Photoemission spectra of metals on clean diamond (100) and (111) surfaces. A low energy peak indicative of a metal induced NEA is observed for all cases shown.

From the results on Ni and Co it can be concluded that the Schottky barrier height for metals deposited on clean diamond surfaces is less than that for surfaces terminated by hydrogen or oxygen. Metal–diamond interfaces with a lower Schottky barrier also exhibit a lower electron affinity. Indeed, surface preparation can significantly affect the Schottky barrier height and the electron affinity for metals on diamond.

Electron Affinity of AlGaN Surfaces

The UV photoemission spectra of AlN, GaN and the two alloy samples are shown in Fig. 6 [20,21]. Samples were biased with 2-3 V to overcome the work function of the analyzer, and all spectra were shifted to be aligned at the valence band maximum. The spectra were scaled such that the strongest emission was the same for all curves.

The first aspect to be noted is that the spectra of the Al rich alloy and AlN exhibit sharp strong features at the highest binding energy, which corresponds to the lowest kinetic energy. These features are often indicative of a negative electron affinity. As noted in the introduction, the feature is attributed to emission from electrons quasi-thermalized to the conduction band minimum. The emission from the $Al_{0.13}Ga_{0.87}N$ sample is significantly weaker, and the GaN emission does not show the sharp peak at all.

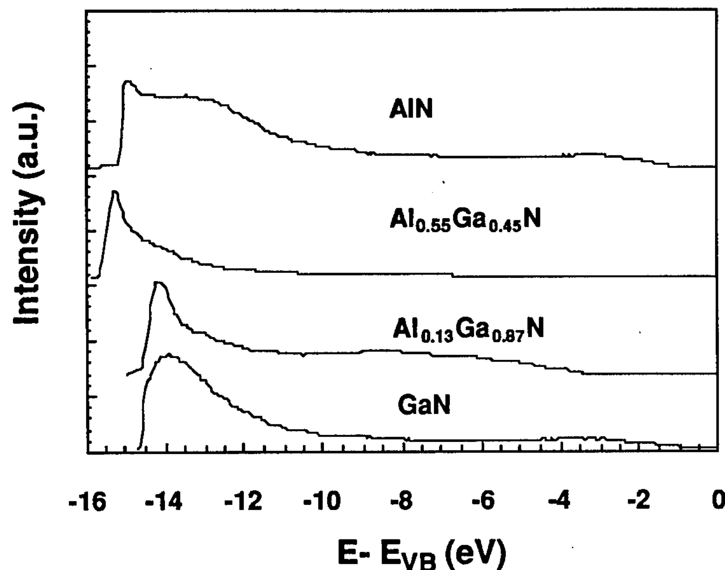

Figure 6. The UV photoemission spectra of $Al_xGa_{1-x}N$ films grown on 6H-SiC.

A second indication of the change in electron affinity with alloy concentration is the extension of the $Al_xGa_{1-x}N$ spectra to lower energy as x is decreased. A more precise description of the relation of the NEA is obtained from the spectral width. To determine the energy position of the valence band maximum, each spectrum was magnified, and the intensity was extrapolated to 0 emission. The spectral widths obtained from the $Al_xGa_{1-x}N$ samples were 14.5, 14.5, 15.5, and 15 eV for x=0, 0.13, 0.55, and 1.0, respectively. To apply the relations noted above, the bandgap of each sample must also be known. The reported values of the AlN and GaN bandgaps are 6.2 and 3.4 eV respectively. The band gap of the alloy samples was determined from the respective cathodoluminescence measurement. Using the relations described above, the AlN satisfies the relations for a NEA, while the $Al_{0.55}Ga_{0.25}N$ surface exhibits a low but positive electron affinity. The GaN and $Al_{0.13}Ga_{0.87}N$ surfaces, do not satisfy the relations for a NEA. We can, however, determine the value of the electron affinity of these materials and find that χ = 3.3 eV and 2.9 eV for x = 0 and 0.13, respectively.

Another aspect that is evident from the photoemission spectra is the position of the surface Fermi level relative to the valence band maximum. It was found that E_F ranges from 2 to 3.5 eV above the valence band maximum for each sample. For the GaN and $Al_{0.13}Ga_{0.87}N$ surfaces, these values position E_F in the upper part of the gap while for the Al rich samples, the values indicate that the surface Fermi level is pinned near midgap. The surface Fermi level position and the bandgap of the alloys are indicated in Fig. 7. The pinning at midgap may be an indication of surface states or increased impurity incorporation. In particular, the strong affinity of Al with oxygen may result in increased oxygen incorporation at the surface or in the bulk of these films.

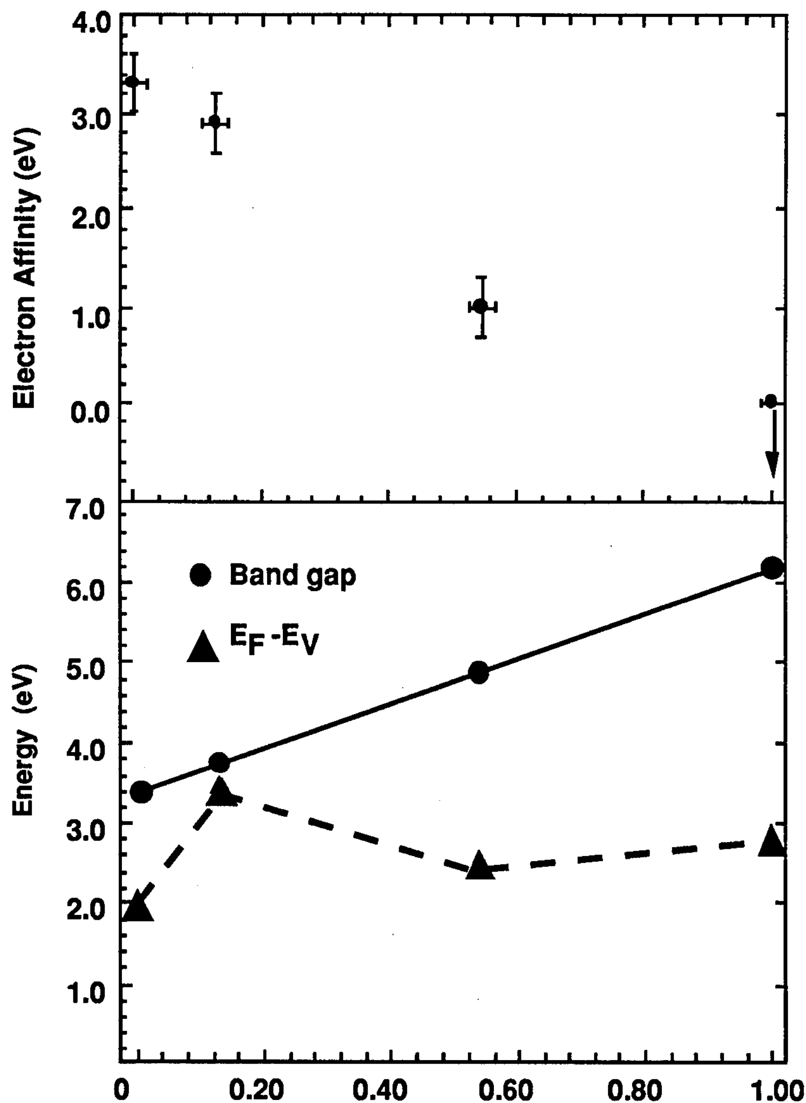

Figure 7. The dependence of the electron affinity (upper panel), bandgap (filled circles) and surface Fermi level position (triangles) for the AlGaN alloys. The electron affinity and surface Fermi level are obtained from the UPS spectra of Fig. 6.

The deduced electron affinities versus alloy concentration are shown in Fig. 7. Again, we note that the photoemission measurements cannot be used to determine the position of the vacuum level for a NEA surface. Therefore, the electron affinity of the the AlN is indicated at $\chi = 0$ with an arrow to larger negative values. The results suggest that the electron affinity depends on the alloy concentration. It should be noted that we have made no effort to control the surface termination for these samples. As shown above for diamond, it was found that the observation of a NEA is critically dependent on the surface termination. Future studies will explore whether the electron affinity of AlGaN materials is also affected by different surface preparations.

Electron Emission from a Negative Electron Affinity Surface

The major device related goal of these studies is the development of a cold cathode electron emitter. Three steps can be considered in understanding the emission process: (1) electron supply to the semiconductor, (2) transport from the supply electrode to the surface, and (3) the emission into vacuum. This study has focused only on the last of these processes. Other measurements such as field emission involves all three process and secondary electron emission which largely involves steps 2 and 3.

There have been many studies of field emission from point emitters (Spindt tips). The sharp point emitters result in a field enhancement at the tip and a possible reduction in the work function due to the steps on the surface. The current versus voltage from a field emitter follows the Fowler-Nordheim expression.

In contrast, the I-V dependence of an ideal NEA based emitter would exhibit emission at any (negative) voltage. At low fields the current would be limited by the space charge in the vacuum around the emitter (following Child-Langmuir dependence) and at higher voltage the current would be limited by the resistance of the semiconductor and the contact. The energy distribution of the emitted electrons from a NEA cathode should be very narrow (~kT), and it should exhibit a noise component related to the resistance of the semiconductor and contact. This is in contrast to either thermal emitters (i.e. hot cathodes) or field emitters that exhibit fluctuations based on the statistics of the highest energy part of the electron distribution.

An electron emitter based on a negative electron affinity material would have several unique advantages over pointed field emitters. These would include low turn on voltage, high current, low erosion, and low noise. In addition the field emitter requires a significant field established through a potential between the tip and a nearby grid layer. In contrast, the NEA device would be controlled by a small field established by the grid to balance the anode to cathode field.

Concluding Remarks

The results presented here demonstrate that a negative electron affinity surface can be obtained for diamond and other wide bandgap semiconductors. Figure 8 summarizes the hexagonal lattice constant and bandgap dependence for the nitride and carbon related materials. We also show on this figure the materials that have been shown to exhibit a NEA. In addition to the measurements described here, recent results have also demonstrated that BN exhibits a negative electron affinity. It is interesting to note that all materials from this group with a bandgap larger than diamond exhibit an negative electron affinity.

For development of cold cathodes, the electron supply may be as critical as the emission properties. Future studies of diamond will focus on methods to supply electrons to the conduction band. Certainly n-type diamond would be an important breakthrough.

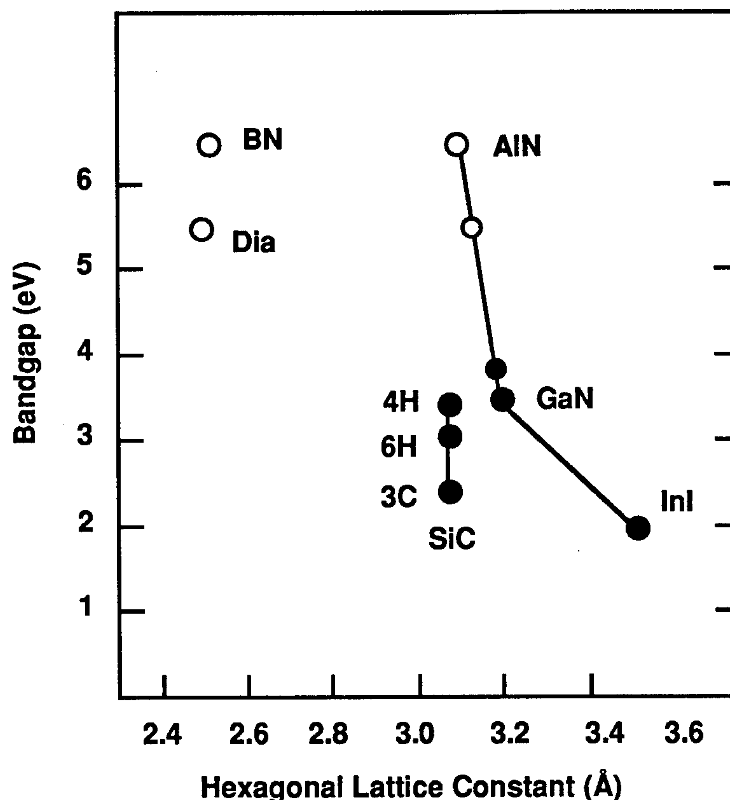

Figure 8. The bandgap vs. hexagonal lattice constant for a group of wide bandgap semiconductors. For the cubic materials, the lattice constant is the unit cell in the (111) plane. The open circles represent materials that have been shown to exhibit a negative electron affinity.

Studies of nitride surfaces are just beginning, but important issues here are also related to n-type doping. While Si is an effective n-type dopant for GaN, we have not observed n-type surfaces for the Al rich AlGaN films. An important future study will be the measurement of the electron affinity of a series of well characterized AlGaN alloys, and the experimental progress should be paralleled with theoretical studies. These measurements may lead to a better understanding of the relative role of the band gap of the semiconductor and the surface termination.

Acknowledgment

We gratefully acknowledge helpful discussions with S. Bozeman. This work was supported in part by the Office of Naval Research.

References

1. S. P. Bozeman, P. K. Baumann, B. Ward, R. J. Nemanich, and D. Dreifus, (this proceedings).
2. A. Zangwill, (1988), *Physics at Surface*, (Cambridge).

3. F. J. Himpsel, J. A. Knapp, J. A. van Vechten, and D. E. Eastman (1979), Phys. Rev. **B20**, 624.
4. B. B. Pate, (1986). Surf. Sci. **165**, 83.
5. van der Weide, J., and R. J. Nemanich, Applied Physics Letters **62**, 1878-1880 (1993).
6. C. Bandis and B.B. Pate, Phys. Rev. Lett. **74**, 777(1995).
7. P. K. Baumann, T. P. Humphreys and R. J. Nemanich, in: Diamond, SiC and Nitride Wide Bandgap Semiconductors, Eds. C. H. Carter, G. Gildenblat, S. Nakamura, R. J. Nemanich, Mater. Res. Soc. Proc. **339**, Pittsburgh, PA (1994) 69.
8. J. van der Weide, Z. Zhang, P. K. Baumann, M. G. Wensell, J. Bernholc and R. J. Nemanich, Phys. Rev. B **50** (1994) 5803.
9. P. K. Baumann and R. J. Nemanich, Proc. of the 5th European Conference on Diamond, Diamond-like and Related Materials, Eds. P.K. Bachmann, I.M. Buckley-Golder, J. T. Glass, M. Kamo: J. Diamond Rel. Mat., **4** (1995) 802.
10. J. van der Weide and R. J. Nemanich, Appl. Phys. Lett. **62** (1993) 1878.
11. J. van der Weide and R. J. Nemanich, Phys. Rev. B, **49** (1994) 13629.
12. J. van der Weide and R. J. Nemanich, J. Vac. Sci. Technol. B **10** (1992) 1940.
13. P. K. Baumann and R. J. Nemanich, Proc. of the 5th International Conference on the Formation of Semiconductor Interfaces, to be published in Applied Surface Science (1995).
14. S. C. Erwin and W. E. Pickett, Surf. Coat. Technol. **47** (1991) 487.
15. S. C. Erwin and W. E. Pickett, Solid State Commun. **81** (1992) 891.
16. W. E. Pickett and S. C. Erwin, Phys. Rev. B **41** (1990) 9756.
17. W. E. Pickett and S. C. Erwin, Superlatt. Microsruct. **7** (1990) 335.
18. W. E. Pickett, M. R. Pederson and S. C. Erwin, Mater. Sci. Eng. B **14** (1992) 87.
19. W. R. L. Lambrecht, Physica B **185** (1993) 512.
20. M. C. Benjamin, C. Wang, R. F. Davis, R. J. Nemanich, Appl. Phys. Lett. **64**, (1994).
21. M. C. Benjamin, C. Wang, R. S. Kern, R. F. Davis, R. J. Nemanich, Mat. Res. Soc. Symp. **339**, 81 (1994).
22. M. J. Powers, M. C. Benjamin, L. M. Porter, R. J. Nemanich, R. F. Davis, J. J. Cuomo, G. L. Doll and S. J. Harris. Submitted to Applied Physics Letters, 1995.
23. C. Bandis, W-Y. Chang, B. B. Pate, this volume.

VI. Field Emission Characteristics of Diamond Coated Silicon Field Emitters

A. Introduction

In recent years diamond has become a preferred candidate material for the next generation of solid state microelectronic devices due to its excellent thermal, chemical, and other possible electronic properties such as negative electron affinity (NEA) [1]. New cathode devices, such as those based on epitaxial diamond substrates and ion implantation, have been fabricated and evaluated during recent years [2]. In the newly emerging field of vacuum microelectronics, diamond is also regarded as the most suitable material for field emitters, as well as for coatings for microfabricated field emitter devices. Because of its well-established microprocessing technology, silicon is still a favored material for fabricating field emitter devices. However, severe contamination of pure silicon emitters could cause significant performance deterioration and even failure for the emitters. It is highly desirable that a thin diamond film be developed on silicon emitter surfaces in order to enhance and stabilize the electron emission.

Table I lists some properties of diamond in comparison to silicon from the point of view of the application as field emission devices. Diamond possesses the superior chemical and electrical properties which will be ideal for a field emitter material. Successful development of diamond coatings on silicon or metal field emitters is expected to significantly improve their performance and also enhance the economic viability of device production compared with direct use of bulk diamond. In addition, the study of diamond coating on field emitters can further facilitate the information of the mechanism of diamond nucleation and heteroepitaxial growth on a highly curved surface.

Table I. Comparisons of Diamond and Silicon for Field Emission Applications

Property	Silicon	Diamond	Advantages of Diamond
Electron affinity	4.05 eV	NEA on some facets	Lower operating voltage, higher efficiency
Electrical breakdown field	2×10^5 V/cm	1×10^7 V/cm	Higher power applications
Thermal conductivity	1.5 W/cm °C	20 W/cm °C	Higher emission current
Electron mobility	1.5×10^3 cm^2/V s	2.0×10^3 cm^2/V s	Higher limit of current saturation
Surface chemical stability	Sensitive to adsorption	Relatively inert to adsorbates	Higher stability, larger emitting area

B. Experimental Procedures

Silicon Emitter Specimen Preparation. Needle-shaped single crystal Si field emitters were used in this study. They were fabricated based on a vapor-liquid-solid mechanism [3] and were n-doped to a level of about $10^{17}/cm^3$. Silicon whiskers were first grown on a <111> oriented silicon substrate by eutectic techniques. After the regular chemical sharpening process, repeated dry oxidation and subsequent HF-etching were performed on Si tips to achieve a uniformly fine scale for the radius of curvature. The resultant Si emitters usually have radii of curvatures of 30 nm or less. A scanning electron microscopy (SEM) image of such a Si emitter is shown in Fig. 1. The heights of these emitters were usually about 150μm and the spacing between tips in the arrays was about 60μm. Both single emitters and emitter arrays were used in this study.

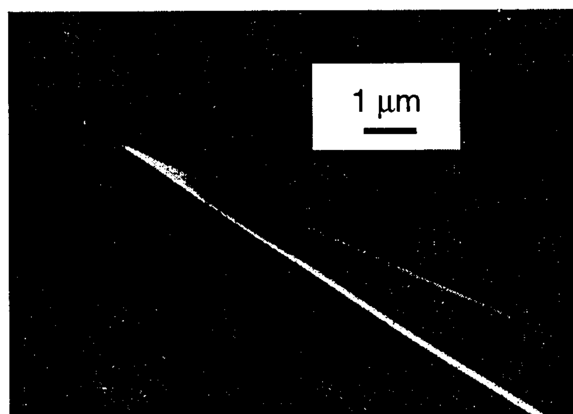

Figure 1. SEM micrograph of a single crystal Si field emitter used in this study.

These specimens are ideal samples for studies of field emission microscopy (FEM), field ion microscopy (FIM), and high resolution electron microscopies. Transmission electron microscopy (TEM) can easily be performed on these emitters without any further sample preparation, thus eliminating any post-treatment altering or damaging of the specimens. This has been an important advantage to the current study.

Diamond Deposition on Si Field Emitters. The process of diamond deposition on these nanometer scale curved Si field emitter surfaces include three steps: H_2 plasma pretreatment (cleaning), bias-enhanced nucleation (BEN), and growth. All these steps were carried out in a high vacuum microwave plasma chemical vapor deposition (MPCVD) reactor chamber [4]. The Si emitter specimens were first cleaned using a concentrated HF solution to remove the native oxide and other contaminants before loading into the reactor chamber. The *in vacuo* cleaning pretreatment was undertaken by placing the Si samples downstream from the H_2 plasma with a pressure of 25 Torr. This step lasted about 15 minutes and reached a temperature of 500-600 °C. The BEN process was then performed using a CH_4/H_2 ratio of 5% and a substrate

bias of -250 Vdc. A biasing duration of up to 25 minutes was used in the experiments. After the biasing step, some samples were further treated by diamond growth at about 25 Torr with a CH_4/H_2 ratio of 0.2% varying the growth time to as long as 45 minutes.

The BEN process, used as an *in situ* pretreatment for diamond nucleation, was found to be very suitable for the diamond growth on the surface of a field emitter since it does not involve any scratching by diamond abrasive or other conventional forms of nucleation enhancement. It also minimized the possibility of tip damage and oversized growth of diamond crystals.

High resolution electron microscopy, performed on JEOL 640OF field emission SEM and two TOPCON 002B TEMs, was used to study the surface morphology and interfacial structures of the diamond coated emitters. Field emission characterizations were carried out in an UHV FIM/FEM system. Emission data were taken by a computer controlled Keithley 617 electrometer through an IEEE-488 interface. Each data point was sampled 30 to 50 times to determine the average value of emission current, as well as its percentage of fluctuation.

C. Results And Discussions

Electron Microscopy Studies. It was found in our processing experiments that diamond nucleation was observable on the Si emitter surface within 5 minutes under the negative biasing conditions employed. The nucleation density, varying with biasing time and location, was measured to exceed $10^{10}/cm^2$ after 20 minutes biasing treatment. Figure 2 shows a typical Si emitter after 20 minutes of the BEN process. This diamond nucleation rate on the Si emitter surface is considerably higher than that on a flat Si substrate under the same conditions. The size of the diamond grains was found to range from a few nm to tens of nm. Nearly continuous diamond coverage was also observed on some emitter surfaces. High resolution TEM and diffraction studies reveal the polycrystalline nature of these diamond coatings formed on the single crystal Si emitter surface (Fig. 3). A SiC polycrystalline interfacial layer was always

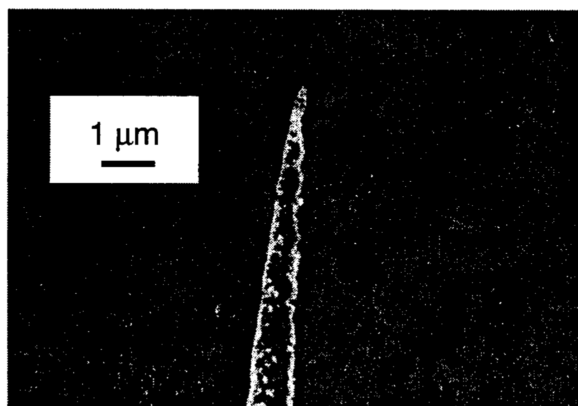

Figure 2. A typical Si tip obtained after 20 minutes treatment of diamond nucleation by bias-enhanced nucleation.

Figure 3. A TEM diffraction pattern shows polycrystalline diamond coating on the single crystal Si tip. A diffraction fringe of the polycrystalline SiC interfacial layer can also be seen inside the diamond ring.

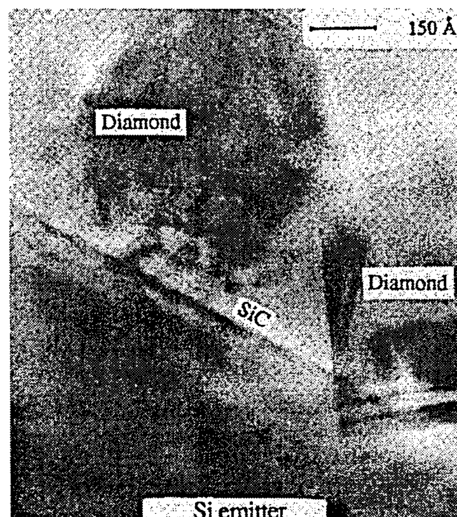

Figure 4. TEM micrograph shows inverted pyramidal diamond grains which nucleated on a thin polycrystalline SiC interfacial layer.

found between the diamond and Si emitter, as deduced from electron diffraction studies. A detailed interface structure between the diamond and the Si emitter surface is shown in Fig. 4. Rooted on a SiC interfacial layer, diamond nuclei started to grow and form in an inverted pyramidal shape. A similar result was obtained earlier by Stoner *et al.*[5].

Electrical Characteristics. Field emission current-voltage (I-V) measurements were performed on diamond coated Si single emitters as well as on coated multi-emitter arrays. For the purpose of comparison, uncoated pure Si emitters were also studied under similar operating conditions. Under the FEM operating mode, a negative bias was applied to these free standing emitters to create the necessary electric field for electron emission. A Faraday cup shaped anode

was positioned at 10 mm away to collect the electron emission current. The vacuum pressure was kept at 10^{-9} Torr or better. Total emission currents of a few μA per tip were usually obtained during measurements. To avoid tip destruction, however, our measurements were carried out in the medium current range. Three sets of I-V characteristic curves, from a pure Si tip, a diamond coated Si tip, and a diamond coated Si 12-tip array, at the early stage of the emission, are shown in Fig. 5. Compared to pure Si emitters, diamond coated Si emitters appeared to have a lower turn-on voltage and a higher increase rate of current (transconductance). To understand these behaviors, detailed analyses of work function and geometrical effect are required and will be discussed in the following section. Full range Fowler-Nordheim plots are given in Fig. 6. Emission data from each sample were taken by several consecutive measurements and excellent repeatability was observed.

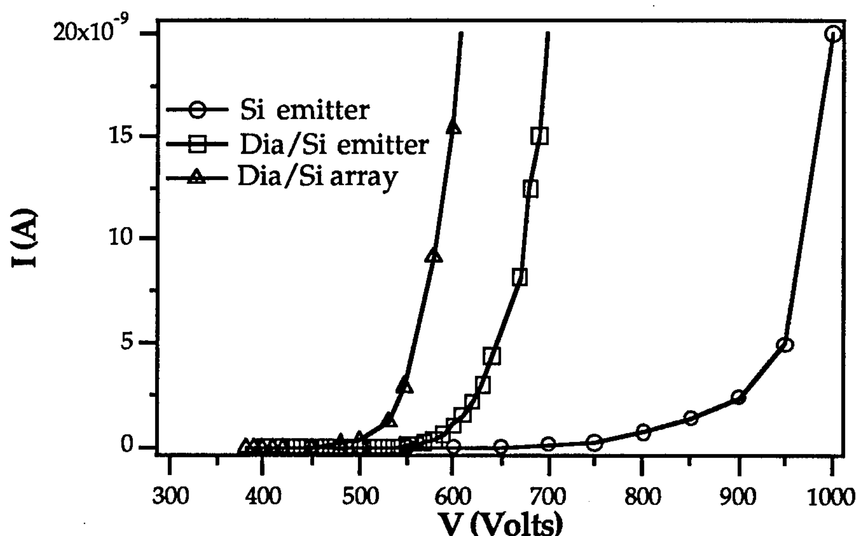

Figure 5. Field emission characteristics for pure and diamond coated Si emitters.

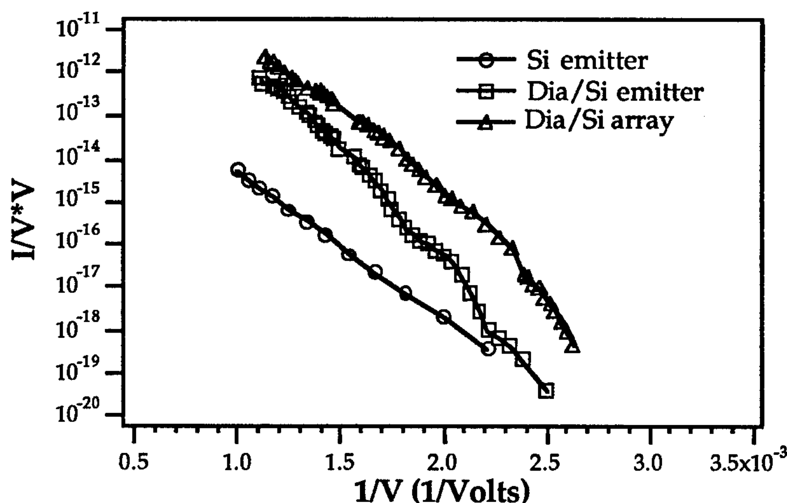

Figure 6. Full range Fowler-Nordheim plots for pure and diamond coated Si emitters.

Emitting Area and Work Function. All the field emission data obtained from our measurements were analyzed using conventional ß-modified Fowler-Nordheim (FN) theory [6]. A particularly striking result from this analysis is that the effective emitting area from diamond coated Si emitters was found to be surprisingly large compared to that of other uncoated emitters. As measured from both diamond coated single emitters and a multi-tip array, the effective emitting area was determined to be between 10^{-12} to 10^{-11} cm^2 per emitter. A surface work function of ø=4.0 eV for these emitters was assumed during the analysis. The same procedures applied to pure Si emitters (without coatings) yielded very small emitting areas ranging between 10^{-16} to 10^{-15} cm^2. This is very similar to the results obtained by many previous investigators on both Si and metal emitters [7,8]. Table II summarizes our measured results for different types of emitters. For diamond-coated emitters, the effective radius of the emitting area was found to be very close to the value of the tip radius of curvature of the emitter ($\sim 3\times10^{-6}$ cm). This interesting finding for diamond coated emitters may imply that electrons were being emitted out of the full tip surface area (emitter surface areas are approximately 10^{-12} cm^2), as compared to the emitting area of only a few atoms ($\sim 10^{16}$ cm^2) for most conventional emitters. This phenomena could be a very important mechanism for the improved operation of field emitters. A larger emitting area would be favorable for higher emission currents and better current stability.

Table II. Field Emission Parameters Obtained from a Fowler-Nordheim Analysis

Specimen (single tip)	Emitting Area α per tip (cm^2)	Effective radius of emitting area $\sqrt{\alpha}$ (cm)	Tip radius of curvature *r*
Si	2.21×10^{-16}	1.49×10^{-8}	3.01×10^{-6}
Diamond coated Si	9.97×10^{-12}	3.16×10^{-6}	4.28×10^{-6}
Diamond coated Si tip array (12-tip)	5.49×10^{-12}	2.34×10^{-6}	3.90×10^{-6}

Using FN curve fitting, relations between the tip radius of curvature *r* and the effective surface work function ø were obtained. They can be used to determine the value of *r* and ø if either of them is known. Fig. 7 shows schematically the relationships between *r* and ø which were obtained from our experiments and FN analyses. A conical model was used to represent the geometry of the tip surface and the ß factor was taken to be 1/5*r*. The field strength on the tip surface was described by the general form: F=ßV. For pure Si emitters, a radius of curvature of 30 nm was determined since its surface work function is known to be 4.1 eV.

This is in excellent agreement with our previous investigations of the tip geometry. Using the estimation of r~35 nm for the diamond coated emitters, however, an effective work function near 5.0 eV was found for the polycrystalline diamond surface. Of course, determination of a more accurate result of the effective work function will require a more precise measurement of the tip radius of curvature of the emitter. On the other hand, for a polycrystalline diamond covered emitter surface, the multiple emitting sites may have altered our model of the tip geometry. Some modifications to the FN equation, such as considering local geometry and the heterojunction, may be needed for a complete understanding of the emission behavior.

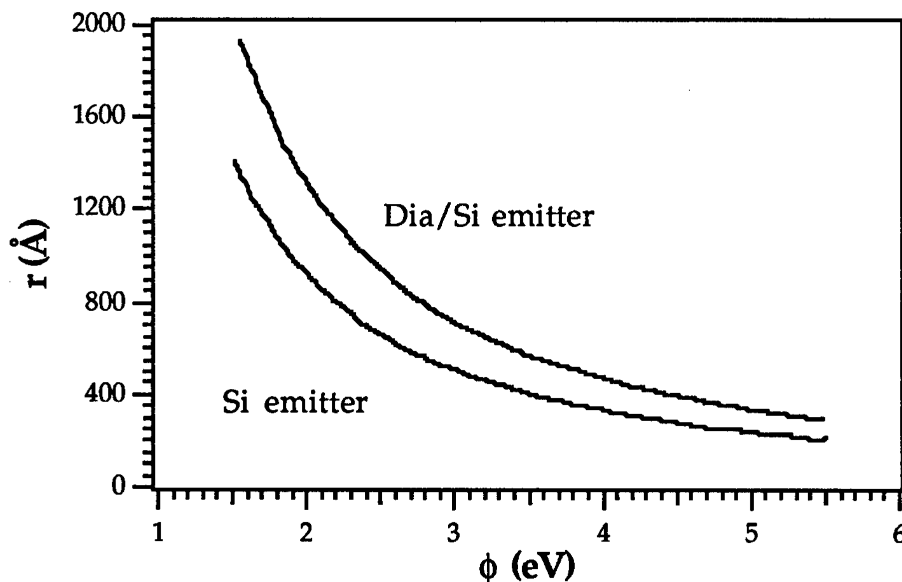

Figure 7. Schematic relations between the tip radius of curvature and surface work function which were determined from experimental measurements and FN analyses.

Emission Stability. During our measurements of the emission current, the value of ∂I, defined as (Imax - Imin)/Iav under constant emitter voltage, was recorded versus total current to illustrate the operating stability over a wide current range. Figure 8 shows measured emission current stability from pure silicon and diamond coated emitters and arrays. It was found that the current stability of diamond coated Si emitters was one to two orders of magnitude better than that of pure Si emitters. This result provides obvious evidence of the stabilizing effect of the diamond coating to the emitting surface. Excellent long-term current stability and reproducibility in the range of a few μA's over a period of several hours was also obtained from these diamond coated emitters.

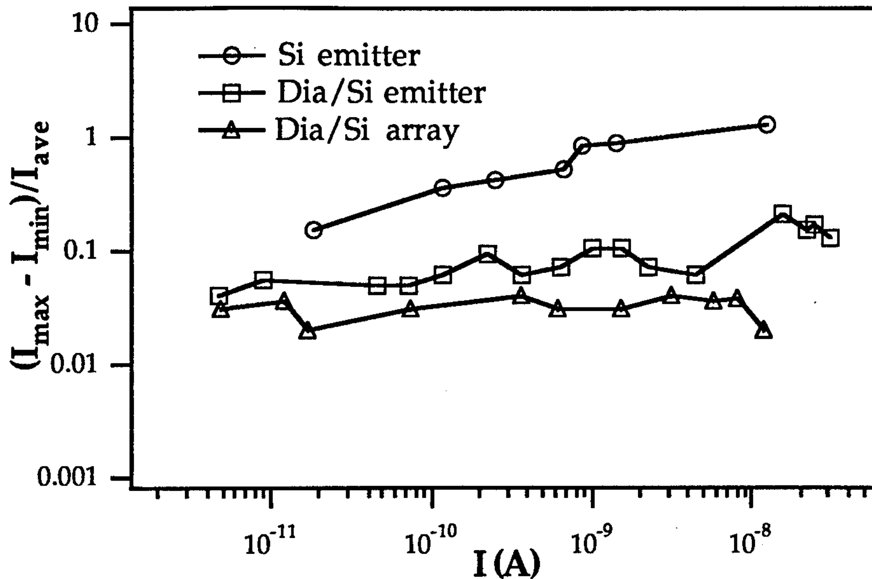

Figure 8. Measured emission stability versus total current for pure and diamond coated Si emitters.

D. Summary

Diamond formation on single crystal Si field emitters was successfully carried out using bias-enhanced nucleation MPCVD. Field emission characterization of diamond coated Si emitters has shown many exciting results such as large emitting area and high emission current with high stability. Diamond coated emitters have demonstrated their significant enhancement in emission performance as compared to uncoated pure Si emitters. This new approach has shown very promising results both for the emitter processing technology and the operating mechanism. Successful diamond coatings may provide field emitters with chemically inert and electrically stable surfaces, as well as superior performance.

E. Acknowledgments

This work was supported in part by Kobe Steel USA Inc. and also by BMDO/ITS through the Office of Naval Research.

F. References

1. M. N. Yoder, *Diamond and Diamond-Like Films and Coatings*, edited by R. E. Clausing *et. al* (Plenum, New York, 1991), p. 1.
2. M. W. Geis, N. N. Efremow, J. D. Woodhouse, M. D. McAleese, M. Marchywka, D. G. Socker, and J. F. Hochedez, IEEE Electron Device Lett. EDL-12, 456 (1991).
3. E. I. Givargizov, J. Vac. Sci. Technol. B **11**, 449 (1993).
4. S . D. Wolter, B. R. Stoner, J. T. Glass, P. J. Ellis, D. S. Buhaenko, C. E. Jenkins, and P. Southworth, Appl. Phys. Lett. **62**, 1215 (1993).
5. B. R. Stoner, G.-H. M. Ma, S. D. Wolter, and J. T. Glass, Phys. Rev. B **45**, 11067 (1992).

6. C. A. Spindt, I. Brodie, L. Humphrey, and E. R. Westerberg, J. Appi. Phys. **47**, 5248 (1976).
7. I. Brodie and C. A. Spindt, Adv. Electron. Electron Phys. **83**, 1 (1991).
8. H. H. Busta, J. E. Pogemiller, and B. J. Zimmerman, IEEE Trans. Electron Devices ED-40, 1530 (1993).

VII. *Ex Situ* Cleaning Techniques for 6H-SiC Surfaces

A. Introduction

Silicon carbide (SiC) is a wide bandgap, compound semiconductor which has considerable potential in numerous electronic device applications involving high-power, high-speed, and high temperatures. The consideration of SiC as the semiconductor for these applications is based on the outstanding materials properties that it exhibits in demanding conditions including: high temperature stability (T_m=2800°C, under 30 atm Si), excellent oxidation resistance to 1000°C, high thermal conductivity, good radiation hardness and excellent thermal shock resistance [1]. Due to moderately close lattice matching and electrical conductivity, SiC has also become important as a heteroepitaxial substrate for III-V nitride compounds and alloys ($\Delta a/a_o$ SiC/AlN = 0.9%, SiC/GaN = 3.5%) which are the current materials of choice for yellow-blue-UV optoelectronic devices. The wide bandgap of the nitrides and their high saturated electron drift velocities at high fields also make these materials candidates for high-power and high-frequency microelectronics devices [2]. The development of SiC into the semiconductor/substrate of choice for these applications has been hampered by defects (i.e. micro-pipes, inversion domain boundaries (IDB's), double position boundaries (DPB's), stacking faults and twins) formed during bulk crystal growth and homo/heteroepitaxy. Though the solution to the further reduction of many of these defects in both SiC and III-N's may lie in other materials issues, a continued reduction in defect densities (dislocations, stacking faults, IDB's, etc.) may eventually depend on a better understanding and development of SiC surface preparation and cleaning. In fact, a clear relation between surface cleaning/preparation and device performance has already been demonstrated in Si and GaAs semiconductor technologies [3, 4].

In silicon homoepitaxy, improper removal of surface contamination and oxides prior to epitaxy has been clearly shown to result in an increase in the density of line and planar defects (i.e. dislocations, stacking faults, and twins), from $<10^4/cm^2$ to $>10^{10}/cm^2$ [5-10]. More importantly from an economic point of view, increased epitaxial defect densities have been shown to result in a significant drop in device yield [5,6]. Surface cleaning has also been found important in the formation of metal contacts (Ohmic or Schottky). Improper removal of surface oxides prior to metal deposition has been shown to result in higher contact resistances, thermal instability, and lack of parameter uniformity [11-15]. Further, the Schottky barrier height in metal contacts can also be influenced by the existence and density of surface/interface states in the band gap of a semiconductor. These interface states can pin the position of the Fermi level in the semiconductor and determine the Schottky barrier height. As most surface/interface states are related to surface dangling bonds, surface preparation/cleaning can be used to passivate these dangling bonds and control the existence and density of surface/interface states in metal

contacts [15-18]. In MIS devices, control of interface states densities is also important as they can produce swings in threshold voltages. Drift in MIS parameters has also been linked to the presence of alkali ions at the interface and this in part can also be controlled by surface cleaning prior to insulator deposition [19,20]. In summary, it has been demonstrated in other materials systems that surface cleaning/preparation can permeate all aspects of semiconductor processing, adversely affecting: epitaxy, contacts (Ohmic or Schottky), and insulator performance. For these reasons, it should not be surprising that 50% of all yield losses in silicon IC fabrication are attributed to micro contamination.

The intent of this study, therefore, has been to examine *ex situ* cleaning techniques for SiC surfaces which have been found useful in Si and GaAs technologies. However, the focus of this study has been to not only find techniques which obtain "clean" SiC surfaces but to also obtain a more fundamental understanding of the chemistry which takes place at SiC surfaces. In this study, "clean" will be taken to mean complete removal (within the detection limits of the analytical techniques employed) of the two principle contaminants on SiC surfaces, namely, oxygen and non-carbidic carbon. Other contaminants such as fluorine, alkali ions, etc. can also be present on SiC surfaces which can equally create defects and ruin SiC devices. However, these contaminants have not yet been addressed in this study. The two *ex situ* cleaning techniques addressed so far in this study include wet chemical oxide removal using HF based solutions and/or UV/ozone oxidation for non-carbidic carbon removal. Both of these techniques have been found very useful in Si technology.

For silicon, HF etches have been found very beneficial as it not only etches away any silicon oxide at the surface, but passivates all of the silicon dangling bonds at the surface with hydrogen. The hydrogen termination inhibits re-oxidation of the silicon surface on removal from the HF solution and produces a very hydrophobic surface [21,22]. UV/Ozone oxidation treatments have been found very useful in Si and GaAs cleaning for mainly removing carbon contamination from these surfaces. In this technique, Si or GaAs samples are exposed to UV radiation from a Hg lamp which emits light at 253.7 nm (90%) and 184.9 nm (5%). The 253.7 nm light is absorbed by most hydrocarbons and will excite C-C and C-H bonds. The 253.7 nm line is also absorbed by ozone. The 185 nm light is absorbed by O_2 and creates O_3 (Ozone) [23,24]. The effect is that adventitious carbon is excited, oxidized, and removed from the Si or GaAs surface. The oxide formed on the surface by the O_3 exposure can then be removed by either wet chemicals or by *in situ* thermal desorption.

B. Experimental Procedure

Substrates. The samples used in these experiments were 1" diameter, n-type ($N_d=1\times10^{18}$), $(0001)_{Si}$ and $(0001)_C$ 6H-SiC wafers obtained from Cree Research (Durham, NC). For the (11-20) and (10-10) orientations, roughly 7 mm × 7 mm fragments of n-type wafers, also from

Cree, were used. On axis and off axis "vicinal" (4° off toward (11-20)) $(0001)_{Si}$ 6H-SiC wafers were also investigated. All wafers came with an ≈ one micron epi layer ($N_d=5\times10^{17}$) and an ≈ 500-1000Å thermal oxide both grown by Cree. The use of thermal oxides was based on work by L. Porter who found this oxide layer was instrumental in generating a stoichiometric SiC surface after removal with HF. For these studies, the thermal oxide was removed using a 10% HF solution. Further cleaning of this surface was then examined by immersion in other acid/base solutions or by re-oxidizing the SiC surface using a UV/ozone treatment followed by wet chemical treatment. UV/ozone treatments described in this study employed UV/Ozone box which positioned a high intensity Hg lamp in close proximity to the SiC wafer and has been described elsewhere [23,24]. The wet chemistries examined included 10% HF, 10% Buffered HF (7:1 NH_4F:HF), 40% NH_4F, HCl:HF and NH_3OH:HF solutions, HNO_3, H_2SO_4, Acetic, and Lactic acid. Except where noted, after all wet chemical cleans the samples were rinsed in DI water (18MOhm) and blown dry with N_2 (UHP). All wet chemicals were of CMOS grade purity (J. T. Baker). Surfaces prepared in the above manner were then subsequently mounted to a molybdenum sample holder for analysis by AES, XPS, EELS, and LEED.

Analytical Procedure. All of the surface analysis described in this paper was conducted in a unique ultra high vacuum (UHV) system which integrates several completely independent UHV units via a 36 ft. long transfer line (see Fig. 1). The details of this integrated system have been given in previous ONR reports [25]. Briefly, it currently incorporates a remote H-plasma/CVD system, an ASTeX diamond deposition system, *in situ* Raman Spectroscopy, a VSW angle resolved ultra-violet photoelectron spectroscopy system (AR-UPS), an e-beam Si and Ge MBE, an analysis system including a Perkin Elmer Auger electron spectrometer and Princeton Instruments LEED (low energy electron diffraction) optics, a five source (Al, Au, Cu, Ti, Zr) e-beam metal deposition system, a III-V nitride GSMBE, and an X-ray photoelectron spectroscopy (XPS) system.

XPS System. X-ray photoelectron spectroscopy experiments were performed in a stainless steel UHV chamber equipped with a dual anode (Mg/Al) x-ray source (VG XR3E2) and a 100 mm hemispherical electron energy analyzer (VG CLAM II). The base pressure in this system was 1×10^{-10} Torr and was pumped by 220 l/s ion pump (Varian). All XPS spectrums reported here were taken using Al Kα radiation (hυ=1486.6 eV) with 12 kV and 25 mA emission current. XPS analysis required less than 1 hour during which the pressure never rose above 9×10^{-10} Torr. Calibration of the binding energy scale for all scans was achieved by periodically taking scans of the Au $4f_{7/2}$ and Cu $2p_{3/2}$ peaks from standards and correcting for the discrepancies in the measured and known values of these two peaks (83.98 and 932.67 eV, respectively). Curve fitting of most data was performed using the software package

GRAMS 386. A combination Gaussian-Lorentzian curve shape with a linear background was found to best represent the data.

AES/LEED/EELS. The Auger electron spectrometer (Perkin Elmer 10-155 CMA) and the low energy electron diffraction optics (Princeton Instruments) were mounted on a six-way cross off the transfer line and pumped through the transfer line. In AES analysis, a 3 keV, 1 mA beam was used and the Auger spectrum was collected in the undifferentiated mode and then numerically differentiated. In EELS and LEED, an 80 eV, 1 mA beam was used. EELS spectrums were also collected in the undifferentiated mode.

C. Results

$(0001)_{Si}$ - Wet Chemical. After removal of the thermal oxide with a 10% HF solution, AES, XPS, and EELS of all the 6H-SiC orientations (i.e. $(000\text{-}1)_C$, $(0001)_{Si}$, and (11-20) and (10-10)) all showed the surfaces to contain various amounts of oxygen and non-carbidic carbon. As it was difficult with these spectroscopies to distinguish major differences between the various orientations after thermal oxide removal, data from an off axis, vicinal $(0001)_{Si}$ 6H-SiC surface will be presented first to represent the general trends observed. The finer details of *ex situ* cleaning for the other orientations will then be presented.

Figure 1a shows an XPS spectrum of the O 1s peak from a vicinal $(0001)_{Si}$ 6H-SiC wafer after removal of the thermal oxide by dipping in 10% HF. As can be clearly seen, there is still a significant amount of oxygen on the SiC surface even though a chemically shifted Si 2p oxidation peak was not was seen from the this surface. For comparison purposes, Fig. 1b shows the O 1s from a vicinal Si (111) wafer after dipping in 10% HF. There is a striking difference in the amount of oxygen left on the two surfaces after HF dipping. This complements the observation that the Si surface was hydrophobic after HF dipping and the SiC surface hydrophilic. Specifically, the Si wafer could be pulled dry from the HF solution whereas when withdrawing a SiC wafer from HF, the HF solution still wetted the SiC surface. After HF dipping, the O 1s position occurs at 533.1 eV for the SiC surface and 531.5-531.8 eV for the Si (111) wafer. For further comparison, the O 1s from a CVD diamond film on silicon was measured and found at 532.0-532.6 eV. The reason for these differences will be discussed later. Small amounts of fluorine on the SiC surface after HF dipping were also detected by XPS. The amount of fluorine detected varied from day to day and appeared to be dependent on the DI rinsing time. (1×1) LEED patterns were easily obtained from both on and off axis $(0001)_{Si}$ SiC surfaces after dipping in 10% HF. The LEED patterns were intense with a diffuse background. The LEED spots, however, were large and fuzzy and could not be focused into dots. This is presumably due to the significant disorder produced in the surface after oxide removal with HF. All of the above observations were also made for on axis $(0001)_{Si}$ 6H-SiC.

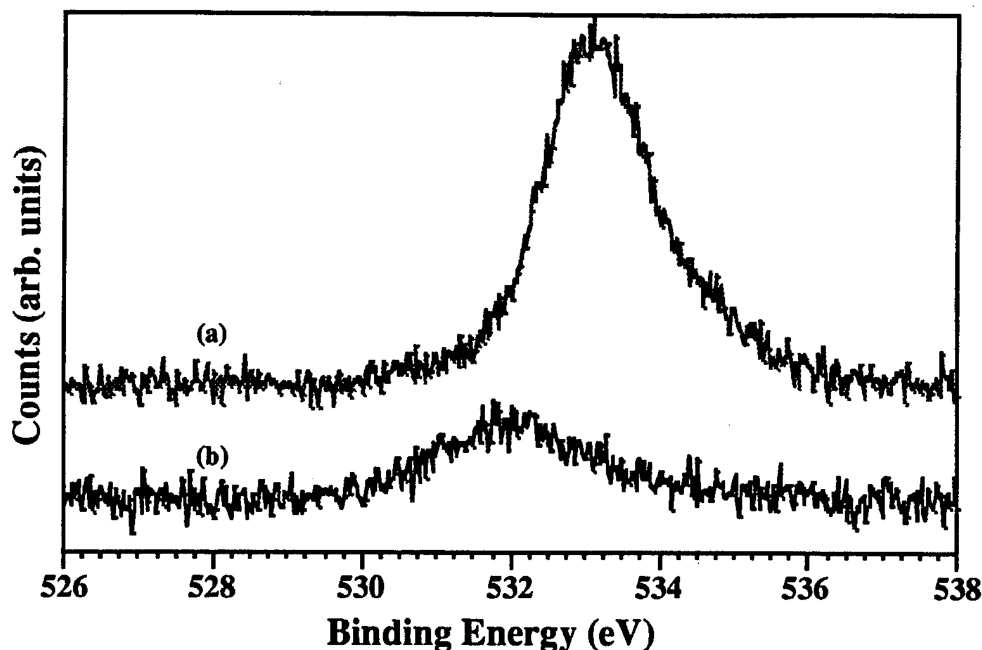

Figure 1. XPS of O 1s from (a) vicinal $(0001)_{Si}$ 6H-SiC and (b) off axis Si (111) after dipping in 10% HF 5 min., DI rinse, and N_2 blow dry.

To illustrate that an HF dip does remove silicon oxides from SiC surfaces (which may form due to ambient exposure), a vicinal $(0001)_{Si}$ 6H-SiC wafer was intentionally re-oxidized by annealing in a unbaked GSMBE. Figure 2a shows an XPS spectrum of the Si 2p peak from the re-oxidized vicinal $(0001)_{Si}$ 6H-SiC wafer. Two peaks are clearly distinguished. The most intense peak at 101.5 eV (FWHM=1.4 eV) is characteristic of Si-C bonding and is from the SiC wafer. The less intense peak/shoulder at 103.2 eV (FWHM=2.6 eV) is characteristic of silicon in a +4 oxidation state (i.e. O-Si-O bonding) and is from a silicon oxide layer which has formed on the SiC wafer. The width of the 103.2 eV peak is 2.6 eV and is probably a mixture of +2, +3, and +4 oxidation states (i.e. Si-O, O-Si-O, and Si-OH). Figure 3a shows an XPS spectrum of the C 1s peak from the same SiC wafer. This spectrum also shows two peaks. The narrow peak at 283.6 eV (FWHM=1.1 eV) is indicative of C-Si bonding, whereas the broad peak at 285.5 eV (FWHM=1.9 eV) is probably a mixture of C-H, C-O, and C-C bonding presumably from dust, organic particulates, bacteria etc. The O 1s core level for this surface was located at 531.1 eV which is indicative of silicon dioxide. LEED patterns were not obtained from this surface. It should be noted that SiC wafers exposed to ambient at room temperature for several days to months after dipping in HF do not exhibit this level of oxidation.

Dipping the above vicinal wafer in 10% HF was found to remove the silicon oxide layer and some of the hydrocarbon contamination from the SiC surface. Figure 2b shows an XPS

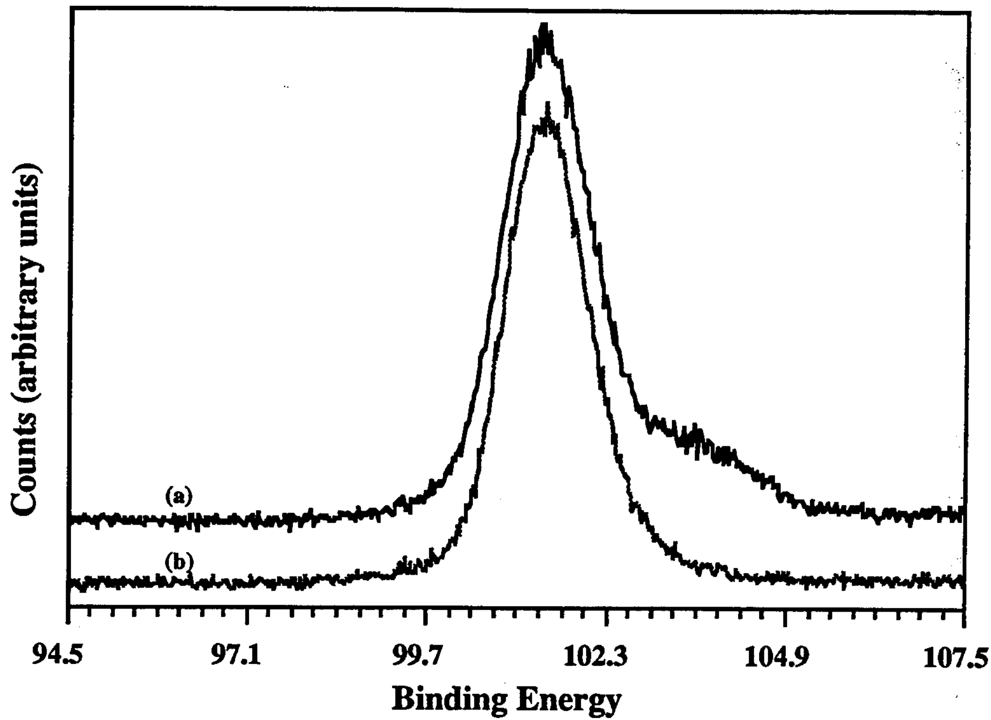

Figure 2. XPS of Si 2p from vicinal $(0001)_{Si}$ 6H-SiC surface: (a) after oxidation in GSMBE during bakeout and (b) after dipping in 10% HF for 5 min., DI rinse, and N_2 blow dry.

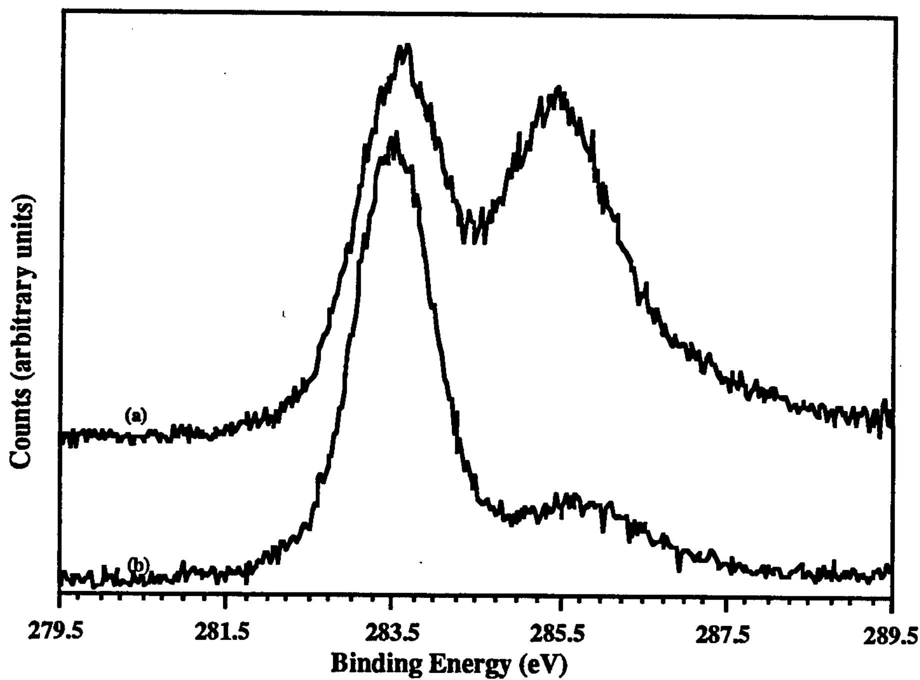

Figure 3. XPS of C 1s from vicinal $(0001)_{Si}$ 6H-SiC surface: (a) after oxidation in GSMBE during bakeout and (b) after dipping in 10% HF for 5 min., DI rinse, and N_2 blow dry.

spectrum of the Si 2p peak from the same SiC wafer immediately after dipping in 10% HF. In comparison with Fig. 2a, there is no peak at 103.2 eV indicating removal of the silicon oxide layer from the SiC surface. As seen in the XPS spectrum of the C 1s (Fig. 3b), dipping in HF also reduces (though incomplete) the level of noncarbidic contamination on the SiC surface. The presence of non carbidic carbon after HF dipping is also detected in EELS via a π-π^* loss peak typically at 2-3 eV labeled "non carbidic" carbon in Fig. 4a. In EELS, surfaces are exposed to low energy electrons (E_p typically 100 eV) and the energy distribution of the back scattered electrons are measured. Most of the electrons are elastically scattered from the surface (i.e. no energy loss) and return to the detector with energy equal to the beam energy. A smaller number ($\approx$ 0.1-1%) of the electrons are inelastically scattered due to collisions and excitation of plasma frequencies in the semiconductor conduction band. As the elastic peak is so large with respect to the rest of the loss features, it is usually truncated in order to more easily display the pertinent loss data. The broad features ranging from 10 to 25 eV are due to excitation of both SiC surface and bulk plasmons (16 and 23 eV, respectively). The loss peak at 2-3 eV is always directly correlated with a strong C 1s XPS peak at 285-286 eV and is not thought to be due to graphite which would have a loss peak at 6 eV.

In order to find a wet chemistry which produces a more hydrophobic SiC surface, several $(0001)_{Si}$ 6H-SiC wafers were dipped in various acids and bases and the wetting characteristics

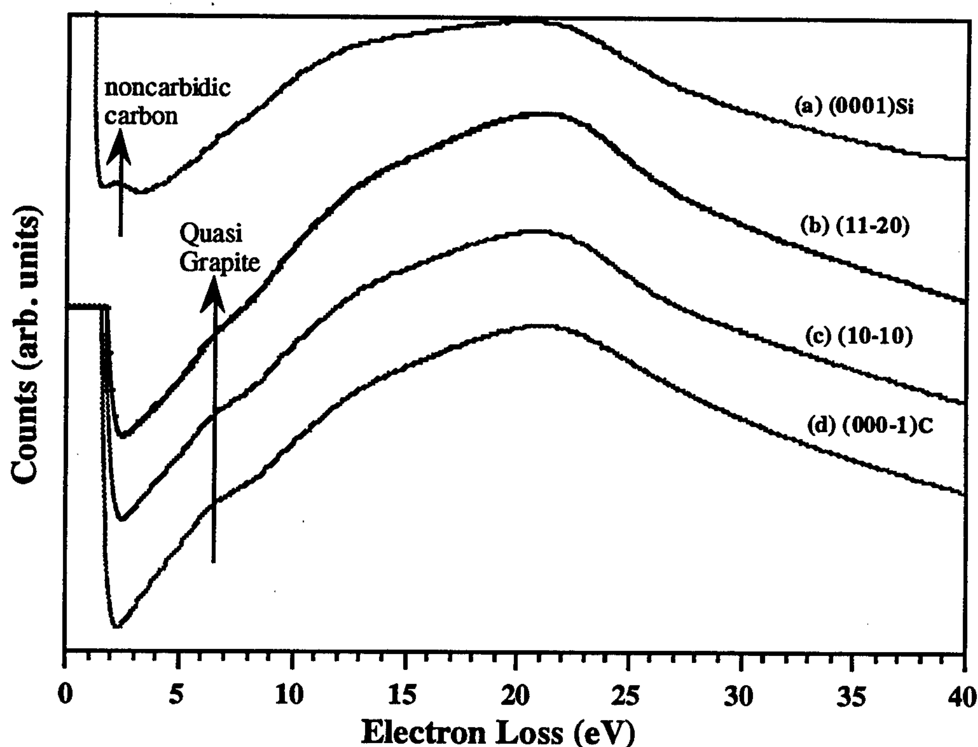

Figure 4. EELS of different 6H-SiC orientations after dipping in 10% HF 5 min., DI rinse, and N_2 blow dry: (a) $(0001)_{Si}$, (b) (11-20), (c) (10-10), (d) $(000\text{-}1)_C$.

of these surfaces in de-ionized water were monitored visually. The acids and bases examined included: HF, NH_4F, NH_3OH, HCl, HNO_3, H_2O_2, H_2SO_4, Acetic, and Lactic acid. For comparison purposes Si (111) and (100) wafers were also dipped simultaneously in each acid with the SiC wafer. All wafers (Si or SiC) were initially dipped in 10% HF to remove any native oxides from the surfaces before dipping in the acid of interest. For Si, the surfaces remained hydrophobic when dipped in NH_3OH, HCl, or H_2O_2. Dipping the Si wafers in HNO_3 or H_2SO_4 removed the hydrophobic nature of the surface. Dipping Si in the organic acids resulted in a strongly adhering thin film of the acid to the silicon surface which could be rinsed off in DI leaving a hydrophobic Si surface. For SiC, all acids and bases wetted the surface and nothing was found which produced a hydrophobic SiC surface. HF solutions with various pH's adjusted from strongly acidic, neutral, and to strongly basic using HCl, NH_4F, and NH_3OH, respectively, were also examined as they have been reported to produce better hydrogen termination of Si surfaces. In these experiments the dipping times were held constant at 10 min. and no changes in the wetting characteristics of the $(0001)_{Si}$ SiC surface in HF solutions with different pH's were found. In one experiment, the dipping time was varied from 5 min. to 1 hr. and once again no differences were found. Additionally, neither XPS nor AES indicated a significant change (within AES and XPS experimental accuracy) in the amount of surface oxygen on $(0001)_{Si}$ SiC wafers after dipping in HF solutions of various pH. No differences were observed between on axis and vicinal surfaces, as well.

$(0001)_{Si}$ UV/Ozone. Figure 5a shows an XPS spectrum of the C 1s peak from a $(0001)_{Si}$ 6H-SiC surface prior to exposure to UV/Ozone oxidation. As in Fig. 3, two C 1s peaks are clearly distinguished at 285.7 eV and 283.5 eV which are due to non-carbidic carbon and carbidic carbon, respectively. This surface had been previously dipped in 10% HF to remove any silicon oxide from the SiC surface. Figure 5b shows the C 1s from this surface after exposure to UV/Ozone for 5 hours. As can be seen, there are still two C 1s peaks. However, the non-carbidic carbon peak has shifted from 285.7 eV to 285.2 eV whereas the carbidic carbon peak remains unshifted at 283.5 eV. Further as shown in Fig. 6, a chemically shifted Si 2p peak at $\approx$ 103 eV is also detected after the UV/ozone exposure indicating the formation of some silicon oxide. Unfortunately, longer exposures (18 hours) were not found to produce any further changes in the amount or position of the non-carbidic C 1s peak.

$(000\text{-}1)_C$, (11-20), and (10-10). Figure 7(a-d) shows a series of AES spectrums taken from surfaces of the four primary orientations of 6H-SiC: $(0001)_{Si}$, $(000\text{-}1)_C$, (11-20), and (10-10). Each spectrum is normalized to make the carbon KLL Auger peak to peak height (pph) the same. As shown in Fig. 7, the oxygen levels after HF dipping for the $(000\text{-}1)_C$, (11-20), and (10-10) surfaces were not found to differ appreciably from those found for the vicinal $(0001)_{Si}$ surface. Table I lists the Si/C, O/Si, and O/C pph AES ratios (uncorrected for differences in sensitivity) calculated for each surface.

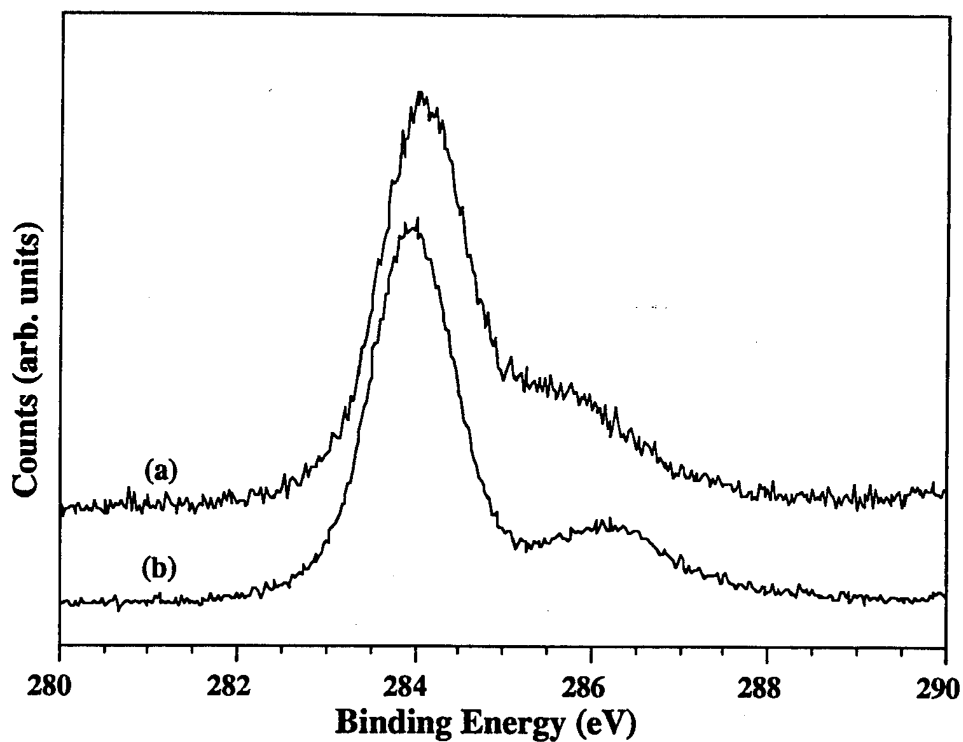

Figure 5. XPS of C 1s from $(0001)_{Si}$ 6H-SiC: (a) before UV/Ozone oxidation and (b) after 5 hours of UV/Ozone oxidation.

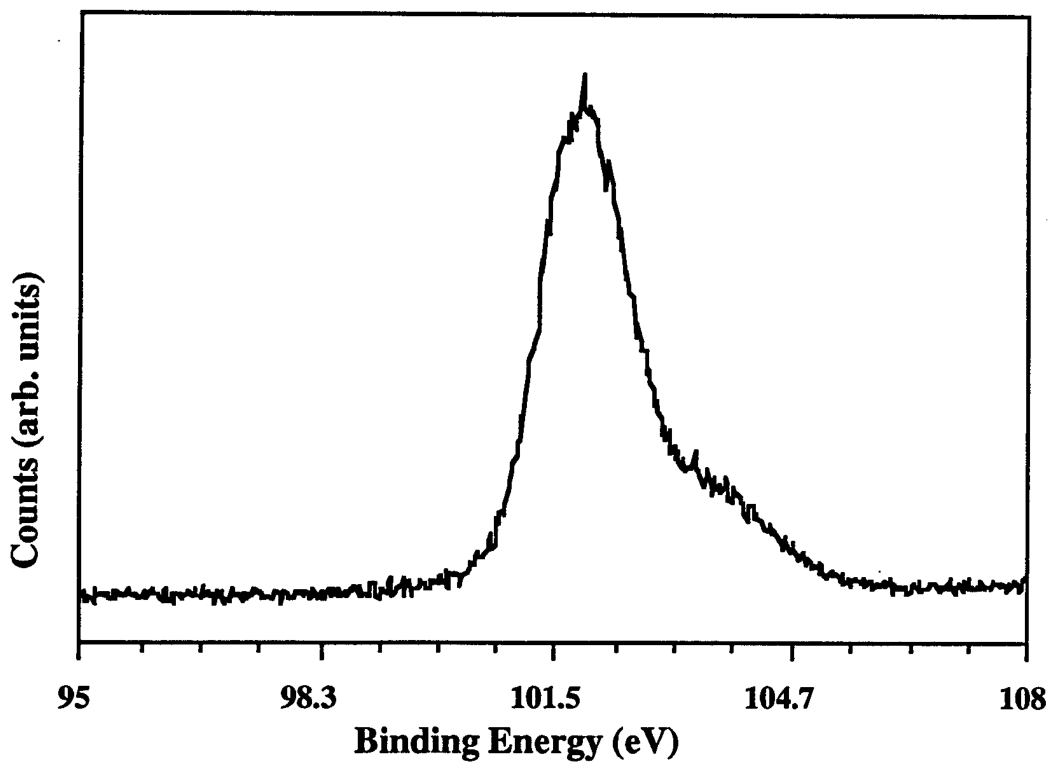

Figure 6. XPS of Si 2p from $(0001)_{Si}$ 6H-SiC after UV/Ozone oxidation for 5 hr.

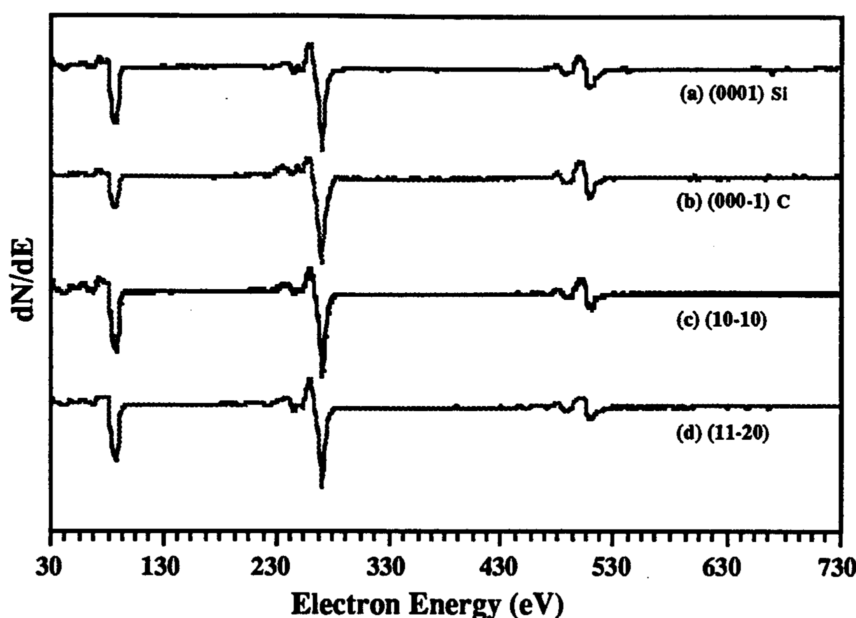

Figure 7. AES spectrum from 6H-SiC surfaces of different orientations after dipping in 10% HF 5 min., DI rinse, and N_2 blow dry: (a) $(0001)_{Si}$, (b) $(000\text{-}1)_C$, (c) (10-10), and (d) (11-120).

Table I. Peak to Peak Height (pph) Ratios for Various 6H-SiC Surfaces

	$(0001)_{Si}$	$(000\text{-}1)_C$	(11-20)	(10-10)
Si/C	0.60	0.34	0.61	0.65
O/Si	0.52	0.99	0.37	0.43
O/C	0.31	0.34	0.23	0.28

Table I shows the O/C ratio for all the different orientations of 6H SiC surfaces to be centered around 0.3. Given that two of these surfaces are polar and the others non polar, it surprising that they would exhibit this similarity. Further, the Si/C ratio for the $(0001)_{Si}$, (11-20), and (10-10) surfaces are all centered around 0.6 which is also surprising in that ideally the $(0001)_{Si}$ surface would be terminated exclusively with Si, whereas the (10-10) and (11-20) are nonpolar surfaces ideally with equal numbers of carbon and silicon atoms at the outermost surface. The $(000\text{-}1)_C$ surface, however, shows a Si/C ratio half that found for the $(0001)_{Si}$ which is expected based on the differences in polarity for these two surfaces. The O/Si ratio for the $(000\text{-}1)_C$ surface was found to be twice that for the other orientations indicating the possibility that a significant amount of oxygen is actually bonded to carbon at SiC surfaces.

Like the $(0001)_{Si}$ face, EELS of the $(000\text{-}1)_C$ surface shows a non carbidic π-π^* carbon loss peak which is interestingly shifted to 4-5 eV. This is much closer to where one would expect to find a loss peak for graphite (see Fig. 4(d)). EELS of the $(000\text{-}1)_C$ surface also shows a more drastic drop off at 10-15 eV than the $(0001)_{Si}$ surface. XPS of the $(000\text{-}1)_C$ surface like the $(0001)_{Si}$ surface shows two C 1s peaks but the values are shifted to lower binding energies of 282.8 eV and 285.0 eV (FWHM=1.1 and 2.5 eV respectively). The non-carbidic C 1s peak at 285.0 eV (like the EELS peak) is close to the value of 284.5 eV which has been reported for graphite. This result indicates that the non carbidic carbon left on the $(000\text{-}1)_C$ 6H-SiC surface after HF dipping is closer in similarity with graphite than the noncarbidic carbon on the $(0001)_{Si}$ surface. XPS of the Si 2p and O 1s from the $(000\text{-}1)_C$ 6H-SiC surface after HF dipping are also shifted to lower binding energies with the Si 2p at 100.7 eV (FWHM=1.3 eV) and the O 1s at 532.5 eV (FWHM=2.3 eV). The lower core level values for the $(000\text{-}1)_C$ face could be due to differences in doping, wafer growth and processing, step density, band bending etc., but the position of the O 1s core level at 532.5 eV is intriguingly close to the previously mentioned value from a CVD diamond film.

Surprisingly, EELS spectrums of the (11-20) and (10-10) surfaces are identical to those taken from the $(000\text{-}1)_C$ surfaces which contrasts with the AES results which showed similarities between the $(0001)_{Si}$ and the (11-20) and (10-10) surfaces (see Fig. 4(b,c)). XPS of the (11-20) and (10-10) surfaces gave results intermediary between those found for the $(0001)_{Si}$ and $(000\text{-}1)_C$ surfaces. The values obtained for the (11-20) Si 2p, C 1s, and O 1s are respectively: 101.6 eV, 283.5 and 284.7 eV, and 532.5 eV. The Si and C core levels are similar to those for the $(0001)_{Si}$ surface. However, the non carbidic C 1s and O 1s core levels are closer to those found for the $(0001)_C$ surface.

LEED patterns were easily obtained from the $(000\text{-}1)_C$, (11-20), and (10-10) surfaces after HF dipping. The $(000\text{-}1)_C$ surface exhibited a (1×1) pattern similar to that observed for the $(0001)_{Si}$ surface after HF dipping. The (11-20) and (10-10) surfaces revealed rows of dots which have been tentatively assigned to (1×1) patterns.

The wetting characteristics of the $(000\text{-}1)_C$, (11-20), and (10-10) 6H-SiC surface orientations in various acids and bases were also examined. In all cases, these surfaces exhibited wetting characteristics similar to those found for $(0001)_{Si}$. The only exception found was one particular $(000\text{-}1)_C$ wafer which was found to pull dry from HF. AES and XPS analysis revealed this wafer to contain an uncharacteristically significant amount of nitrogen at the surface. Investigations are currently underway to locate the source of this nitrogen.

D. Discussion

$(0001)_{Si}$ 6H-SiC-Wet Chemistry. The AES and XPS spectrums obtained in this study from $(0001)_{Si}$ 6H-SiC wafers after HF dipping are similar to those published in previous

studies [26-29]. Unfortunately, none of these papers attempted to address the nature of the remaining oxide and to what the surface oxygen was bonded. Figure 1(a, b) illustrates that the amount of oxygen left on the SiC surface after HF dipping is much larger than that for a silicon surface of the same crystallographic orientation. The position of the O 1s in XPS for both of these surfaces is also different with the O 1s for SiC at 532.5-533.1 eV and the O 1s for Si at 531.5-531.8 eV. This is important as the 6H-SiC $(0001)_{Si}$ surface has been assumed by many to be similar to the Si (111) surface. Ignoring band bending effects and interpreting based strictly on chemical shifts, Table II would seem to indicate that after HF dipping the oxygen left on the SiC surface is predominantly silicon oxide while the oxygen left on Si is predominantly a hydroxide. This interpretation is difficult to accept based on the fact that HF is known to etch SiO_2 at a rate of 10000Å/sec. However, this conclusion could be in error as it ignores the possibility of carbon and oxygen bonding at the SiC surface. Even though the $(0001)_{Si}$ surface ideally is silicon terminated, perhaps the differences observed between the Si (111) and 6H-SiC $(0001)_{Si}$ surfaces lie in the possibility of oxygen termination of carbon atoms. Recent STM studies of 6H-SiC surfaces have shown that a significant number of steps exist with step

Table II. Observed Si 2p, C 1s, and O 1s Core Level Positions for Different Materials from XPS Handbook

Si 2p			
SiO_2	103.6 eV	Si	99-100 eV
SiO_2-alpha crist	103.3 eV	Si_3N_4	101.8 eV
SiO_2-apha quartz	103.6 eV	$Ph_3SiOSiPh_3$	101.3 eV
SiO_2-Vycor	103.5 eV		
C 1s			
Graphite	284.3-285.5 eV	$(C^*HCOH)_3$	284.8 eV
CO_2	291.9 eV		
$(CHC^*OH)_3$	286.6 eV		
$CaCO_3$	289.6 eV		
$Fe(CO)_5$	288.0 eV		
Benzene	284.7 eV		
$C_6H_5C^*H_3$	284.7 eV		
HCHO	287.7 eV		
O 1s			
Sapphire	531.0 eV	p-Benzoquinone	532.2 eV
Alpha-Al_2O_3	531.8 eV	Hydroquinone	533.5 eV
Gamma-Al_2O_3	530.9 eV	Methylsilicone Resin	532.7 eV
$Al(OH)_3$-Bayerite	531.4 eV	Phenylsilicone Resin	532.6 eV
$Al(OH)_3$-Gibbsite	531.5 eV	SiO_2	532.5-533.0 eV
AlOOH-Boehmite	531.5 eV	SiO_2, alpha quartz	533.2 eV
$Ph(CONH_2)$	532.2 eV	SiO_2, gel	532.8 eV

heights of 20-40Å where plenty carbon atoms are exposed at the surface. Additionally, surface studies of air exposed diamond have shown this surface to be oxidized, as well [30-32]. So it is reasonable to consider the possibility of both C-O and Si-O bonding at the SiC surface. In a separate study by the authors, XPS was used to examine an air exposed CVD diamond film (grown on Si). For this surface, the O 1s peak position was located at 532.6 eV as received and 532.0 eV after cleaning. This appears to rule out the possibility of carbon-oxygen bonding at the SiC surface. However, band bending is known to occur at both diamond and SiC surfaces due to the presence of surface states, and this can affect the position of the O 1s core level on both of these surfaces. Table II also shows that the O 1s ranges from 532-533 eV for both compounds containing C-O and Si-O bonds. Thus, analysis of the O 1s peak position therefore can not confirm or exclude the possibility of carbon-oxygen bonding at the SiC surface. Therefore, it may be better to look for chemically shifted components on the Si 2p and C 1s core levels.

Figure 2b clearly shows that after HF dipping, a chemically shifted Si 2p peak at 103.2 eV does not exist and this excludes the presence of a thin silicon dioxide layer. However, this does not exclude the presence of lower silicon oxidation states which would be chemically shifted by lesser amounts. Hollinger and Himpsel [33] using SXPS were able to distinguish four different chemically shifted oxidation states of silicon after low pressure oxidation which were: $Si^{(+1)}$ - 1.0 eV, $Si^{(+2)}$ - 1.8 eV, $Si^{(+3)}$ - 2.7 eV, and $Si^{(+4)}$ - 3.5 eV. As the chemical shift for Si to SiC ranges from 1.0 to 1.8 eV, identification of silicon atoms in lower oxidation states at the SiC surface is complicated due to overlap with the main Si-C Si 2p peak. Further complication arises from the asymmetric peak shape of the Si 2p which is actually two peaks (Si $2p_{3/2,1/2}$ doublet) which are unresolvable with our XPS instrument. The combined resolution and overlap problems, preclude the identification of Si-O and Si-OH bonding through the Si 2p photoelectron peak. For the C 1s these problems do not exist. Figure 3b, shows the presence of both a broad (1.9 eV) and a narrow (1.1 eV) C 1s peak at 283.8 and 285.5 eV respectively. The lower binding energy C 1s peak is due to C-Si bonding and is from the SiC substrate. The higher binding energy peak is from carbon at the surface in a mixture of CH_2 (284.6 eV), C-O (286.3 eV), and some O-C=O (288.4 eV) bonding configurations [34-35]. Based on these values, it is tempting to assign all of the carbon in the 285.5 eV C 1s peak to being predominantly C-O. These results are also in good agreement with those of Miyauchi *et al.* who found that surface carbon remaining on Si (100) after dipping in 5% HF was composed predominantly of C-O bonding [35]. Using higher concentrations of HF (49%), they found the surface carbon to contain predominantly more O-C=O bonding where as low HF concentrations (0.05-0.5%) left surface carbon predominantly in CH_2 bonding. Unfortunately, this does not account for all the oxygen at the SiC surface.

An alternative explanation for the difference in surface oxygen coverage for HF dipped Si (111) and SiC $(0001)_{Si}$ surfaces could be an inability of HF to hydrogen terminate the SiC surface or an instability of the hydrogen termination produced. It has been well documented that for silicon, HF dipping removes the surface oxide and terminates the surface with hydrogen [21,22,33]. On removal from HF, the hydrogen passivation of the silicon surface prevents re-oxidation of the silicon surface by DI rinsing or exposure to air. This may not be true for SiC surfaces, though. Dipping in HF may not create a hydrogen passivated SiC surface or alternatively, the hydrogen passivation of the SiC surface could be weaker and more susceptible to oxidation in the HF solution or air. For diamond, HF has not been found to produce a hydrogen terminated surface [36]. A possible explanation for weaker hydrogen termination of $(0001)_{Si}$ SiC surfaces in HF may lie in the differences in the underlying bonding. Though both Si (111) and $(0001)_{Si}$ 6H-SiC surfaces are terminated with Si atoms with one dangling bond each, the underlying bonding of the silicon surface atoms for these two surfaces is completely different. Si atoms at the surface of Si (111) have three underlying Si-Si bonds whereas in $(0001)_{Si}$ SiC there are three underlying Si-C bonds. Since C is more electronegative than Si, most of the Si valence electrons in SiC will be drawn toward the underlying C atoms leaving less electrons at the SiC surface for silicon-hydrogen bonding than for silicon surfaces. This could make the Si-H bond in $(0001)_{Si}$ SiC surfaces weaker than those formed in Si (111) surfaces, thus making H termination more difficult to achieve with HF (a weak acid) and maintain on removal from HF and exposure to air. This line of reasoning is somewhat supported by the work of Didziulis *et al.* [37] who using SXPS and molecular orbital theory conducted a detailed analysis of the $(000\text{-}1)_C$ face of 6H-SiC. Their findings indicated that the highest occupied energy levels in SiC are mostly of C 2p character and that carbon atoms would be the preferred site for an electron withdrawing adsorbate. This implies that oxidation of the SiC surface is more likely to initiate at carbon sites than at silicon sites (which prefer electron donating adsorbates). Considering the equilibrium in aqueous solutions is usually a balance between H^+ and OH^- ions. Carbon sites would be preferred for H^+ adsorption and silicon sites would be preferred for OH^- adsorption. Since HF aggressively breaks Si-O bonds by the formation of SiF_6^{2-} (the overall reaction is $SiO_2 + 6HF = 2H^+ + SiF_6^{2-} + H_2O$), it would be expected that all Si-O species would be quickly removed as soon as they are generated [38,39]. This would eventually leave a carbon rich surface with lots of free carbon at the surface (assuming that HF doesn't remove this free carbon). The free surface carbon would be mostly of C-H and C-OH bonding. This is in fact exactly what is observed. Given that AES is more sensitive to silicon than carbon, the AES Si/C pph ratios in Table I clearly show that the SiC surface is carbon rich even though crystallography indicates that it should be silicon terminated. Further, XPS and EELS both show the presence of sizable

amounts of noncarbidic carbon at the surface which are much larger than what is typically observed for silicon.

Perhaps the ideal analytical technique for determining whether hydrogen termination of SiC surfaces is achieved with HF would be high resolution electron energy loss spectroscopy (HREELS). HREELS is ideally suited for answering this type of questions as it can detect C-O, Si-O, Si-OH, Si-H, C-H "molecular" vibrations at semiconductor surfaces. Unfortunately, the work of M. Dayan and Starke *et al.* [40,41] indicates that this technique is not suitable for studying SiC surfaces as excitation of Fuchs-Kliewer phonons interferes and dominates the EELS spectrum. Due to the overlap with the FK loss peaks, Starke *et al.* were not able to exclude or conclude the presence of Si-H bonding at the SiC surface. However, they were at least able to use HREELS to identify the presence of OH^- groups at the $(0001)_{Si}$ surface after HF dipping. This agrees well with the observed hydrophilic nature of the SiC surface after HF dipping.

Perhaps the strongest argument against the possibility of hydrogen termination of SiC surfaces by HF dipping is the simple observation that for 10% HF solutions SiC surfaces are still hydrophilic on removal from HF whereas Si wafers are hydrophobic. The nature of the termination of the $(0001)_{Si}$ 6H-SiC surface could depend on the chemistry of the HF solution. HF is a very weak acid (i.e. very little dissociation of HF into H^+ and F^-) which means that there are not very many hydrogen ions in the solution. With this in consideration, it would seem possible that better hydrogen termination of $(0001)_{Si}$ SiC surfaces could be achieved by HF solutions with lower pH (i.e. higher H^+ concentration). However, the experiments conducted using HCl:HF (pH=0.1) found this solution to also wet the SiC surface seemingly indicating that hydrogen termination of the $(0001)_{Si}$ SiC surface can not be achieved. The fact that solutions of higher OH^- concentration (HF:NH_3OH (pH=8-9) and 7:1 NH_4F:HF (pH=4)) concentrations equally wetted the SiC surface points to the fact the $(0001)_{Si}$ 6H-SiC surface is terminated with OH rather than H. This agrees very well with the previously mentioned HREELS results of Starke *et al.* [41] which found OH^- groups at the $(0001)_{Si}$ surface. Unfortunately, these findings are completely opposite to what has been observed by MIRIRS (multiple internal reflection IR spectroscopy) and HREELS for Si (111) [42-45]. Using MIRIRS and HREELS, it has been found that for HF solutions of pH<7 a mixture of silicon hydrides (SiH, SiH_2, and SiH_3) are observed on the Si (111) surface. Further, MIRIRS studies have shown that for Si (111) hydrogen termination is achieved even using HF solutions with pH's as high at 10. By increasing the pH to ≥ 10, a Si (111) surface can be obtained which exhibits only silicon monohydrides (Si-H) [42-45]. Perhaps, MIRIRS is the technique of choice for studying the surface termination of SiC after HF dipping.

Finally, consideration must also be made of the presence of many steps on the vicinal $(0001)_{Si}$ 6H-SiC surface. It has been suggested that the observed oxygen levels after HF

dipping are due to more strongly bound oxides at the SiC steps. However, the results shown in Fig. 1 from Si (111) and $(0001)_{Si}$ 6H-SiC were taken from samples which were both off axis by 4-5° degrees in the same crystallographically equivalent directions. Ideally, these surfaces would have similar step densities and the argument could be made that the steps are not responsible for the observed oxygen levels. In reality, the number and nature of steps on the Si (111) and $(0001)_{Si}$ 6H-SiC surfaces are completely different. At a SiC step, both a carbon and a silicon atom are exposed allowing oxygen to be bonded to both these atoms instead of just to silicon as on Si (111). As HF is not known to remove oxides from diamond, oxygen at a silicon carbide step may be equally difficult to remove by HF. Also recent STM images of $(0001)_{Si}$ surfaces show a plethora of steps and risers with heights ranging from 3-12 monolayers high (i.e. 15-40Å) This exposes a significant amount of the (11-20) and (10-10) surfaces. In contrast, off axis Si (111) wafers exhibit only steps of two monolayers and do not significantly expose the (001) and (011) surfaces. Therefore it is possible for the (11-20) and (10-10) surfaces to be responsible for the observed oxygen. The AES spectrums of the (11-20) and (10-10) surfaces shown in Fig. 7(b,c) do show oxygen levels equal to those of the $(0001)_{Si}$ surface confirming this as a possibility. However, the authors feel that the step densities even on SiC are still to small to account for the all the oxygen observed on the $(0001)_{Si}$ surface after HF dipping. Further, if oxygen is harbored at the steps of SiC surfaces, less oxygen should be detected for on axis SiC wafers than for vicinal surfaces and this has not been observed.

UV/Ozone. Figures 5 and 6 show that UV/ozone oxidation treatment of SiC surfaces does not remove all of the non-carbidic carbon from (0001)Si 6H-SiC surfaces but does oxidize the SiC surface. This is shown via the appearance of a chemically shifted Si 2p peak and the downward shifting of the non-carbidic C 1s peak. This result is contradictory to what has been observed for UV/Ozone cleaning of Si and GaAs surfaces [21,22]. Although definite explanation for this observation is not yet at hand, the authors feel that using deeper UV lamps such as D_2 or Xe with or without the Hg lamp may work better for SiC. This is based on the assumption that generation of electron-hole pairs may assist the oxidation and removal non-carbidic carbon. As 6H-SiC has a much larger bandgap than both Si and GaAs (3.0 vs 1.1 and 1.4 eV), the higher energy light from the D_2 and Xe lamps may be more efficient at generating electron-hole pairs in SiC.

$(000\text{-}1)_C$ 6H-SiC. For $(0001)_C$ HF dipped surfaces, similarities to $(0001)_{Si}$ surfaces after HF dipping were observed. First, (1×1) LEED patterns from the $(000\text{-}1)_C$ surface were obtained after HF dipping which were similar to those found from the $(0001)_{Si}$ surface after HF dipping. Additionally, similarities in the oxygen and non-carbidic carbon levels were found. However, the nature of the oxygen and non-carbidic carbon were found to be significantly different. First, the position of the O 1s core level from the $(0001)_C$ surface was

found at 532.5 eV instead of 533.1 eV as for $(0001)_{Si}$. The value of 532.5 eV for the O 1s position on the $(0001)_C$ surface is very close to that observed from both CVD and natural diamond surfaces. Given the lower Si/C ratio, this strongly indicates that for the $(000\text{-}1)_C$ surface (and possibly the $(0001)_{Si}$ as well) all the surface oxygen is bonded to carbon instead of silicon.

The nature of the non-carbidic carbon for the $(000\text{-}1)_C$ surface after HF dipping was also observed to be different from that on the $(0001)_{Si}$ surface. Both EELS and XPS indicated that the non carbidic carbon on the $(000\text{-}1)_C$ face after HF dipping was much closer in nature to graphite. Looking at Table III, the C 1s value of 285.0 eV measured from noncarbidic carbon on the $(000\text{-}1)_C$ surface agrees exactly with previously published values measured from benzene and benzene related compounds. As benzene with its six fold ring shape is similar to graphite, it would not be unreasonable to expect to observe a $\pi\text{-}\pi^*$ transition similar to that of graphite in EELS. This all suggests that the non-carbidic carbon observed on the $(000\text{-}1)_C$ face after HF dipping is related to benzene related and other similar hydrocarbons. Perhaps a detailed analysis of the $\pi\text{-}\pi^*$ transition in organic molecules can be used to more accurately determine the nature of the non-carbidic carbon for both the $(000\text{-}1)_C$ and $(0001)_{Si}$ surfaces.

(11-20) and (10-10). The (11-20) and (10-10) surface exhibited results intermediary to those found for the $(0001)_{Si}$ and $(000\text{-}1)_C$ surfaces. AES spectrums of both surfaces revealed the Si/C ratios to be exactly equal to those found for the $(0001)_{Si}$ surface. Further, XPS of the (11-20) surface found the Si 2p and C 1s core levels positions for this surface to be the same as those found for the $(0001)_{Si}$ surface. In contrast, EELS spectrums taken from the (11-20) and (10-10) surfaces looked almost exactly like those taken from the $(000\text{-}1)_C$ surface both exhibiting loss peaks at 5 eV due to non carbidic carbon of benzene like origin. XPS of the non-carbidic C 1s peak from the (11-20) surface also exhibited was also similar to that observed from the $(000\text{-}1)_C$ surface. The fact that the non-polar (11-20) and (10-10) surfaces exhibit split similarities between the polar $(0001)_{Si}$ and $(000\text{-}1)_C$ surfaces is rather surprising.

From the above discussion it appears evident that unlike Si (111), a hydrogen terminated silicon surface for $(0001)_{Si}$ 6H-SiC is not achieved by dipping in 10% HF. Owing to the presence of Si-C backbonds, the outermost silicon surface atoms of the $(0001)_{Si}$ surface are extremely unstable in HF and are removed/etched away by the HF leaving a carbon rich surface terminated with a mixture of C-O and C-H bonding. This begs the question: Is there an *ex situ* cleaning procedure which can eliminate the C-O bonding and or remove the non-carbidic carbon? A review of diamond research unfortunately indicates that the only "wet chemical" found to achieve hydrogen termination of diamond is surprisingly, olive oil.

E. Conclusions

Wet chemical cleaning of 6H-SiC surfaces was investigated. HF based wet cleans were found to leave carbon rich SiC surfaces which were hydrophilic in nature. The hydrophilic

nature of these SiC surfaces suggests that HF dipping does not produce a hydrogen terminated SiC surface analogous to HF dipped Si surfaces. UV/Ozone oxidation was investigated as a means of removing non-carbidic carbon from 6H-SiC surfaces. UV/ozone exposure was not found to completely remove all non-carbidic carbon from the SiC surface. The UV/O_3 treatment, however, did induce a change in the chemical state of the non-carbidic carbon. This was seen in XPS via a shift in the non-carbidic carbon C 1s peak from 285.7 to 285.2 eV.

F. Future Research

Research to be conducted in the next reporting period includes:

- Investigation of UV/ozone cleaning of SiC with D_2 and Xe lamps,
- Investigation of use of Si capping layers on 6H-SiC as a passivating layer in *ex situ* cleaning, and
- Investigate difluoro-dioxygen (FOOF) as a wet chemical clean for SiC surfaces.

G. References

1. R. F. Davis, G. Kelner, M. Shur, J. Palmour, J. A. Edmond, Proc. of the IEEE, **79** 677 (1991).
2. See for example: S. Strite and H. Morkoc, J. Vac. Sci. and Technol. B **10**, 1237 (1992); J. H. Edgar, J. Mater. Res. **7**, 235 (1992); R. F. Davis, Proc. of IEEE **79**, 702 (1991), H. Morkoc and S.N. Mohammad, Science **267**, 51 (1995).
3. W. Kern, J. Electrochem. Soc. **137**, 1997 (1990).
4. R. Williams, *Modern GaAs Processing Methods*, 2nd ed. (Artech House, Inc., New York, 1990), pp. 81-114.
5. G. R. Srinivasan and B. S. Meyerson, J. Electrochem. Soc. **134** (6), 1518 (1987).
6. B. S. Meyerson, E. Ganin, D. A. Smith, and T.N. Nguyen, J. Electrochem. Soc. **133** (6), 1232 (1986).
7. C. Galewski, J. Lou, W. G. Oldham, IEEE Transactions on Semiconductor Manufacturing **3** (3), (1990).
8. M. Racanelli, D. W. Greve, M. K. Hatalis, L. J. van Yzendoorn, J. Electrochem. Soc. **138** (12), 3783 (1991).
9. J. H. McFee, R. G. Swartz, V. D. Archer, S. N. Finegan, and L. C. Feldman, J. Electrochem. Soc. **130** (10), 3083 (1989).
10. A. J. Pidduck, D. J. Robbins, A. G. Cullis, D. B. Gasson, and J. L. Glasper, J. Electrochem. Soc. **136** (10), 3083 (1989).
11. F. Ren, A. B. Emerson, S. J. Pearton, T. R. Fullowan, and J. M. Brown, Appl. Phys. Lett. **58** (10), 1030 (1991).
12. M. Kodama, Electronics Letters **30** (1), 89 (1994).
13. L. L. Yeh, Y. Xie, and P. H. Holloway, J. Appl. Phys. **65** (9), 3568 (1989).
14. Z. L-Weber, N. Newman, J. Washburn, and E. R. Weber, Appl. Phys. Lett. **54** (4), 356 (1989).
15. K. Prasad, Vacuum **46** (2), 127 (1995).
16. A. Zangwill, *Physics at Surfaces*, (Cambridge University Press, New York, 1988) pp. 221-231.
17. Y. T. Yeow, D. R. Lamb, and S. D. Brotherton, J. Phys. D: Appl. Phys. **8**, 1495 (1975).
18. E. H. Rhoderick, and R. H. Williams, *Metal-Semiconductor Contacts*, 2nd ed. (Oxford University Press, New York, 1988), pp. 5-17.

19. E. H. Snow, A. S. Grove, B. E. Deal, and C. T. Sah, J. Appl. Phys. **36** (5), 1664 (1965).
20. E. Yon, W. H. Ko, and A. B. Kuper, IEEE Trans. Electron Devices **13** (12), 276 (1966).
21. B.S Meryson, F. J. Himpsel, and K. J Uram, Appl. Phys. Lett. **57**, 1034 (1990).
22. M. Grundner and H. Jacob, Appl. Phys. A **39**, 73 (1986).
23. J. A. McClintock, R. A. Wilson, and N. E. Byer, J. Vac. Sci. Technol. **20**, 241 (1982).
24. R. F. Kopf, A. P. Kinsella, and C. W. Ebert, J. Vac. Sci. Technol. B **9**, 132 (1991).
25. Atomic Layer Epitaxy of Group IV Materials: Surface Processes, Thin Films, Devices and Their Characterization, Semiannual Technical Report, R. F. Davis, Grant #N00014-91-J-1416, Office of the Chief of Naval Research, July 1994.
26. F. Bozso, J. Muehlhoff, M. Trenary, W. J. Choyke, and J. T. Yates Jr., J. Vac. Sci. Technol. **A2** (3), 1272 (1984).
27. A. N. Andreev, M. M. Anikin, A. L. Syrkin, V. E. Chelnokov, Semiconductors **28** (6), 577 (1994).
28. S. Nakanishi, H. Tokutaka, K. Nishimori, S. Kishida, and N. Ishihara, Applied Surface Science **41/42**, 44 (1989).
29. L. M. Porter, J. S. Bow, M. J. Kim, R. W. Carpenter, and R. F. Davis, J. Mater. Res. **10** (3), 668 (1995).
30. R. E. Thomas, R. A. Rudder, and R. J. Markunas, J. Vac. Sci. and Technol. A **10**, 2451 (1992).
31. V. S. Smentkowski, J. Jansch, M. A. Henderson, J. T. Yates Jr., Surface Science **330**, 207 (1995).
32. O. M. Kuttel, L. Diederich, E. Schaller, O. Carnal, L. Schlapbach, Surface Science **337** L812, (1995).
33. Hollinger and Himpsel, Appl. Phys. Lett. **44**, 93 (1984).
34. A. Miyauchi, Y. Inoue, M. Ohue, N. Momma, T. Suzuki, and M. Akiyama, J. Electrochem. Soc. **137**, 3257 (1990).
35. A. Miyauchi, Y. Inoue, T. Suzuki, M. Akiyama. Appl. Phys. Lett. **57**, 676 (1990).
36. Personnel Communication with Jacob van der Weide.
37. S. V. Didziulis, J. R. Lince, P. D. Fleischauer, and J. A. Yarmoff, Inorg. Chem. **30**, 672 (1991).
38. S. Verhaverbeke, I. Teerlinck, C. Vincker, G. Stevens, R. Cartuyvels, and M.M. Heyns, J. Electrochem. Soc. **141** 11, 2852 (1994).
39. J. S. Judge, J. Electrochem. Soc. **118** 11, 1773 (1971).
40. M. Dayan, Surface Science **149**, L133 (1985).
41. U. Starke, Ch. Bram, P.-R. Steiner, W. Hartner, L. Hammer, K. Heinz, and K. Muller, Appl. Surf. Sci. **89**, 175 (1995).
42. T. Suzuki ans S. Adachi, Jpn. J. Appl. Phys. **33**, 5599 (1994).
43. L. Li, H. Bender, T. Trenkler, P. W. Mertens, M. Merius, W. Vandervorst, and M.M Heyns, J. Appl. Phys. **77**, 1323 (1995).
44. G. S. Higashi, R. S. Becker, Y. J. Chabal, A. J. Becker, Appl. Phys. Lett. **58**, 1656 (1991).
45. G. S. Higashi, Y. J. Chabal, G. W. Trucks, and K. Raghavachari, Appl. Phys. Lett. **56**, 656 (1990).

VIII. Electrical Characterization of SiC Grown by Gas-source Molecular Beam Epitaxy

A. Introduction

Silicon carbide (SiC) is a wide bandgap material that exhibits polytypism, a one-dimensional polymorphism arising from the various possible stacking sequences of, e. g., the silicon and carbon layers along the directions of closest packing. There are approximately 250 SiC polytypes [1]. Included in these is one cubic polytype. This single cubic polytype, β-SiC, crystallizes in the zincblende structure, has a room temperature bandgap of 2.3 eV, and is commonly referred to as 3C-SiC. (In the Ramsdell notation, the three (3) refers to the number of Si and C bilayers necessary to produce a unit cell and the C indicates its cubic symmetry.) The other rhombohedral and hexagonal polytypes are classed under the heading of α-SiC. The most common of these latter polytypes is 6H-SiC with a room temperature bandgap of ≈ 3.0 eV.

Since the 1950's, monocrystalline single crystals of 6H-SiC have been grown using the Lely sublimation process [2]. However, nucleation was uncontrolled using this process and control of resultant polytypes was difficult. In the last decade, using a seeded sublimation-growth process, commercial wafers cut from boules of single polytype 6H-SiC of >1 inch diameter have been grown of much higher quality than that obtained using the Lely process. The use of single crystals of the 6H polytype cut from these boules has given a significant boost to SiC research and device development.

Silicon carbide epitaxial thin film growth on hexagonal SiC substrates has been reported since the 1960's. The use of nominally on-axis SiC substrates has usually resulted in growth of 3C-SiC films. Films of 3C-SiC(111) grown by CVD have been formed on 6H-SiC substrates less than 1° off (0001) [3]. Films of 3C-SiC on 6H-SiC substrates have typically had much lower defect densities than those grown on Si substrates. The major defects present in β-SiC/6H-SiC films have been double positioning boundaries (DPB) [4]. Despite the presence of DPBs, the resultant material was of sufficient quality to further device development of SiC. The use of off-axis 6H-SiC(0001) substrates has resulted in growth of high-quality monocrystalline 6H-SiC layers with very low defect densities [5].

In addition, the use of more advanced deposition techniques, such as molecular beam epitaxy (MBE), has been reported for SiC in order to reduce the growth temperature from about 1400-1800°C on 6H-SiC substrates. Silicon and C electron-beam sources have been used to epitaxially deposit SiC on 6H-SiC (0001) at temperatures of 1150°C [6].

B. Experimental Procedure

Thin, epitaxial films of SiC were grown on the Si face of 6H-SiC(0001) substrates supplied by Cree Research, Inc. These included both vicinal 6H-SiC(0001) wafers oriented

3-4° towards [11$\bar{2}$0] containing a 0.75 μm epitaxial 6H-SiC layer deposited via CVD and on-axis 6H-SiC(0001) wafers. All wafers were received with a thermally oxidized 75 nm layer to aid in wafer cleaning. Wafers are prepared for growth by a 10% HF dip and a 10 minute anneal at 1050°C in UHV as well as a silane exposure and boil-off, a technique detailed in previous reports and based on the work of Kaplan [7].

All films were grown using a specially designed and previously described [8] GSMBE system. The base and operating pressures were 10^{-9} Torr and 10^{-3}–10^{-6} Torr, respectively. All films were grown between 1050–1500°C using different ratios of silane (SiH_4, 99.999% purity) and ethylene (C_2H_4, 99.99% purity) with total source inputs ranging from 0.6-2.0 sccm on both vicinal and on-axis α(6H)-SiC(0001). Similar to the results described in the previous report, 6H-SiC films were produced only when >5.0 sccm H_2 were included in the reactant gas flow and the substrate temperature was maintained at >1350°C. Thin 2H-AlN(0001) buffer layers, grown on on-axis α(6H)-SiC(0001), were also used as substrates for 3C-SiC(111) layers. The thin AlN layers were grown for 1 minute in the same system at 1050°C using a standard Al (99.9999% purity) effusion cell source, operating at 1250°C, and a compact electron cyclotron resonance (ECR) source to activate 3.5 sccm of N_2 (99.9995% purity). (This procedure has been described previously [10, 11]). For the purposes of the doping studies, the 6H polytype, grown on vicinal 6H-SiC, was investigated. Solid aluminum, evaporated from a standard MBE effusion cell, was used for p-type doping and ammonia (NH_3, diluted to 300 ppm in H_2) was used for n-type doping.

Reflection high-energy electron diffraction (RHEED) at 10 kV and high-resolution transmission electron microscopy (HRTEM) were used for structural and microstructural analyses. Samples were prepared for HRTEM using standard techniques [11]. A Topcon EM 002B high-resolution transmission electron microscope was used at 200 kV for the HRTEM analysis. Secondary ion mass spectrometry (SIMS), using both a Cameca IMS-3f and a UHV-compatible Cameca IMS-4f ion microprobe operating at 10 keV, was employed to determine the atomic concentrations of H, O, N and Al. Carrier concentrations for undoped SiC films, grown on insulating AlN layers, as well as p-type and n-type doped films were measured at room temperature by C-V and by standard Hall techniques at 3.5 kG. Nickel contacts, RF sputtered at room temperature then annealed at 1000°C for 30 s in Ar, were used on the undoped and n-type films and aluminum contacts, evaporated in a standard evaporator and annealed at 500°C for 30 seconds in Ar, were used on p-type films.

C. Results

Undoped films of α(6H)-SiC(0001) have been grown on vicinal 6H-SiC(0001) substrates at temperatures above 1350 °C. Optimum conditions for growth were determined to be a substrate temperature of 1450 °C using 0.6 sccm SiH_4 and either 0.375 or 0.6 sccm C_2H_4.

Growth rates approaching 1500 Å per hour were achieved. C-V and Hall electrical measurements made on some of the thicker SiC films (≈1.0 μm) have shown the films to be n-type with electron concentrations as low as 6×10^{14} cm^{-3} and mobilities as high as 72 $cm^2V^{-1}s^{-1}$. Figure 1 shows a typical SIMS profile of a MBE epilayer on top of a CVD epilayer. While both layers are of comparable structural quality, the MBE layer has a considerably lower concentration of residual nitrogen.

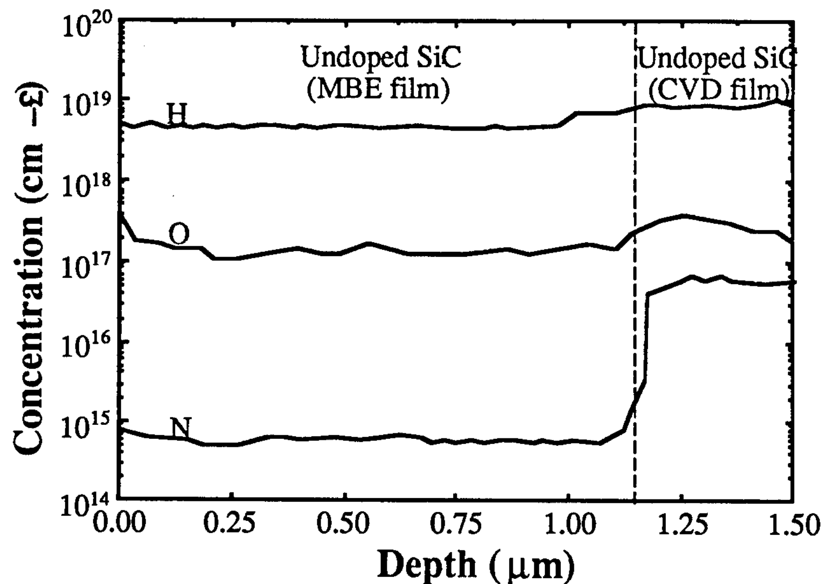

Figure 1. SIMS profile of a MBE epilayer grown on a CVD epilayer. Note the reduced nitrogen content in the MBE layer.

Undoped films of β-SiC(111) have been grown on thin, insulating layers of 2H-AlN(0001) at 1350°C using 0.6 sccm SiH_4 and 0.6 sccm C_2H_4. Growth was initiated at 1100 °C and the temperature was increased to 1350 °C at a rate of 10 °C min^{-1}. Growth rates approaching those achieved for homoepitaxial growth of SiC on vicinal SiC were measured. C-V and Hall electrical measurements made on some of the thicker SiC films (≈1.0 μm) have shown the films to be n-type with electron concentrations as low as 2×10^{15} cm^{-3} and mobilities as high as 681 $cm^2V^{-1}s^{-1}$. Figure 2 shows a typical SIMS profile of a MBE epilayer on top of an AlN layer grown on a CVD epilayer. While both SiC layers are of comparable quality (though different polytypes), the MBE layer has a considerably lower concentration of residual nitrogen.

P-type Doping. Homoepitaxial SiC films on n-type substrates were doped p-type with Al at several different impurity concentrations. Carrier concentrations were measured on a number of Al-doped 6H-SiC films by C-V and the Hall technique. These films were grown under the previously stated conditions. Four different doping levels were achieved with Al effusion cell

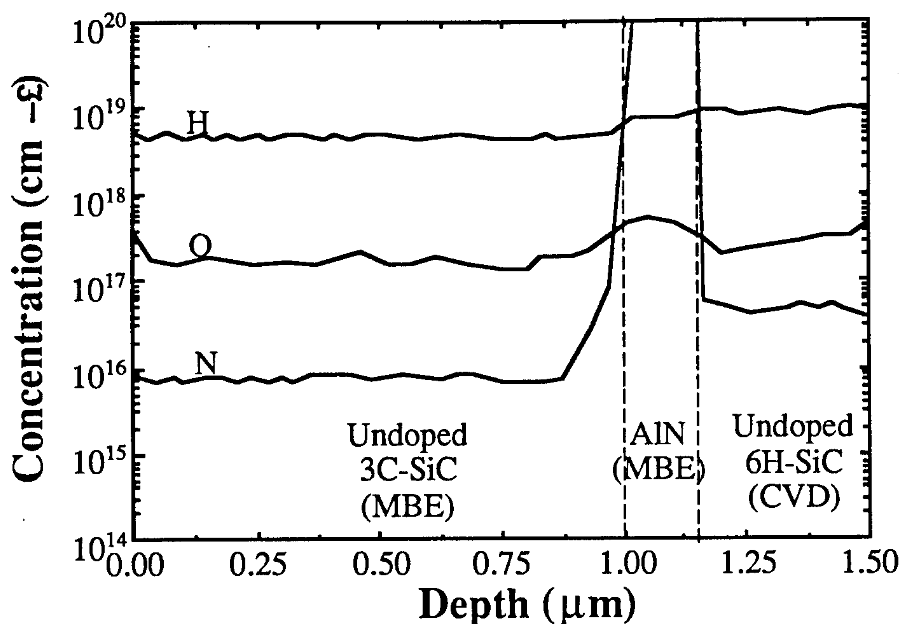

Figure 2. SIMS profile of a MBE epilayer grown on an AlN layer on a CVD epilayer. Note the reduced nitrogen content in the MBE layer.

temperatures held at 770°C, 840°C, 920°C and 1010°C. The Hall results are shown in Table I. Figure 3 shows SIMS profiles for the same p-type films as displayed in Table I. Compared to our previously reported [12] p-type doped films, these profiles are very smooth and uniform.

Table I. Hall Concentrations and Mobilities of Various P-type SiC Films

Aluminum Cell Temperature (°C)	Hole Concentration (cm^{-3})	Hole Mobility ($cm^2V^{-1}s^{-1}$)
770	4.6×10^{15}*	N/A
840	6.7×10^{16}	30
920	8.7×10^{17}	24
1010	9.1×10^{18}	18

* Too resistive for Hall characterization. Carrier concentration determined by C-V.

N-type Doping. Homoepitaxial SiC films on p-type substrates were doped n-type using NH_3, diluted to 300 ppm in H_2, at several different impurity concentrations. Carrier concentrations were measured on a number of N-doped 6H-SiC films by C-V and the Hall

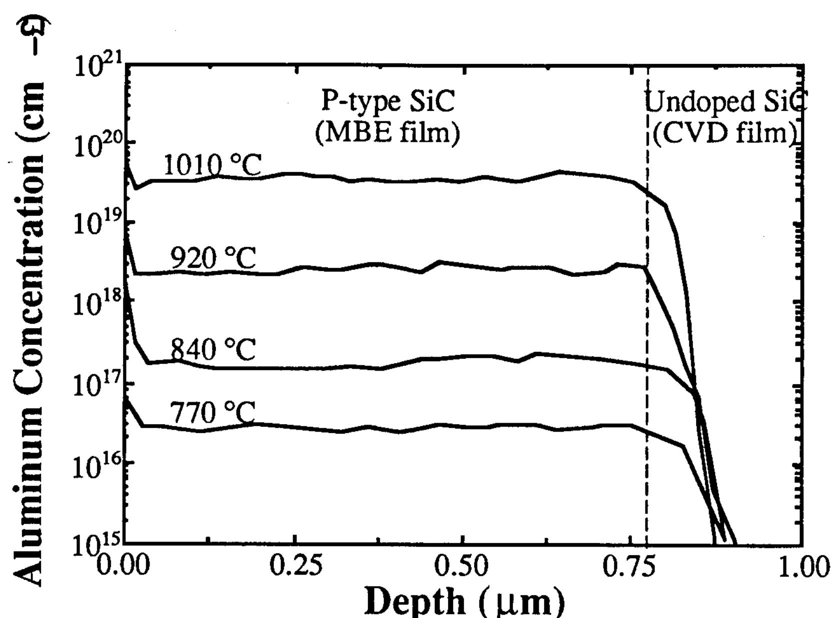

Figure 3. SIMS profiles for 6H-SiC films doped with Al from an MBE effusion cell at different source temperatures.

technique. These films were grown under the previously-stated conditions. Three different doping levels were achieved with NH_3/H_2 flow rates at 0.08, 0.6 and 5.0 sccm. The Hall results are shown in Table II. Figure 4 shows SIMS profiles for the same n-type films as displayed in Table II.

Table II. Hall Concentrations and Mobilities of Various N-type SiC Films

NH_3/Ar Flow Rate (sccm)	Electron Concentration (cm^{-3})	Electron Mobility ($cm^2V^{-1}s^{-1}$)
0.08	1.8×10^{15}	58
0.60	2.1×10^{16}	41
5.00	9.8×10^{17}	26

D. Discussion

The results of the Hall measurements on undoped β-SiC, grown on AlN on on-axis 6H-SiC, represent some of the lowest unintentional doping levels ever reported in the cubic polytype. Molecular beam epitaxy is also shown to produce very pure layers with very low

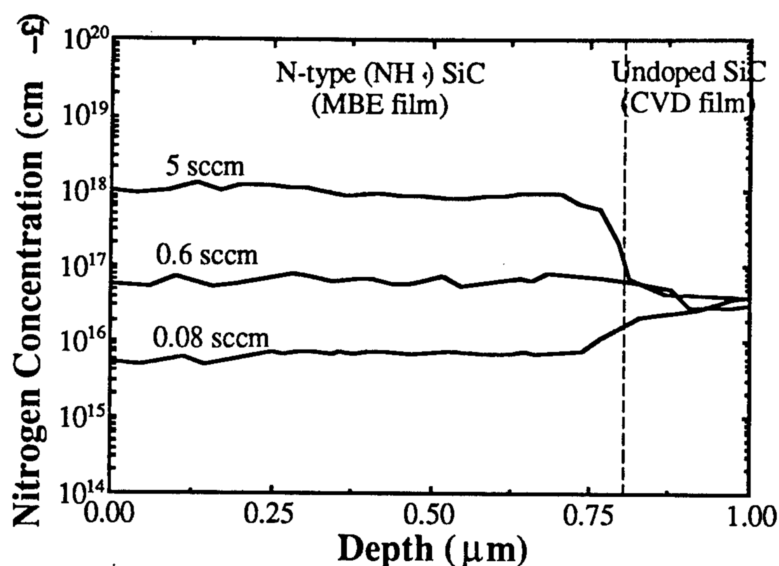

Figure 4. SIMS profiles for 6H-SiC films doped with N from an NH_3/H_2 mix.

impurity concentrations. The Hall measurements listed in Tables I and II and the SIMS data displayed in Figs. 3 and 4 represent the first intensive attempt at SiC doping ever attempted by MBE. As expected, the concentration of both impurity atoms and carriers increased as the source flux increased. The profiles in Fig. 3 and the data in Table I are of the same order of magnitude indicating a much higher activation efficiency in p-type SiC than previously reported by CVD [13]. Similar data are also shown for the n-type samples.

E. Conclusions

Films of 6H- and 3C-SiC have been grown between 1050-1500°C by GSMBE using SiH_4 and C_2H_4 on different orientations of α(6H)-SiC(0001) and on thin buffer layers of AlN. Growth of SiC on AlN represents a possible means of growing higher quality β-SiC(111) than previously reported. Hall electrical measurements on these films revealed carrier concentrations as low as 2×10^{15} cm^{-3} and room temperature mobilities as high as 681 cm^{2}V^{-1}s^{-1}.

Doped films of 6H-SiC have been grown on vicinal α(6H)-SiC(0001) at T>1350°C. The films (doped p-type with Al and n-type with N) showed carrier concentrations that increased with increasing impurity flux. SIMS profiles for Al incorporation are of the same order of magnitude indicating a much higher activation efficiency than previously reported by CVD.

F. Future Research Plans and Goals

Further work on doping both 3C- and 6H-SiC will be performed. Studies related to the doping of SiC with N_2 will be initiated. Additionally, further studies will be initiated to study

the role that hydrogen and other gases may play in the activation efficiency of carriers in SiC films. Hydrogen incorporation is postulated [14] as a possible retardant to impurity activation.

G. References

1. G. R. Fisher and P. Barnes, Philos. Mag. B **61**, 217 (1990).
2. J. A. Lely, Ber. Deut. Keram. Ges. **32**, 229 (1955).
3. H. S. Kong, J. T. Glass, and R. F. Davis, Appl. Phys. Lett. **49**, 1074 (1986).
4. H. S. Kong, B. L. Jiang, J. T. Glass, G. A. Rozgonyi, and K. L. More, J. Appl. Phys. **63**, 2645 (1988).
5. H. S. Kong, J. T. Glass, and R. F. Davis, J. Appl. Phys. **64**, 2672 (1988).
6. S. Kaneda, Y. Sakamoto, T. Mihara, and T. Tanaka, J. Cryst. Growth **81**, 536 (1987).
7. R. Kaplan, Surface Sci. **215**, 111 (1989).
8. L. B. Rowland, S. Tanaka, R. S. Kern and R. F. Davis, in *Proceedings of the Fourth International Conference on Amorphous and Crystalline Silicon Carbide and Related Materials*, edited by C. Y. Yang, M. M. Rahman and G. L. Harris (Springer-Verlag, Berlin, 1992) p. 84.
9. L. B. Rowland, R. S. Kern, S. Tanaka and R. F. Davis, J. Mater. Res. **8**, 2310 (1993).
10. L. B.Rowland, R. S. Kern, S. Tanaka and R. F. Davis, Appl. Phys. Lett. **62**, 3333 (1993).
11. S. P. Withrow, K. L. More, R. A. Zuhr, and T. E. Haynes, Vacuum **39**, 1065 (1990).
12. R. S. Kern, S. Tanaka and R. F. Davis, in *Transactions of the Second International High Temperature Electronics Conference* (1994) p. P-141.
13. H. J. Kim and R. F. Davis, J. Electrochem. Soc. **133**, 2350 (1986).
14. E. Bringuier, personal communication.

IX. Fabrication and Characterization of Al/AlN/SiC MIS Diodes Grown by Gas-source Molecular Beam Epitaxy

A. Introduction

Silicon carbide (SiC) is a wide bandgap material that is attractive for the fabrication of electronic devices that operate in a variety of harsh environments. Silicon carbide has a wide bandgap (≈3.0 eV at room temperature), excellent thermal stability [1-3], a high thermal conductivity (4.9 W $cm^{-1}K^{-1}$) [4], a high breakdown field (2×10^6 V cm^{-1}) [2] and a high saturated electron drift velocity (2×0^7 cm s^{-1}) [3]. In the last few years, blue light emitting diodes (LEDs), junction field effect transistors (JFETs) and metal-oxide-semiconductor field effect transistors (MOSFETs) have become commercially available. Excellent reviews of these devices have been published [5-11].

Since metal-insulator-semiconductors (MIS) structures are an important part of today's microelectronics industry, MIS diodes (using SiO_2, in particular, as the insulator) have been studied by a number of researchers. The majority of the studies have been done on 6H-SiC substrates. Although some work [12-16] has also been done on 3C-SiC, the defective nature of the material makes most of the measurements difficult to interpret since the resulting interface state densities and fixed oxide charge densities are very high. Most of this work has centered around the optimization of the oxidation both kinetically and electrically; however, the chemical character of the oxide has also been studied by Auger electron spectroscopy [17, 18] and secondary ion mass spectroscopy [16, 19, 20]. Nearly all reports (see, for example, [21]) show that the MOS diodes can be easily accumulated and depleted at room temperature; however, inversion cannot be obtained using typical testing procedures. The lowest reported values of fixed charge densities and interface state densities are 3×10^{11} cm^{-2} and 1.5×10^{11} cm^{-2} eV^{-1}, respectively. To date, there has only been one report [23] of a MIS diode made with an insulator other than SiO_2. In this case, Si_3N_4 was used, but had only minimal success due to very large density of defects and large leakage currents.

Aluminum nitride possesses a direct bandgap of 6.28 eV at 300 K [24], a melting point in excess of 2275 K [25], a thermal conductivity of 3.2 W cm^{-1} K^{-1} [26] and a low dielectric constant ($K_{AlN} = 8.5 \pm 0.2$) [27]. As such, it is a candidate material for high-power and high-temperature microelectronic and optoelectronic applications with the latter employment being particularly important in the ultraviolet region of the spectrum [24]. These properties strongly indicate that superior surface acoustic wave devices, operational in aggressive media and under extreme conditions both as sensors for high temperatures and pressures and as acousto-optic devices, can be developed [28-30]. However, progress regarding these (and other) applications is hampered by the lack of high-quality single crystal material.

Because of its thermal stability and wide bandgap, AlN has been investigated as a potential insulating material for Si [31-36], GaAs [35, 37-41] and InP [41, 42] based electronic device structures. Although Stevens *et al.* [43] have fabricated an operational Si-MISFET using AlN as the gate, only moderate success has been accomplished using AlN gates due to difficulties in growing high-quality films on these substrates. The purpose of this work was to study the feasibility of forming MISFET devices in SiC using AlN as the gate dielectric.

B. Experimental Procedure

Thin, epitaxial films of several thicknesses of AlN were grown on n-type (N_D-N_A $\approx 4\times10^{16}$ cm^{-3}) Si-face α(6H)-SiC(0001) substrates supplied by Cree Research, Inc. Each of the wafers contained a 0.8 μm epitaxial SiC layer deposited via CVD and a thermally oxidized 75 nm layer to aid in wafer cleaning. The surfaces were prepared by a 10% HF dip and a 10 minute anneal at 1050 °C in UHV, as well as a silane exposure and boil-off described in previous reports.

All growth experiments were carried out in the GSMBE system detailed in previous reports. Films of AlN were grown at 1100 °C. Source were aluminum (99.9999% purity), evaporated from a standard MBE effusion cell operated in all cases at 1150°C, and 7.0 sccm ammonia (99.999% pure). Typical base pressures of 10^{-9} Torr were used. Aluminum contacts (area = 4.558×10^{-3} cm^2) were deposited on the AlN by means of a standard evaporator and In-Sn solder was used as a backside contact to the SiC.

High frequency capacitance-voltage measurements were performed on samples ≈1000 Å thick using a HP 4284A LCR meter operating at 1 MHz. Samples could be tested in the dark and under illumination by a halogen lamp at temperatures up to 300 °C. The typical measurement sequence involved illuminating the sample while it is biased under depletion conditions until a stable capacitance is reached, switching the light off, sweeping the voltage from depletion into accumulation and sweeping from accumulation back to depletion. From the C-V curve and the knowledge of a few physical constants, several important parameters can be calculated.

From the C-V curve , the flat band voltage, V_{FB}, can be determined from the flat band capacitance, C_{FB}. The flat band capacitance is calculated by

$$C_{FB} = \frac{K_{AlN}\varepsilon_0}{d_{AlN} + \left(\frac{K_{AlN}}{K_{SiC}}\right)L_D} \tag{1}$$

where K_{AlN} (≈9) and K_{SiC} (≈10) are the dielectric constants of AlN and SiC, ε_0 is the permittivity of free space, d_{AlN} is the AlN thickness and L_D is the extrinsic Debye length in SiC. The Debye length can be calculated according to the relation

$$L_D^{SiC} = \sqrt{\frac{K_{SiC}\varepsilon_0 kT}{Nq^2}} \quad (2)$$

where k is Boltzmann's constant, T is temperature, N is the doping level in the SiC and q is the carrier charge.

Having determined the flat band capacitance, the flat band voltage can be read directly from the C-V curve. The deviation of this number from ideality (determined by the difference in the work functions of the Al metal and the SiC) can, in turn, be used to determine the interface charge trap density per unit area, N_t, which takes into account the density of interface states over the entire energy range of the bandgap. This density of interface charge traps can be calculated by

$$N_t = \frac{C_{AlN}^{max}}{qA}(V_{FB}-\phi_{ms}) \quad (3)$$

where C_{AlN}^{max} is the maximum capacitance of the AlN (read from the C-V curve), A is the contact area and ϕ_{ms} is the difference in the work functions of the metal (Al) and the semiconductor (SiC). Since the value of ϕ_{Al} is 4.28 V [44] and the value of ϕ_{SiC} is 4.5 V [45], ϕ_{ms} has a value of 0.22 V.

Another interesting consequence of these measurements is the ability to determine experimentally the value of the AlN dielectric constant. Knowing the thickness of the insulator, determined by HRTEM, profilometry, SEM or some other method, the AlN dielectric constant can be calculated by the following relation

$$K_{AlN} = \frac{d_{AlN}C_{AlN}^{max}}{\varepsilon_0 A}. \quad (4)$$

C. Results

In all cases, the diodes could be accumulated and depleted with the application of small gate voltages. However, deep depletion and inversion were not achieved in any case. Figure 1 shows a C-V curve for a typical 1000 Å sample measured at room temperature. In this particular case, where N_D-$N_A \approx 4\times10^{16}$ cm^{-3}, the Debye length can be calculated from Eq. 2 to be $\approx$190 Å.

Using the known data and others determined the from the graph, several other important points can be gleaned. First of all, the flat band capacitance and voltage are 310 pF and 0.7 V, respectively. Since only 0.22 V can be accounted for by the difference in the work functions of the metal (Al) and the semiconductor (SiC), the theoretical shift from flat band voltage is 0.48 V. Using Eq. 3, this translates to a density of (negatively charged) interface charge traps

of $\approx 2\times10^{11}$ cm^{-2}. From Eq. 4, the dielectric constant for AlN can be calculated to be 8.67 which fits other measured data [27] for AlN.

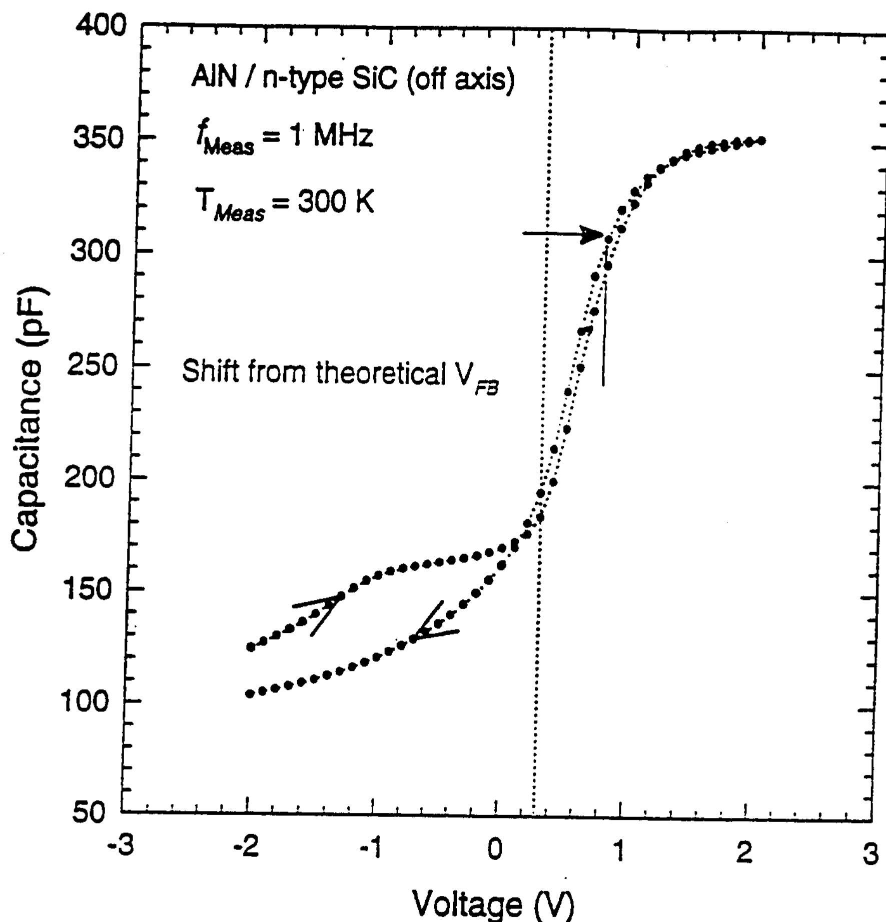

Figure 1. Room temperature C-V measurement of an Al/AlN/SiC MIS diode.

Figure 2 shows the side-by-side comparison of the same sample swept over the voltage range at room temperature while in the dark and while under illumination. The most significant features of this figure are the shift in the flat band voltage and the increased hysteresis observed under illumination.

Figure 3 displays the effect that temperature plays on the C-V measurements. The broadening of the curve (i.e., the hysteresis) is shown to occur with increasing temperature. In contrast to the effect shown by SiO_2/SiC interfaces, the flat band voltage shift *decreases* in the case of AlN insulators. As a result of this effect, the net interface trap density appears to be reduced as the temperature of the measurement is made.

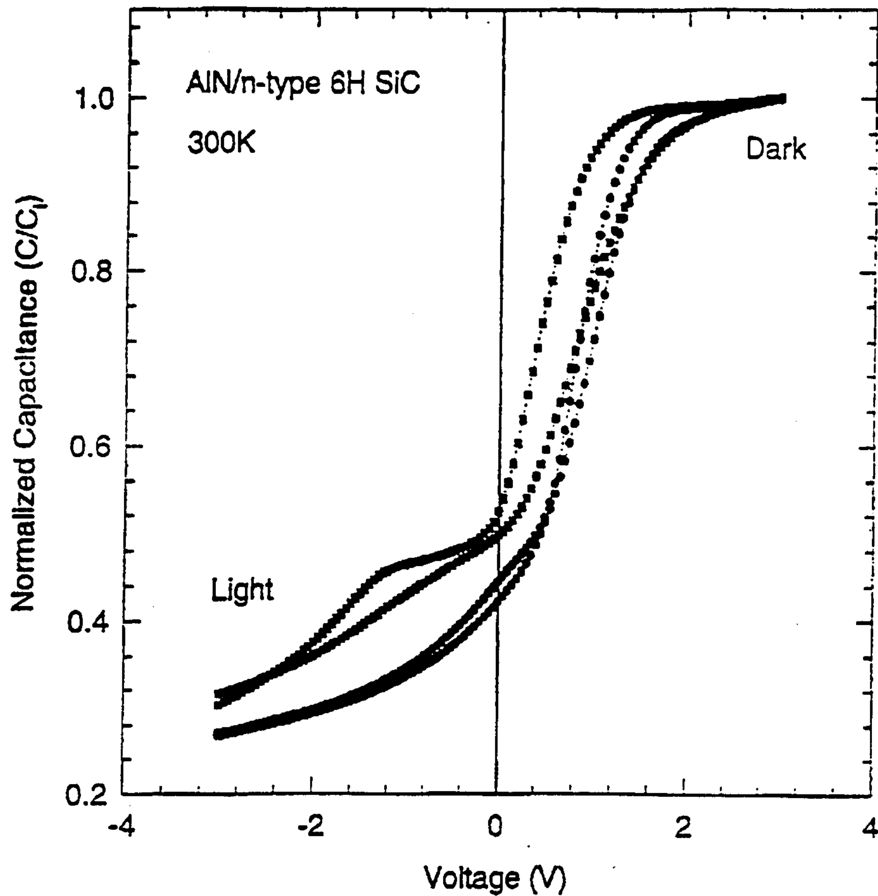

Figure 2. Room temperature C-V measurements of an Al/AlN/SiC MIS diode measured with and without illumination.

D. Discussion

Figure 1 shows the accumulation and depletion of a typical Al/AlN/SiC diode. Attempts to invert these samples at room temperature were unsuccessful. This is due to several factors. The extremely low intrinsic carrier concentration in SiC ($\approx 10^{-6}$ cm^{-3}) and the low carrier generation significantly reduce the number of minority carriers available in the SiC surface region. The low interface charge trap density and the very small amount of hysteresis make this insulator comparable to any reported thermally grown oxide layer. This curve is very similar to those done on SiO_2/Si MIS structures at very low temperatures ($\approx$150 K) which indicates that the traps present in this interface are very slow to react to the voltage and the frequency shift. In this case, the most likely origin of the traps is unsaturated bonds at the interface and, perhaps, a slight amount of intermixing at the interface creating a number of unsatisfied bonds. Since the interface is made up of a nonisovalent bonding configuration made up primarily of Si^{+4} and N^{-3} atoms which create a net positive charge in the vicinity of the interface, the interface traps are negatively charged in order to maintain charge neutrality.

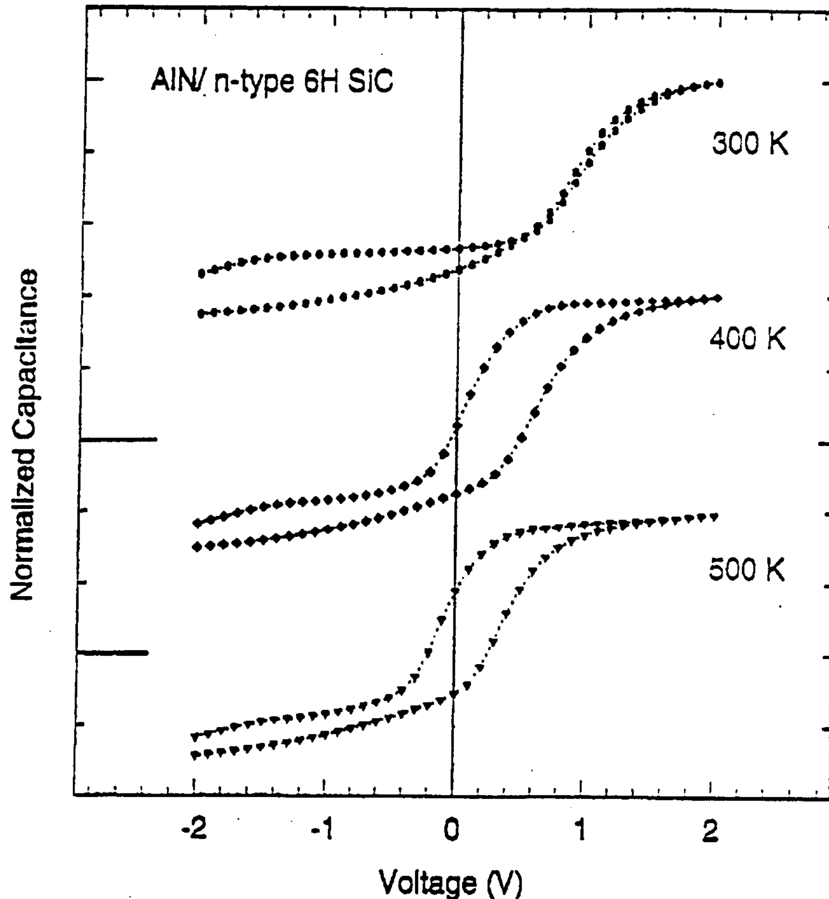

Figure 3. Temperature dependence of C-V measurements of an Al/AlN/SiC MIS diode.

The effects shown in Figs. 2 and 3 are particularly interesting in their relationship to the device physics associated with the AlN/SiC interface. Figure 2 shows that the charge contained in the traps can be modulated by the application of light. Though these traps are very slow when considering only a voltage bias, their electron population can be reduced and increased by the application and removal of light. Figure 3 shows the competition between the negatively charged (acceptor-like) traps and a donor-like trap of unknown origin. At higher temperatures, the latter trap begins to control the shift in V_{FB} and pushes it to smaller values. At this point, the nature of these traps is unknown, but is speculated to be associated with the relatively high level ($\approx 10^{20}$ cm^{-3}) of oxygen tied up at the interface of the AlN layer.

E. Conclusions

Thin AlN insulating layers on SiC have been used in MIS diode structures. The resulting diodes can be accumulated and depleted but cannot be inverted by high frequency C-V characterization. Layers thinner than 1000 Å are too leaky to measure, but 1000 Å thick layers

are sufficient. Very low interface trap densities ($\approx 2\times10^{11}$ cm^{-2}) and very accurate dielectric constant (8.67) values have been determined. The role of illumination and temperature have also been studied.

F. Future Research Plans and Goals

Growth will be attempted on other SiC orientations to attempt to further low the interface trap density. Passivating layers will also be deposited on the AlN to help reduce leakage currents and prevent oxidation of the material. Other attempts to reduce the impurity content are also underway.

E. References

1. R. B. Campbell and H.-C. Chang, in *Semiconductors and Semimetals, Vol. 7B*, edited by R. K. Willardson and A. C. Beer (Academic Press, New York, 1971), p. 625.
2. W. von Muench and I. Pfaffeneder, J. Appl. Phys. **48**, 4831 (1977).
3. W. von Muench and E. Pettenpaul, J. Appl. Phys. **48**, 4823 (1977).
4. G. A. Slack, J. Appl. Phys. **35**, 3460 (1964).
5. R. F. Davis, J. W. Palmour and J. A. Edmond, Mater. Res. Soc. Symp. Proc. **162**, 463 (1990).
6. R. F. Davis, in *The Physics and Chemistry of Carbides; Nitrides and Borides*, edited by R. Freer (Kluwar Academic Publishers, The Netherlands, 1990), p. 589.
7. R. F. Davis, G. Kelner, M. Shur, J. W. Palmour and J. A. Edmond, Proc. IEEE **79**, 677 (1991).
8. R. F. Davis, J. W. Palmour and J. A. Edmond, Diam. Rel. Mater. **1**, 109 (1992).
9. R. F. Davis, Phys. B **185**, 1 (1993).
10. P. A. Ivanov and V. E. Chelnokov, Semicond. Sci. Technol. **7**, 863 (1992).
11. J. A. Powell, P. G. Neudeck, L. G. Matus and J. B. Petit, Mater. Res. Soc. Symp. Proc. **242**, 495 (1992).
12. K. Shibahara, S. Nishino and H. Matsunami, Jpn. J. Appl. Phys. **23**, L862 (1984).
13. R. E. Avila, J. J. Kopanski and C. D. Fung, Appl. Phys. Lett. **49**, 334 (1986).
14. S. M. Tang, W. B. Berry, R. Kwor, M. V. Zeller and L. G. Matus, J. Electrochem. Soc. **137**, 221 (1990).
15. M. Shinohara, M. Yamanaka, S. Misawa, H. Okumura and S. Yoshida, Jpn. J. Appl. Phys. **30**, 240 (1991).
16. C. Raynaud, J.-L. Autran, J.-B. Briot, B. Balland, N. Bécourt and C. Jaussaud, J. Electrochem. Soc. **142**, 282 (1995).
17. R. W. Kee, K. M. Geib, C. W. Wilmsen and D. K. Ferry, J. Vac. Sci. Technol. **15**, 1520 (1978).
18. R. Berjoan, J. Rodriguez and F. Sibieude, Surf. Sci. **271**, 237 (1992).
19. C. Raynaud, J.-L. Autran, B. Balland, G. Guillot, C. Jaussaud and T. Billon, J. Appl. Phys. **76**, 993 (1994).
20. C. Raynaud, J.-L. Autran, F. Seigneur, C. Jaussaud, T. Billon, G. Guillot and B. Balland, J. Phys. III **4**, 937 (1994).
21. A. Rys, N. Singh and M. Cameron, J. Electrochem. Soc. **142**, 1318 (1995).
22. J. N. Shenoy, G. L. Chindalore, M. R. Melloch, J. A. Cooper, Jr., J. W. Palmour and K. G. Irvine, J. Electron. Mater. **24**, 303 (1995).
23. G. E. Morgan, C. C. Tin, J. R. Williams and R. Ramesham, in *Silicon Carbide and Related Materials*, edited by M. G. Spencer, R. P. Devaty, J. A. Edmond, M. A. Khan, R. Kaplan, and M. Rahman (Institute of Physics, Bristol, 1994), p. 645.
24. W. M. Yim, E. J. Stofko, P. J. Zanzucchi, J. I. Pankove, M. Ettenberg and S. L. Gilbert, J. Appl. Phys. **44**, 292 (1973).

25. M. G. Norton, P. G. Kotula and C. B. Carter, J. Appl. Phys. **70**, 2871 (1991).
26. G. A. Slack, J. Phys. Chem. Solids **34**, 321 (1973).
27. S. Strite and H. Morkoc, J. Vac. Sci. Technol. B **10**, 1237 (1992).
28. J. K. Liu, K. M. Lakin and K. L. Wang, J. Appl. Phys. **46**, 3703 (1975).
29. M. Morita, N. Uesugi, S. Isogai, K. Tsubouchi and N. Mikoshiba, Jpn. J. Appl. Phys. **20**, 17 (1981).
30. G. D. O'Clock, Jr. and M. T. Duffy, Appl. Phys. Lett. **23**, 55 (1973).
31. S. Mirsh and H. Reimer, Phys. Stat. Sol. **11**, 631 (1972).
32. J. Bauer, L. Biste, D. Bolze and G. Eichorn, Phys. Stat. Sol. **399**, 173 (1977).
33. M. Morita, S. Isogai, K. Tsubouchi and N. Mikoshiba, Appl. Phys. Lett. **38**, 50 (1981).
34. M. Morita, K. Tsubouchi and N. Mikoshiba, Jpn. J. Appl. Phys. **21**, 728 (1982).
35. M. Koshinaka, H. Fujii, K. Nakanishi and Y. Shibuya, Vacuum **41**, 1971 (1990).
36. A. U. Ahmed, A. Rys, N. Singh, J. H. Edgar and Z. J. Yu, J. Electrochem. Soc. **139**, 1146 (1992).
37. F. Alexandre, J. M. Masson, G. Post and A. Scavennec, Thin Solid Films **98**, 75 (1982).
38. S. Fujieda, J. Mizuki and Y. Matsumoto, Jpn. J. Appl. Phys. **27**, L296 (1988).
39. S. Fujieda, Y. Mochizuki, K. Akimoto, I. Hirosawa, Y. Matsumoto and J. Matsui, Jpn. J. Appl. Phys. **29**, L364 (1990).
40. Y. Mochizuki, M. Mizuta, S. Fujieda and Y. Matsumoto, J. Appl. Phys. **67**, 2466 (1990).
41. P. Bhattacharya and D. N. Bose, Jpn. J. Appl. Phys. **30**, L1750 (1991).
42. S. Fujieda, K. Akimoto, I. Hirosawa, J. Mizuki, Y. Matsumoto and J. Matsui, Jpn. J. Appl. Phys. **28**, L16 (1989).
43. K. S. Stevens, M. Kinniburgh, A. F. Schwartzman, A. Ohtani and R. Beresford, Appl. Phys. Lett. **66**, 3179 (1995).
44. R. M. Eastment and C. H. B. Mee, J. Phys. F **3**, 1378 (1973).
45. J. A. Dillon, Jr., R. E. Schlier and H. E. Farnsworth, J. Appl. Phys. **30**, 675 (1959).

X. Rectifying and Ohmic Contacts for P-type Alpha (6H) Silicon Carbide

A. Introduction

While the wide bandgap of SiC is responsible for its use in opto-electronic, high-power, and high-temperature devices, this property also adds to the difficulty of controlling the electrical properties at the metal-semiconductor contacts in these devices. The primary parameter used to quantify the electrical relationship at these interfaces is the Schottky barrier height (SBH), or the energy barrier for electrons traversing the interface. A small SBH is desired for a contact which obeys Ohm's Law, while a relatively large SBH is necessary to create a good rectifying contact.

The formation of low resistivity and thermally stable ohmic contacts to 6H-SiC remains a serious problem in the development of SiC device technology. For SiC power devices to have the advantage over Si, the contact resistivities must be below 1×10^{-5} Ω-cm^2 [1]. In addition, the electrical characterization of state-of-the-art SiC films depends on the ability to fabricate ohmic contacts on material with low carrier concentrations. Therefore, better ohmic contacts are needed both for improving device performance and for improving the quality of films which can be grown. The thermal stability of ohmic contacts is of particular concern for p-type SiC, which have traditionally relied on Al or Al alloys to dope the SiC surface below the contacts. While the fabrication of ohmic contacts to SiC also has usually depended on very heavily-doped surfaces, the introduction of high levels of dopants in the near surface device region of the epilayer prior to the deposition of the contact or by ion implantation through the contact makes probable the introduction of point and line defects as a result of the induced strain in the lattice. Based on all of these issues and experiments already performed at NCSU, our goals are to produce contacts which are thermally stable and have low contact resistivities while also reducing the need for doping by ion implantation.

Low resistance contacts to p-type SiC remain a substantial challenge for high temperature and high-power devices. An Al-Ti alloy [2] annealed at 1000°C for 5 min. was reported to yield contact resistances ranging from 2.9×10^{-2} Ω cm^2 for a carrier concentration of 5×10^{15} cm^{-3} to 1.5×10^{-5} Ω cm^2 for 2×10^{19} cm^{-3}. The thermal stability of these contacts was not reported. Aluminum deposited on a heavily-doped 3C-SiC interlayer on a 6H-SiC substrate and subsequently annealed at 950°C for 2 min. reportedly yielded contact resistivities of 2–3×10^{-5} Ω cm^2 [3]. Because of its low melting point (660°C), however, pure Al would be unsuitable for high temperature applications. Platinum contacts annealed from 450 to 750°C in 100°C increments were also used as ohmic contacts to p-type SiC [4]. These contacts, which rely on the combination of a highly-doped surface and the high work function of Pt, have not been known to yield contact resistivities as low as those for the contacts containing Al.

B. Experimental Procedure

Vicinal, single-crystal 6H-SiC (0001) wafers provided by Cree Research, Inc. were used as substrates in the present research. The wafers were doped with N or Al during growth to create n- or p-type material, respectively, with carrier concentrations of $1–5\times10^{18}$ cm^{-3}. Homoepitaxial layers (1–5 μm thick) grown by chemical vapor deposition (CVD) were Al-doped with carrier concentrations ranging from 1×10^{16} to 1×10^{19} cm^{-3}. The surfaces were oxidized to a thickness of 500–1000 Å in dry oxygen. The substrates were simultaneously cleaned and the oxide layer etched from the surface using a 10 min. dip in 10% hydrofluoric acid, transferred into the vacuum system, and thermally desorbed at 700 °C for 15 min. to remove any residual hydrocarbon contamination.

A UHV electron beam evaporation system was used to deposit the NiAl and Ni films. After depositing 1000 Å of NiAl, 500–1000 Å of Ni was deposited as a passivating layer. Pure Ni (99.99%) and pure Al (99.999%) pellets were arc melted to form alloyed pellets of 50:50 atomic concentration for evaporation of NiAl. The films were deposited onto unheated substrates at a rate of 10–20 Å/s. The pressure during the depositions was between 5×10^{-9} and 5×10^{-8} Torr.

Circular contacts of 500 μm diameter were fabricated for electrical characterization by depositing the metal films through a Mo mask in contact with the substrate. Silver paste served as the large area back contact. For contact resistance measurements, TLM patterns [6] were fabricated by photolithography. The Ni/NiAl films were etched in phosphoric acid : acetic acid : nitric acid (12 : 2 : 3) at 50 °C (etch rate ≈ 30 Å/s). The contact pads were 300×60 μm with spacings of 5, 10, 20, 30 and 50 μm. Mesas in the substrate were not fabricated. All subsequent annealing was conducted in a N_2 ambient in a rapid annealing furnace.

Electrical characteristics were obtained from current-voltage and capacitance-voltage measurements. Current-voltage (I-V) measurements were obtained with a Rucker & Kolls Model 260 probe station in tandem with an HP 4145A Semiconductor Parameter Analyzer. Capacitance-voltage (C-V) measurements were taken with a Keithley 590 CV Analyzer using a measurement frequency of 1 MHz.

Auger electron spectroscopy (AES) was performed with a JEOL JAMP-30 scanning Auger microprobe. The films were sputtered with Ar ions at a beam current and voltage of 0.3 μA and 3 kV, respectively, to obtain composition profiles through the thickness of the films.

C. Results

Modifications to Deposition System. To better control the deposition of compounds for SiC contacts by electron beam deposition, a second Leybold Inficon film thickness monitor was installed in the UHV chamber. Linear motion shifts on both thickness monitors allowed the monitors to be moved relative to the location of the deposition sources. Cylindrical material

directors placed around the crystals were used to try to isolate the flux reaching the crystal from one deposition source while eliminating the flux from the other source. As of this writing preliminary results have shown that some cross-deposition of material is inevitable, but it can probably be kept low enough to give satisfactory estimates of the amount of each material deposited while running both sources simultaneously. The necessity of having two thickness monitors will be elaborated in the Future Plans and Goals section of this report.

Chemical Characterization of As-deposited Films. An Auger depth profile of a film deposited from the NiAl source showed that the overall composition remained relatively stable. The relative compositions of Ni and Al were calculated by referencing to pure Ni and pure Al standards and accounting for their corresponding sensitivity factors. The average atomic composition was approximately 50:50.

Schottky Contacts. In the as-deposited condition the Ni/NiAl contacts were rectifying on p-type SiC with carrier concentrations of 1.6×10^{16} and 3.8×10^{18} cm^{-3} in the epilayer. The sample with the lower carrier concentration displayed leakage current densities of $\sim1\times10^{-8}$ A/cm^2 at 10 V and ideality factors between 1.4 and 2.4, while the latter sample displayed approximately five orders of magnitude higher leakage current densities and similar ideality factors. The average Schottky barrier heights (SBH's) calculated for the samples with the lower and higher carrier concentrations were 1.37 and 1.26 eV, respectively. The lower SBH calculated for the former sample is likely due to enhanced thermionic field emission through the upper energy region of the barrier because of the narrower depletion region. Hence, the 1.37 eV value is believed to be more accurate.

Similar results were obtained for as-deposited Ni and Au contacts on p-type (2.1–4.5×10^{16} cm^{-3}) 6H-SiC (0001). These samples displayed similar leakage currents and ideality factors of 1.3–2.1 and <1.1, respectively. From these measurements SBH's of 1.31 eV for the Ni contacts and 1.27 eV for the Au contacts were calculated. In comparison, as-deposited Ni on n-type (4.1×10^{16} cm^{-3}) 6H-SiC (0001) yielded ideality factors below 1.1, similar leakage current densities to those stated above, and SBH's of 1.14 eV and 1.21 eV calculated from I-V and C-V measurements, respectively.

Our measurements on p-type SiC have shown consistent differences from measurements on n-type 6H-SiC. The SBH's tended to be higher on p-type than on n-type material. While leakage currents for Au, NiAl, and Ni contacts on p-type 6H-SiC were comparable to Ni contacts on n-type 6H-SiC, the ideality factors were higher on p-type SiC. These ideality factors and SBH's are higher than for Ni contacts (and other previously studied contacts) on n-type 6H-SiC (0001). The higher ideality factors indicates that thermionic emission was not the dominant current transport mechanism in the p-type SiC and may indicate the occurrence of recombination at deep levels.

On the other hand, the relationship between the SBH's of the metals on p-type SiC and their respective work functions was similar to that which we previously found for n-type SiC. The calculated SBH's on p-type SiC are plotted vs. the metal work functions in Fig. 1. The work function for NiAl was taken to be the average of the work functions for pure Ni and pure Al since a value was not found in the literature for NiAl. The slope of the line fit to the empirical data was -0.16 as compared to a slope of -1.0 for the theoretical data. These results indicate that surface states on p-type 6H-SiC (0001) cause a partial pinning of the Fermi level, in agreement with the results of our previous, extensive study on n-type SiC.

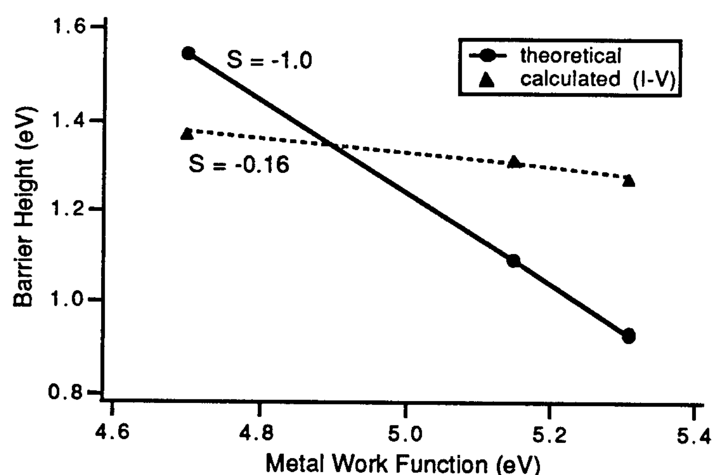

Figure 1. Graph of calculated and theoretical barrier heights of as-deposited NiAl, Ni, and Au contacts on p-type 6H-SiC vs. metal work function. The calculated values were determined from I-V measurements, and the theoretical values were calculated according to the Schottky-Mott limit. The slopes, S, of the lines fit to each set of data are indicated on the graph.

Ohmic Contacts. The Ni/NiAl contacts were sequentially annealed for total times of 10–80 s at 1000 °C in a N_2 ambient. This temperature was used because (1) limited intermixing of Al and SiC was reported at 900 °C [7] and (2) other papers report annealing in this temperature range for Al-based ohmic contacts on p-type SiC [2, 3, 8]. Because of the extremely high thermodynamic driving force for Al to form an insulating oxide layer (ΔG_f (Al_2O_3) ~ -1300 kJ/mol at 1000 °C [JANAF - Chase, M., *et al.*, JANAF Thermochem. Tables, 3d Ed. J. Phys. Chem. Ref. Data, 1985. 14(Supp. 1)]), 1000 Å of Ni was deposited on top of the NiAl contacts to slow the oxidation process.

Table I summarizes the results of I-V measurements taken at selected intervals through the annealing series for three samples with various carrier concentrations in the SiC epitaxial layer (1.4×10^{18}, 5.7×10^{18}, and 1.5×10^{19} cm^{-3}). The two samples with the lower carrier concentrations were not truly ohmic but became ohmic-like after annealing for 80 s. This annealing series will be continued to determine whether ohmic behavior in these two samples

will ensue; however, the additional force on the probes needed to obtain consistent results indicates that an oxide has begun to form at the surface and may cause problems with further annealing. The sample with the higher carrier concentration was ohmic after annealing for 10 s. The calculated specific contact resistivity remained approximately $2.0\times10^{-2}\ \Omega\ cm^2$ through annealing for 60 s. A slight increase to $3.1\times10^{-2}\ \Omega\ cm^2$ was calculated after annealing for 80 s. This increase is believed to be due to the surface oxide layer.

Table I. Estimated specific contact resistivities / electrical behavior of Ni (1000 Å) / NiAl (1000 Å) / p-SiC after annealing at 1000 °C for 20, 40, 60, and 80 s for three samples with the carrier concentrations indicated. The specific contact resistivities were calculated from non-mesa etched linear TLM patterns.

Annealing Time	20 s	40 s	60 s	80 s
1.4×10^{18} cm^{-3}	non-ohmic	non-ohmic	non-ohmic	almost ohmic
5.7×10^{18} cm^{-3}	non-ohmic	non-ohmic	non-ohmic	almost ohmic
1.5×10^{19} cm^{-3}	$2.0\times10^{-2}\ \Omega\ cm^2$	$1.9\times10^{-2}\ \Omega\ cm^2$	$2.2\times10^{-2}\ \Omega\ cm^2$	$3.1\times10^{-2}\ \Omega\ cm^2$

The high contact resistivities may be a result of a few causes. It is believed that the SiC may be depleted of carriers near the surface, possibly due to thermal oxidation. A depletion of carriers near the surface would result in higher than expected contact resistivity values because current transport across the contact depends on the carrier concentration in the SiC at the SiC surface. To investigate this potential problem we plan to compare the contacts described above with contacts on SiC implanted with Al and also on SiC which has not been thermally oxidized. The values of specific contact resistivity stated above should only be considered as preliminary estimates since only one level of the TLM measurement pattern was used. In the near future we plan to employ a circular TLM measurement structure [9], which consists of only one level and does not involve etching of the substrate. A photolithography mask for fabricating this structure was recently designed and fabricated at NCSU for this project.

D. Discussion

An Auger depth profile (Fig. 2b) of Ni/NiAl/SiC annealed at 1000 °C for 80 s shows that the surface oxide is thicker than that on the as-deposited sample (Fig. 2a). After sputtering for a couple of minutes, the O concentration dropped to below detectable limits; however, the data shows a decreasing Al concentration in the direction toward the SiC interface. This indicates that the kinetics are more favorable for the Al to diffuse toward the surface and react with O than for the Al to react with the SiC. Some of the Ni has probably reacted with Si at the interface to form a silicide, as indicated by the local maximum in the Ni intensity near the SiC interface, while the peak in the C intensity indicates the presence of an adjacent C-rich layer.

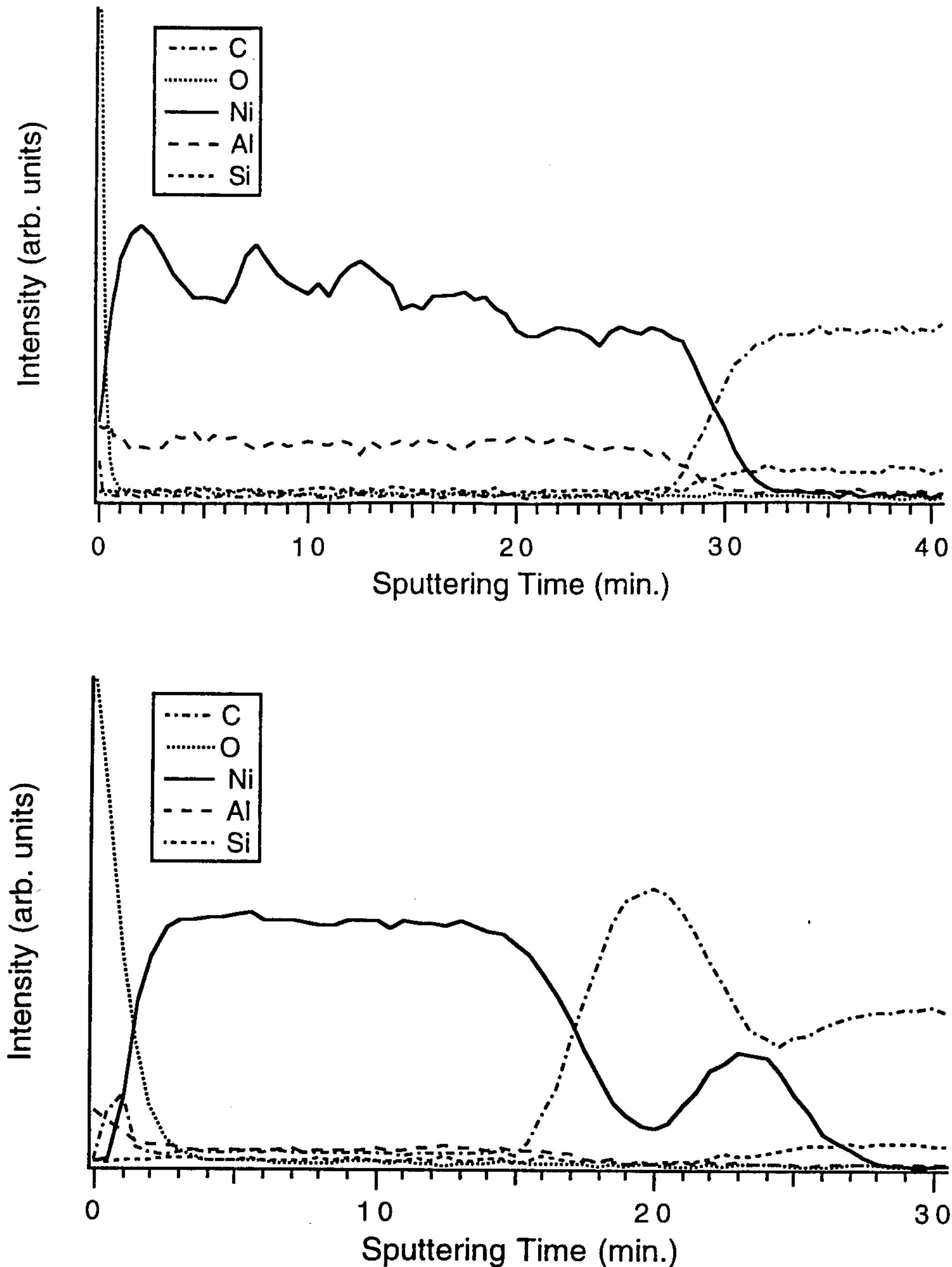

Figure 2. AES composition profile of (a) NiAl (1000 Å) deposited at room temperature on (0001) 6H-SiC and (b) Ni (1000 Å) / NiAl (1000 Å) / 6H-SiC annealed at 1000 °C for 80 s in N_2.

The demonstrated oxidation problem with Al necessitates the development of ohmic contacts which do not consist of substantial concentrations of Al. To reduce this problem we have chosen to investigate selected materials which contain B as an alternative to Al.

The main reasons for choosing B are that it is also a p-type dopant in SiC, its oxide is not as stable, and it is a much faster diffusant in SiC. Table II compares some important properties of B, Al, and their associated oxides. Although the B acceptor level in 6H-SiC is substantially

deeper than that of Al, the fact that B is an acceptor makes it worth investigating as a component in p-type ohmic contacts. Also, boron compounds tend to be more stable at high temperatures than aluminum compounds which suffer from the low melting point of Al. As shown in Table II, the diffusion coefficient of B is at least three orders of magnitude greater than that of Al. Therefore, more B than Al will diffuse into the SiC at lower temperatures. As discussed in this report, a major problem with Al-based contacts is the strong driving force for forming an insulating oxide layer. This situation is shown by the extremely low equilibrium partial pressure, p_{O_2}, for Al_2O_3 formation. While B_2O_3 also has a low p_{O_2}, it is significantly higher than that for Al_2O_3, indicating that the driving force for B to form an oxide is significantly lower. In addition, the melting point of boron oxide is notably low.

Table II. Selected Properties of B, Al, and Their Associated Oxides

Element	Activation Energy in 6H-SiC (meV)	Solid Source Diffusion, D_{SiC} @ 1800°C (cm^2/s)	Equilibrium partial pressure of O_2, p_{O_2} @ 700°C (torr)	Melting temp. of the associated oxide, T_{melt} (°C)
B	700	10^{-11} [10-11]	10^{-35}	450
Al	240	$<10^{-14}$ [12]	10^{-47}	2040

Several boron compounds which possess reasonably low resistivities and high melting temperatures are listed in Table III. Of the compounds listed, the simplest to form by electron beam deposition would probably be CrB_2, VB_2, and ZrB_2. The refractory nature of these compounds increases the chance of forming ohmic contacts which will be stable at high temperatures.

Table III. Resistivities and Melting Points of Selected Boron Compounds

Compound	Electrical Resistivity (μΩ-cm) 298 K [13]	Melting Temperature (°C) [14]
CrB_2	30	2200
GdB_4	31	2650
MoB	45	2600
NbB_2	26	3000
TaB_2	33	3037
VB_2	23	2747
ZrB_2	10	2972

E. Conclusions

Nickel-aluminum was investigated primarily as an ohmic contact for p-type 6H-SiC because of the p-type doping of Al in SiC, the high melting point of NiAl (as compared to Al), and the tendency of Ni to form silicides but not carbides. This latter property potentially could have resulted in extraction of Si from the SiC lattice in exchange for Al, thereby enhancing the p-type carrier concentration at the surface. Although the I-V measurements indicate that some Al may be diffusing into the SiC after the longest annealing time performed (80 s at 1000 °C), this potential for reaction between Al and SiC appears to be exceeded by the driving force for Al to diffuse to the surface and react with O. A concentration profile obtained from AES analysis shows that Al has diffused through the 1000 Å Ni overlayer to form a thin (200 Å estimated) oxide layer.

In addition to the ohmic behavior resulting from annealing the NiAl contacts, as-deposited Ni, NiAl, and Au contacts deposited at room temperature on p-type ($N_A < 5\times10^{16}$ cm^{-3}) 6H-SiC (0001) were rectifying with low leakage currents, ideality factors between 1.3 and 2.4, and SBH's of 1.31, 1.27, and 1.37 eV, respectively. These results indicate that the Fermi level is partially pinned at p-type SiC surface, in agreement with our previous results on n-type SiC.

An alternative to Al for fabricating ohmic contacts to 6H-SiC is the use of boron compounds. The metal borides listed in Table III are strong candidates for p-type SiC metallization because their low resistivities and high melting temperatures should allow the formation of high temperature contacts. Electron beam deposition of these materials ought to be possible.

F. Future Research Plans and Goals

The position of the two crystal thickness monitors during simultaneous electron beam deposition needs to be optimized. First, the ratio of the actual thickness being deposited to the thickness read by each monitor needs to be determined. This can be accomplished by measuring the actual thickness deposited from familiar metal sources. With the completion of these system modifications to allow co-deposition of compound metal films, we are prepared to deposit B-based contacts as an alternative to Al-based metallization.

An attempt to fabricate ohmic contacts to p-type SiC using boron compounds will be made. The deposition of some of the low resistivity, refractory borides listed previously in Table III will be carried out by electron beam evaporation. Careful electrical characterization needs to be performed to determine if annealing will improve the contact properties. In addition, the deposited films will be chemically analyzed by Auger electron spectroscopy to determine if the proper phases form.

Another alternate approach to Al-based ohmic contacts for p-type SiC will incorporate p-type semiconducting interlayers. The goal of this approach is to find a semiconducting

material which has a favorable band lineup with SiC (i.e., reduce the band bending) and to which an ohmic contact can easily be made. We have chosen to examine the $In_xGa_{1-x}N$ system for interlayer materials because of the lower density of surface states (and hence less band bending) and the range of bandgaps over the composition range. It is planned to measure the valence band offsets and electrical characteristics between various compositions of $In_xGa_{1-x}N$ (starting with x=0) and SiC. If a low energy barrier at the interface results, metals will be investigated for ohmic contacts for the interlayer / SiC structure.

To extend the study on NiAl ohmic contacts for p-type SiC, the contact resistivities for annealing series at 1000 °C will be repeated using circular TLM patterns and two different substrates: 1) SiC implanted with Al to increase the surface carrier concentration and 2) SiC which has not been thermally oxidized to investigate whether the bulk carrier concentration can be maintained at the surface. A photolithography mask with the circular TLM patterns was recently designed and will be used in the research on ohmic contacts in the very near future.

G. References

1. D. Alok, B. J. Baliga, and P. K. McLarty, IEDM Technical Digest **IEDM 1993**, 691 (1993).
2. J. Crofton, P. A. Barnes, J. R. Williams, and J. A. Edmond, Appl. Phys. Lett. **62**(4), 384 (1993).
3. V. A. Dmitriev, K. Irvine, and M. Spencer, Appl. Phys. Lett. **64**(3), 318 (1994).
4. R. C. Glass, J. W. Palmour, R. F. Davis, and L. S. Porter, U.S Patent No. 5,323,022 (1994).
5. J. L. Murray, Ed. *Phase Diagrams of Binary Titanium Alloys* (ASM International, Metals Park, Ohio, 1987).
6. H. H. Berger, Solid State Electronics **15**(2), 145 (1972).
7. V. M. Bermudez, J. Appl. Phys. **63**(10), 4951 (1988).
8. T. Nakata, K. Koga, Y. Matsushita, Y. Ueda, and T. Niina, in *Amorphous and Crystalline Silicon Carbide and Related Materials II*, M. M. Rahman, C. Y.-W. Yang, and G. L. Harris, Eds., Vol. 43 (Springer-Verlag, Berlin, 1989).
9. G. K. Reeves, Solid State Electronics **21**, 801 (1978).
10. E.N. Mokhov, Y.A. Vodakov, G.A. Lomakina, Soviet Physics - Solid State **11**(2), 415 (1969).
11. C. van Opdorp, Solid State Electronics **14**, 613 (1971).
12. E. Mokhov, Y. A. Vodakov, G. A. Lomakina, V. G. Oding, G. F. Kholuyanov, and V. V. Semenov, Soviet Physics - Semiconductors **6**(3), 414 (1972).
13 Samsonov, G. V. and I. M. Vinitskii, *Handbook of Refractory Borides*, (Plenum Press, New York, 1980).
14. *Binary Alloy Phase Diagrams, 2nd Ed.*, T. B. Massalski editor, (ASM International, 1990).

Nitrogen-based Materials

XI. Growth and Doping of $Al_xGa_{1-x}N$ Deposited Directly on α(6H)-SiC(0001) Substrates Via Organometallic Vapor Phase Epitaxy

M. D. Bremser, W. G. Perry, N. V. Edwards, T. Zheleva, N. Parikh*, D. E. Aspnes**, R. F. Davis

Department of Materials Science and Engineering, North Carolina State University, Box 7907 Raleigh, NC 27695-7907
*Department of Physics and Astronomy, University of North Carolina at Chapel Hill, Chapel Hill, NC 27514
**Department of Physics, North Carolina State University, Raleigh, NC 27695-8202

ABSTRACT

Monocrystalline $Al_xGa_{1-x}N(0001)$ ($0.05 \leq x \leq 0.70$) thin films, void of oriented domain structures and associated low-angle grain boundaries, have been grown at high temperatures via OMVPE *directly on* vicinal and on-axis α(6H)-SiC(0001) wafers using TEG, TEA and ammonia in a cold-wall, vertical, pancake-style reactor. The surface morphologies were smooth and the densities and distributions of dislocations were comparable to that observed in GaN(0001) films grown on high temperature AlN buffer layers. Double-crystal XRC measurements showed a FWHM value as low as 186 arc sec for the (0002) reflection. Spectra obtained via CL showed strong near band-edge emissions with FWHM values as low as 31 meV. The compositions of the $Al_xGa_{1-x}N$ films were determined using EDX, AES and RBS and compared to the values of the bandgap as measured by spectral ellipsometry and CL emissions. A negative bowing parameter was found. Controlled n-type, Si-doping of $Al_xGa_{1-x}N$ for $x \leq 0.4$ has been achieved with net carrier concentrations ranging from $\approx 2\times10^{17}$ cm^{-3} to 2×10^{19} cm^{-3}. Acceptor doping with Mg for $x < 0.13$ was also successful.

Presented at the 1995 Fall Meeting of Materials Research Society, Boston, MA, USA.

A. Introduction

The numerous potential semiconductor applications of the wide bandgap III-Nitrides has prompted significant research regarding their growth and development. GaN (wurtzite structure), the most studied in this group, has a bandgap of ≈3.4 eV and forms continuous solid solutions with both AlN (6.2 eV) and InN (1.9 eV). As such, materials with engineered bandgaps are feasible for optoelectronic devices tunable in wavelength from the visible to the deep UV. The relatively strong atomic bonding of these materials also points to their potential for high-power and high-temperature microelectronic devices.

Single crystal wafers of GaN are not commercially available. Sapphire(0001) is the most commonly used substrate, although its lattice parameter and coefficients of thermal expansion are significantly different from that of any III-Nitride. The heteroepitaxial nucleation and growth of monocrystalline films of GaN on any substrate and AlN on sapphire are difficult at elevated (>900°C) temperatures. Therefore, at present, for successful organometallic vapor phase epitaxy (OMVPE) of GaN films on sapphire, the use of the initial deposition of an amorphous or polycrystalline buffer layer of AlN [1,2] or GaN [3,4] at low-temperatures (450°-600°C) is necessary to achieve both nucleation and relatively uniform coverage of the substrate surface. Subsequent deposition at higher temperatures and concomitant grain orientation competition has resulted in films of GaN(0001) and various nitride alloys of improved quality and surface morphology relative to that achieved by growth directly on this substrate.

By contrast, we have observed that AlN and $Al_xGa_{1-x}N$ alloys containing even low ($x \geq 0.05$) concentrations of AlN deposited on 6H-SiC(0001) substrates at high (≥1000°C) temperatures undergo two-dimensional nucleation and growth with resulting uniform surface coverage. In our research, the use of a 1000 Å, monocrystalline, high-temperature (1100°C) AlN buffer has resulted in GaN films void of oriented domain structures and associated low-angle grain boundaries [5,6] Monocrystalline films of $Al_xGa_{1-x}N$ ($0.05 \leq x \leq 0.70$) of the same quality have also been achieved *directly on* 6H-SiC(0001) wafers at 1100°C. The presence of AlN in the films, the enhanced surface mobility of the adatoms at high temperatures and the reduced mismatch in lattice parameters between $Al_xGa_{1-x}N(0001)$ and 6H-SiC(0001) ($a/a_o \approx 1$-3%) relative to that between $Al_xGa_{1-x}N$ and sapphire (11-13%) [2] have promoted the growth of these films [7]. The following is the first known published report of the deposition of undoped and doped high quality $Al_xGa_{1-x}N$ alloys without the use of a buffer layer.

B. Experimental Procedures

As-received vicinal 6H-SiC(0001) wafers [8] oriented 3°-4° off-axis toward $\langle 11\bar{2}0 \rangle$ were cut into 7.1 mm squares. These pieces were degreased in sequential ultrasonic baths of trichloroethylene, acetone and methanol and rinsed in deionized water. The SiC substrates were

then dipped into a 10% HF solution for 10 minutes to remove the thermally grown oxide layer and blown dry with N_2 before being loaded onto the SiC-coated graphite susceptor contained in a cold-wall, vertical, pancake-style, OMVPE deposition system. The system was evacuated to less than 3×10^{-5} Torr prior to initiating growth. The continuously rotating susceptor was RF inductively heated to the $Al_xGa_{1-x}N$ deposition temperature of 1100°C (optically measured on the susceptor) in 3 SLM of flowing H_2 diluent. Hydrogen was also used as the carrier gas for the various metalorganic precursors. Deposition of $Al_xGa_{1-x}N$ was initiated by flowing various ratios of triethylaluminum (TEA) and triethylgallium (TEG) in combination with ammonia (NH_3). The NH_3 and total metalorganic precursor flow rates were 1.5 SLM and 32.8 μmol/min, respectively. The system pressure was 45 Torr. Silicon doped n-type $Al_xGa_{1-x}N$ samples were achieved via the addition of SiH_4 (12.4 ppm in a balance of N_2) at flow rates between 0.05 nmol/min and 15 nmol/min. Magnesium doped p-type $Al_xGa_{1-x}N$ samples were achieved via the addition of Cp_2Mg at flow rates between 200 nmol/min and 400 nmol/min.

The structural, microstructural, optical and electrical characteristics of the epitaxial $Al_xGa_{1-x}N$ thin films were analyzed using several techniques. Scanning electron microscopy (SEM) was performed using a JEOL 6400FE operating at 5 kV which was equipped with an Oxford Light Element Energy Dispersive X-ray (EDX) Microanalyzer. Conventional and high resolution transmission electron microscopy (TEM) was conducted using a Topcon EM-002B microscope operating at 200 kV. Double-crystal x-ray rocking curve (DCXRC) measurements were made on a Philips MR3 thin films diffractometer. The catholuminescence (CL) properties of the $Al_xGa_{1-x}N$ films were determined at 4.2 K using a Kimball Physics EMG-14 electron gun as the excitation source. Spectral ellipsometry (SE) was performed using a rotating analyzer ellipsometer with a xenon arc lamp (1.5eV–5.75eV). Capacitance-Voltage (CV) measurements were conducted using a MDC Model CSM/2-VF6 equipped with a mercury probe. Auger electron spectroscopy (AES) was performed using a Perkin-Elmer Model 660 equipped with Zalar rotation. Rutherford backscattering analysis was performed using 1.9 MeV He^+ ions with the detector at an angle of 165°.

C. Results and Discussion

Previous research in our laboratories has shown that thin films of GaN deposited directly on 6H-SiC(0001) substrates at high and low temperatures had columnar-like grains, faceted surfaces and high net carrier concentrations (n_D-n_A > 1×10^{19} cm^{-3}) [9]. In contrast, in the present research monocrystalline thin films of $Al_xGa_{1-x}N$ ($x \leq 0.05$) have been deposited directly on the same type of SiC substrates *without the use of a buffer layer* with no misorientation or low-angle grain boundaries, determined by selected area diffraction (SAD) and microstructural analysis via TEM. The stacking fault density was also very low. These results are apparent in

the representative cross-sectional TEM micrograph shown in Fig. 1a. Inserts in the micrograph show SAD patterns from the top layer of $Al_{0.13}Ga_{0.87}N$ and the film/substrate interface. Overlapping spots from the 6H-SiC(0001) substrate are seen in the latter pattern. The dislocation density of these films at the interface appears to similar to GaN films deposited on a high temperature (HT) buffer layer [5,6] The dislocation density of the $Al_xGa_{1-x}N$ film decreases rapidly as a function of thickness, as shown in Fig. 1a, and only threading dislocations which result from misfit dislocations at the interface persist through the film. High resolution TEM of the AlGaN/SiC interface is shown in Fig. 1b.

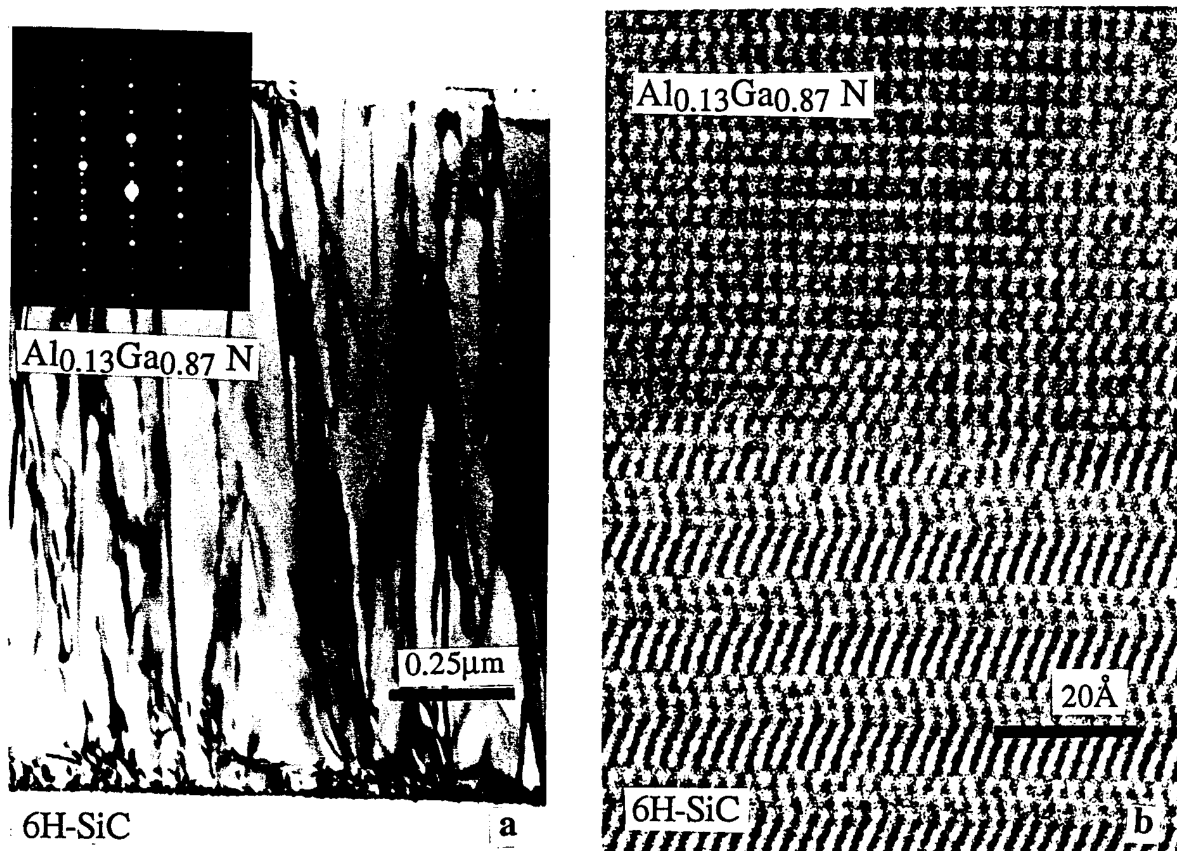

Figure 1. a) Cross-sectional TEM micrograph of a 1.8 μm AlGaN(0001) film deposited at 1100°C and 45 Torr via OMVPE directly on a vicinal 6H-SiC(0001) substrate. The inset shows the selected area diffraction. b)High resolution TEM of the AlGaN/SiC interface

The surfaces of the $Al_xGa_{1-x}N$ films exhibited a slightly mottled appearance, as shown in Fig. 2, probably as a result of the step and terrace features on the growth surface of the vicinal 6H-SiC(0001) substrates. Random pinholes, caused by incomplete coalescence of the two dimensional islands which occurred as an intermediate growth stage between the initial nucleation and the final layer-by-layer growth stage representative of the majority of the film,

were also observed. For $Al_xGa_{1-x}N$ compositions for $x > 0.5$, a significant number of pinholes appeared on the surface. Based on previous work with GaN, the pinhole density can be decreased with increasing growth temperature due to the enhanced surface mobility of the adatoms at higher temperatures [5,6] The higher growth rate of films grown on off-axis material is due to the increased density of steps on the substrate and film. DCXRC measurements taken on the 1.8 μm $Al_{0.13}Ga_{0.87}N$ film shown in Fig. 1 revealed the FWHM of the (0002) reflection to be 186 arc sec. For a 0.9 μm film of the same composition, the FWHM value of the same reflection was 315 arc sec. The reduction in FWHM values is consistent with the decrease in alloy concentration.

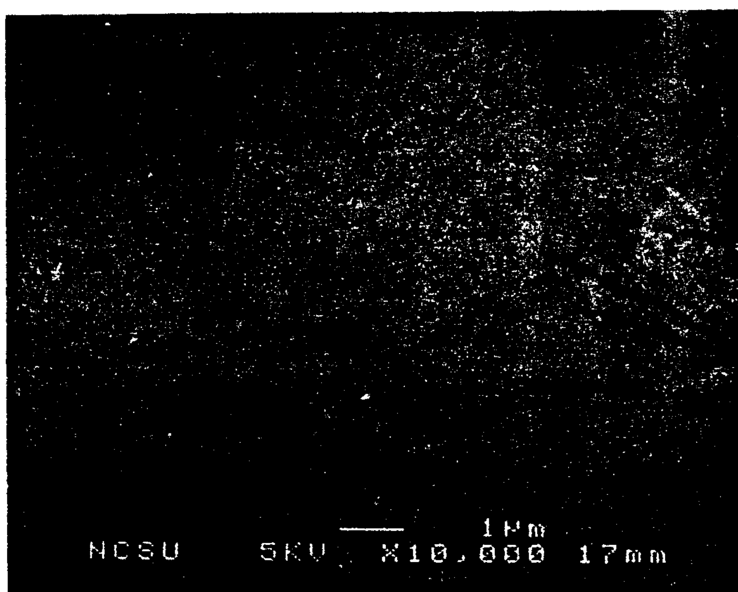

Figure 2. Representative SEM micrograph of the surface of an AlGaN(0001) film similar to that shown in Fig. 1.

The low-temperature (4.2K) CL spectra of the undoped $Al_xGa_{1-x}N$ films for various compositions ($0.05 \leq x \leq 0.70$) revealed an intense near band-edge emission which has been attributed to an exciton bound to a neutral donor (I_2-line emission) [10,11]. Broadening of this emission is attributed to both exciton scattering in the alloys, as well as small variations in alloy composition in the film. The lowest FWHM value observed for the $Al_xGa_{1-x}N$ alloys was 31 meV. Strong defect peaks, previously ascribed to donor-acceptor pair recombination [12], were observed at midgap energies. The broad peak centered at 545 nm (2.2 eV) for GaN, commonly associated [13] with deep-levels (DL) in the bandgap, was also observed; however, these emissions shifted sublinearly with changing composition. The nature of this behavior is under investigation.

The compositions of seven films grown under different conditions were determined using EDX, AES and RBS. Standards of AlN and GaN grown in the same reactor under similar conditions were used for the EDX and AES analyses. After careful consideration of the errors (±3 at.%) involved with each technique, compositions were assigned to each film. The data from EDX and AES measurements showed excellent agreement. The RBS data did not agree as well with the other two techniques due to small compositional variations through the thickness of the film. Simulation of the composition determined by RBS was conducted only on the surface composition. Analysis via EDX revealed that the $Al_xGa_{1-x}N$ grown on the on-axis SiC substrates tended to be slightly more Al rich than those grown off-axis SiC. It is thought that the presence of steps on the growth surface favors the adhesion of the gallium adatoms. In all cases except one, this difference was less than 2 atomic percent. Under the most aluminum rich growth conditions, the difference was 6-8 atomic percent. This difference was revealed by all three techniques. At this time, the reason for this large difference is unclear.

In Figs. 3 and 4, these compositions are compared with their respective CL emission peaks and bandgap as determined by SE. Using a parabolic model, the following relationships describe the bandgap (Eq. 1) and CL (I_2-line emission) (Eq. 2) as a function aluminum mole fraction for $0 \leq x \leq 0.70$:

$$E_g(x) = 3.40 + 1.35x + 1.01x^2, \quad (1)$$

$$E_{I2}(x) = 3.47 + 1.07x + 0.96x^2. \quad (2)$$

Clearly, both measurements show a negative deviation from a linear fit. This is in agreement with earlier research by other investigators [10,11].

Undoped, high quality $Al_{0.05}Ga_{0.95}N$ films grown directly on vicinal 6H-SiC(0001) exhibited residual, n-type background carrier concentrations of $\leq 1\times10^{18} cm^{-3}$. The carrier concentration rapidly decreased with increasing Al content and was $<1\times10^{16} cm^{-3}$ for $Al_{0.35}Ga_{0.65}N$, as determined by CV measurements. The origin of this residual carrier concentration is under investigation, since concentrations of $<1\times10^{15} cm^{-3}$ have been measured for GaN films grown on AlN buffer layers in the same reactor. However, the controlled introduction of SiH_4 allowed the reproducible achievement of donor carrier concentrations within the range of $2\times10^{17} cm^{-3}$ to $2\times10^{19} cm^{-3}$ in films with $x \leq 0.4$. The growth of p-type $Al_xGa_{1-x}N$ films for $x \leq 0.13$ via the introduction of Mg has been successful. All attempts to similarly dope films with $x > 0.13$ have been unsuccessful.

D. Conclusions

$Al_xGa_{1-x}N(0001)$ $(0.05 \leq x \leq 0.70)$ thin films void of low-angle grain boundaries and resultant domain microstructures have been grown via OMVPE directly on vicinal and on-axis

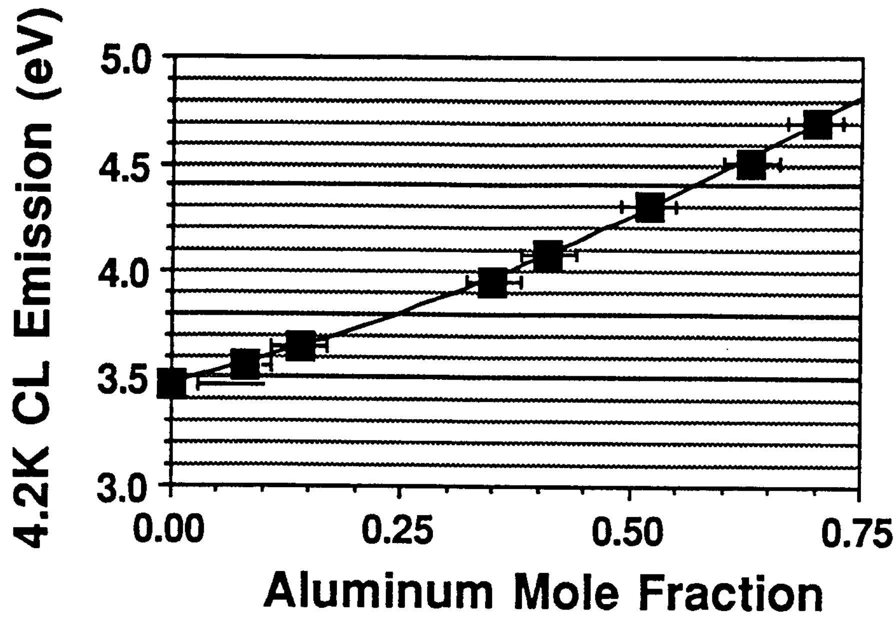

$CL=3.47 + 1.07x + 0.96x^2$
$R^2=0.999$

Figure 3. Low-temperature (4.2K) CL emissions of $Al_xGa_{1-x}N$ films as a function of aluminum mole fraction.

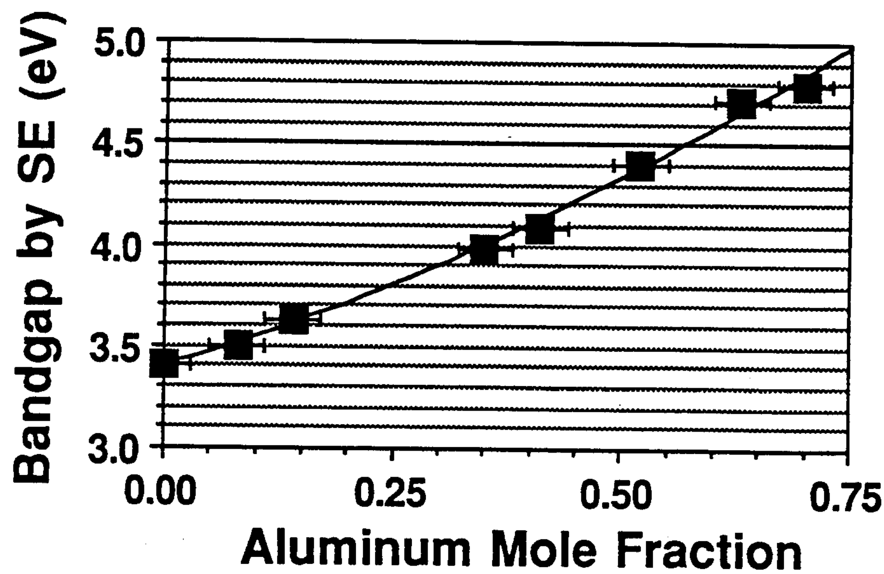

$BG=3.40 + 1.35x + 1.01x^2$
$R^2=0.995$

Figure 4. Bandgaps measured by spectral ellipsometry of $Al_xGa_{1-x}N$ films as a function of aluminum mole fraction.

α(6H)-SiC(0001) substrates. A significant reduction in dislocation density with increasing thicknesses was observed via TEM. Low-temperature CL spectra of the films showed intense near band-edge emissions. For a 1.8 μm $Al_xGa_{1-x}N$ film (x=0.13), DCXRC measurements revealed a FWHM value of 186 arc sec for the GaN(0002) reflection. The composition of the $Al_xGa_{1-x}N$ films was determined using EDX, AES and RBS and compared to the values of the bandgap measured by spectral ellipsometry and CL emissions. A negative bowing parameter was found. Controlled n-type Si-doping of $Al_xGa_{1-x}N$ has been achieved for net carrier concentrations ranging from $\approx 2\times10^{17}$ cm^{-3} to $\approx 2\times10^{19}$ cm^{-3} for $x \leq 0.4$. The p-type doping with Mg of $Al_xGa_{1-x}N$ for $x < 0.13$ has also been successful.

E. Acknowledgments

The authors express their appreciation to Cree Research, Inc. of Durham, North Carolina for providing the SiC wafers and C-V measurements and Dr. A. D. Batchelor and Dr. K. Hiramatsu for their assistance. This research was supported by the Office of Naval Research on Contracts N00014-92-J-1720 and N00014-92-J-1477 and monitored by Mr. Max Yoder.

F. References

1. M. A. Khan, J. N. Kuznia, D. T. Olson and R. Kaplan, J. Appl. Phys. **73**, 3108 (1993).
2. H. Amano, I. Akasaki, K. Hiramatsu, N. Koide and N. Sawaki, Thin Solid Films **163**, 415 (1988).
3. J. N. Kuznia, M. A. Khan, D. T. Olson, R. Kaplan and J. Freitas, J. Appl. Phys. **73**, 4700 (1993).
4. S. Nakamura, Jpn. J. Appl. Phys. **30**, L1705 (1991).
5. T. W. Weeks, Jr., M. D. Bremser, K. S. Ailey, E. P. Carlson,W. G. Perry, R. F. Davis, Appl. Phys. Lett. **67**, 401 (1995)
6. T. W. Weeks, Jr., M. D. Bremser, K. S. Ailey,W. G. Perry, E. P. Carlson, E. L. Piner, N. A. El-Masry, R. F. Davis, J. Mat. Res. to be published.
7. R. F. Davis T. W. Weeks, Jr., M. D. Bremser, K. S. Ailey, W. G. Perry, Z. Sitar, C. Wang and K. Linthicum, Topical Workshop on III-V Nitrides, Nagoya, Japan, September 21-23 (1995).
8. Cree Research, Inc., 2810 Meridian Parkway, Suite 176, Durham, NC 27713.
9. T. W. Weeks, Jr., D. W. Kum, E. Carlson, W. G. Perry, K. S. Ailey and R. F. Davis, Second International High Temperature Electronics Conference, Charlotte, NC, June 5-10 (1994).
10. M. R. H. Khan, Y. Koide, H. Itoh, N. Sawaki, I. Akasaki, Solid State Commun. **60** 753, (1986).
11. B. V. Baranov, V. B Gutan U. Zhumakulev, Sov. Phys.-Semicond. **16**, 819, (1982).
12. R. Dingle and M. Ilegems, Solid State Commun. **9**, 175 (1971).
13. W. Götz, N. M. Johnson, R. A. Street, H. Amano and I. Akasaki, Appl. Phys. Lett. **66**, 1340 (1995).

APPENDIX

In addition to growth research in the area of $Al_xGa_{1-x}N$, an ongoing effort is in place to further optimize and improve the growth of GaN. Much of this work is driven by the need to overcome challenges presented by device design.

A. Optimization of Deposition Temperature

Growth of GaN at different temperatures was investigated using a 1000Å AlN buffer deposited at 1100°C prior GaN deposition. This is a continuation of earlier work on GaN deposition. GaN was deposited in the 950°C to 1200°C temperature range. Below 1100°C, the growth rate was constant with increasing deposition temperature, thereby indicating a diffusion limited process. At 1100°C, a significant reduction in the growth rate was observed indicating a marked increase in GaN desorption during growth. Above 1100°C, very little GaN was deposited. Therefore, 1050°C has been chosen as the preferred deposition temperature due to its strong near-band edge photoluminscence (PL) emission at 4.2K, smooth pit-free surfaces, low double crystal x-ray rocking curves (DCXRC), full width at half-maximums (FWHM) and repeatedly n-type background carrier concentrations below 1×10^{16} cm^{-3}.

B. Buffer Layer Elimination

Previous research showed that deposition of GaN directly on 6H-SiC resulted in low quality films with a columnar structure; however, only deposition in the range of 500-950°C was investigated. In an attempt to eliminate growth of the AlN buffer layer, GaN was deposited directly on SiC at temperatures of 1100°C to 1200°C, but no significant amount of GaN nucleated on the surface of the SiC. Based on the deposition of AlGaN directly on SiC and the ability to dope $Al_xGa_{1-x}N$ n-type for $x<0.4$, it is believed that the development of a conducting $Al_xGa_{1-x}N$ buffer layer for small x is possible. This would facilitate the use of backside contacts for vertical device structures, as well as minimize the band offset between the SiC substrate and the buffer layer.

C. Full Wafer Deposition

In order to meet the needs of several characterization techniques, several samples of GaN were deposited on whole 30 mm SiC wafers under normal deposition conditions. During this deposition, the temperature variation across the samples was measured to be less than 5°C using an Ircon IMAX infrared optical pyrometer. The difference in the susceptor temperature and wafer temperature was measured to be about 35°C. The thickness varied from 3.71 µm at the center of the sample to 3.61 µm at the edge. This corresponds to a thickness varience of less than 3% across the sample. The uniformity in growth temperature and thickness will be important for the deposition of device structures.

D. Atomic Force Microscopy Studies

Preliminary studies of the roughness of GaN surface grown by OMVPE have been undertaken. GaN grown on on-axis SiC substrates has been repeatedly shown to have a root mean squared (RMS) roughness of < 2Å for a 1 μm square area, while simultaneously deposited GaN on off-axis SiC has a RMS roughness in the range of 10-20Å. However, it should be noted that larger area scans of GaN on off-axis substrate showed large parallel ridge-like features which vertical dimension in excess of 50Å. Corresponding on-axis material did not exhibit these structures.

Both off-axis and on-axis SiC substrates were also examined as received from Cree Research. The off-axis SiC substrates had a RMS roughness of <5Å over a 5 μm square area while the on-axis SiC exhibited a RMS roughness of 11 Å for the same size area. It should be noted that the off-axis wafers have ~ 1 μm epitaxial layer of SiC on them while the on-axis wafers do not. Interestly, on a typical on-axis wafer most of the wafer is extremely flat except for randomly oriented trenches with depths as great as 100 Å which probably are the result of the mechanical polishing of the wafers.

This work is preliminary, but provides some insight into the nature of the surface upon contacts for device will be placed, as well as lend itself to quantification damage due to etching of the material during device fabrication.

E. Future Work

Intense efforts are under way to achieve n-type GaN below 1×10^{17} cm^{-3} which will be needed for fabrication of microelectronic devices. Concomitantly, work is being done to dope AlGaN for $x > 0.4$ for n-type and $x > 0.13$ for p-type; the former effort being directed towards the development of high current cold cathode emitters. Simultaneously, the completion of the development of undoped AlGaN for $x > 0.7$ is underway and the nature of the residual background carriers is being actively addressed. Initial investigations of superlattice structures by TEM and the intense optical emissions of AlGaN under electron beam irradiation indicate that efforts to study single and multiple quantum wells should be undertaken. Finally, devices will be concurrently engineered as deposition and fabrication techniques develop. At this time p-n junctions, metal-semiconductor field effect transistors (MESFET) and metal-insulator-semiconductor field effect transistors (MISFET) devices are under active development.

F. Acknowledgments

The author would like to acknowledge the following list of collaborators who have assisted in the characterization and testing of samples.

Cree Research—wafers, electrical characterization
NASA-Goddard (Huang)—photodetector testing

NRL (Freitas, Carlos, Glaser)—optical characterization
UNIPRESS (Suski)—high pressure studies
Westinghouse—microelectronic device fabrication
Wright Laboratories (Litton)—electrical characterization
Xerox PARC (Goetz)—O-DLTS, defect studies
Case Western Reserve Univ. (Pirouz, Ning, Chien)—TEM
Oklahoma State Univ. (Song)— optical characterization
UNC-CH (Parikh)—Rutherford Backscattering

NCSU:
- E. Piner / Prof. N. El-Masry—DCXRC
- N. Edwards / Prof. D. Aspnes—spectroscopic ellipsometry
- M. Benjamin / Prof. R. Nemanich—NEA studies

Davis Group:
- B. Perry—PL, CL, X-Ray analysis
- T. Zheleva—TEM , X-Ray analysis
- E. Carlson and D. Bray—ion implantation
- S. King—surface cleaning and analysis
- L. Smith and K. Tracy—contacts
- S. Smith and S. King—etching
- M. Behbehani and B. Therrien—device fabrication

XII. Structural Characterization of III-Nitride Films and Interfaces by TEM and XRD

A. Introduction

The potential application of the Group III-nitrides in electronic and opto-electronic devices based on their wide band-gaps (3.4eV for GaN and 6.2eV for AlN) has led to an extensive research of the factors which affect the device performance [1-3]. It is well recognized that the smaller lattice and thermal mismatch, as well as the similarity in the interfacial bonding, are the most important properties that influence the structural quality of the heterojunctions [4-6]. It is energetically favorable for the films to strain elastically in order to either reduce or eliminate the misfit between the two crystals. If the misfit is reduced but not eliminated by the elastic strain, the remaining strain is accommodated by misfit dislocations. The amount of the misfit accommodated by the elastic strain and misfit dislocations depends on the difference between the two bulk lattice parameters, on the thickness of the film, on the bonding across the interface, on the elastic constants of the two materials, and on the geometry of the dislocations [7].

Extensive studies of the type of defects accommodating the lattice and thermal mismatch in type III nitrides have been performed by numerous research groups [8-13]. Due to the common film structure, the type of defects observed in GaN films grown on sapphire and on 6H-SiC are similar [13] despite the difference in the lattice mismatch. Typical line defects usually observed in the hexagonal crystals, including GaN and AlN films are: threading edge dislocations **b**=1/3[11$\bar{2}$0]GaN, prism-plane dislocation half loops **b**=[0001]GaN, basal dislocations **b**=1/3[11$\bar{2}$0]GaN. The plane defects which are usually observed in the GaN and AlN are stacking faults, double positioning boundaries and inversion domain boundaries [10, 12]. These types of defects are expected in the AlGaN alloys, as well.

B. Experimental Procedure

The $Al_xGa_{1-x}N$ (x=0.13) films are grown by OMVPE on 6H-SiC(0001) wafers 3°-4° off-axis oriented toward <11$\bar{2}$0> at 1100°C at 45 Torr. A description of the system and deposition parameters is given elsewhere [14]. The structural properties of these epitaxial hetero-structures have been analyzed by transmission electron microscopy (TEM) and x-ray diffrac-tion (XRD). The samples were observed with a TOPCON EM-002B high resolution trans-mission electron microscope, operating at 200kV and point-to-point resolution 0.18nm. Samples for TEM have been prepared by conventional methods using mechanical grinding and polishing and Ar^+ ion-milling at a low angle in the final stages. Cross-sectional samples were prepared in <11$\bar{2}$0> zone axis of the 6H-SiC substrate. X-ray diffraction studies have been performed on two GaN/AlN/SiC (0001) samples with different thickness 1.5 μm and 3.7 μm, respectively. High resolution ω/ω-2θ scans, x-ray rocking curves, and ω-scans, have been performed using a triple axis diffractometer (Philips Materials Res. Diffractometer), using four-bounce Ge (220)

incident beam optics (two channel cut Ge crystals) and two-bounce Ge (220) diffracted beam optics (one channel cut Ge crystal) for the area maps, and anti-scatter slit analyser diffracted beam optics for the rocking curves. The resolution limit with this optic is 12 arcsec.

C. Results and Discussion

TEM of $Al_xGa_{1-x}N/SiC$ (0001). A typical low-magnification TEM micrograph of $Al_xGa_{1-x}N/SiC$ (0001) heterostructure is shown in Fig. 1. The morphology is dominated by

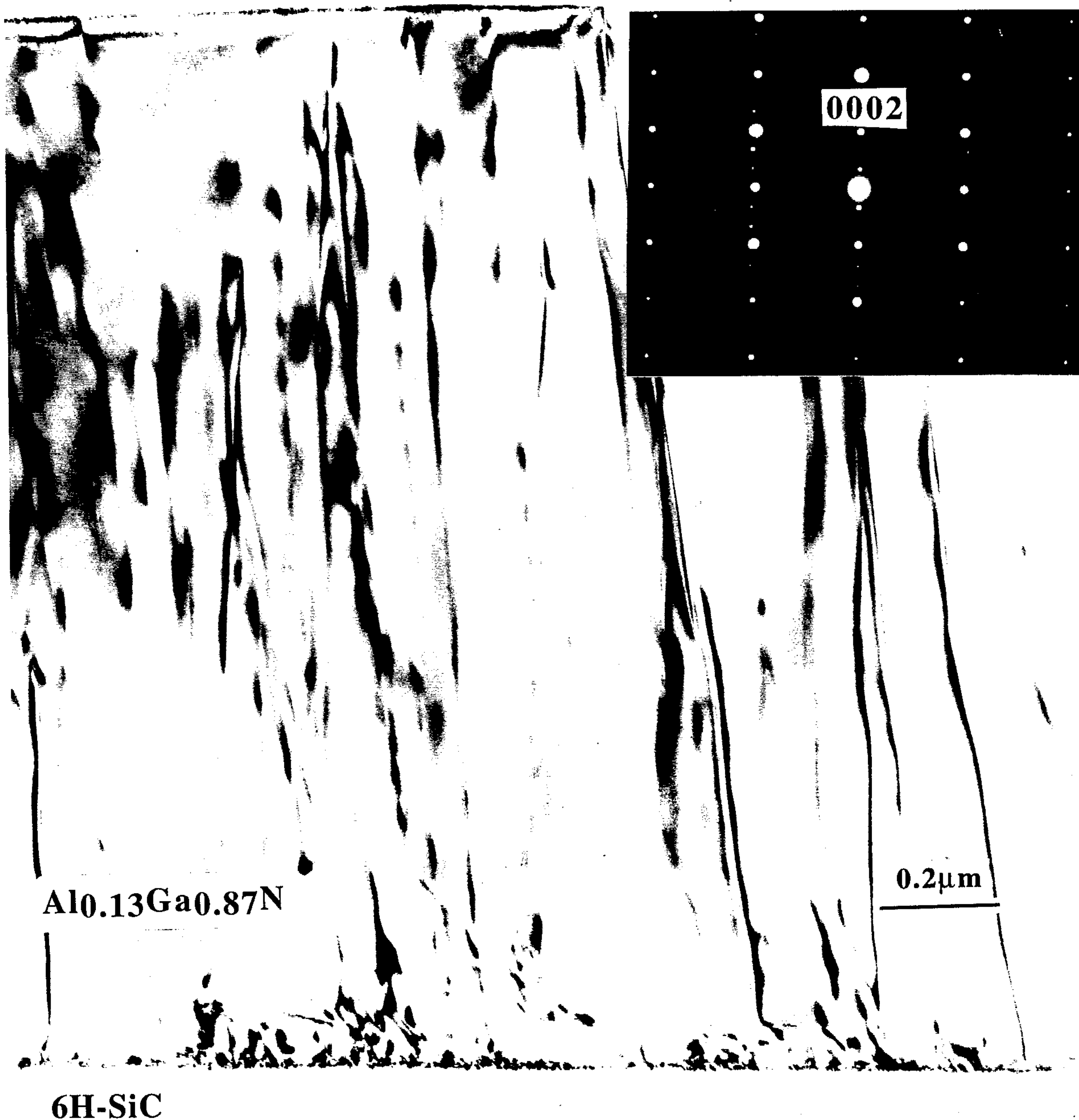

Figure 1. Cross-sectional image of the AlxGa1-xN/SiC (0001) with the selected area diffraction inset.

threading dislocations extended from the substrate to the top of the film. In addition, a smaller amount of dislocation half-loops elongated along the c-direction are observed at distances of a few hundred angstroms from the film/substrate interface. Their existence can be attributed mainly to interfacial strain. Low-magnification images at the interface do not reveal the appearance of stacking defects parallel to the interface. The selected area diffraction pattern (SADP), shown in the inset, represents the superposition of the wurtzite $Al_xGa_{1-x}N$ and 6H-SiC diffraction pattern in <11$\bar{2}$0> zone axis. The diffraction spots without arcs or streaks confirm the epitaxial quality of the film. No extra diffraction spots originating from the zinc-blende phase can be identified from the SADP.

Atomic scale resolution TEM image at the same interface is shown in Fig. 2. An abrupt interface without misoriented grains or amorphous areas is clearly seen at the interfacial region.

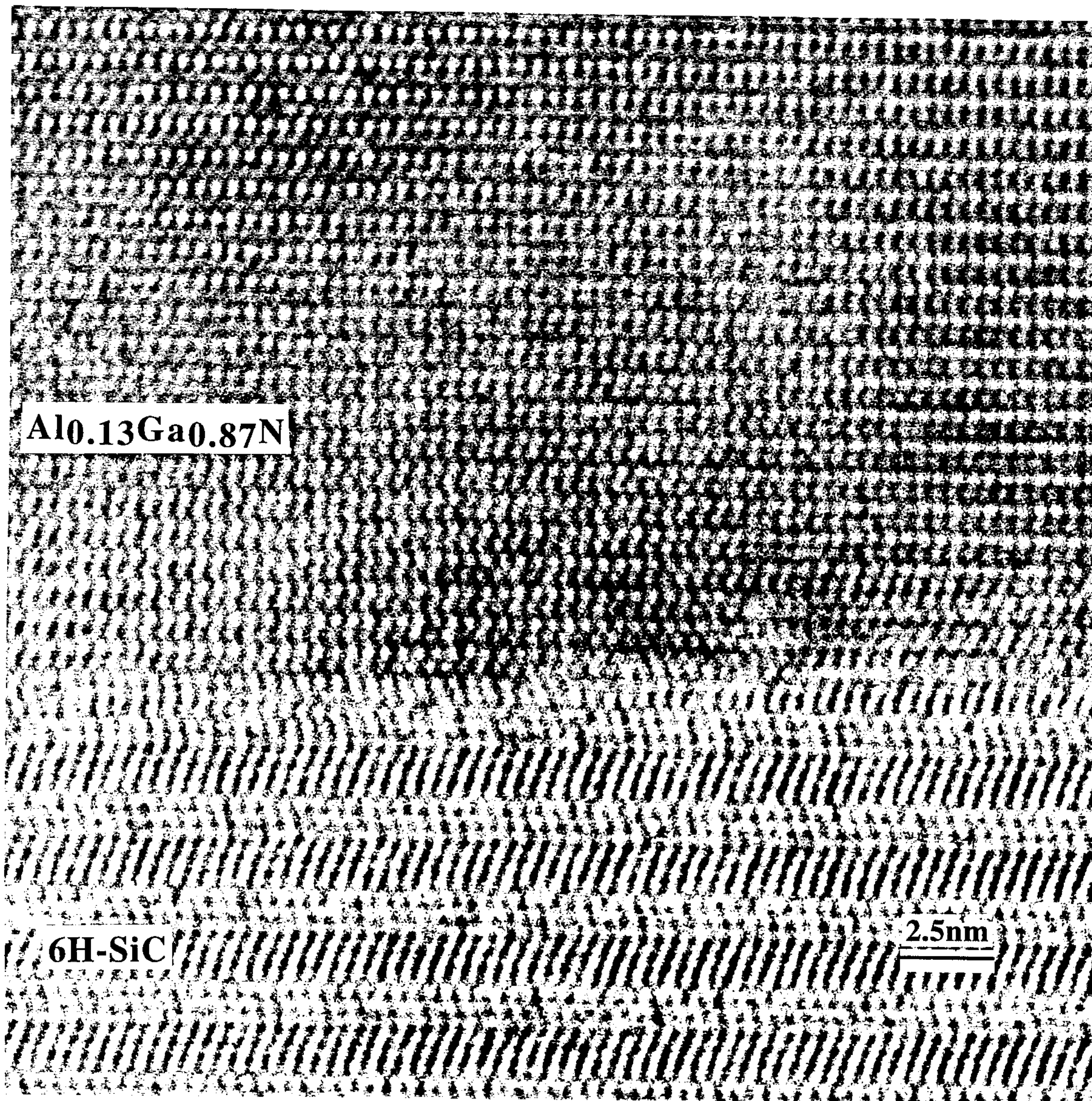

Figure 2. High resolution TEM image of $Al_xGa_{1-x}N$/SiC (0001) interface.

Large areas within the $Al_xGa_{1-x}N$ film are defect free. A defect structure close to the interface, is shown in Fig. 3. The stair-like appearance of these stacking faults parallel to the interface is in the order of 50Å to 200Å distance away from the interface boundary. Also, the steps of the substrate are replicated by these stacking faults. This indicates that the surface geometry, in addition to the interfacial lattice mismatch strain, plays an important role in the formation of these type of defects.

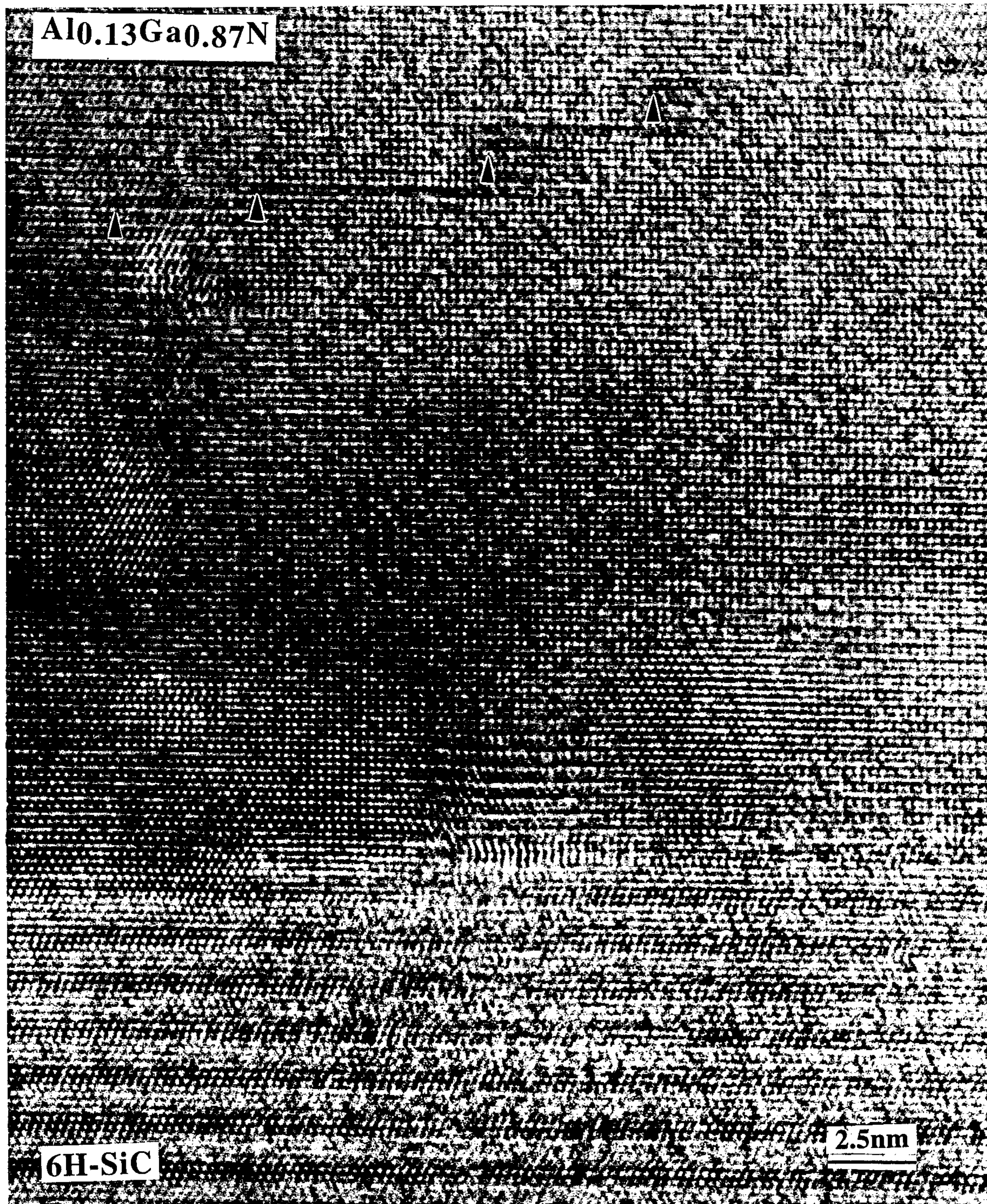

Figure 3. Stair-like stacking faults parallel to the $Al_xGa_{1-x}N$/SiC interface.

TEM of GaN/$Al_xGaN_{1-x}N$ (x=0.2) Superlattice (SL). Analysis of defects and interfaces in a GaN/$Al_xGaN_{1-x}N$ (x=0.2) superlattice (SL) has been performed. A schematic of the structure is shown in Fig. 4. Low magnification TEM micrograph from the SL is shown in Fig. 5. A high defect density was observed at the AlN/SiC(0001) interface. Almost all of the strain is relieved within the AlN film and at the AlN/SiC interface via misfit dislocations. Smaller amounts of threading dislocations parallel to the c-axis and stacking faults parallel to the interface are seen close to the GaN/AlN interface. The top half of the GaN film, closer to the interface is defect-free except for random threading dislocations which originate from the GaN/AlN interface. The superlattice films are monocrystalline and with abrupt interfaces free of defects as shown in Fig. 6. This is due mostly to the fact that the elastic strains at the consecutive SL interfaces are with opposite signs. TEM plan view, shown in Fig. 7 reveals the significantly reduced defect density in the top most GaN film. Most of the defects are screw dislocation loops and edge components of dislocations.

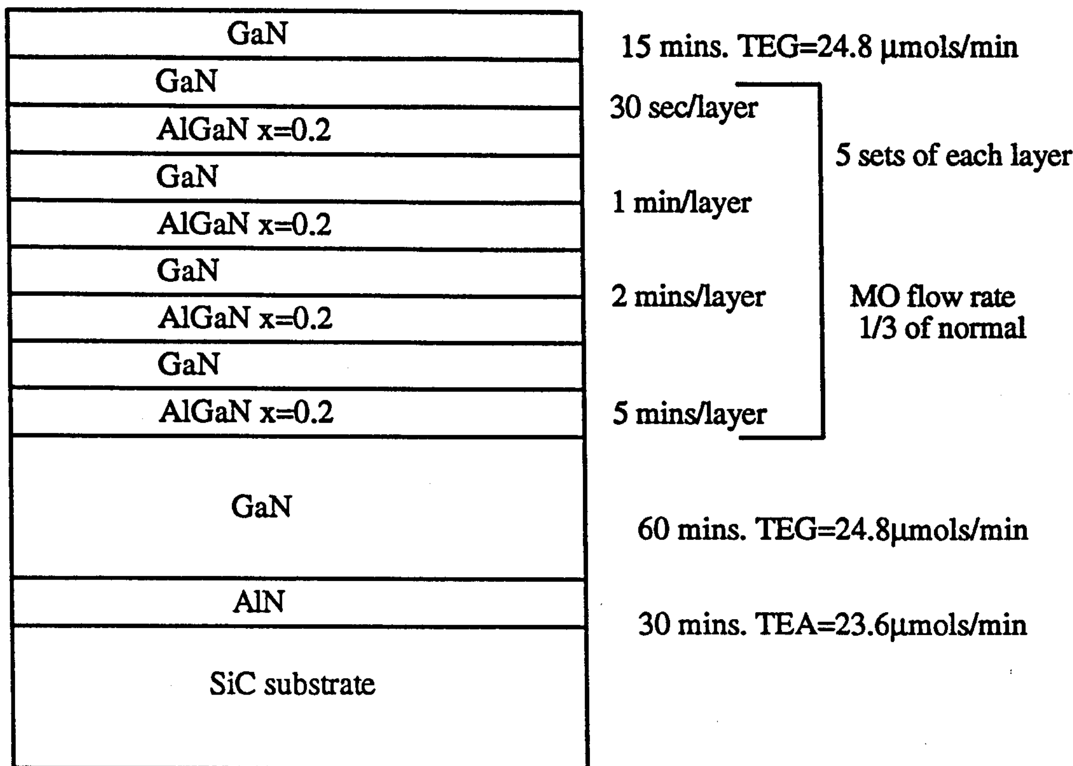

Figure 4. A schematic of the GaN/$Al_xGa_{1-x}N$ superlattice.

X-ray Diffraction Studies. X-ray diffraction studies have been performed on two GaN/AlN/SiC(0001) 3°-4° off-axis samples with different thicknesses of 1.5 μm and 3.7 μm, respectively. It is well known that with the increase of the film thickness, the FWHM of the rocking curves decrease. The FWHM of the rocking curves (ω scans) are obtained as

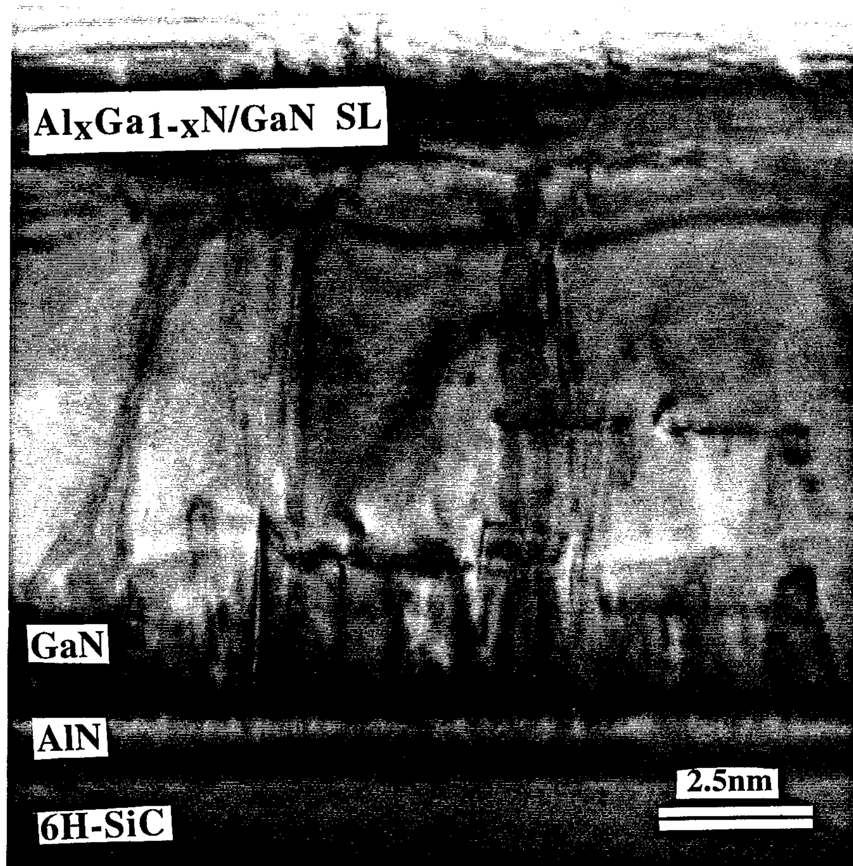

Figure 5. Low magnification TEM micrograph from the heterostructure shown in Fig. 4.

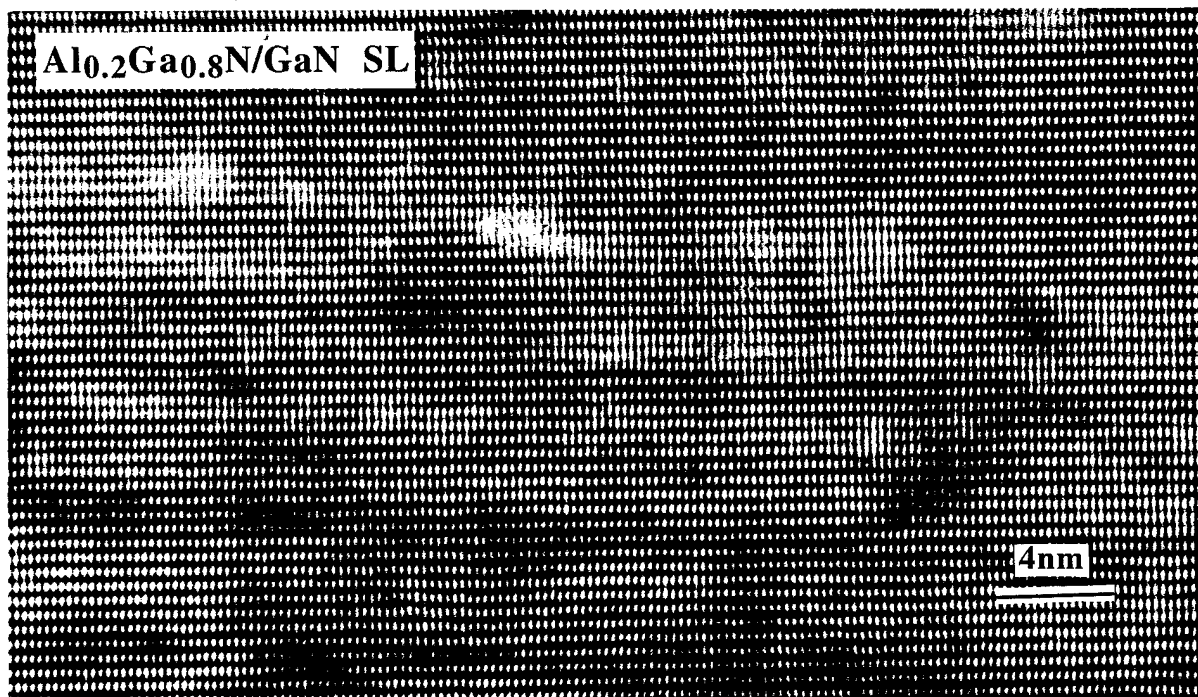

Figure 6. Atomic resolution TEM image of the $GaN/Al_xGa_{1-x}N$ superlattice.

Figure 7. Low magnification plan-view bright field micrograph from the near surface region of the GaN film.

follows: for the thinner film, 249 arcsec for GaN peak and 321 arcsec for the AlN peak; for the thicker film, 144 arcsec for the GaN peak and 210 arcsec for the AlN film. The FWHM for the SiC peak were 63 arcsec and 41 arcsec for the thinner and thicker films, respectively. Typical rocking curves from film 1 are shown in Fig. 8. It is also known that while the ω scan provides information about the mosaic structure of the sample, the width of the peak in ω-2θ scan provides direct information about the particle size broadening or the crystal coherence length. Thus, from the X-ray area maps or the ω/ω-2θ scans, one can easily distinguish between mosaicity and the crystal coherence length. The area map from film 2 is presented in Fig. 9. The (002) GaN and AlN peaks and (006) SiC peaks are mapped over ω and ω-2θ. The broadening of the peaks in the ω axis is due to the mosaicity in the film, while the elongation in the ω-2θ axis is due to the crystal coherence length and the heterogeneous strain distribution.

D. Conclusions

Monocrystalline $Al_xGa_{1-x}N$ have been grown epitaxially directly on 6H-SiC(0001) substrates. There are no oriented domain structures and related low-angle grain boundaries. The predominant defects are threading dislocations. Most of the misfit is accommodated within 100Å–200Å distance from the interface. The superlattice $GaN/Al_xGa_{1-x}N$ films are monocrystalline with abrupt, defect-free interfaces. TEM studies reveal significant reduction of the defect density with the increasing distance from the interface for both types of crystal structures. X-ray studies reveal good monocrystalline quality of the GaN films grown on AlN/SiC(0001).

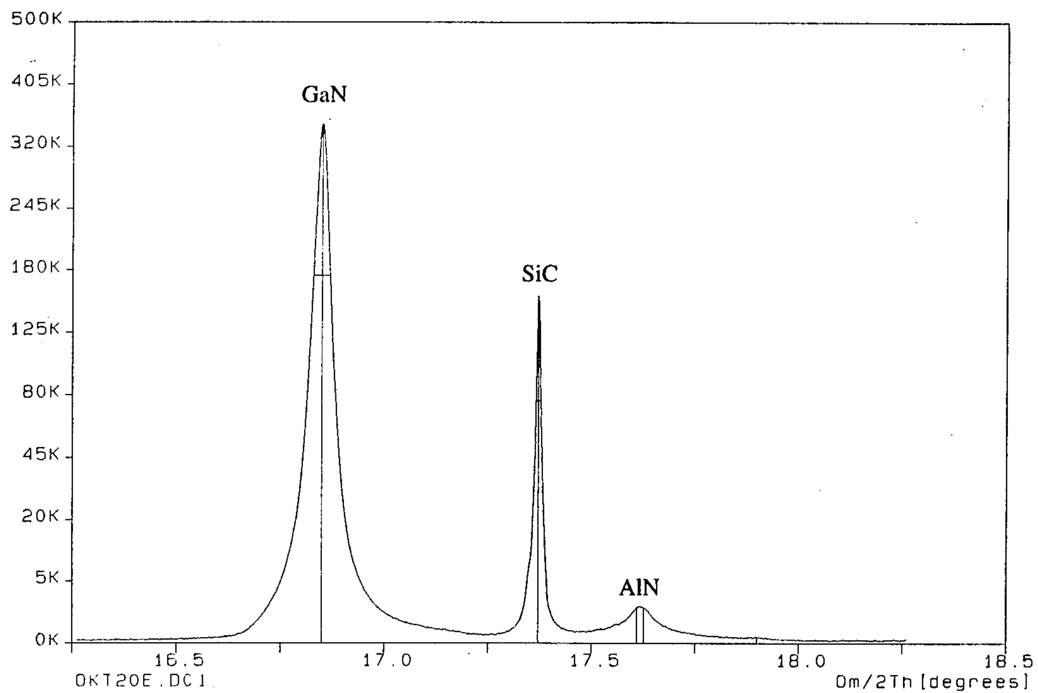

Figure 8. X-ray rocking curves from AlN/GaN/6H-SiC sample; AlN and GaN (0002) reflection, and SiC (0006) reflection.

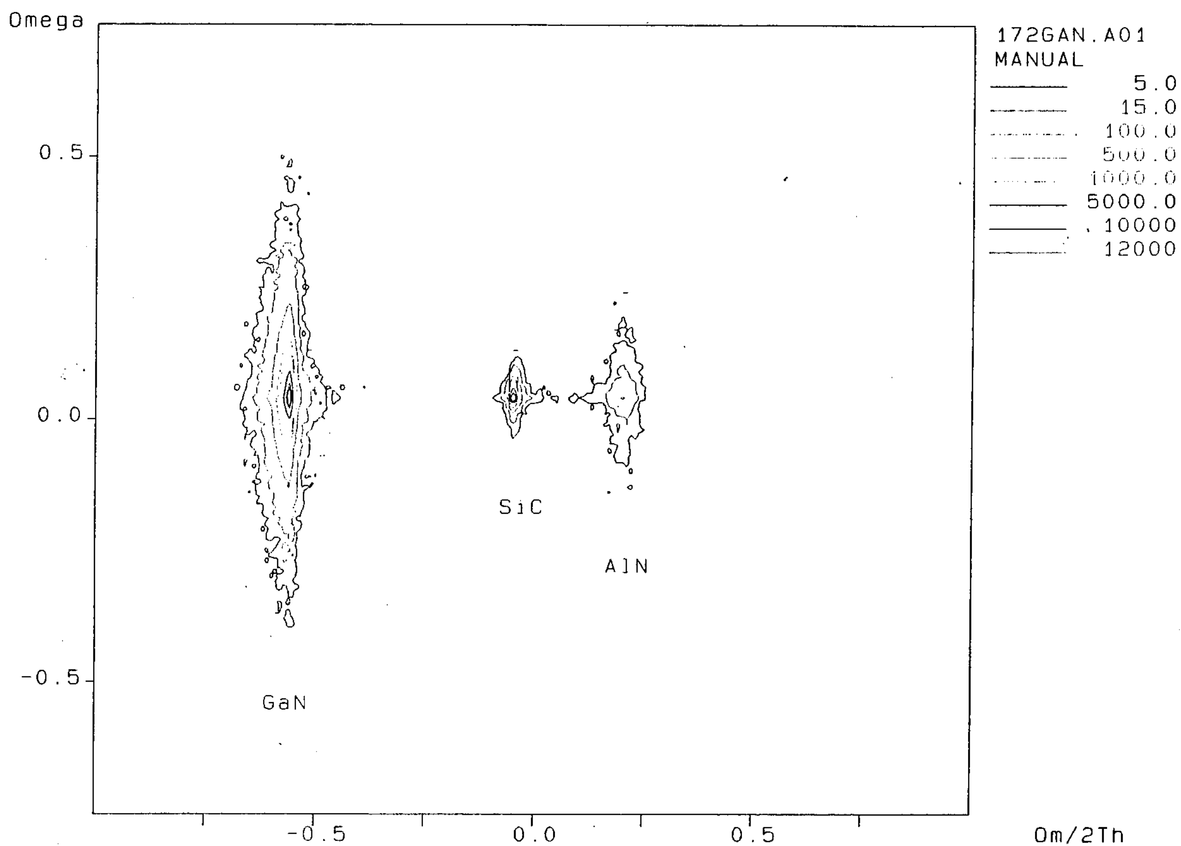

Figure 9. A reciprocal space map of the X-ray scattering intensity in the vicinity of the GaN and AlN (0002) and the SiC (0006) reflections.

E. Future Research Plans and Goals

Further work will be undertaken to study defects and stress distribution in GaN/AlN/SiC(0001) films by x-ray diffraction. The shifts in the rocking curves peaks position at different points in the sample are associated with the stress states in the films due to the lattice and thermal mismatch between the films and the substrate in these heterostructures. Preliminary results indicate stresses in the films of the order of $1.2\text{-}1.5\times10^8$Pa for the GaN/AlN/SiC heterostructures. Also, correlation between the stress and strain distribution at the interfaces studied by TEM and x-ray has to be demonstrated.

F. References

1. P. Rees, C. Cooper, P. Blood, P.Smowton and J. Hegarty, IEE, May, (1995).
2. G. Mohs, B. Fluegel, H. Giessen, H. Tajalli, N. Peyghambarian, P.-C. Chiu, B. Philips and M.Osinski, Appl. Phys. Lett. **67**, 1515 (1995).
3. A. Zubrilov, V. Nikolaev, D. Tsvetkov, V. Dimitriev, K. Irvine, J. Edmond and C. H. Carter, Appl. Phys. Lett. **67**, 533 (1995).
4. F. Ponce, B. Krusor, J. Major, Jr., W. Plano and D. Welch, Appl. Phys. Lett. **67**, 410 (1995).
5. T.W. Weeks, Jr., M. Bremser, K. Ailey, E. Carlson, W. Perry and R. F. Davis, Appl. Phys. Lett. **67**, 401 (1995).
6. B. Sverdlov, G. Martin, H. Morcoc and D. Smith, Appl. Phys. Lett. **67**, 2063 (1995).
7. J. H. van der Merve, J. Appl. Phys, **34**, 117 (1963).
8. M. McCartney, R. Youngman and R.Teller, Ultramicroscopy, 40, 291 (1992).
9. D. Smith, D. Chandrasekhar, B. Sverdlov, A. Botchkarev, A. Salvador and H. Morcoc, Appl. Phys. Lett. **67**, 13 (1995).
10. X. Ning, F. Chien, P. Pirouz, J. Yang and M. Khan, submitted in J. Mat. Res. March, (1995), and references therein.
11. S. Tanaka, R. Kern, J. Bentley and R. F. Davis, submitted in Japn. J. Appl. Phys. Nov. (1995).
12. A. Westwood, R. Youngman, M. McCartney, A. Cormack and M. Notic, J. Mater. Res. **10**, 1270 (1995), and references therein.
13. Z. Liliental-Weber, H. Sohn, N. Newman and J. Washburn, J. Vac. Sci. & Technol. B **13** 4 (1995).
14. M. Bremser, W. Perry, N. Edwards, T. Zheleva, N. Parikh, D. Aspnes and R. F. Davis, Proceedings MRS, Boston (1995).

XIII. Luminescence Studies of GaN

A. Introduction

Luminescence is the emission of photons due to excited electrons in the conduction band decaying to their original energy levels in the valance band. The wavelength of the emitted light is directly related to the energy of the transition, by $E=h\nu$. Thus, the energy levels of a semiconductor, including radiative transitions between the conduction band, valance band, and exciton, donor, and acceptor levels, can be measured [1,2]. Various methods exist to excite the electrons, including photoluminescence (photon excitation), and cathodoluminesence (electron-beam excitation). Measurements are often performed at low temperatures (4.2 K using liquid He) to improve luminescence efficiency and distinguish individual transitions.

Both photoluminescence (PL) and cathodoluminescence (CL) analysis have been performed on AlN, GaN, and their solid solutions [3-20]. GaN, with a bandgap of 3.5 eV (354 nm) at 4.2 K, is readily studied by PL using UV sources such as He-Cd and frequency-doubled Ar^+ lasers. This section will focus on GaN; the CL of AlGaN will be discussed in the section devoted to AlGaN growth and characterization.

In the past, GaN grown on vicinal α(6H)-SiC$(0001)_{Si}$ wafers has been studied [21]. The PL revealed an intense near band-edge emission at 357.4 nm (3.47 eV), which is attributed to annihilation of excitons bound to neutral donors. The FWHM of this peak, 4 meV, indicated the high quality of the sample. The donor-bound exciton line, often designated the I_2 line, is the signature peak for high quality GaN films. Recently, others have detected free exciton (FE) emission, and evidence of it has been seen in our materials, as well [22-24]. FE emission indicates both the high quality of our materials and a lack of residual donors.

A very weak defect peak ascribed to donor-acceptor pair (DAP) transitions and two associated LO phonon replicas were also discussed previously, with the zero phonon line at 379 nm. Additional structure is found on the low energy side of the 3.27 eV peak at approximately 3.24 eV. Recent work has indicated this structure is due to both DAP transitions and band-acceptor (eA) recombination [25, 26]. This designation has previously been made for transitions at temperatures above 120 K as the thermal energy approaches the shallow donor binding energy. Others believe the additional structure at low temperature is due to a second donor-acceptor pair [27, 28].

Undoped GaN is always n-type, and the origin of the residual donors has been the subject of serious debate. Donors of both extrinsic and intrinsic nature have been proposed. Nitrogen vacancies (V_N) have long been suspected and recent theatrical calculations give credence to this idea [29, 30]. These calculations also suggest that gallium vacancies (V_{GA}) partially compensate n-type GaN. Impurities such as Si and O introduced during growth also increase the carrier concentration and should be minimized.

The identity of the shallow acceptor is unclear, although carbon is a strong possibility [25]. The binding energy of carbon is proposed to be either 200 or 230 meV, depending on whether the transition at 3.27 eV is DAP or eA in nature. The probable source of carbon is the ethyl and methyl radicals used as precursor gases.

B. Experimental Procedures

A combined photo- and cathodoluminesence system is used to measure the luminescence from the III-V nitrides, see Fig 1. Each sample is attached to a cryostat that provides a test temperature range of 4.2 to 300 K. A McPherson model 219 vacuum monochromator with a focusing mirror chamber is used to collect the emitted light. The focal length of the monochromator is .5 m, with a wavelength resolution of .02 nm at 313.1 nm for a 1200 G/mm grating. A photon counting detection scheme is used to measure the light intensity, with a Photomultiplier tube (PMT) that possesses a wavelength range of 180-650 nm.

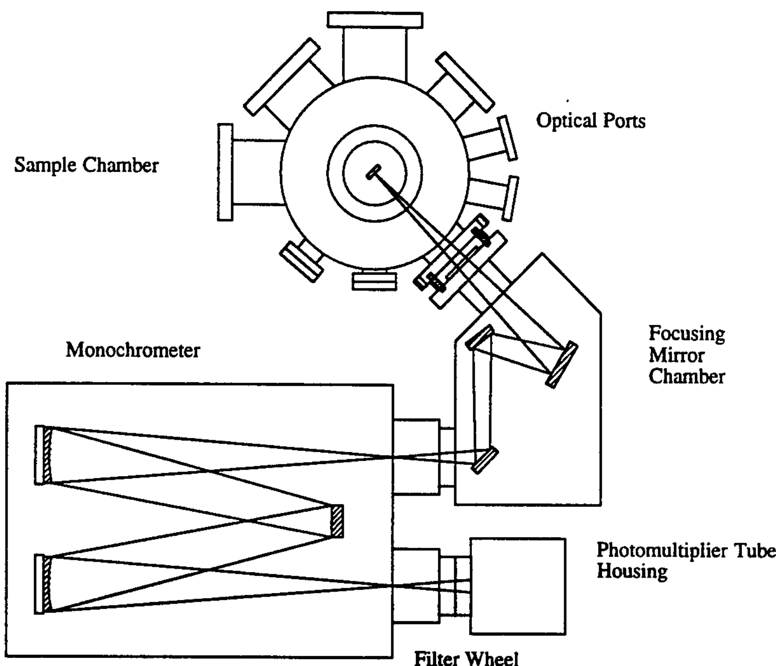

Fig. 1. Schematic view of combined photo- and cathodoluminescence system.

A Liconix He-Cd laser is the photo-excitation source. It is a continuous wavelength laser that operates at a wavelength of 325 nm (3.8 eV), with a power of 15 mW. It is used for PL of GaN and low $Al_xGa_{1-x}N$ alloys, but a lower wavelength source is required to test the full range of $Al_xGa_{1-x}N$ solid solutions. A Kimball Physics electron gun is used for cathodoluminesence measurements. It has a maximum beam voltage of 10 keV and a maximum beam current of 450 uA. CL experiments are usually performed with a beam voltage of 5 keV and a beam current of 100 uA. A Faraday cup will soon be added to measure the specimen current.

C. Results and Discussion

Photoluminescence measurements were performed on GaN films grown via OMVPE on vicinal and on-axis α(6H)-SiC(0001)$_{Si}$ wafers. The buffer layer for each sample was AlN. All tests were performed at 4.2 K, unless otherwise noted.

In a previous report, both free and bound exciton emission were reported for a 1.4 µm GaN layer deposited on on-axis SiC [22]. The assignment of these peaks has been verified by temperature-dependent PL and the results are shown in Fig. 2. At 4.2 K, the free exciton (FE) peak is at 357.11 nm (3.472 eV) and the bound-exciton (I_2) peak is at 357.79 nm (3.465 eV). As temperature increases, the I_2 intensity decreases much faster than the FE intensity. This behavior is expected and is due to the dissociation of bound excitons as thermal energy (kT) exceeds the binding energy (E_b). Curve fitting performed on the 4.2 K data is displayed in Fig. 3. A Lorentzian energy distribution was assumed for both peaks. The energy difference between the fitted FE and I_2 lines, 7.0 meV, is a measure of E_b. The FWHM of the FE and I_2 lines is 4.86 meV and 4.46 meV, respectively. This is expected, as the bound excitons possess no kinetic energy. Line width is another indication of the identity of both transitions [31].

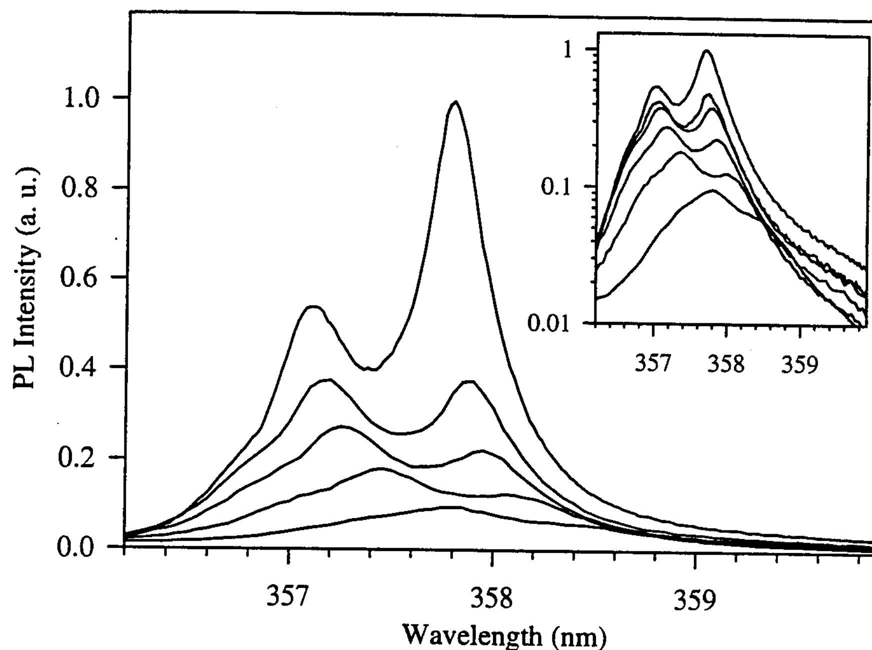

Figure 2. PL of GaN/on-axis SiC at T=4.2, 25, 35, 50, 70 and 100 K.

In previous work, the PL of GaN at various film thicknesses revealed a shift in the donor-bound exciton peak to lower energies as film thickness increased [22]. This shift was attributed to a change in the bandgap due to strains in the film [31]. A unique sample was used to further study and verify this phenomenon. GaN grown on a whole SiC wafer resulted in a thickness variation of 1.5 µm at the sample center to 1.0 µm at the edge. PL was performed along this

thickness gradient and the results are shown in Fig. 4. These peaks are due to donor-bound excitons, as confirmed by temperature-dependent PL. The energy and wavelength of each peak is displayed in Table I.

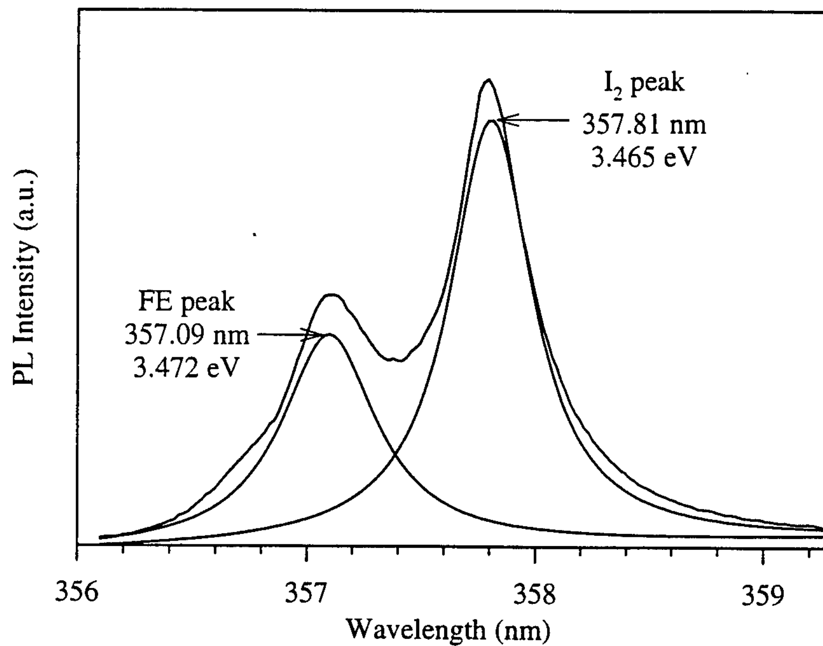

Figure 3. Curve fitting results for the free exciton (FE) and bound excitor (I_2) PL peaks of GaN on on-axis SiC.

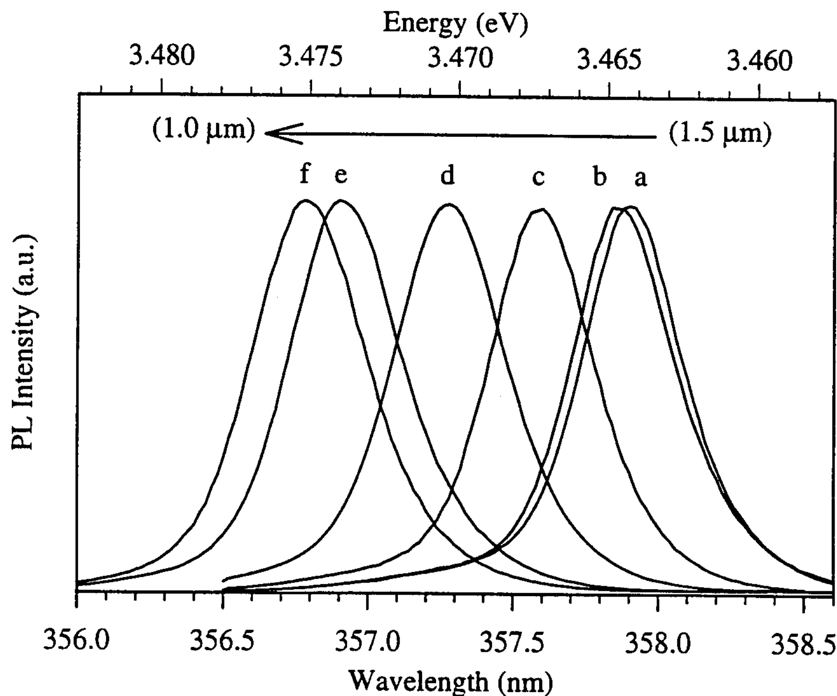

Figure 4. PL intensity of GaN on SiC at 4.2 K as a function of film thickness.

Table I

Sample	Peak Location (nm)	Peak Location (eV)
a	357.9	3.464
b	357.84	3.465
c	357.6	3.467
d	357.28	3.47
e	356.9	3.474
f	356.78	3.475

The energy shift of 11 meV between peaks *a* and *f* is significant, and indicative of a variation in the bandgap of the material due to strain [31].

As film thickness decreases below 1 μm the ratio of DAP to I_2 peak emission intensity increases dramatically. Donor-acceptor pair transition intensity generally increases as the ratio of the number of donors to the number of acceptors (N_D/N_A) approaches unity. Given that undoped GaN is always n-type, an increase in the DAP intensity implies an increase in the number of shallow acceptors. One indication of this is electrical compensation.

Previous work showed the peak ratio for a film grown at 1000°C to be much higher than one at 900°C for the same time period [32]. However, the growth rate also decreased with temperature; the film grown at 900°C was .79 μm and the 1000°C film was .67 μm. Thus, there are two parameters to account for: film thickness and growth temperature. All films were autodoped by precursor impurities and no discernible trend was seen in the electrical data.

After this study, improvements in the growth system have led to higher growth temperatures and better films, with 1050°C the typical growth temperature. Autodoping effects were greatly diminished by changes in the precursor gases. Hence, a similar study was performed for GaN films grown at 950, 1000, 1050 and 1100°C for one hour. The results displayed in Fig. 5 use a log scale for the PL intensity. They confirm that as growth temperature increases (and film thickness decreases), the ratio of the DAP peak intensity to the bound-exciton peak intensity increases. The carrier concentration also decreased with growth temperature and was not able to be measured at the highest growth temperature.

To differentiate between thickness and growth temperature effects, films of equal thickness were grown at 1050 and 1100°C. The PL for both off- and on-axis SiC wafers is displayed in Figs. 6 and 7. The bound exciton and DAP peak intensities are remarkably similar and indicate the decrease in film thickness leads to the intense DAP peaks. The origin of the peak shifts to lower energies for the 1100°C films is unknown. One explanation is that film quality improves with growth temperature, resulting in less mechanisms for strain relief. Further work will be carried out for verification.

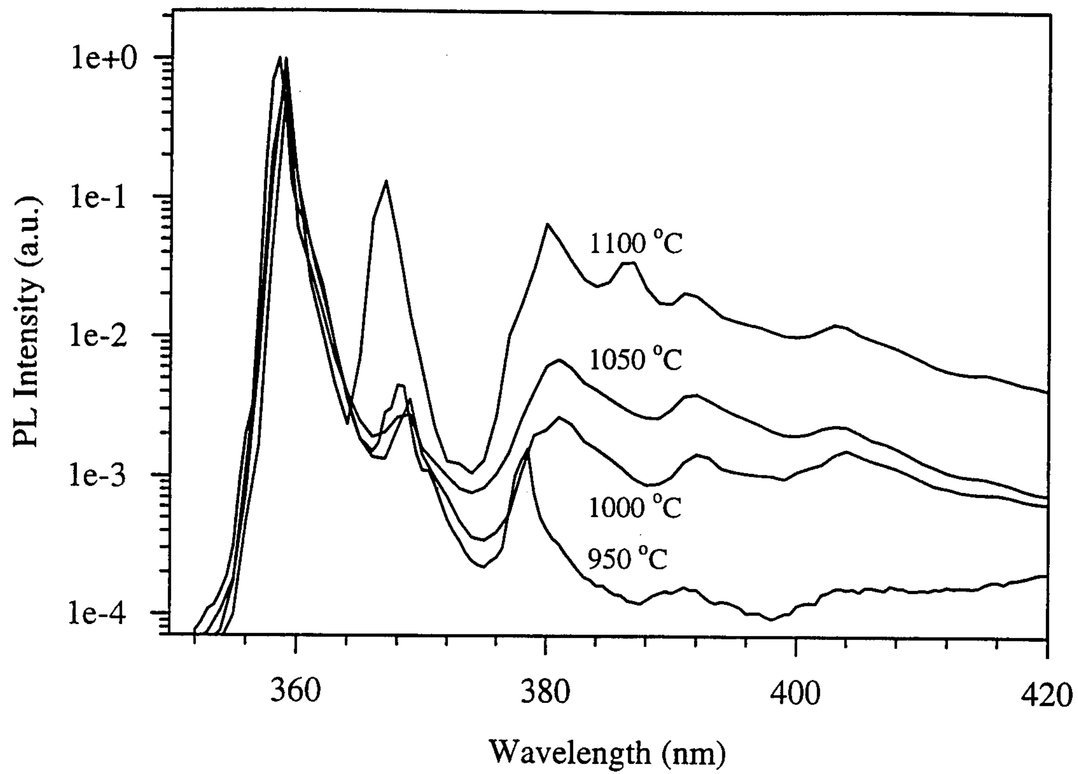

Figure 5. PL of GaN on SiC at 4.2 K as a function of growth temperature.

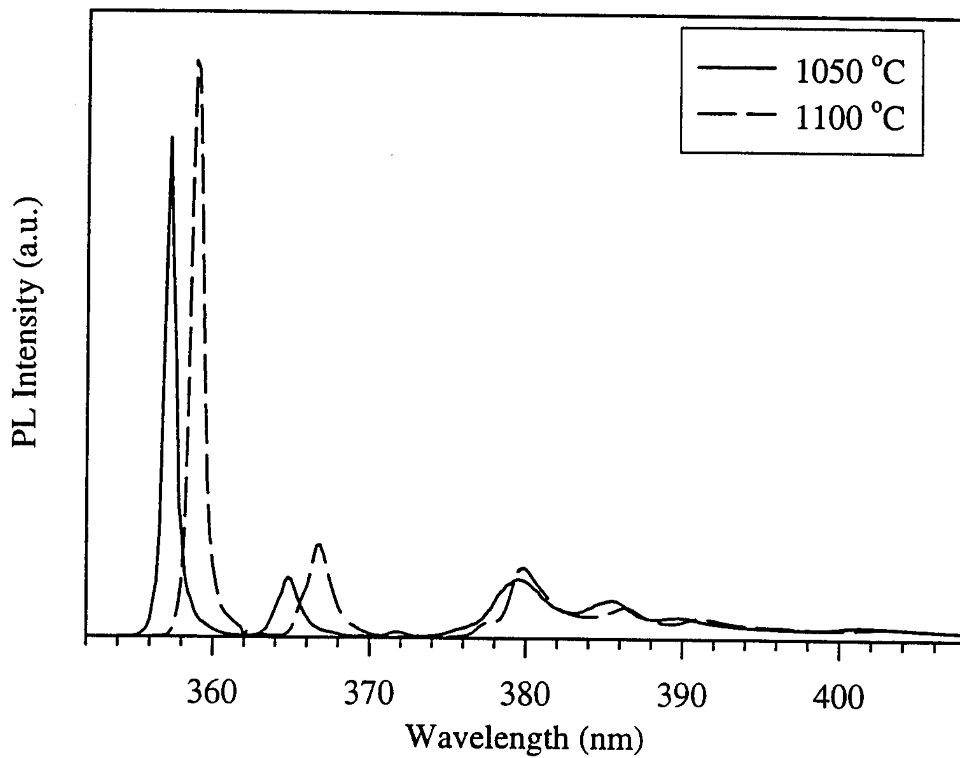

Figure 6. PL of GaN on off-axis SiC with the same thickness.

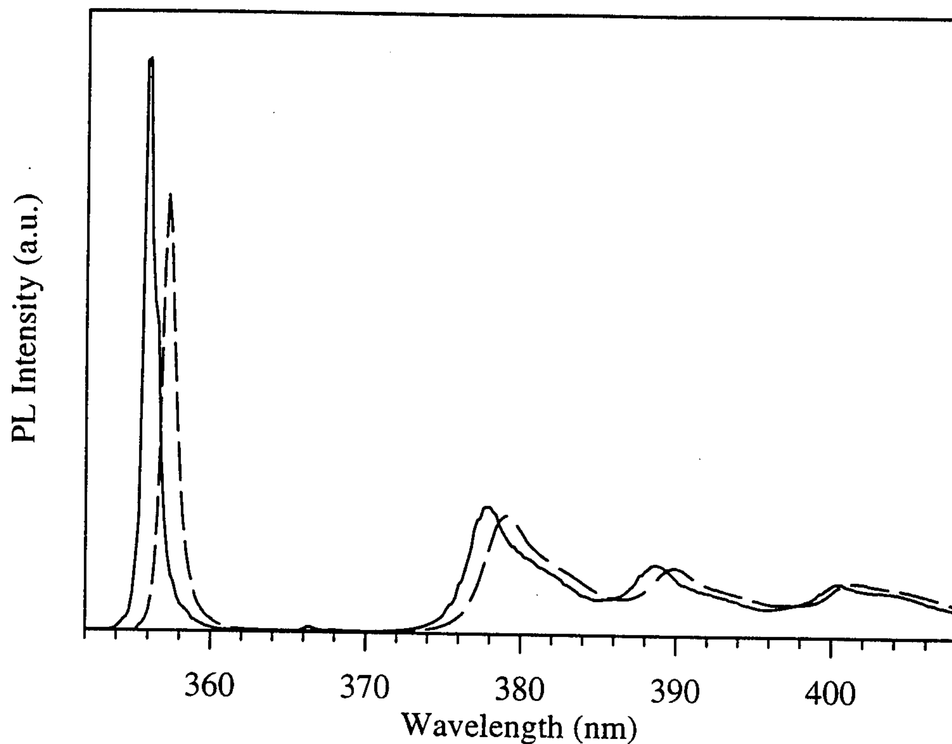

Figure 7. PL of GaN on on-axis SiC with the same thickness.

These results indicate the increase in DAP peak intensity is due to an increase in N_A near the film/substrate interface. The decrease in film conductivity supports this, as an increase in shallow donors would lead to higher carrier concentrations. Also, n-type doping of GaN by Si shows no increase in DAP peak intensity, while low level p-type doping with Mg does, proof that SAP peaks increase as N_D/N_A approaches unity.

Fischer *et al.* propose carbon as the shallow acceptor, with a binding energy of 230 meV [25]. Carbon has been used successfully as a p-type dopant for GaN grown by MOMBE, although no PL was reported [26]. There are two possible sources of carbon, the SiC wafer and TEG, the gallium source. The SiC wafer is unlikely given the stability of SiC at high temperatures and the presence of the AlN buffer layer. Furthermore, others have similar results for GaN on sapphire. Thus, TEG is the likely source. The high growth temperatures ensure the gallium atoms are detached from the ethyl radicals, eliminating the growth temperature correlation seen typically for GaAs. SIMS profiling of GaN does not indicate higher concentrations of C near the interface, but the variation in concentration required to alter PL may be below the SIMS resolution. In this respect PL is a more sensitive technique.

In related work, Keller *et al.* varied the V/III ratio during growth of GaN. As the V/III ratio decreased, the DAP peak intensity increased. They attribute this to an increase in the nitrogen vacancies (V_N) donors due to a deficiency of active nitrogen species. A preferred explanation is

that the V_N are sites for carbon to occupy (C_N), which act as a shallow acceptor. SIMS analysis in a similar study confirms that both the carbon concentration and DAP intensity increases as the V/III decreases [33]. The question, then, is why would there be more vacancies near the film/substrate interface?

One explanation is related to the film microstructure. The majority of threading dislocations ($\sim 1\times10^9$ cm^{-2}) are within the first .5 μm for these films and eventually decrease by two orders of magnitude with increasing thickness [21]. It is plausible these dislocations are very efficient at trapping residual donors and acceptors. Given the absorption length of the He-Cd laser is roughly .2 μm in GaN, a noticeable change in the PL spectrum for films .7 μm or thinner should be seen; this is indeed the case.

The threading dislocations form during film growth due to the lattice mismatch between GaN and SiC (3.4 %). It is possible that carbon and other species could segregate to the dislocation core along the surface or at a later time at the growth temperature. In general point defects such as impurities and vacancies segregate to dislocations to reduce their strain energy with the lattice.

Recent work Sverdlov *et al.* supports this explanation [34]. They propose the vertical defects observed in GaN are stacking mismatch boundaries (SMBs), which are boundaries between differently stacked domains originating at the SiC substrate steps. The lattice is severely distorted at these boundaries, which can be interpreted as a two-dimensional network of quasinterstial atoms or quasivacancies. This network may act as an effective sink for introduced impurities. Carbon is a very small atom and so it is reasonable large amounts could pile up at these defects and act as shallow acceptors.

Electron spin resonance (ESR) and Hall-Vander Pauw measurements by Carlos *et al.* showed strong evidence of compensation near the film/substrate interface for GaN on sapphire using an AlN buffer layer [35]. They attributed this to an increase in shallow acceptors near the interface, possibly due to the aforementioned dislocations. A similar trend for a GaN buffer layer did not occur, however, indicating the AlN buffer layer used for our materials may be a source of compensating acceptors.

The arrows in Figs. 8 and 9 point out additional peaks unusual for GaN. They are most intense in two samples grown at 1100°C, but they also present (albeit weaker) in Figs. 6 and 7. The peak at 365.8-366.2 may be due to an acceptor-bound exciton (I_1), although no report of a bound exciton at such a low energy exists. The peaks at 385.1-.4 appear to be a second donor-acceptor pair. Given that the sample appears to be compensated, it is believed this is due to a second acceptor level, possibly one that gives the I_3 peak noted above. There is no indication of additional impurities introduced into these samples.

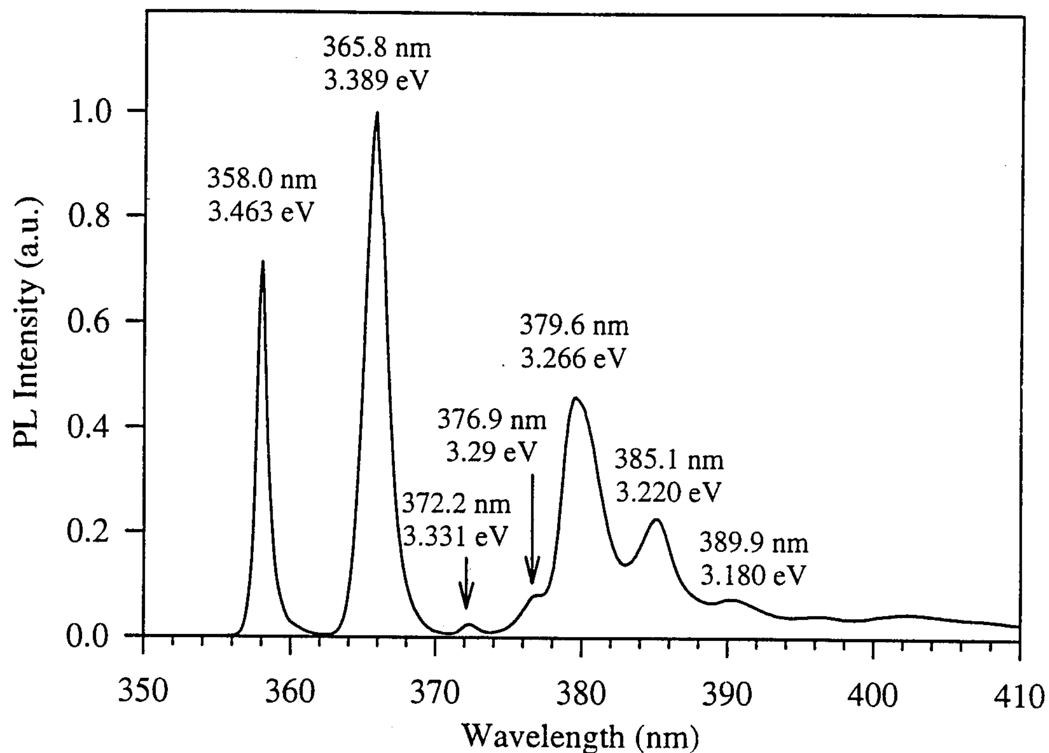

Figure 8. PL of GaN on on-axis SiC at 1100°C.

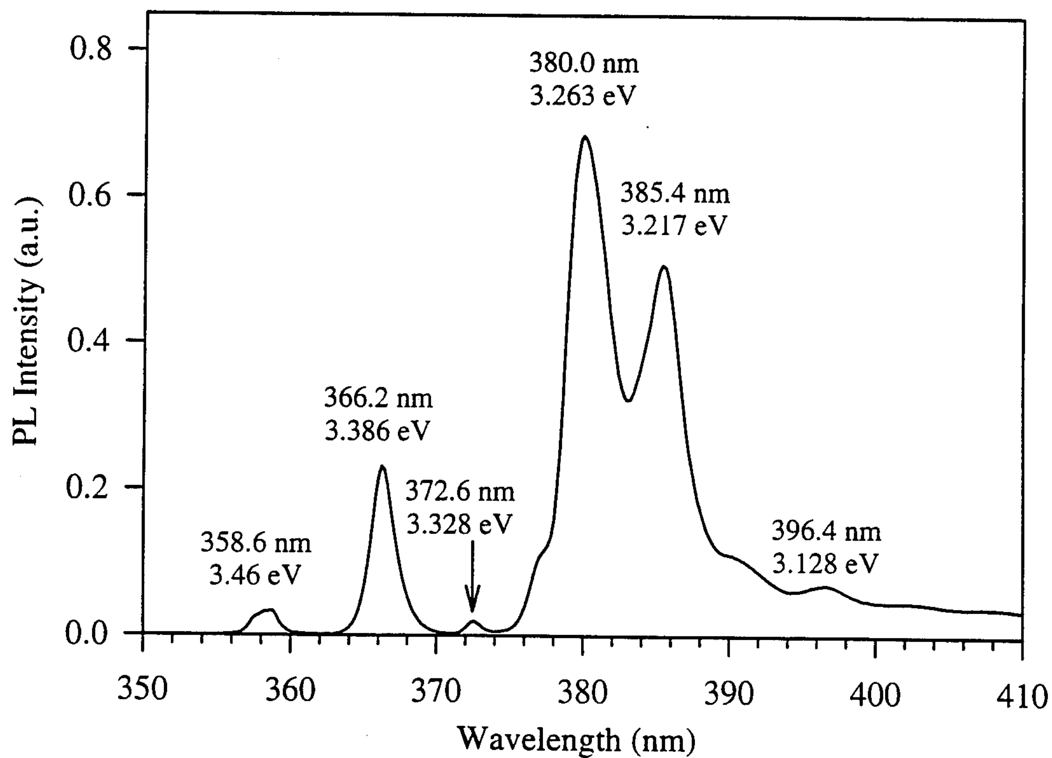

Figure 9. PL of GaN on off-axis SiC at 1100°C.

D. Conclusions

Temperature dependent PL was used to verify free exciton emission for GaN on SiC. Curve fitting showed the binding energy of the excitons to neutral donors to be 7 meV. The smaller FWHM of the free exciton peak is further confirmation of it's nature.

An 11 meV shift in the I_2 line was observed for a GaN film with a .5 μm thickness variation. This shift is considerable and results from a variation in the bandgap energy due to strain effects.

The ratio of DAP to I_2 peak emission intensity increased dramatically as film thickness decreased below .8 μm. This behavior is attributed to an increase in shallow acceptors near the film interface, with carbon the likely acceptor. We believe the high density of threading dislocations (SMBs) act as traps for carbon, either at interstitial and/or vacancy sites.

E. Future Work

The relationship between film thickness and the donor-bound exciton peak position will be further investigated. X-ray diffraction and Raman spectroscopy will be used to measure film strain and it will be correlated to PL data.

The increase in DAP peak intensity as film thickness decreases will be further studied using films thinner than .5 μm. It is possible the intensity of the extra peaks in Figs. 8 and 9 will increase as thickness decreases.

Optically detected magnetic resonance (ODMR) in collaboration with Evan Glaser at Naval Research Lab (NRL) will be utilized to see if the second DAP peak is due to a second donor or acceptor level. A collaboration with Dr. Haugland at NASA Lewis will investigate the compensation in GaN films thinner than .7 μm. Photoluminescence excitation (PLE) and power-dependent PL of thin GaN films and AlGaN will be performed in collaboration with Dr. Jaime Freitas at NRL.

E. References

1. B. G. Yacobi and D. B. Holt, *Cathodoluminescence Microscopy of Inorganic Solids*, Plenum Press, New York (1990).
2. M. D. Lumb, Ed., *Luminescence Scpectroscopy*, Academic Press, New York (1978).
3. S. Strite and H. Morkoç, J. Vac. Sci. Technol. B **10** (4), 1237 (1992).
4. R. A. Youngman and J. H. Harris, J. Am. Ceram. Soc. **73** [11], 3238 (1990).
5. S. Nakamura, T. Mukai, and M. Senoh, Jpn. J. Appl. Phys. **30** (10A), 1708 (1991).
6. V. F. Veselov, A. V. Dobrynin, G. A. Naida, P. A. Pundur, E. A. Slotensietse, and E. B. Sokolov, Inorganic Materials **25** (9), 1250 (1989).
7. J. N. Kuznia, M. A. Kahn, D. T. Olson, R. Haplan, and J. Freitas, J. Appl. Phys. **73** (9), 4700 (1993).
8. H. Murakami, T. Asahi, H. Amano, K. Hiramatsu, N. Sawaki, and I. Akasaki, J. Crystal Growth **115**, 648 (1991).
9. K. Maier, J. Schneider, I. Akasaki, and H. Amano, Jpn. J. Appl. Phys. **32** (6), 846 (1993).
10. I. Akasaki, and H. Amano, J. Crystal Growth **99**, 375 (1990).

11. S. Yoshida, H. Okumura, S. Misawa, and E. Sakuma, Surf. Sci. **267** (7), 50 (1992).
12. S. Nakamura, T. Mukai, and M. Senoh, Jpn. J. Appl. Phys. **31** (9), 2883 (1992).
13. S. Nakamura, N. Iwasa, T. Mukai, and M. Senoh, Jpn. J. Appl. Phys. **31** (5), 107 (1992).
14. S. Nakamura, T. Mukai, and M. Senoh, Jpn. J. Appl. Phys. **30** (12A), 1998 (1991).
15. S. Strite, J. Ruan, Z. Li, N Manning, A. Salvador, H. Chen, D. J. Smith, W. J. Choyke, and H. Morkoç, J. Va. Sci. Technol. B **9** (4), 1924 (1991).
16. W. J. Choyke and I. Linkov, Inst. Phys. Conf. Ser. **137**, 141 (1993).
17. S. Pacesova and L. Jastrabik, 1979 Phys. Stat. Sol. B **93**, K111.
18. S. Yoshida, S. Misowa, Y. Fujii, S. Takada, H. Hayakawa, S. Gonda, A. and Itoh, J. Vac. Sci. Technol. **16** (4), 990 (1979).
19. E. R. Glaser, T. A. Kennedy, H. C. Crookham, J. A. Freitas, Jr., M. Asif Khan, D. T. Olson, and J. N. Kuznia, Appl. Phys. Lett. **63** (19), 2673 (1993).
20. E. R. Glaser, in *Proceedings of the 18th International Conference on Defects in Semiconductors*, to be published.
21. T. W. Weeks, Jr., M. D. Bremser, K. S. Ailey, E. Carlson, W. H. Perry and R. F. Davis, Appl. Phys. Lett. **67** (3) 17, (1995).
22. R. F. Davis, M. D. Bremser, K. Gruss, K. Linthicum, B. Perry. and T. W. Weeks, Jr., Semiannual Technical Report for ONR Grant #N00014-92-J-1720, June 1995.
23. W. Shan, T. J. Schmidt, X. H. Wang, S. J. Hwang, J. J. Song, and B. Goldenbergm Appl. Phys. Lett. **66**, 985 (1995).
24. D. Volm, T. Strebl, B. K. Meyer, T. Detchprohm, H. Amano, and I Akasaki, Sol. St. Comm. **96** (2), 53 (1995).
25. S. Fischer, C. Wetzel, E. E. Haller, and B. K. Meyer, Appl. Phys. Lett. 67 (9), 1289 (1995).
26. C. R. Abernathy, J. D. MacKenzie, S. J. Pearton, and W. S. Hobson, Appl. Phys. Lett. **66** (15), 1969 (1995).
27. R. Dingle and M. Ilegems, Solid State Commun. **9**, 175 (1971).
28. E. R. Glaser, T. A. Kennedy, S. W. Brown, J. A. Freitas, Jr., W. G. Perry, M. D. Bremser, T. W. Weeks, and R. F. Davis, to be published.
29. P. Boguslawski, E. L. Briggs, and J. Bernholc, Phys. Rev B. **51** (17), 255 (1995).
30. J. Neugebauer and C. G. Vad de Walle, Phys. Rev. B **50**, 8067 (1994).
31. J. I. Pankove, *Optical Processes in Semiconductors*, Dover, New York (1971).
32. R. F. Davis, M. D. Bremser, K. Gruss, K. Linthicum, B. Perry. and T. W. Weeks, Jr., Semiannual Technical Report for ONR Grant #N00014-92-J-1720, December 1994.
33. A. Ishibashi, H. Takeishi, M. Mannoh, Y. Yabuuchi, and Y. Ban, to be published.
34. B. N. Sverdlov, G. A. Martin, H. Morkoc and D. J. Smith. Appl. Phys. Lett. **67** (14), 2063 (1995).
35. W. E. Carlos, J. A. Freitas, Jr., M. A. Khan, D. T. Olson, and J. N. Kuznia, Phys. Rev. B. **48** (24), 17878 (1993).

XIV. Measurement of the Electron Flux from Diamond and III-V Nitride Surfaces

A. Introduction

The search for cold cathode devices has received much attention recently. To find a device that can emit electrons with the application of just a few volts is a goal for both research and industry. In the past, there have been several potential solutions for electron emission. One advanced method uses high electric fields produced by metal tips to cause electrons to tunnel into vacuum. However, these cathodes are unstable at high current densities. Another method uses conventional semiconductors such as Si or GaAs covered with a layer of Cs. Due to band bending, the conduction band of the material lies below the vacuum energy level. When a bias is applied, high current densities of greater than 1500 A/cm^2 can be measured. The disadvantage of such a device is that it is easily contaminated after exposure to O_2. A third method would be to use wide-bandgap materials such as AlN or diamond which can have their conduction band close to the vacuum energy level even in the presence of O_2 or H_2O. These materials can be doped or grown in different ways to make them acceptable electron emitters [1]. Whatever the method employed, a testing station is needed to characterize the electron emission.

An example of a device pursued by M. Geis *et al.* [2] using diamond is shown in Fig. 1. The diodes are fabricated by carbon ion implantation into p-type diamond and covered with one micron of aluminum. The diode current ID was varied from 0.1 mA to 10 mA with a bias voltage VD of -60 to -150 V. The voltage between the anode and the p-type diamond substrate was usually 100V, and the anode current IA varied from 1e-13A to 5e-7A.

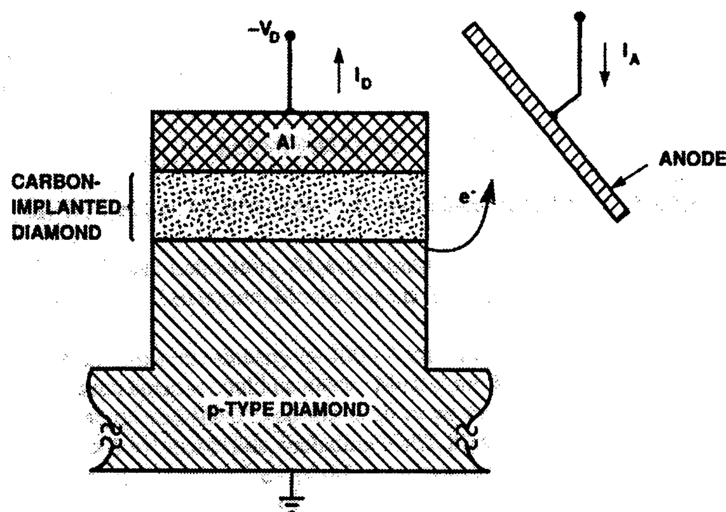

Figure 1. A typical diamond cold cathode built by M. Geis *et al.*

B. Experimental Procedure

The layout of the High Vacuum I-V / Optics Station is shown in Fig. 2. The chamber, pumps, data acquisition, and source-measure components have been obtained and assembled. The vacuum chamber will be used for carrying out the measurements described below. With the existing pumps on the system, a pressure of 5×10^{-8} Torr can be obtained.

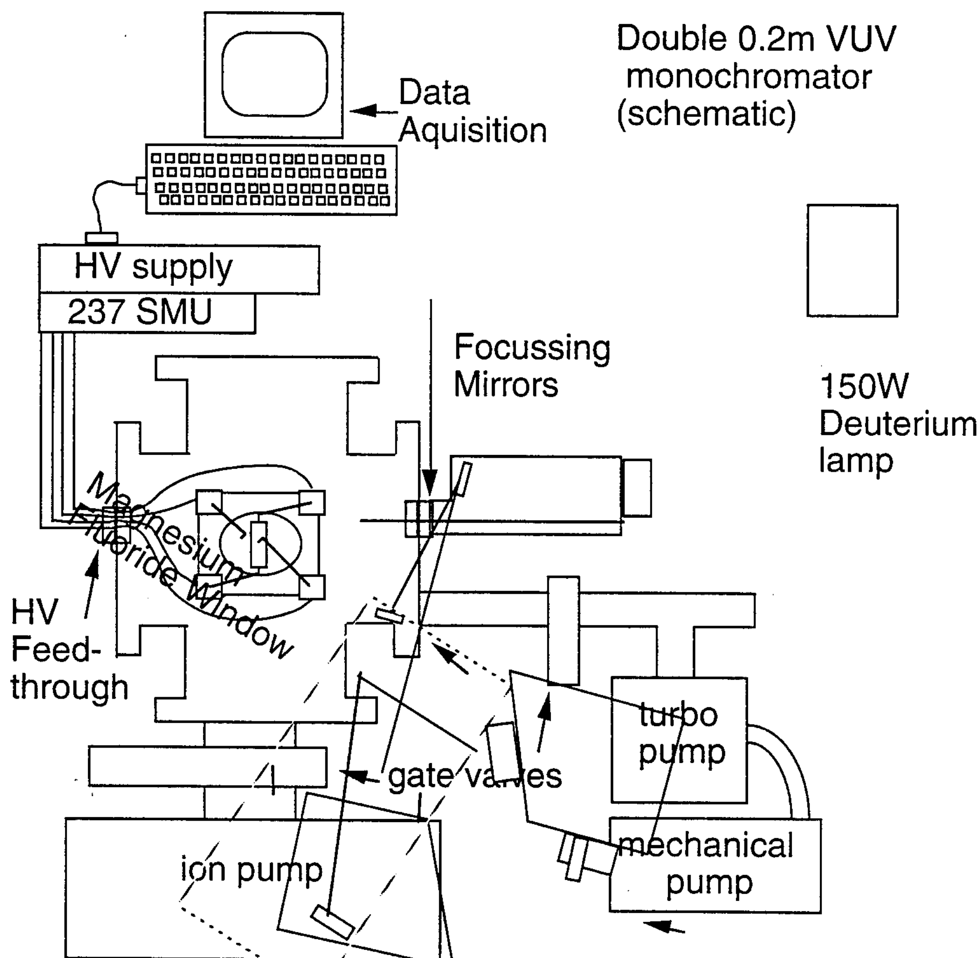

Figure 2. High Vacuum I-V / Optics Station

The first of the measurements attempted is a simple two-pole DC measurement as shown in Fig. 3. A collector is used to draw the electrons out of the sample. The collector consists of a 2 mm diameter platinum wire imbedded in a Teflon block. The voltage between the collector and the sample can be varied between -1100 Volts and +1100 Volts using a Keithley 237 Source Measure Unit. The distance between the collector and the sample can be adjusted from outside of the vacuum chamber with an ultra-high vacuum stepper motor. With this motor, the collector distance was controlled such that one step yielded a translation of 0.44 µm. The

current-voltage (I-V) measurements were taken at several distances. The relative travel of the collector was determined by the number of steps and the step size established by the translation stage. I-V curves were measured at intervals as the collector approached the sample and the absolute distance was calculated when the probe tip touched the sample. Using this procedure, the measurements were made before the collector tip touched the sample. The sample area probed is approximately 2-3 mm in diameter. While the field emission properties of the samples may not be uniform, this non-uniformity is expected to be on a microscopic scale so that the probe area averages over the variation in emission sites.

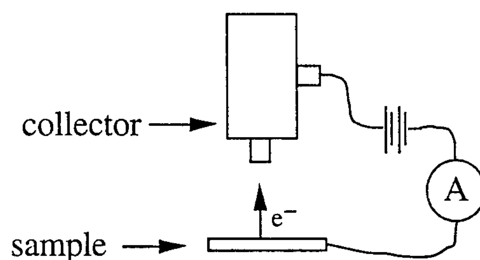

Figure 3. A two-pole DC measurement with a platinum wire imbedded in a Teflon block as a collector. The diameter of the platinum wire is 2.0mm.

The second DC measurement to be carried out will be a three-pole measurement as shown in Fig. 4. The collector will be attached to a micrometer or a piezo-electric positioner. Electrons are emitted from the surface by applying a voltage across the sample. The current between the sample and the collector will be measured as a function of sample bias.

The third DC measurement will be a four-pole measurement where the set-up would be the same as that for the three-pole measurement with a gate included for amplification of the current. Current-voltage readings between the collector and the sample can be taken as a function of gate bias.

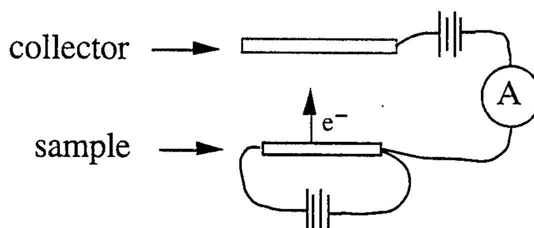

Figure 4. A three-pole DC measurement using a micrometer or piezo-electric positioner as a collector.

A fourth type of measurement is a quantum efficiency measurement. Quantum efficiency is defined as the ratio of the number of electrons emitted from a sample per photon incident on that sample. The photo-excitation of the sample will be carried out with a monochromatic light source. The wavelength range that can be covered with a high vacuum monochromator would be from 120nm to 400nm using a 150 W Deuterium light source. The bandgaps of both diamond and AlN fall well within this range. Operating in this wavelength range would give an understanding of any defect level that may be present in the bandgap of the material. If electrons are emitted from the sample, they can be collected with a grid as shown in Fig. 5.

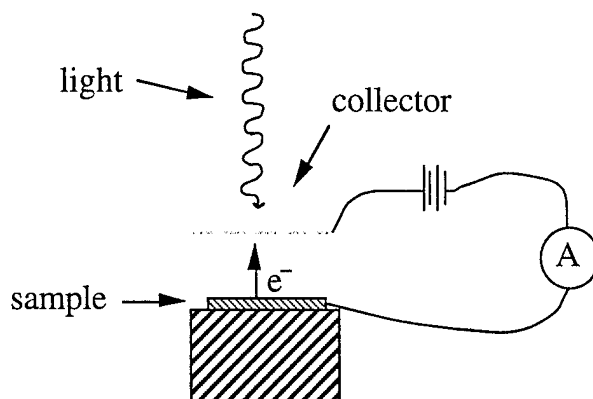

Figure 5. Photo-excitation of the sample with monochromatic light.

C. Results

Field emission I-V curves were measured for gold, diamond and AlN. The curves are shown in Fig. 6. The threshold voltage for a current of 1×10^{-9} Amps and the collector distance are shown in Table I for each of the three samples. With this information, a value of the threshold field can be calculated from dividing the threshold voltage by the collector distance. Information about the samples studied can be found in Table II.

Table I. Threshold Field for Gold, Diamond and AlN

	Voltage for 1 nA	Anode Distance	Field at 1 nA
Gold	570 V	6.5±1.5 μm	88 V/μm
Diamond	190 V	6.2±0.9 μm	31 V/μm
AlN	230 V	7.5±1.3 μm	31 V/μm

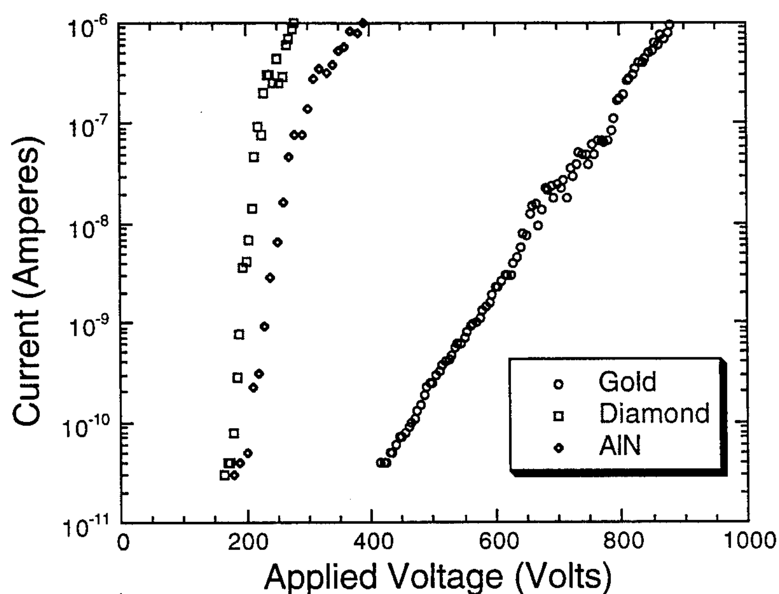

Figure 6. Field Emission from gold, diamond and AlN.

Table II. Sample Preparation

	Substrate	Deposition Temperature	Doping	Thickness
Gold	Silicon	Sputtered	-	100 Å
Diamond	Intrinsic Silicon		1e+19 cm^{-3}	50 μm
AlN	n-type 6H-SiC (0001)	1050 °C	none	150 Å

D. Discussion and Conclusion

As can be seen from Fig. 6 and Table I, the emission properties of the diamond and AlN samples are dramatically different from that of the gold sample. The difference can be attributed in part by field penetration into the dielectric [3]. Another reason could be field enhancement due to the surface morphology. This difference is worth further study.

The reason for the quantum efficiency measurement, other than applying a merit value to the device in question, would be to study any competing mechanisms which could inhibit electron emission. A quantum efficiency number would indicate just how much these mechanisms inhibit electron emission.

Two competing mechanisms are shown in Fig. 7. After an electron is excited into the conduction band from the valence band, one of three events can happen. One, if there is a defect level in the lattice, the electron can be captured at an empty center. If the defect level

captures a hole from the valence band also, then an indirect transition has occurred. Two, the electron has a certain probability of decaying to the valence band instead of being emitted. The electron has made a direct transition in this case. Three, if neither of the previous events occur, then the electron has a probability of being emitted. These two competing mechanisms, indirect transition through a defect level or direct transition to the valence band can inhibit electron emission and cause the device quality to be poor.

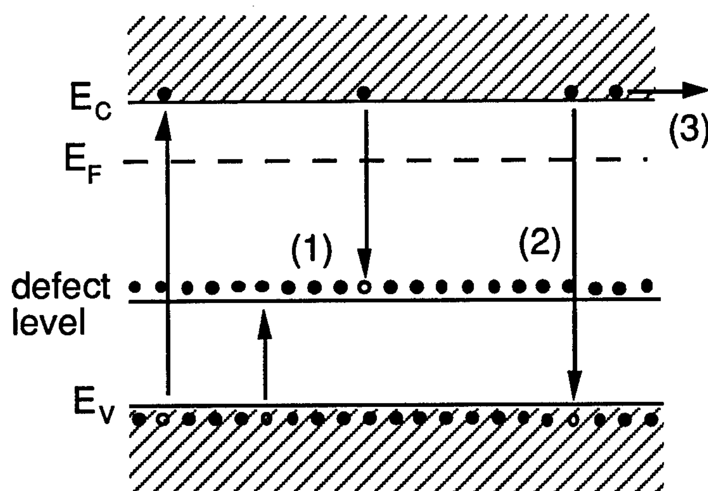

Figure 7. Two competing mechanisms: (1) indirect transition and (2) direct transition. If neither of these events occur then (3) the electron can be emitted.

In conclusion, DC measurements and photo-excitation measurements can give us an understanding of how to design a cold cathode device. Each device that is fabricated can be characterized in vacuum using these methods.

E. Future Plans and Goals

Future work will involve the implementation of the electron emission characteristics described in this report for various diamond and nitride film structures with different surface preparations.

F. References

1. M. W. Geis, N. N. Efremow, J. D. Woodhouse, M. D. McAleese, M. Marchywka, D. G. Socker and J. F. Hochedez, IEEE Electron Device Letters **12**, 456 (1991).
2. M. W. Geis, N. N. Efremow, J. D. Woodhouse and M. D. McAleese, "Diamond Cold Cathodes," in *Proceedings of the First International Conference on the Applications of Diamond Films and Related Materials,* Y. Tzeng, M. Yoshikawa, M. Murakawa and A. Feldman, Ed., Elsevier Science Publishers, 1991, pp 309-310.
3. R. V. Latham, Vacuum **32**, 137 (1981).

XV. (Negative) Electron Affinity of AlN and AlGaN Alloys

R. J. Nemanich, M. C. Benjamin, S. P. Bozeman, M. D. Bremser, S. W. King, B. L. Ward, R. F. Davis, B. Chen, Z. Zhang, and J. Bernholc

Department of Physics and Department of Materials Science and Engineering, North Carolina State University, Raleigh, NC 27695-8202

The electron affinity of a semiconductor defines the relationship of the vacuum level and the semiconductor band structure. It is dependent on the atomic orbitals of the material and the surface termination. We report experimental and theoretical results that support the presence of a negative electron affinity on AlN and the Al rich AlGaN alloys. The GaN surface is found to exhibit a (positive) electron affinity of 3.3eV. The experimental measurements employ UV-photoemission spectroscopy on *in situ* gas-source MBE samples and on CVD samples. Theoretical results indicate that the (negative) electron affinity of AlN depends sensitively on the surface reconstruction and adatom termination. The experimental dependence of the electron affinity on alloy concentration is presented. The results indicate that AlGaN alloys with band gap similar or greater than that of diamond will exhibit a negative electron affinity. Field emission results are reported, and the characteristics are similar to those obtained from a diamond film. Issues related to cold cathode electronic devices based on NEA surfaces are noted.

To be published in the Proceedings of the MRS Symposium AAA-Fall '95.

Introduction

Wide bandgap semiconductors have the potential of exhibiting a negative electron affinity (NEA). These materials could be key elements of cold cathode electron emitters which could be used in applications that include flat panel displays, high frequency amplifiers, and vacuum microelectronics. The surface conditions have been shown to be of critical importance in obtaining a negative electron affinity on diamond surfaces [1–4]. In this paper, angle resolved UV-photoemission spectroscopy (ARUPS) is used to explore this effect on AlN [5], GaN and AlGaN alloy surfaces. The value of UV photoemission in characterizing electron emission is that the technique emphasizes effects of the emission process. To fully characterize electron emission properties it is necessary to also employ additional measurements such as field emission, and secondary electron emission. The measurements are interpreted with the help of theoretical calculations. Measurements of field emission from AlN on 6H-SiC are presented to demonstrate the device potential of the materials.

The electron affinity of a semiconductor is defined as the energy required to remove an electron from the conduction band minimum to a distance macroscopically far from the semiconductor (i.e. away from image charge effects.). At the surface this energy can be shown schematically as the difference between the vacuum level and the conduction band minimum. The electron affinity is not, in general, dependent on the Fermi level of the semiconductor. Thus, while doping can change the Fermi level in the semiconductor and the work function will change accordingly, the electron affinity is unaffected by these changes. An alternative view is that the electron affinity is a measure of the heterojunction band offset between the vacuum and a semiconductor of interest. For most semiconductors, the conduction band minimum is below the vacuum level and electrons in the conduction band are bound to the semiconductor by an energy equal to the electron affinity. In some cases, surface conditions can be obtained in which the conduction band minimum is above the vacuum level. In that case, the first conduction electron would not be bound to the sample but could escape with a kinetic energy equal to the difference in energy of the conduction band minimum and the vacuum level. This situation is termed a negative electron affinity. (Note that the electron is still bound to the vicinity of the sample by coulomb forces.)

The electron affinity or work function of a material is usually ascribed to two aspects of the material: (1) the origin of the atomic levels, and (2) the surface dipole due to the surface termination [6]. These effects are shown schematically in Fig. 1. The atomic levels are more or less intrinsic to a material and cannot be changed. This is not the case for the surface dipole. The surface dipole can be substantially affected by surface reconstructions and surface adsorbates. Recent results on diamond have indicated a positive electron affinity of ~0.5eV for clean or oxygen terminated surfaces and a NEA of approximately 1.5eV for hydrogen terminated surfaces [7,8]. These changes are directly attributed to changes of the surface

dipole. Because of the large effect of the surface dipole, it is essentially impossible to determine if a material is "intrinsically NEA." Thus the surface termination is critical in describing the electron affinity (or NEA) properties of a material.

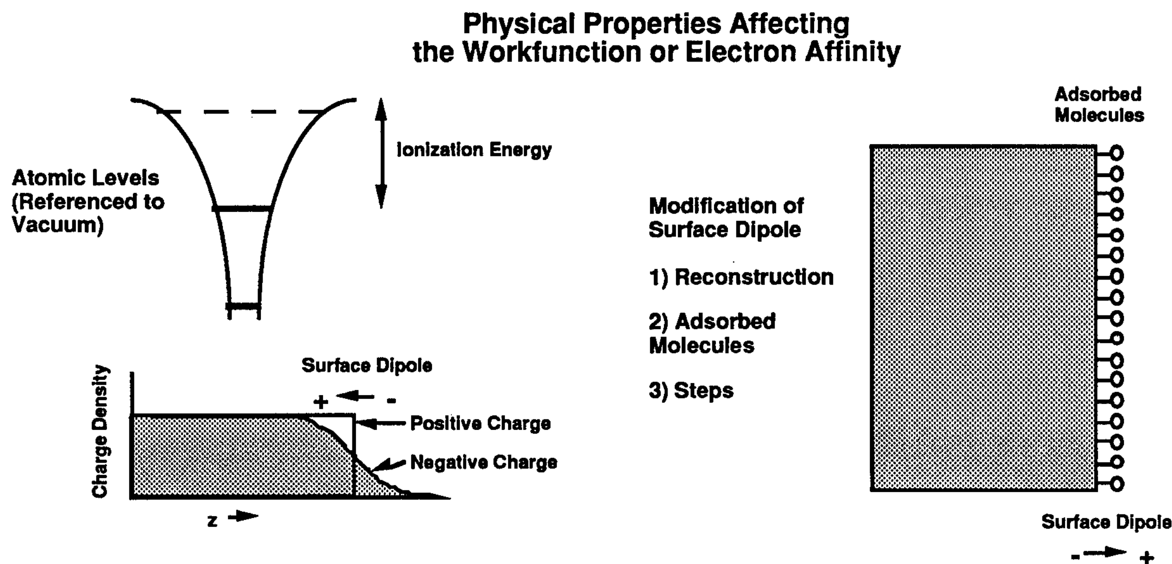

Figure 1. A representation of the effects which contribute to the work function (or electron affinity) of any material. While the atomic levels are an intrinsic property of the material, changes in the surface bonding can substantially affect the work function or electron affinity.

One method to explore aspects of the electron affinity of a semiconductor is UV-photoemission [1,2]. For a material with a positive electron affinity the value can be directly deduced from the measurements (see below). Furthermore, the UV-photoemission can be used to indicate the presence of a NEA. The changes in the spectra due to a NEA are indicated in Fig. 2 [3]. The electrons from the valence band are excited into the conduction band. In transiting towards the surface, electron scattering occurs and a large number of secondary electrons accumulate at the conduction band minimum. For materials with a positive electron affinity these electrons cannot escape, while for a NEA the electrons can be emitted directly and will be observed with a low kinetic energy. Thus the two effects which signify a NEA are an extension of the spectral range to lower energy and the appearance of a sharp peak at low kinetic energy. This feature will appear at the largest (negative) binding energy in typical presentations of UPS spectra.

In addition to the sharp feature that is often evident in the spectra of a NEA semiconductor, the width of the photoemission spectrum (W) can be related to the electron affinity (χ). The

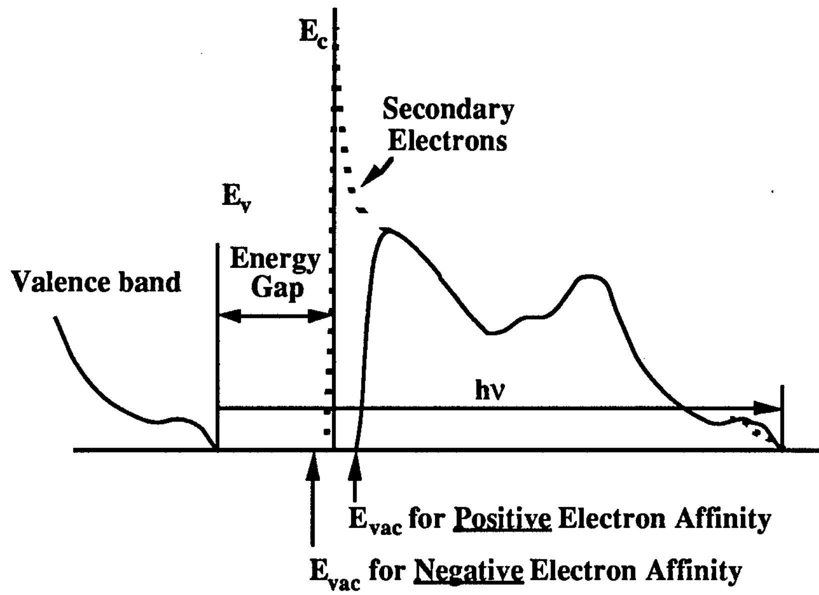

Figure 2. A schematic of how NEA affects the photoemission spectra. For a NEA surface the spectrum is broadened to lower kinetic energy, and a peak due to quasi thermalized electrons is detected at the lowest kinetic energy (highest negative binding energy).

spectral width is obtained from a linear extrapolation of the emission onset edge to zero intensity at both the low kinetic energy cutoff and at the high kinetic energy end (reflecting the valence band maximum). From Fig. 2, it is evident that we can write the following relations:

$\chi = h\nu - E_g - W$ for a positive electron affinity, and

$0 = h\nu - E_g - W$ for a negative electron affinity

where E_g is the bandgap and hν is the excitation energy. We stress that the photoemission measurements cannot be used to determine the energy position of the electron affinity for the NEA surface. Careful measurements of the width of the spectra are helpful in distinguishing whether the effect is direct emission of the electrons from conduction band states or whether excitons are involved in the emission process. The effects of excitons have recently been reported by Bandis and Pate [9].

In addition to measurement of the electron affinity, UV photoemission can be used to determine the position of the surface Fermi level. The Fermi level of the sample will be the same as that of the metal sample holder, and the Fermi level of the metal can easily be determined. The energy difference of the valence band maximum and the metal Fermi level then gives the position of the surface Fermi level of the semiconductor. The position of the surface Fermi level will be critical in determining the band bending near the surface.

Theoretical Results

Previous theoretical studies of the electron affinity of wide bandgap semiconductors have focused on non-polar surfaces, namely diamond [7,8,10]. The study of polar surfaces is substantially more complicated, and special techniques were developed to deal with charge transfer effects inherent at such surfaces.

The theoretical technique is based on ab initio molecular dynamics (Car-Parrinello method [11]). A plane wave basis was employed, and soft core, norm conserving pseudopotentials were used to describe the ions. The supercells consisted of 10-12 layers of AlN with 4-16 atoms in each layer. For most calculations, a 12Å vacuum region separated the surfaces. One side of each slab was terminated by hydrogen atoms to reduce charge transfer caused by the finite width of the slab.

A surface created by truncating the bulk always has dangling bonds. To achieve a more stable state, the partially filled dangling bonds must be eliminated - a process which involves the formation of new bonds that inevitably increases the strain between the surface and the subsurface layers. The balance between the lowering of the energy due to the elimination of the dangling bonds and the induced strain determines the nature of the surface reconstruction. In the calculations, reconstruction patterns were chosen based on either experimental observations or physical intuition. In the case of a polar surface, the difference of the work functions between two different sides of the slab causes a non-physical dipole field in the ideal bulk-cleaved slab. The work functions of two different sides of the slab are not independent. This problem is aggravated when dealing with a polar surface, since the electrons will move to the side which has the higher work function in order to lower the total energy. In a real physical system, the effect of the surface from one side is screened within the distance of a few lattice constants. This is not true in a thin slab which is only 10-12 layers thick. To reduce this "screening" problem in these calculations, one side of the slab was terminated with hydrogen atoms. The charge transfer caused by the infinite slab width was then reduced to less than 0.02 electrons per surface atom. The other problem is the periodic boundary conditions that result in a slope of the electrostatic potential in the vacuum region when the slab consists of two non-equivalent surfaces. To solve this problem, we employed a compensating field deep inside of the vacuum region, which cancels out the effect caused by the periodic boundary conditions. The details of this technique will be discussed elsewhere [12].

The electron affinity of a semiconductor can be related to the bulk average potential through the following:

$$\chi = D - (E_c - V_{bulk})$$

where D is defined as the surface dipole potential that determines the relative energies of the bulk electron states and the vacuum level and $(E_c - V_{bulk})$ is the position of the conduction band

minimum relative to the bulk-averaged electrostatic potential. The surface dipole potential was obtained in these calculations from the difference of the electrostatic potential across the surface. The electron affinities of different surface configurations of AlN are listed in Table I, where prior results for diamond (111) surface are also listed.

Table I. The Calculated Results of Electron Affinities [in eV] for Different Surface Configurations

Surface Species	Bare Surface	H-terminated (1×1)	Vacancy (2×2)
Diamond (111)	positive	-1.5	N.A.
Al - AlN	+0.85	+1.60	-0.70
N - AlN	+0.30	+0.05	+1.40

The results exhibit trends for changes between clean and chemisorbed surfaces. Once chemisorption occurs, the adsorbates saturate the dangling bonds by bonding with the surface atoms. The bonding causes a charge transfer between the adsorbates and the surface atoms, and an additional dipole field occurs. The strength and direction of the additional dipole field determines the change of the electron affinity.

In general the electronegativity can be used as a good indicator of the sign of the surface dipole. For an adsorbate with a lower electronegativity than the surface atoms, when the adsorbate atoms attach to the surface atoms, the bond charge will tend to get closer to the surface atom, which results in an additional dipole field pointing outwards with respect to the surface. This field will reduce the surface barrier or lower the electron affinity of a semiconductor. An opposite charge transfer would result in an additional dipole directed towards the surface, which would increase the electron affinity.

In AlN, Al has a lower electronegativity than H, while the opposite is true for N. Thus hydrogen adsorbed on the Al-terminated surface is expected to result in an increased electron affinity, and this is reflected in the full calculations. Moreover, from their electronegativities, it is expected that both Al- and N-terminated AlN surfaces with chemisorbed Li or Be should exhibit reduced or negative electron affinities.

Experimental Procedure

The experiments described in this summary paper were carried out in an integrated UHV system with surface preparation, film growth and surface characterization capabilities. The system consists of eight chambers interconnected by a linear sample transfer mechanism. The

overall length of the sample transfer chamber is ~35ft. A portion of the system is shown schematically in Fig. 3. This figure shows the positions of the UV photoemission system, the plasma surface processing system, the LEED/Auger systems, and the MBE chamber. In the experiments described here, the UV-photoemission measurements were made with HeI (21.21eV) radiation and the electrons were analyzed with a VSW HAC50 50mm mean radius hemispherical electron analyzer. The spectra were collected at normal emission with a collection angle of ~2°. The sample was biased with ~1 to 3V so that the low energy electrons can overcome the work function of the analyzer. While higher sample bias can be employed, the low bias used here is to minimize spectral distortions that occur due to changes in the effective collection angle for the higher sample bias.

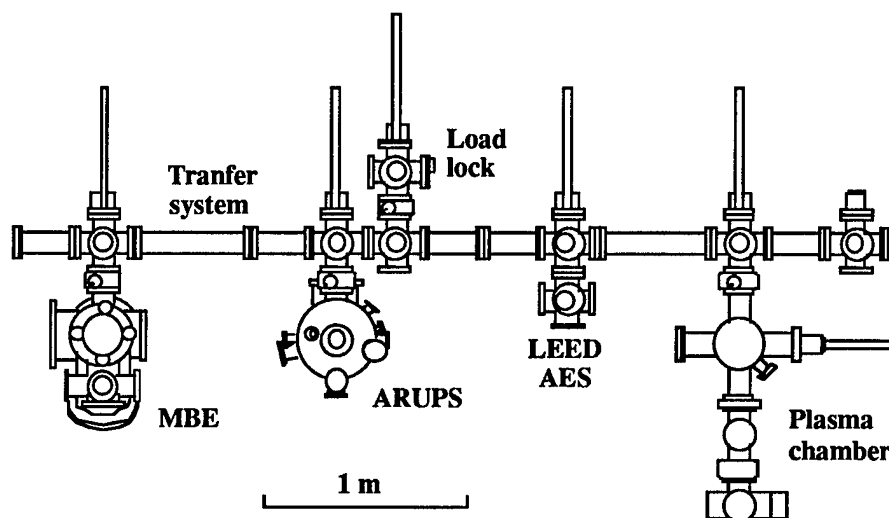

Figure 3. A schematic of a portion of the integrated surface processing and characterization system used in the studies described here.

To avoid charging and to obtain high quality epitaxy, the AlGaN films were grown on (0001) 6H-SiC substrates. The substrates were supplied by Cree Research, Inc. [1]. The SiC wafers were n-type with doping concentrations of 10^{16} to $10^{18}/cm^3$. The AlGaN alloy samples were grown by CVD (OMVPE) in a remote location and transported in ambient to the analysis system. Clean, as-grown surfaces of AlN and GaN were prepared in the integrated UHV transfer system (described above) by gas source molecular beam epitaxy (GSMBE), and transferred directly to the UPS system. The Al concentration of the alloy samples was estimated from respective cathodoluminescence measurements.

Field emission measurements were obtained within a separate high vacuum chamber (pressure < 10^{-5} Torr). During the experiment, samples were placed beneath a 2 mm diameter

movable platinum anode with a flat tip. The anode was controlled by a stepper motor such that one step yielded a translation of 0.44 μm. The current-voltage (I-V) measurements were taken at several distances ranging from 2 to 20 μm and for bias voltages in the range of 0 to 1100 volts. The relative travel of the probe was determined by the number of steps and the step size established by the translation stage. The I-V curves were measured at intervals as the probe approached the sample and the absolute distance was calculated when the probe tip touched the sample. Using this procedure, the measurements were made before the probe tip touched the sample. In both the field emission and UV-photoemission, the techniques probed a similar sample area of 2-3 mm in diameter. While the field emission properties of the samples may not be uniform, this nonuniformity is expected to be on a microscopic scale so that the probe area averages over the variation in emission sites.

UV-Photoemission Results

The UV photoemission spectra of AlN, GaN and the two alloy samples are shown in Fig. 4 [20,21]. Samples were biased with 2-3 V to overcome the work function of the analyzer, and all spectra were shifted to be aligned at the valence band maximum. The spectra were scaled such that the strongest emission was the same for all curves.

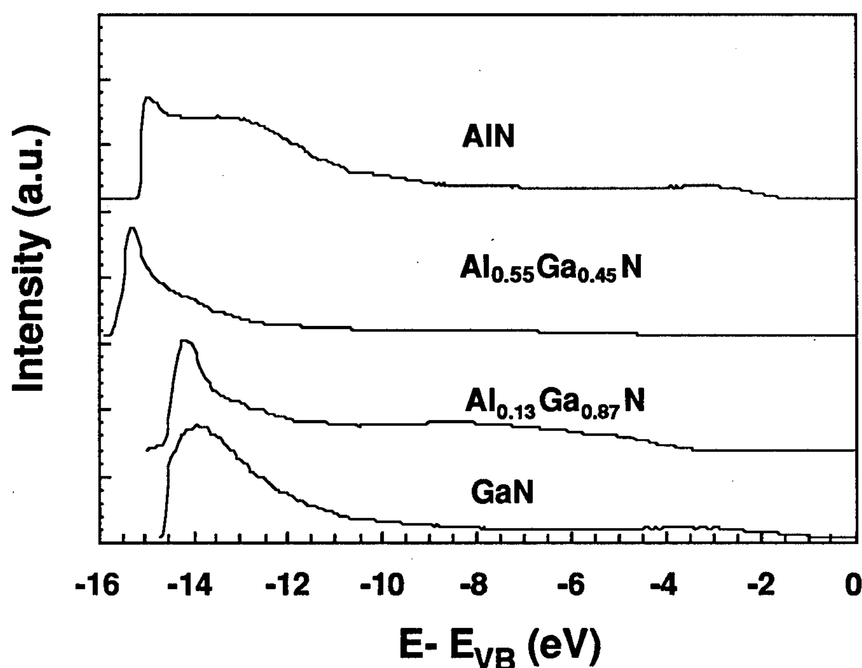

Figure 4. The UV photoemission spectra of $Al_xGa_{1-x}N$ films grown on 6H-SiC. The spectra were excited with 21.21eV HeI radiation. Samples were biased at -3V such that the low energy electrons could overcome the work function of the analyzer. All spectra are aligned at the valence band maximum, and the energy scale references this energy as 0.

The first aspect to be noted is that the spectra of the Al rich alloy and AlN exhibit sharp strong features at the largest (negative) binding energy, which corresponds to the lowest kinetic energy. These features are often indicative of a negative electron affinity. As noted in the introduction, the feature is attributed to emission from electrons quasi-thermalized to the conduction band minimum. The emission from the $Al_{0.13}Ga_{0.87}N$ sample is significantly weaker, and the GaN emission does not show the sharp peak at all.

A second indication of the change in electron affinity with alloy concentration is the extension of the $Al_xGa_{1-x}N$ spectra to lower energy as x is decreased. A more precise description of the relation of the NEA is obtained from the spectral width. To determine the energy position of the valence band maximum, each spectrum was magnified, and the intensity was extrapolated to 0 emission. The spectral widths obtained from the $Al_xGa_{1-x}N$ samples were 14.5, 14.5, 15.5, and 15 eV for x=0, 0.13, 0.55, and 1.0, respectively. To apply the relations noted above, the bandgap of each sample must also be known. The reported values of the AlN and GaN bandgaps are 6.2 and 3.4 eV, respectively. The band gap of the alloy samples was determined from the respective cathodoluminescence measurement. Using the relations described above, the AlN satisfies the relations for a NEA, while the $Al_{0.55}Ga_{0.25}N$ surface exhibits a low but positive electron affinity. The GaN and $Al_{0.13}Ga_{0.87}N$ surfaces, do not satisfy the relations for a NEA. We can, however, determine the value of the electron affinity of these materials and find that $\chi = 3.3$ eV and 2.9 eV for x = 0 and 0.13, respectively.

Another aspect that is evident from the photoemission spectra is the position of the surface Fermi level relative to the valence band maximum. It was found that E_F ranges from 2 to 3.5 eV above the valence band maximum for each sample. For the GaN and $Al_{0.13}Ga_{0.87}N$ surfaces, these values position E_F in the upper part of the gap while for the Al rich samples, the values indicate that the surface Fermi level is pinned near midgap. The surface Fermi level position and the bandgap of the alloys are indicated in Fig. 5. The pinning at midgap may be an indication of surface states or increased impurity incorporation. In particular, the strong affinity of Al with oxygen may result in increased oxygen incorporation at the surface or in the bulk of these films.

The deduced electron affinities versus alloy concentration are shown in Fig. 5. Again we note that the photoemission measurements cannot be used to determine the position of the vacuum level for a NEA surface. Therefore, the electron affinity of the AlN is indicated at $\chi = 0$ with an arrow to larger negative values. The results suggest that the electron affinity depends on the alloy concentration. It should be noted that we have made no effort to control the surface termination for these samples. Previous results for diamond indicate that the observation of a NEA may be critically dependent on the surface termination. This may not be the case with the nitrides. Future studies should explore whether the electron affinity of AlGaN materials is also affected by different surface preparations.

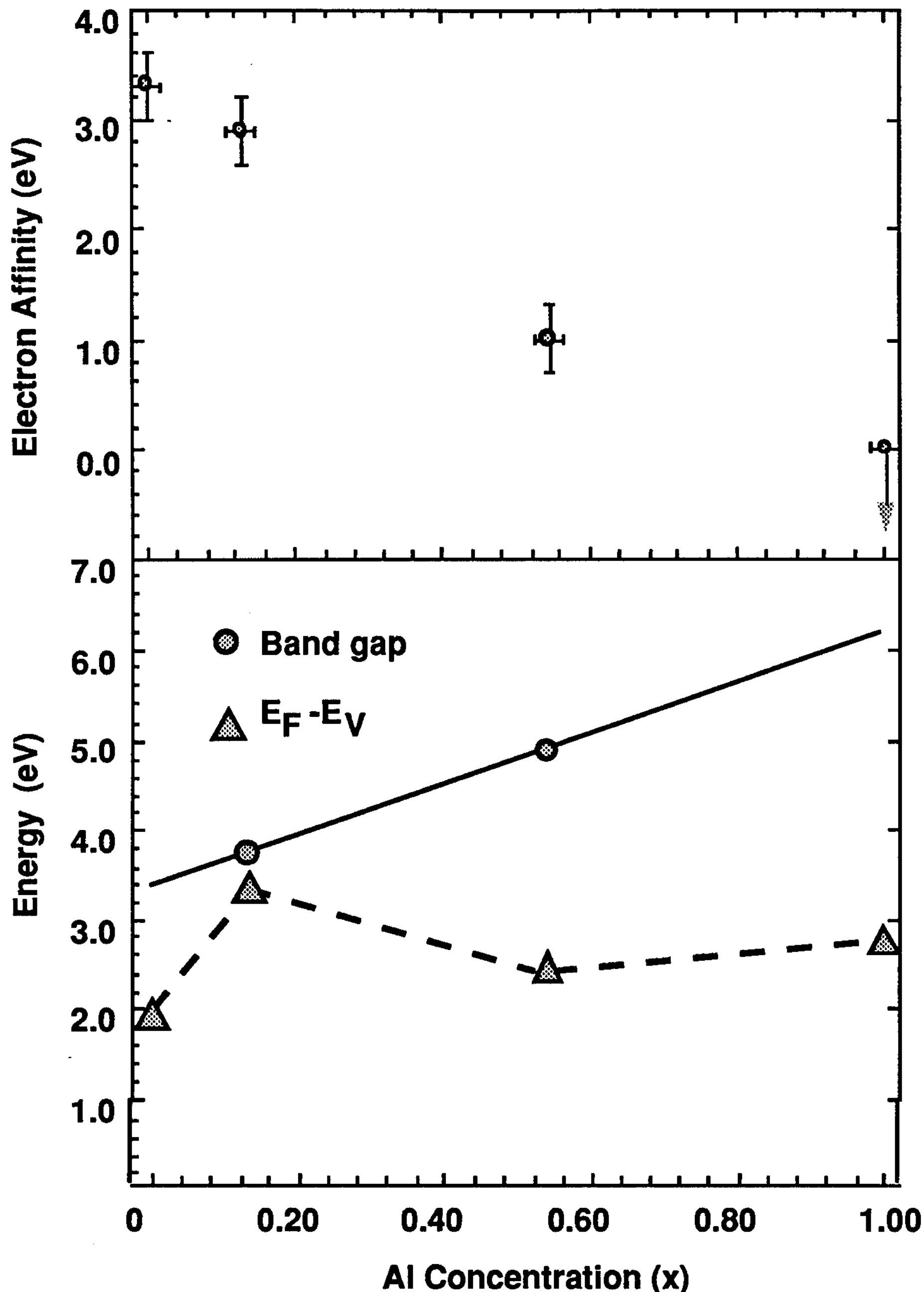

Figure 5. The dependence of the electron affinity (upper panel), bandgap (filled circles) and surface Fermi level position (triangles) for the AlGaN alloys. The electron affinity and surface Fermi level are obtained from the UPS spectra of Fig. 4.

Electron Emission from a Negative Electron Affinity Surface

The major device related goal of these studies is the development of a cold cathode electron emitter. Three steps can be considered in understanding the emission process: (1) electron supply to the semiconductor, (2) transport from the supply electrode to the surface, and (3) the emission into vacuum. The photoemission and theoretical sections above have focused mostly on the last of these processes. In contrast, field emission involves all three processes.

The field emission I/V curves for a thin (10nm) AlN sample is compared to that of p-type diamond and a sputtered gold film in Fig. 6. All measurements were obtained at similar distances so that the electric field dependence near the surface is essentially the same for all three samples. The diamond sample was a 50μm thick p-type film deposited on Si and polished such that the RMS roughness from AFM measurements was ~1nm. While we did not measure the flatness of the AlN and the Au films, we expect a similar surface roughness. Compared to the emission from gold, the AlN and diamond show a significant reduction in the field to obtain similar electron emission currents. It is interesting to note that both semiconductors exhibited emission currents of 1nA at a field of 31V/μm.

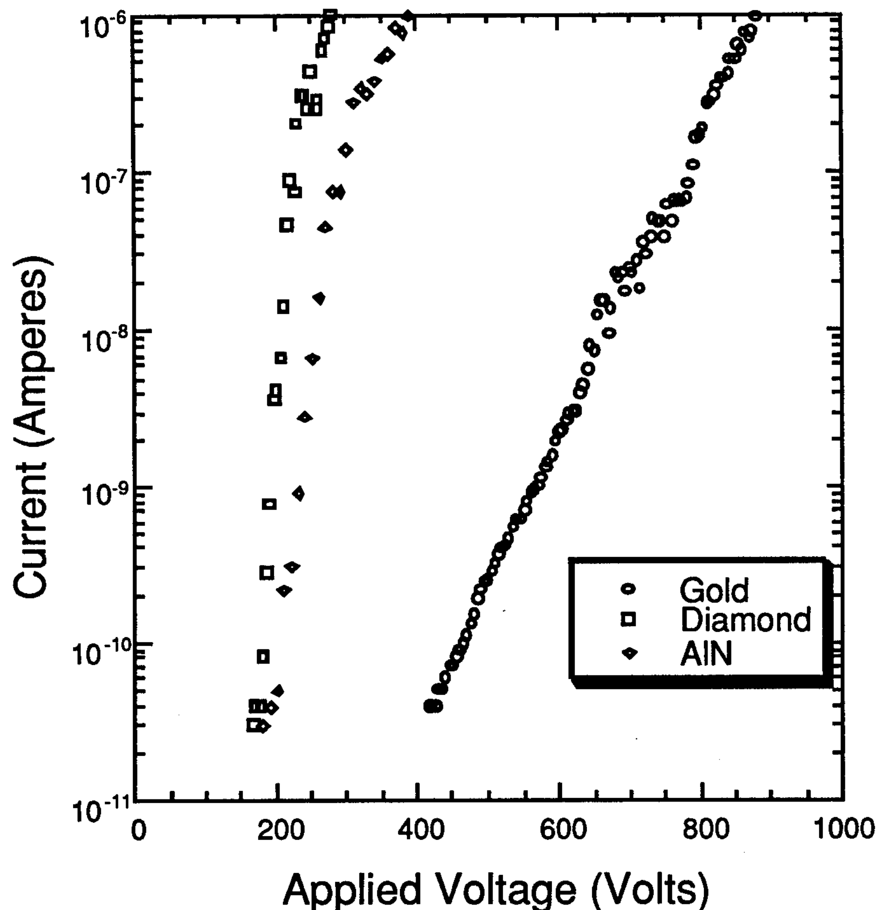

Figure 6. The field emission I-V measurements obtained from AlN (10nm) on 6H-SiC compared to that from a polished p-type diamond film (50μm) and a sputtered gold film. The (Pt) anode to film surface distance of the AlN, diamond and Au measurements were 7.2±1.3, 6.2±0.9, and 6.5±1.5 μm respectively.

All three samples exhibit Fowler Nordheim type dependence in the I-V measurements. The F-N plots for the samples are shown in Fig. 7. The F-N characteristics suggest the presence of a barrier to emission. For metals this is simply the surface barrier due to the work function. There is still considerable discussion on the mechanism of electron emission from p-type

diamond films [13,14,15]. We note that the work function from these films is slightly less than 5eV which is similar to the value for most metals. In contrast, the photoemission results indicate that the Fermi level of the AlN is near the center of the 6.3eV band gap. This would imply a ~3eV work function. The band alignment for the AlN on n-type SiC has previously been discussed[5], and new results are reported in this conference [16]. It was suggested that the AlN-6H-SiC band offset at the conduction band is no larger than 2.7 eV. Thus, it is probable that the F-N field emission characteristics from the AlN is limited by electron injection from the SiC into the AlN.

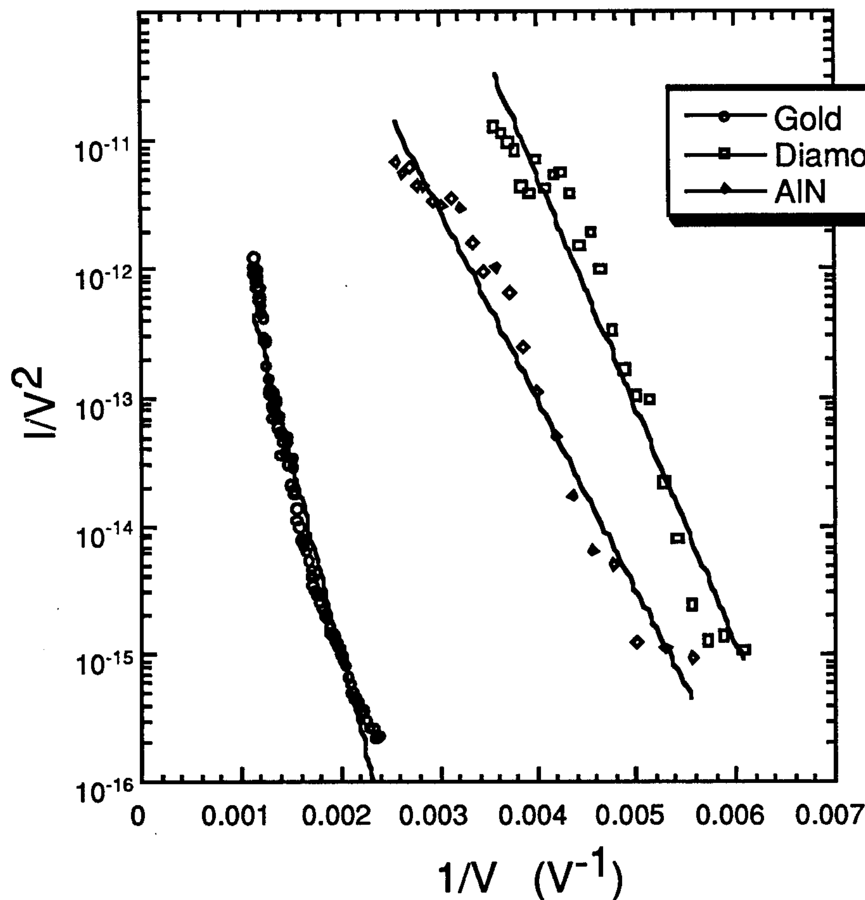

Figure 7. A Fowler-Nordheim plot of the current voltage data shown in Fig. 6. The straight lines show regions in which the emission exhibits F-N characteristics.

There have been many studies of field emission from point emitters (i.e. Spindt tips). The sharp point emitters result in a field enhancement at the tip and a possible reduction in the work function due to the steps on the surface. The I-V characteristics from a field emitter follow the Fowler-Nordheim expression. In contrast, the I-V dependence of an ideal NEA based emitter should exhibit emission at any negative bias. At low fields the current would be limited by the space charge in the vacuum around the emitter (following Child-Langmuir dependence) and at

higher fields the current would be limited by the resistance of the semiconductor and the contact. The energy distribution of the emitted electrons from a NEA cathode should be very narrow (~kT), and the current should exhibit a noise component related to the resistance of the semiconductor and contact. This is in contrast to either thermal emitters (i.e. hot cathodes) or field emitters that exhibit fluctuations based on the statistics of the highest energy part of the electron distribution.

An electron emitter based on a negative electron affinity material would have several unique advantages over pointed field emitters. These would include low turn on voltage, high current density, low sputter erosion, and low noise. In addition, the field emitter requires a significant field established through a potential between the tip and a nearby grid layer. In contrast, a true NEA device would be controlled by a small field established by the grid to modulate the anode to cathode field. Notice that for an ideal NEA structure the grid potential would actually range from 0 to a small negative value. Then, when the grid is at the cathode potential, the potential established at the anode would control the emission. A small negative grid potential would then be used to limit or modulate the electron emission.

Concluding Remarks

The experimental and theoretical results presented here demonstrate that a negative electron affinity surface can be obtained for nitride and other wide bandgap semiconductors. Fig. 8. summarizes the hexagonal lattice constant and bandgap dependence for the nitride and carbon related materials. We also show on this figure the materials that have been shown to exhibit a NEA. In addition to the measurements described here, recent results have demonstrated that BN exhibits a negative electron affinity [17]. It is interesting to note that all materials from this group which have a bandgap larger than that of diamond exhibit an negative electron affinity. The results of the alloy data presented here are also consistent with this value.

For the development of cold cathodes, the electron supply may be as critical as the emission properties. The potential of obtaining n-type nitrides with a NEA offers the real possibility of a high current cold cathode emitter. It is possible that structures based on this material could produce space charge limited currents.

Studies of nitride surfaces are still at a very early stage. While there have been reports of different surface reconstructions, there is still considerable uncertainty as to the stable structure of the surfaces and the dependence on stoichiometry. The theoretical and experimental results presented here suggest further studies of well characterized surfaces.

Acknowledgment

We acknowledge helpful discussions with Peter Baumann. This work was supported in part by the Office of Naval Research.

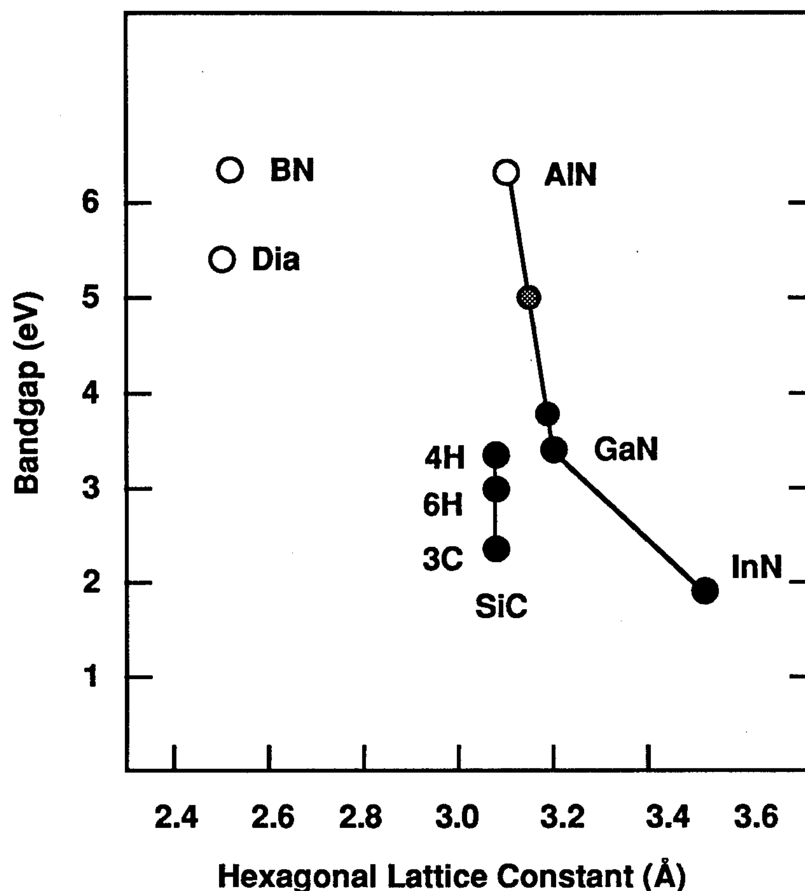

Figure 8. The bandgap vs. hexagonal lattice constant for a group of wide bandgap semiconductors. For the cubic materials, the lattice constant is the unit cell in the (111) plane. The open circles represent materials that have been shown to exhibit a negative electron affinity, while the gray circle represents the low electron affinity GaAlN alloy studied here.

References

1. F. J. Himpsel, J. A. Knapp, J. A. van Vechten, and D. E. Eastman (1979), Phys.Rev. **B20**, 624.
2. B. B. Pate, Surf. Sci. **165**, 83 (1986).
3. J. van der Weide and R. J. Nemanich, Appl. Phys. Lett. **62**, 1878 (1993).
4. P. K. Baumann and R. J. Nemanich, *Proc. of the 5th European Conference on Diamond, Diamond-like and Related Materials*, Eds. P. K. Bachmann, I. M. Buckley-Golder, J. T. Glass, M. Kamo: J. Diamond Rel. Mat., **4** (1995) 802.
5. M. C. Benjamin, C. Wang, R. F. Davis, R. J. Nemanich, Appl. Phys. Lett. **64**, 3288 (1994).
6. A. Zangwill, (1988), *Physics at Surface*, (Cambridge).
7. J. van der Weide, Z. Zhang, P. K. Baumann, M. G. Wensell, J. Bernholc and R. J. Nemanich, Phys. Rev. B **50**, 5803 (1994) .
8. Z. Zhang, M. C. Wensell, and J. Bernholc, Phys. Rev. B **51**, 5291 (1995).
9. C. Bandis and B. B. Pate, Phys. Rev. Lett. **74**, 777 (1995).
10. W. Pickett, Phys. Rev. Lett. **73**, 1664 (1994).
11. R. Car and M. Parrinello, Phys. Rev. Lett. **55**, 2471 (1985).

12. Z. Zhang, B. Chen, and J. Bernholc, to be published.
13. C. Wang, A. Garcia, D. C. Ingram, M. Lake, and M. E. Kordesch, Electron. Lett. **27**, 1459 (1991).
14. N. S. Xu, R. V. Latham and Y. Tzeng, Electron. Lett. **29**, 1596 (1993).
15. Z.- Huang, P. H. Cutler, N. M. Miskovsky and T. E. Sullivan, Appl. Phys. Lett. **65**, 2562 (1994).
16. S. W. King, M. C. Benjamin, R. J. Nemanich, R. F. Davis, W.R.L. Lambrecht, (this volume).
17. M. J. Powers, M. C. Benjamin, L. M. Porter, R. J. Nemanich, R. F. Davis, J. J. Cuomo, G. L. Doll and S. J. Harris, Applied Physics Letters, (in press).

XVI. UV Photoemission Study of Heteroepitaxial AlGaN Films Grown on 6H-SiC

A. Introduction

There is increasing interest in electronic devices composed of III-nitride materials for opto-electronic applications in the blue and UV region [1]. In order to construct viable optical devices, a knowledge of band offsets and electron affinity is needed. An alternative application of these semiconductors is in electron emission devices. Recent studies have demonstrated that diamond surfaces can exhibit a negative electron affinity (NEA). Negative electron affinity surfaces may prove to be critical elements for cold cathode devices, vacuum microelectronics, and photodetectors [2,3]. In addition to diamond, thin films of AlN grown on 6H SiC have been shown to exhibit a NEA and band offsets have been determined [4,5]. The AlN NEA surfaces were obtained from air-exposed surfaces and do not appear to be readily poisoned. In contrast to diamond, AlGaN materials exhibit the wurtzite crystal structure. One of the most significant limitations in the application of diamond is that reliable n-type doping has not been achieved. In contrast, n-type doping has been obtained for GaN and some AlGaN alloys. This study explores further the electron affinity of epitaxial AlGaN films on 6H-SiC.

The wurtzite AlN and GaN form a continuous solid solution of $Al_xGa_{1-x}N$ for $0 \leq x \leq 1$ with bandgaps that range from 3.4 eV (GaN) to 6.2 eV (AlN). Figure 1 displays the bandgap of several materials as a function of the equivalent hexagonal lattice constant. The alloys are also miscible with In, hence the inclusion of InN could extend the range to 1.9 eV. The InGaN alloys will be important in visible light applications. The electron affinity of a semiconductor is related to the surface dipole and to the fundamental energy levels of the materials. Because the valence and conduction bands of the semiconductors have origin in the sp^3 bonding and antibonding levels, it may be suggested that the larger bandgap materials will exhibit a smaller or negative electron affinity. In comparison with diamond, it might be assumed that AlGaN alloys with a bandgap greater than 5.4 eV could exhibit a NEA. Reported here are studies of AlGaN with x values of 0.55 and 0.13 as well as preliminary studies of GaN.

The AlGaN and GaN films used in this study were are grown on vicinal 6H-SiC substrates. The n-type SiC substrates used have a small lattice mismatch with AlN (3.08 Å vs. 3.11 Å) and GaN (a= 3.19Å). The small lattice mismatch enables heteroepitaxial growth of the wurtzite (2H) structure. Furthermore, the fact that the substrates are conducting avoids charging problems associated with photoemission from large bandgap and insulating materials.

The electron affinity of a semiconductor or the presence of a NEA can be determined by ultraviolet photoemission spectroscopy (UPS) [6-8]. The experiments described here involve directing 21.2 eV light (the He I resonance line) to the surface of the sample and detecting the

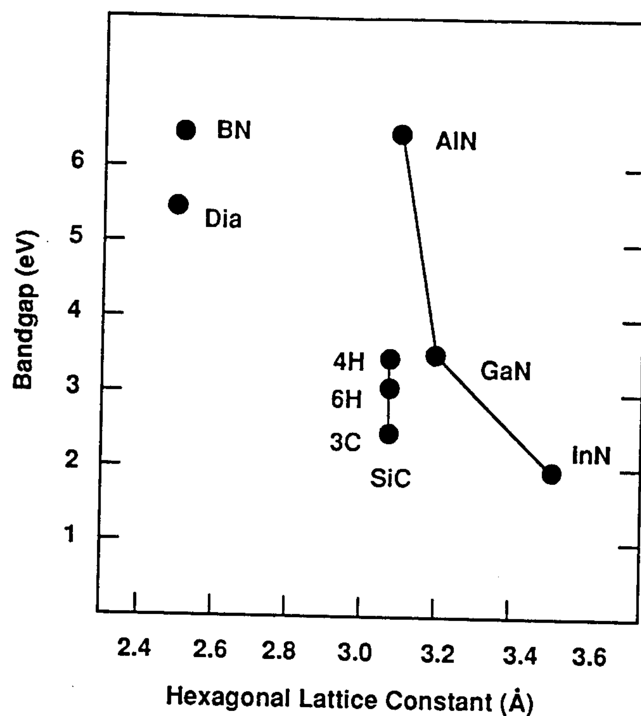

Figure 1. The bandgap vs. hexagonal lattice constant (a) for a variety of wide bandgap semiconductors. The lattice constant for the cubic materials has been determined from the (111) plane.

spectrum of the emitted photo-excited electrons as a function of electron kinetic energy. Typically, UPS is used to obtain a profile of the valence band (VB) electronic states. As such, most studies of UPS of semiconductors present data of the most energetic electrons emitted from the surface. Electrons scattered to lower energy and secondary electrons will be displayed in the spectrum at lower kinetic energies. In addition, for a semiconductor which exhibits a NEA surface, a distinctive peak may be observed at the low kinetic energy (highest binding energy) end of the photoemission spectra. Figure 2 depicts a schematic representation of the photoemission spectra from a semiconductor with a negative or positive electron affinity. The low kinetic energy feature is due to secondary electrons which (quasi) thermalize to the conduction band minimum. Note that the solid line indicates a material with a positive electron affinity while the dashed line is a feature indicative of a NEA. In this paper, samples with both positive and negative affinity surfaces will be discussed.

The sharp features typical of a NEA have been observed from spectra of (111) and (100) diamond surfaces [6-10]. In the studies of diamond, a correlation was made between the presence of hydrogen and the NEA peak [9,10]. In addition, it was also shown that thin metal layers such as Ti or other moderate work function metals could induce a NEA on the diamond surface [10,11]. These measurements verify that the surface dipole can be influenced by surface processing and that the effects contribute to the observation of a NEA.

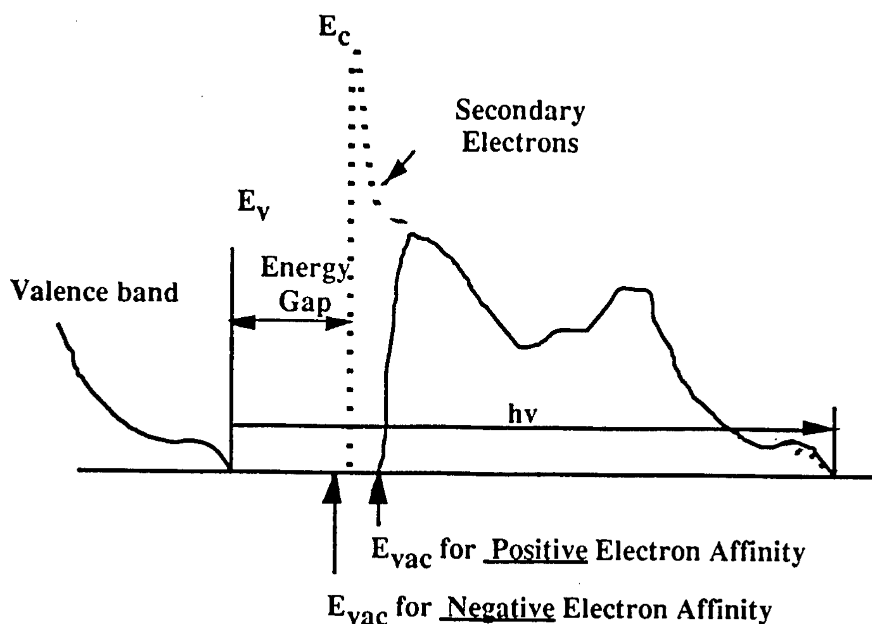

Figure 2. A schematic of the difference in the photoemission spectra of a semiconductor with a positive or negative electron affinity.

B. Experimental Procedure

The 6H-SiC substrates used in this study were supplied by Cree Research, Inc. The samples were n-type with doping concentrations of 10^{16} to $10^{18}/cm^3$. The AlGaN samples were grown by CVD in a remote location and transported in ambient to the analysis system. To avoid surface contamination, AlN and GaN samples were also grown in the integrated UHV transfer system by gas source molecular beam epitaxy (GSMBE). This system includes the UPS system, LEED, Auger, hydrogen and argon plasma processing chamber, and XPS as well as the GSMBE. The system is described elsewhere [9,11]. Recently added is the capability of GSMBE to grow undoped AlN and GaN films.

The AlGaN thin films were grown on vicinal n-type, Si-face α(6H)-SiC(0001) substrates at 1100°C. Vicinal wafers were SiC(0001) 3°-4° off-axis toward the <11$\bar{2}$0>. The as-received SiC wafers were cut into 7.1 mm squares. The SiC pieces were degreased, dipped into a 10% HF solution for 10 minutes to remove the thermally grown oxide layer and blown dry with N_2 before being loaded onto the SiC-coated graphite susceptor. The reactor was evacuated to less than 3×10^{-5} Torr prior to initiating growth. The continuously rotating susceptor was RF inductively heated to the AlGaN deposition temperature of 1100°C in 3 SLM of flowing H_2 diluent. Hydrogen was also used as the carrier gas for the various metalorganic precursors. Once this growth temperature was reached and stabilized, AlGaN deposition was started by flowing triethylaluminum (TEA), triethylgallium (TEG) and ammonia (NH_3) into the reactor at 23.6 μmol/min, 10.5 μmol/min and 1.5 SLM, respectively. The approximate solid solution

alloy concentration using these growth parameters was estimated to be $Al_{0.55}Ga_{0.45}N$ from cathodoluminescence measurements. The AlGaN films were doped with Si from a SiH_4 source (8.2 ppm in N_2 balance) at flow rates between 2.89 and 5 nmol/min to minimize charging problems. The system pressure during AlGaN growth was 45 Torr. The AlGaN layer was grown for 90 minutes resulting in an approximate thickness of 1.5 μm. AlGaN samples were transported in air to the analysis system. Film concentrations were determined from the bandgap values of cathodoluminescence. Auger electron spectroscopy was also used to characterize the surface.

The GaN growth took place in a GSMBE. The cleaning procedure is similar to the above described process but differs in that once in vacuum, the substrate is annealed in a silane flux [12]. The GaN samples were not intentionally doped but since very thin films were employed, charging problems were avoided.

The UPS measurements were excited with 21.21 eV radiation (He I resonance line), and emitted electrons are collected with a hemispherical energy analyzer. The base pressure of the UPS system is 2×10^{-10} Torr and operating conditions involve pressures up to 1×10^{-9} Torr, but the higher pressure is due to the helium inflow and does not contaminate the sample. The 50 mm mean radius hemispherical electron analyzer was operated at a 0.15 eV energy resolution and a 2° angular resolution. The analyzer (VSW HA50) is mounted on a double goniometer and can be tilted with respect to the sample in two independent directions. The samples were fastened with tantalum wire to a molybdenum sample holder. The sample holder is biased by up to 3 V to allow low energy electrons to overcome the work function of the analyzer. The Fermi level of the system (sample and analyzer) is determined by UPS measurement of the sample holder with no sample bias (i.e., grounded). The sample holder can be heated to 1150 °C, and the temperature is measured by a thermocouple.

C. Results and Discussion

The UV photoemission spectra of all four samples studied here are shown in Fig. 3. The AlN and GaN films were prepared by GSMBE and transferred under UHV to the photoemission system. The two alloy samples were prepared by CVD and suffered ambient exposure. Samples were biased with 2-3 V to overcome the work function of the analyzer, and all spectra were shifted to be aligned at the valence band maximum. The spectra were scaled such that the strongest emission was the same for all curves.

The first aspect to be noted is that the spectra of the 50% aluminum alloy and AlN exhibit sharp strong features at the highest binding energy, which corresponds to the lowest kinetic energy. These features are possibly indicative of a negative electron affinity. As noted in the introduction, the feature is attributed to emission from electrons quasi-thermalized to the

conduction band minimum. The emission from the $Al_{0.13}Ga_{0.87}N$ sample is significantly weaker, and the GaN emission does not show the sharp peak at all.

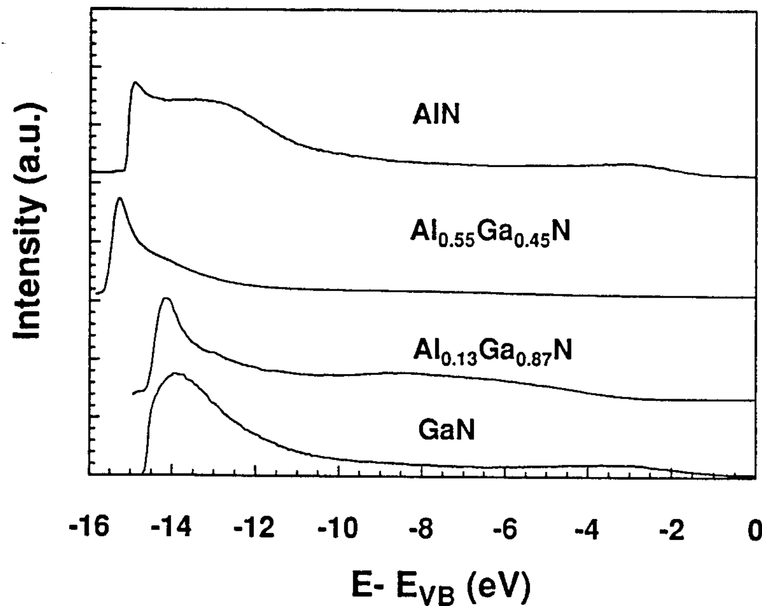

Figure 3. The UV photoemission spectra of $Al_xGa_{1-x}N$ for x=0, 0.13, 0.55, 1. Spectra were aligned at the valence band maximum.

A second indication of the change in electron affinity with alloy concentration is the extension of the $Al_xGa_{1-x}N$ spectra to lower energy as x is decreased. A more precise description of the relation of the NEA is obtained from the spectral width. The spectral width is obtained from a linear extrapolation of the emission onset edge to zero intensity at both the low kinetic energy cutoff and at the high kinetic energy end (reflecting the valence band maximum). For a material with a positive electron affinity, Fig. 2 shows that $\chi = h\nu - E_g - W$, and for a material with a NEA, Fig. 2 indicates that $0 = h\nu - E_g - W$, or rewriting, $h\nu = E_g + W$. This analysis indicates that the 50% aluminum sample does not have a negative affinity but rather a low positive affinity value, as discussed below. We note that the photoemission measurements cannot be used to determine the energy position of the electron affinity for the NEA case.

To determine the energy position of the valence band maximum, the spectral gain was increased, and the intensity was extrapolated to 0 emission. The spectra are aligned in Fig. 3 at the deduced valence band maximum. The spectral widths obtained from the $Al_xGa_{1-x}N$ samples were 14.5, 14.5, 15.5, and 15 eV for x=0, 0.13, 0.55, and 1.0, respectively. In applying the relations noted above, the bandgaps of the bulk AlN and GaN must also be known. The literature values of the AlN and GaN bandgaps are 6.2 and 3.4 eV, respectively. Assuming a linear extrapolation for the bandgap of the alloys, we deduce x=0.55 for

E_g = 4.70 eV and x=0.13 for E_g = 3.80 eV. Using the relations described above, the AlN surface satisfies the relations for a NEA within ±0.2 eV, while the GaN, $Al_{0.55}Ga_{0.45}N$, and the $Al_{0.13}Ga_{0.87}N$ surfaces do not satisfy the relations for a NEA. We can, however, determine the value of the electron affinity of these materials and find that χ = 3.3 eV, 2.9 eV, and 1.0 eV for x = 0, 0.13, and 0.55, respectively.

Another aspect that is evident from the photoemission spectra is the position of the surface Fermi level relative to the valence band maximum. It was found that E_F ranges from 2 to 3.5 eV above the valence band maximum for each sample. For the GaN and $Al_{0.13}Ga_{0.87}N$ surfaces, these values position E_F in the upper part of the gap while for the AlN (deleted rich) and 50 % Al samples, the values indicate that the surface Fermi level is pinned near midgap. The pinning at midgap may be an indication of increased impurity incorporation. In particular, the strong affinity of Al with oxygen often results in increased oxygen incorporation for these films.

To further explore the surface affinity, the effect of annealing in vacuum was explored for the x=0.55 sample. The results are shown in Fig. 4. After annealing to 475 °C and 580 °C for 10 minutes, the photoemission spectra showed a decrease in the relative intensity of the NEA related peak. Furthermore, the width of the spectra also decreases. As these temperatures are much less than the temperatures involved in growth, it is unlikely that a component present during growth is removed. It is possible that some type of contamination was introduced which

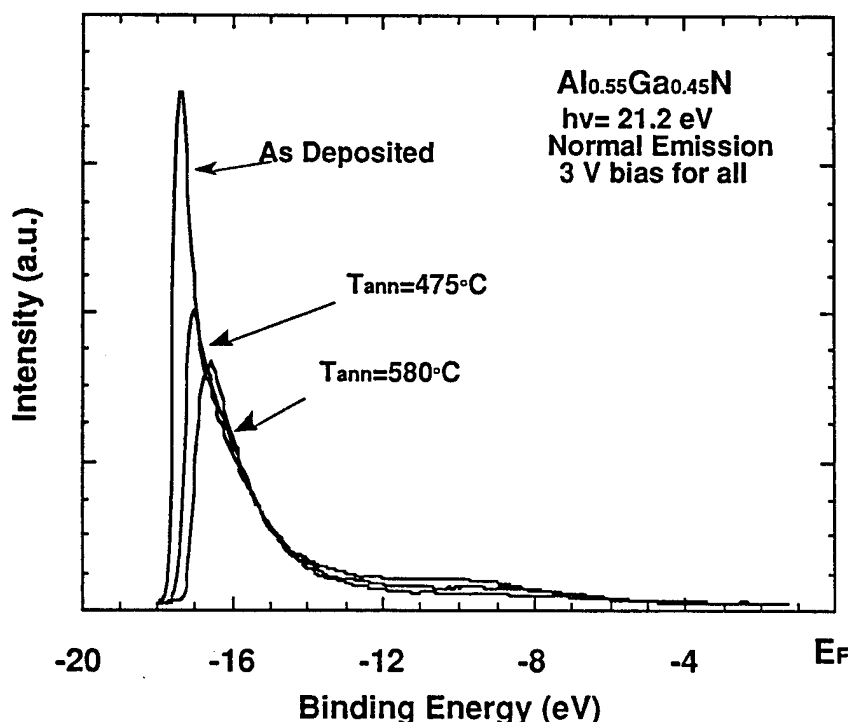

Figure 4. The UV-photoemission from $Al_{.55}Ga_{.45}N$ on 6H-SiC versus annealing temperature.

affected the emission. It is suggested that hydrocarbon contaminants are a likely possibility. No LEED pattern was visible for the $Al_{0.55}Ga_{0.45}N$ sample and the lack of a LEED pattern for the as-loaded samples is possibly related to carbon and oxygen on the surface (attributed to the transport in air). The annealing may result in more complete bonding of the surface adsorbed hydrocarbon layer which results in a change in the surface dipole. Another possibility is that the electron affinity has been affected by adsorbed molecules such as hydrogen. While previous results have shown that hydrogen can induce a NEA surface on diamond [7,10], the AlGaN surfaces have not been intentionally exposed to H. It is evident that further studies are necessary to characterize the surfaces more completely.

The deduced electron affinities versus alloy concentration are shown in Fig. 5. Again, it is noted that the photoemission measurements cannot be used to determine the position of the vacuum level for a NEA surface; this point is indicated at $\chi = 0$ with an arrow to larger negative values. The results suggest that the electron affinity depends on the alloy concentration as originally suggested. Unfortunately, sufficient data is not present at this time to more completely describe the effect. Additionally, no effort to control the surface termination for these samples has been made. For diamond, it was found that the observation of a NEA is critically dependent on the surface termination. Future studies will explore whether the electron affinity of AlGaN materials is also affected by different surface preparations.

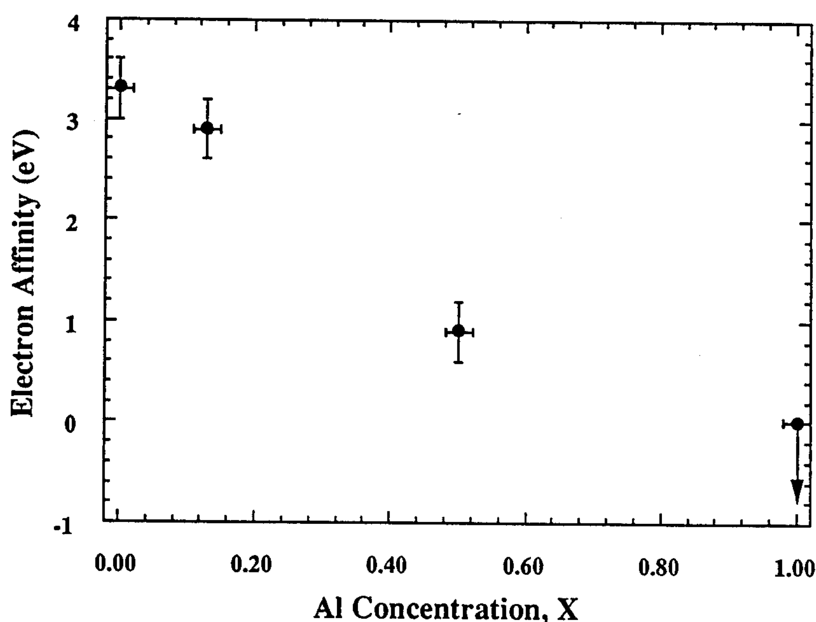

Figure 5. Electron affinities of $Al_xGa_{1-x}N$ alloys vs. Al concentration. The arrow indicates that the electron affinity is less than (or equal) 0, but the value cannot be determined from the UV photoemission measurements.

D. Conclusions

In summary, features in the UPS spectra indicative of a NEA surface on AlN and a low positive electron affinity for $Al_{0.55}Ga_{0.45}N$ have been observed. The AlN spectra exhibited both the sharp features at low kinetic energy that have been found to be characteristic of a NEA; the width of the spectra was also consistent with the observed effect. The UPS spectra of AlGaN alloys did not show a NEA, but the measurements have been used to determine the electron affinity of GaN, $Al_{0.13}Ga_{0.87}N$, and $Al_{0.55}Ga_{0.45}N$ yielding values of 3.3, 2.9, and 01.0 eV, respectively.

The surface Fermi level was found to shift towards the middle of the bandgap for the Al-rich samples. This may indicate an increase in oxygen impurities.

The NEA surfaces were robust, showing the effect even after transfer through ambient. AlN samples grown *in situ* have shown NEA surfaces without the presence of oxygen. The positive affinity surfaces, when annealed, results in a change of the electron affinity. This effect was attributed to a change in the surface layer that affected the surface dipole.

E. Future Work

Future work will involve examining samples to fill in the gaps in the solid solution of AlGaN alloys. Furthermore, whether surface treatments can be employed on the AlGaN alloys to form stable NEA surfaces will be explored. Band offsets will be determined for GaN grown on SiC substrates.

F. Acknowledgments

This work was supported in part by the Office of Naval Research through grants N0014-92-J-1477 and N0014-92-J-1604. The SiC substrates used were supplied by Cree Research. Bill Perry performed the cathodoluminescence measurements.

G. References

1. S. Strite and H. Morkoç, J. Vac. Sci. Technol. B **10** 1237 (1992).
2. J. H. Edgar, J. Mater. Res., 7, 235 (1992).
3. M. D. Williams, M. D. Feuer, S. C. Shunk, N. J. Sauer, and T. Y. Chang, J. Appl. Phys. **71**, 3042 (1992).
4. M. C. Benjamin, C. Wang, R. F. Davis, R. J. Nemanich, Appl. Phys. Lett. **64,** (1994).
5. M. C. Benjamin, C. Wang, R. S. Kern, R. F. Davis, R. J. Nemanich, Mat. Res. Soc. Symp. **339**, 81 (1994).
6. F.J. Himpsel, J.A. Knapp, J.A. van Vechten and D.E. Eastman, Phys. Rev. B **20**, 624 (1979).
7. B. B. Pate, Surf. Sci. **165**, 83 (1986).
8. B. B. Pate, M. H. Hecht, C. Binns, I. Lindau and W.E. Spicer, J. Vac. Sci. Technol. **21**, 364 (1982).
9. J. van der Weide and R. J. Nemanich, J. Vac. Sci. Technol. B **10**, 1940 (1992).
10. J. van der Weide and R. J. Nemanich, Appl. Phys. Lett. **62**, 1878 (1993).
11. J. van der Weide and R. J. Nemanich, Phys. Rev. B**15** 49 13629 (1994).
12. R. Kaplan, Surface Science **215**, 111 (1989).

XVII. High Quality InGaN Films by Atomic Layer Epitaxy

K. S. Boutros, F. G. McIntosh, J. C. Roberts, and S. M. Bedair
Department of Electrical and Computer Engineering, North Carolina State University
Raleigh, North Carolina 27695

E. L. Piner and N. A. El-Masry
Department of Materials Science and Engineering, North Carolina State University
Raleigh, North Carolina 27695

$In_xGa_{1-x}N$ single crystal films were grown at 600–700 °C by Atomic Layer Epitaxy (ALE). InGaN films with compositions of up to 27% indium were achieved. The full width at half maximum (FWHM) of the (0002) $In_xGa_{1-x}N$ peak by double crystal x-ray diffraction (DCXRD) was as small as 6 minutes, the lowest value reported for this ternary alloy. Strong photoluminescence band edge emission between 360 nm to 446 nm was observed at room temperature. These low temperature ALE grown films were achieved without the need to use excessive flows of the In organometallic source and thus demonstrate the potential for growth of this ternary alloy over the entire composition range.

Published in Applied Physics Letters, 67 1797 (1995).

A. Introduction

The $In_xGa_{1-x}N$ ternary alloys have direct bandgaps that cover the entire visible range, and are thus ideal candidates for active layers in light emitting devices. Despite such potential applications, there is a paucity of research on the epitaxial growth of $In_xGa_{1-x}N$ films. Problems with these In related compounds that have hindered their progress can be due to several reasons. For example, the high nitrogen vapor pressure [1] that is required in order to prevent the dissociation of the In-N bond. This problem is compounded when NH_3 is used as the nitrogen source, due to its inefficient thermal cracking at low temperatures. Another problem arises from parasitic gas phase reactions that occur between hydrides and In based organometallic compounds [2], which seem to be more severe for NH_3 as compared to PH_3 and AsH_3. The above difficulties in the growth of $In_xGa_{1-x}N$ can be partially addressed by utilizing low growth temperatures in metalorganic chemical vapor deposition (MOCVD) or molecular beam epitaxy (MBE). However, this has led to films with poor quality. For example, high values of x were obtained by MOCVD [3] at growth temperatures between 500 - 700 °C, however with photoluminescence (PL) dominated by deep levels. Recently films with better optical quality have been grown at growth temperatures of about 800 °C. However, only low values of x, less than 24%, were achieved, and a very high trimethylindium (TMI) vapor pressure relative to trimethylgallium (TMG) was used to achieve these high values of x [4,5]. For example, TMI vapor pressures 12 to 20 times that of TMG were used, leading to the consumption of several grams of this fairly expensive precursor for each run [4,5].

In this paper, we report on the low temperature growth of InGaN by Atomic Layer Epitaxy (ALE). The ALE technique has been established as a low temperature growth approach for several III-V compounds such as GaAs, InGaAs and InGaP where device quality films were achieved at temperatures of about 200 °C less than that usually used in MOCVD [6, 7]. Atomic layer epitaxy also avoids gas phase reactions since the growing surfaces are not simultaneously exposed to organometallics and hydrides. It should be mentioned that ALE growth of GaN with optical properties comparable to MOCVD grown films has previously been reported by us at growth temperatures as low as 550 °C [8] and by others [9] at 900 °C.

B. Experimental Procedure

The ALE system is based on the rotating susceptor approach previously described for other III-V compounds and schematically shown in Fig. 1. Source gases, NH_3, and the metalorganics TMG, trimethylaluminum (TMA) or ethyldimethylindium (EdMIn) are flowing continuously and the sapphire substrate rotates between the two streams of gases. The exposure times to TMG or NH_3 is thus determined by the speed of rotation. For example, for 30 rpm the exposure is estimated at about 0.2 seconds. This rotating substrate approach was previously used to achieve the ALE growth of GaAs at a rate of 2 mm/hour [10]. Due to the

high V/III ratio used in this work, several provisions have been implemented such as the adjustment of the central nitrogen line flow, and the mechanical shearing of the gaseous boundary layers between successive exposures to the reactant gases.

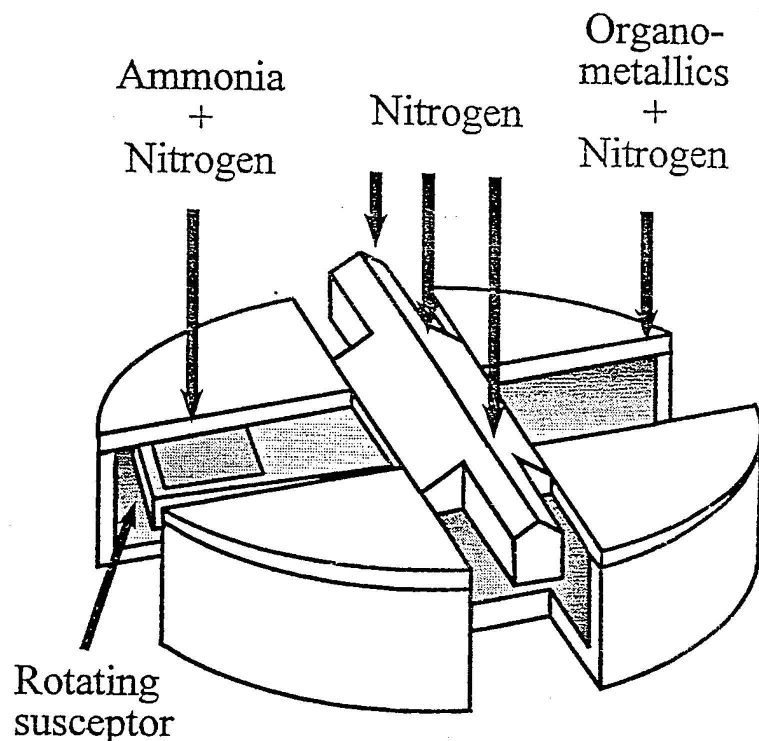

Figure 1. Schematic of the rotating susceptor for the ALE of InGaN.

ALE growth of InGaN was carried out in the 600 - 700 °C temperature range at 100 torr. The primary carrier gas was nitrogen. Sapphire substrates were heated in NH_3 at 1050 °C followed by the ALE growth of prelayers of AlN and GaN deposited at 700 °C. For the growth of the InGaN ternary alloy both TMG and EdMIn flowed simultaneously through the column III entry tube and the solid composition was adjusted by varying the growth temperature and/or the EdMIn partial pressure for a fixed TMG value. The EdMIn partial pressure was varied in the 0.3 to 5.2 mmole/min range. InGaN film thicknesses used in this study ranged from several hundred to several thousand angstroms, with growth rates of 0.2-1Å / ALE cycle. The growth conditions were optimized to obtain high quality films rather than to achieve a monolayer/cycle in a self-limiting fashion. Film thicknesses were estimated from ellipsometry measurements and confirmed by transmission electron microscopy (TEM) studies. The grown films were characterized by double-crystal x-ray diffraction (DCXRD) and photoluminescence (PL) measurements. PL was carried out at room temperature using a He-Cd laser (325 nm), at 20 mW excitation level.

Figure 2 shows the DCXRD for the (0002) diffraction of InGaN films grown on sapphire substrates. Figure 2a corresponds to a sample grown at 650 °C. We estimated the InN mole fraction in the InGaN films by calculating the difference between the peak positions between

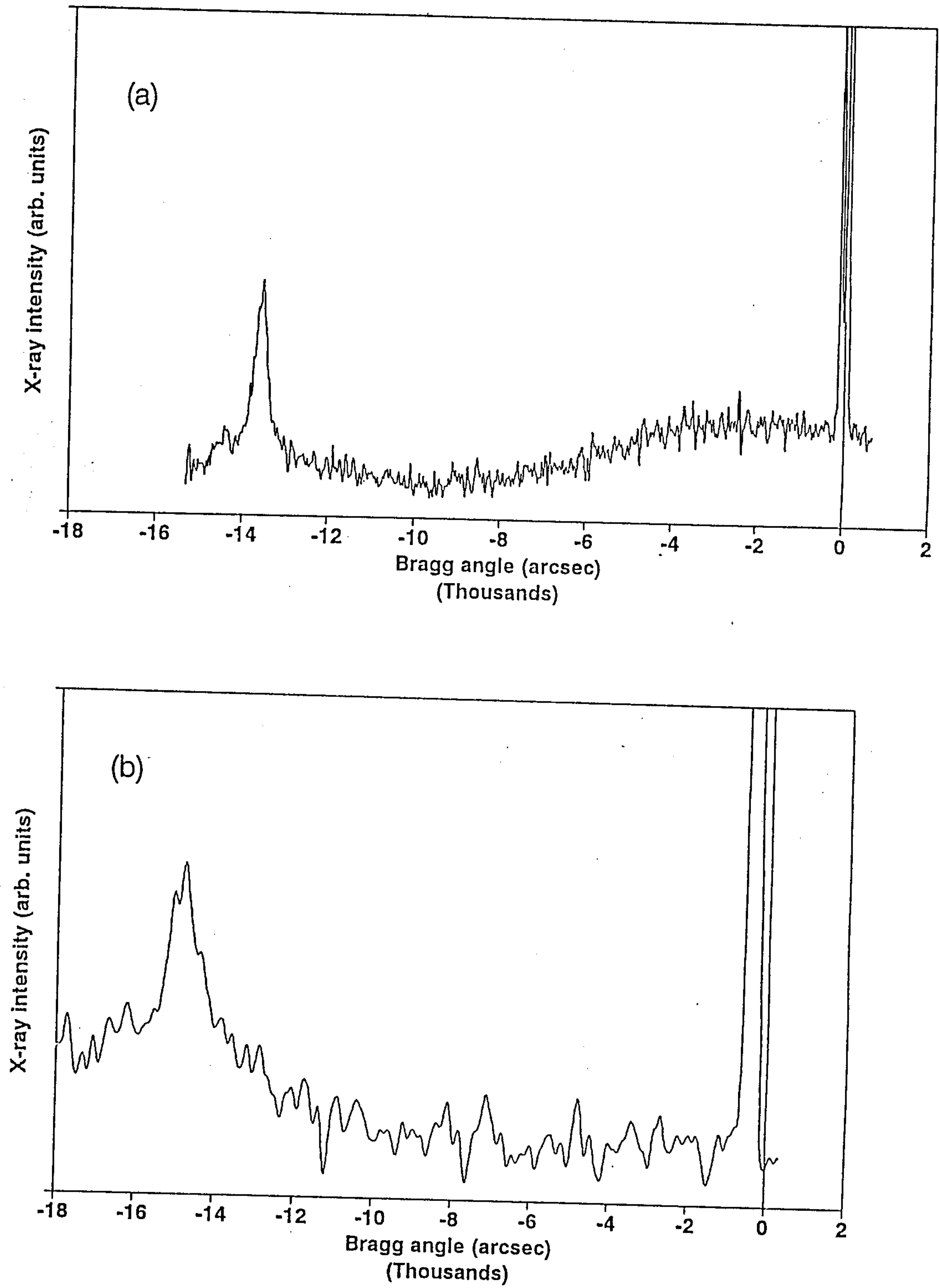

Figure 2. Double crystal X-ray diffraction of InGaN grown on sapphire substrates. Growth temperatures are 650 and 600 °C for curves (a) and (b) respectively.

the InGaN and the sapphire peaks and assuming Vegard's Law is valid for this ternary alloy. The calculated value for the InN mole fraction from Fig. 2a is 14%. Figure 2b corresponds to a sample grown at 600 °C with the same gas flows as for $In_{0.14}Ga_{0.86}N$. The calculated value of x for this 600 °C grown film is 25% The incorporation efficiency of indium in this ternary alloy seems to increase with decreasing growth temperature for the same EdMIn and TMG vapor pressure ratio. The full width at half maximum (FWHM) of the DCXRD is about 6 minutes for the $In_{0.14}Ga_{0.86}N$ film. The $In_{0.25}Ga_{0.75}N$ film shows a fairly weak and broad signal with an estimated FWHM of about 10 minutes. The previously reported FWHM in the MOCVD grown InGaN at 800 °C with comparable compositions are 7 and 25 minutes, respectively [4,5]. Thus, the current ALE approach, in spite of the low growth temperature, produces InGaN films with comparable or even better FWHM than that reported by MOCVD at 800 °C. This may be a result of the two dimensional growth nature of the ALE process coupled with the fairly low growth rate of a fraction of a monolayer per cycle. It should be mentioned that the value of FWHM in MOCVD films increases very rapidly with decreasing growth temperature below 800 °C.

The room temperature PL results are shown in Fig. 3. Figure 3a shows the PL of an InGaN film grown at 650 °C along with the PL of a GaN film grown at 700 °C by ALE for comparison. The PL spectrum shows a band edge emission indicated by an arrow in the figure, however it is dominated by deep level emission which may be originated from nitrogen vacancies and/or carbon related impurities. This PL spectrum is comparable to that reported by MOCVD [3] at 800 °C. Optimizing the growth parameters, such as pausing for one second under the NH_3 flux and minimizing carryover of gases from the NH_3 to the organometallic stream, resulted in improvements in the PL spectrum as shown in Figure 3b. Figure 3b shows the PL of $In_{0.17}Ga_{0.83}N$ and $In_{0.27}Ga_{0.64}N$ grown at 650 °C. These emissions are considered to be the band edge emission since they correspond to the predicted bandgap of these ternary alloys, where the band gap bowing parameters are considered [11]. The absence of deep level emission is indicated from Fig. 3b. The PL emission intensities shown in Fig. 3 are strong and are comparable to those achieved in GaN films grown by MOCVD at 900 °C. This is not consistent with the PL results reported earlier by Nakamura [5] and Matouka [4] where the PL intensity decreases fairly rapidly with decreasing growth temperature. The FWHM is fairly broad, about 200 meV. The fairly broad spectrum can be due to several reasons, such as low growth temperature and related defects, fairly thin films, and relatively high background carrier concentrations. It should be mentioned that the InGaN films are grown on a nonoptimized ALE AlN buffer layer, resulting in fairly high levels of background carrier concentrations. Epilayers grown at 600 °C or lower showed very weak and broad PL spectra.

In the current study, as a result of the low temperature growth, the composition of the solid phase follows the flow rate ratio of indium to the sum of Group III sources as shown in

Table I. For example in order to grow $In_{0.2}Ga_{0.8}N$ at 650 °C, the EdMIn mole fraction in the gas phase EdMIn/(EdMIn + TMG), is about 0.4 in contrast to values of 0.95 previously reported to achieve comparable compositions by MOCVD at 800 °C [4,5]. It should be

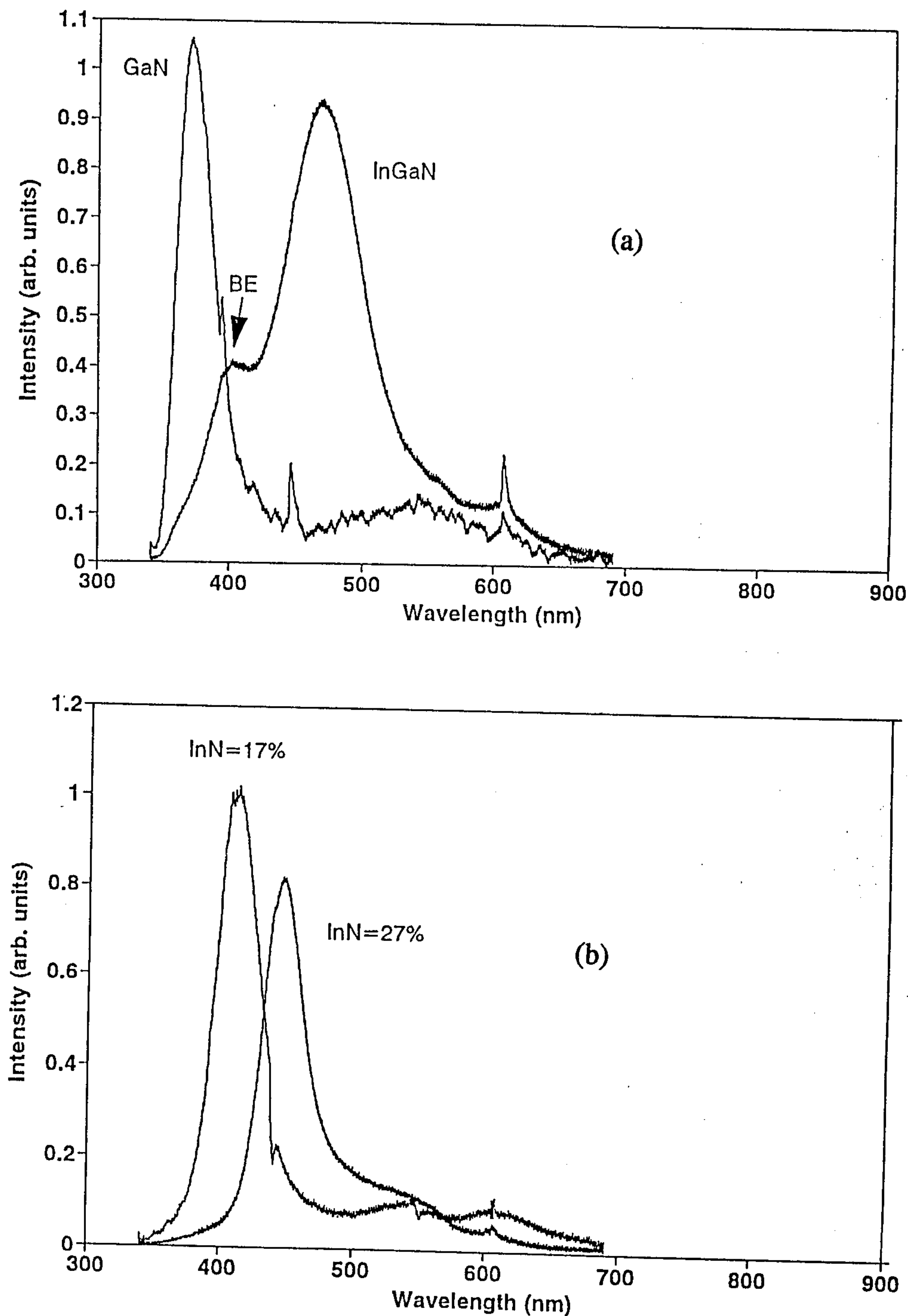

Figure 3. Room temperature photoluminescence (PL) spectra of InGaN grown on sapphire substrates: (a) for GaN and x°= 0.18 grown at 700 and 650 °C, respectively; (b) for x°= 0.17 and 0.27, both grown at 650 °C.

mentioned that for lower ALE growth temperatures (600 °C) the In mole fraction in the solid phase has a one to one correspondence to the EdMIn/(EdMIn + TMG) ratio in the gas phase. These results indicate that the ALE process is capable of cracking NH_3 at lower temperatures than that required for the MOCVD technique. In the ALE process, NH_3 is cracked on a more active surface, a surface covered with Ga and In adatoms or their monomethyl-metal radicals. The reactivity of this surface seems to be much higher than that of one covered or partially covered by the more inert GaN of InGaN molecules. This had been previously observed in our laboratory during the ALE growth of GaP and GaInP at 500 °C [7], at a temperature that is very low for MOCVD growth. Also, the ALE process allows the absorbed species (Ga, In, or N) to migrate at the growing surface with higher surface diffusion as compared to bulk growth techniques such as MOCVD or MBE. Thus this low temperature ALE approach is, in principle, capable of growing $In_xGa_{1-x}N$, in the $0 < x < 1$ composition range.

Table I. The Effect of the Growth Temperature and Gas Phase Composition of the InN % in the Deposited InGaN Ternary Alloy

Growth Temperature (°C)	EdMIn/(EdMIn + TMG)	In % in Epitaxial Film
700	0.14	3
700	0.25	7
650	0.25	14
650	0.4	20
650	0.57	27
600	0.25	23

D. Conclusions

In conclusion, ALE has been used to grow $In_xGa_{1-x}N$ (0 £ x £ 0.27) in the 600 -700 °C temperature range. Also, these high values of x, were achieved without the need of excessively high vapor pressures of the organometallic In source typically required in conventional MOCVD. The DCXRD showed a FWHM as small as 6 minutes, the lowest reported value to date of this ternary alloy. Band edge emission was observed over the entire composition range studied. The ALE technique seems to be capable of addressing the current problems facing the epitaxial growth of InGaN and has the potential of achieving $In_xGa_{1-x}N$ films over the entire composition range ($0 < x < 1$).

We would like to thank Dr. Y. He and Mr. A. Morshed for their assistance. This work is supported by the Office of Naval Research (ONR) through the University Research Initiative (URI).

E. References

1. T. Matsuoka, H. Tanaka, T. Sasaki, and A. Katsui, Inst. Phys. Conf. series N 106, Int. Symp. GaAs and Related Compounds, Japan 1989, p. 141.
2. H. Amano, N. Sawahi, I. Akasaki and Y. Toyoda, Appl. Phys. Lett. **48**, 353 (1986).
3. N. Yoshimoto, I. Matsuoka, T. Sasaki, and A. Katsui, Appl. Phys. Lett. **59**, 2251 (1991).
4. T. Matsuoka, N. Yoshimoto, T. Sasaki, and A. Katsui, J. Elect. Mat. **22**, 157 (1992).
5. S. Nakamura, and T. Mukai, Jpn. J. Appl. Phys. **31**, L1457 (1992).
6. S. M. Bedair, M. A. Tischler, T. Katsuyama, and N. ElMasry, Appl. Phys. Lett., **47**, 51 (1985).
7. B. McDermott, K. Reid, N. ElMasry, and S. M. Bedair, Appl. Phys. Lett. **56**, 1172 (1990).
8. N. H. Karam, T. Paodes, P. Colter, D. McNulty, W. Rowland, J. Schetzina, N. El-Masry and S. M. Bedair, Appl. Phys. Lett. (accepted for publication).
9. M. Asif Khan, R. A. Skogman, J. M. Van Haue, D. T. Olson and J. N. Kuznia, Appl. Phys. Lett. **60**, 1366 (1992).
10. A. Dip, G. Eldallal, P. Colter, N. Hayafuji, and S. M. Bedair, Appl. Phys. Lett. **62**, 2378 (1993).
11. K. Osamura, K. Nakajima, Y. Murakami, P. H. Shingu and A. Ohtsuki, Solid State Communations **11**, 617 (1972).

XVIII. Growth and Characterization of AlInGaN Quaternary Alloys

F. G. McIntosh, K. S. Boutros, J. C. Roberts, and S. M. Bedair
Department of Electrical and Computer Engineering, North Carolina State University
Raleigh, North Carolina 27695

E. L. Piner and N. A. El-Masry
Department of Materials Science and Engineering, North Carolina State University
Raleigh, North Carolina 27695

We are reporting on the deposition of $Al_yIn_xGa_{1-x-y}N$ in the $(0 < y < 0.15)$ and $(0 < x < 0.14)$ composition range by metal organic chemical vapor deposition. AlInGaN quaternary alloys offer a lattice matched platform for InGaN based light emitting heterostructure devices. Epitaxial growth of AlInGaN on (0001) sapphire substrates has been achieved at 750°C. Alloy composition, lattice constants and bandgaps were obtained by energy dispersive spectroscopy, X-ray diffraction, and room temperature PL. Band edge emissions dominate the PL spectra of these quaternary films. Preliminary data suggests that the lattice constant of AlInGaN can be deduced from chemical composition using Vegard's law, indicating solid solution in the grown quaternary films.

To be published in Applied Physics Letters, January 1996.

A. Introduction

Two approaches are being conducted to achieve blue, green and yellow emission from InGaN based heterostructures using AlGaN barrier layers. The first is to dope the InGaN films, with Zn for example, and rely on impurity level to valence band emissions [1,2]. This approach works fairly well in LED's, which operate at low levels of current injection, but at higher current injection levels, such as might be used in laser diodes, impurity transitions can saturate and band to band transitions begin to appear [3]. The second approach is to rely exclusively on band to band transitions from thin quantum well structures containing fairly high percentages of InN in the ternary alloy active layers. To avoid the lattice mismatch between the InGaN well and the AlGaN barriers, a well thickness of about 20Å has been used [4]. The highly strained, extremely thin well will shift the emission to higher energy and will also limit the InN% in the well. Thus for high values of x, the use of AlGaN buffer layers imposes several limitations that can be avoided if replaced by a more versatile $Al_yIn_xGa_{1-x-y}N$ quaternary alloy. By varying the composition of quaternary alloys, the bandgap and the lattice constant can each be independently adjusted in order to achieve AlInGaN/InGaN lattice matched or closely lattice matched structures.

The AlInGaN has not been studied in any detail to date. Deposition of AlInGaN has been achieved [5], but growth on (0001) sapphire was polycrystalline and no band edge photoluminescence was reported. One of the major obstacles in the development of the quaternary is the determination of the optimal growth temperature. Aluminum based compounds generally require higher growth temperatures. Any residual background oxygen impurities in the deposition system or source gases will result in the incorporation of oxygen in the growing films. Therefore, higher temperatures are required in order to desorb these oxides and prevent their incorporation into the epitaxial film. Lower temperatures, however, are required for indium based compounds. Indium has a relatively high vapor pressure and the growth temperature must be lowered in order to increase the indium incorporation and to reduce the dissociation of the In-N bond. The growth temperature will therefore govern the limits to which both In and Al can be incorporated into the AlInGaN quaternary alloy.

In this paper we report on the growth of $Al_yIn_xGa_{1-x-y}N$ with the composition range ($0 < x < 0.14$) and ($0 < y < 0.15$) using a modified MOCVD reactor. We have observed band edge transition of this quaternary alloy by room temperature photoluminescence. These results were achieved by first investigating the MOCVD growth of InGaN and AlGaN at 750°C. This growth temperature seems to be a good compromise for the contradicting requirements for both the gallium and indium containing compounds. The growth parameters and temperatures used for these ternary alloys were used to determine the favorable conditions for the deposition of high quality AlInGaN.

B. Experimental Procedure

The reactor design is based on the rotating susceptor and has been previously described [6,7]. This design allows for three modes of crystal growth: MOCVD, molecular stream epitaxy (MSE), and atomic layer epitaxy (ALE). The organometallics and the ammonia are injected through separate tubes above one of the windows in the graphite susceptor. This configuration is designed to minimize gas phase reactions between the ammonia and the organometallics prior to reaching the surface of the substrate. For MOCVD, the substrate is positioned directly under this window during the entire growth process. For MSE, the lower susceptor rotates, and so the sample is exposed to the organometallic/ammonia stream for only a portion of each growth cycle. This allows a thin layer of material to be deposited and effectively annealed during each rotation cycle.

The growth was conducted at 750 torr on a sapphire substrate. The substrate was first annealed and ammonia passivated at 1050°C. Next an AlN buffer layer and then a GaN buffer layer were grown at 900°C using the MSE technique. Each layer was approximately 400Å thick. The reasoning behind this approach is that the MSE offers a better technique for the growth initiation on the sapphire substrate, although the growth rate is significantly less than with MOCVD. The advantages of the MSE technique is still the subject for further investigation in our laboratory. Once a thin single crystal film of GaN has been deposited by MSE, a thick layer (1500Å) of GaN is deposited by MOCVD at 900° in order to grow away from the defects resulting from the lattice mismatch at the sapphire/AlN interface. For the results presented here, the growth temperature was then lowered to 750°C for the AlInGaN layer deposition. Trimethylaluminum (TMA), trimethylgallium (TMG), ethyldimethylindium (EDMIn) and ammonia were used as precursors. The TMG and ammonia flows were 8 μmol and 50,000 μmol, respectively, and the TMA and EDMIn were varied to change the quaternary composition. Quaternary films with thicknesses of about 0.5 μm were grown and characterized by energy dispersive spectroscopy (EDS), double crystal X-ray diffraction (DCXRD) and room temperature photoluminescence (PL).

C. Results and Discussion

The chemical compositions of the quaternary films were obtained by EDS. First EDS was calibrated for In, Al, and Ga using standards made from InGaN and AlGaN ternary alloy films of known compositions determined from DCXRD and using Vegard's law. Figure 1 shows the EDS spectra, in which are observed gallium, aluminum, and indium peaks, as well as weak nitrogen and carbon peaks. The carbon is due to surface contamination from atmospheric hydrocarbons. The nitrogen signal is relatively weak because the EDS detector has a low sensitivity at the energy corresponding to the nitrogen emission. The EDS spectrum in Fig. 1a indicates that this film has x 14% and y 10% for InN and AlN contents, respectively. The

corresponding values from Fig. 1b are 3% and 10% for InN and AlN, respectively. The accuracy of these values depends on the sensitivity of the EDS technique and the method of calibration described above. Errors can be as large as a few atomic percent in the values of x and y in these quaternary alloys. The values of InN% deduced from Fig. 1b may be very close to the experimental error of this technique.

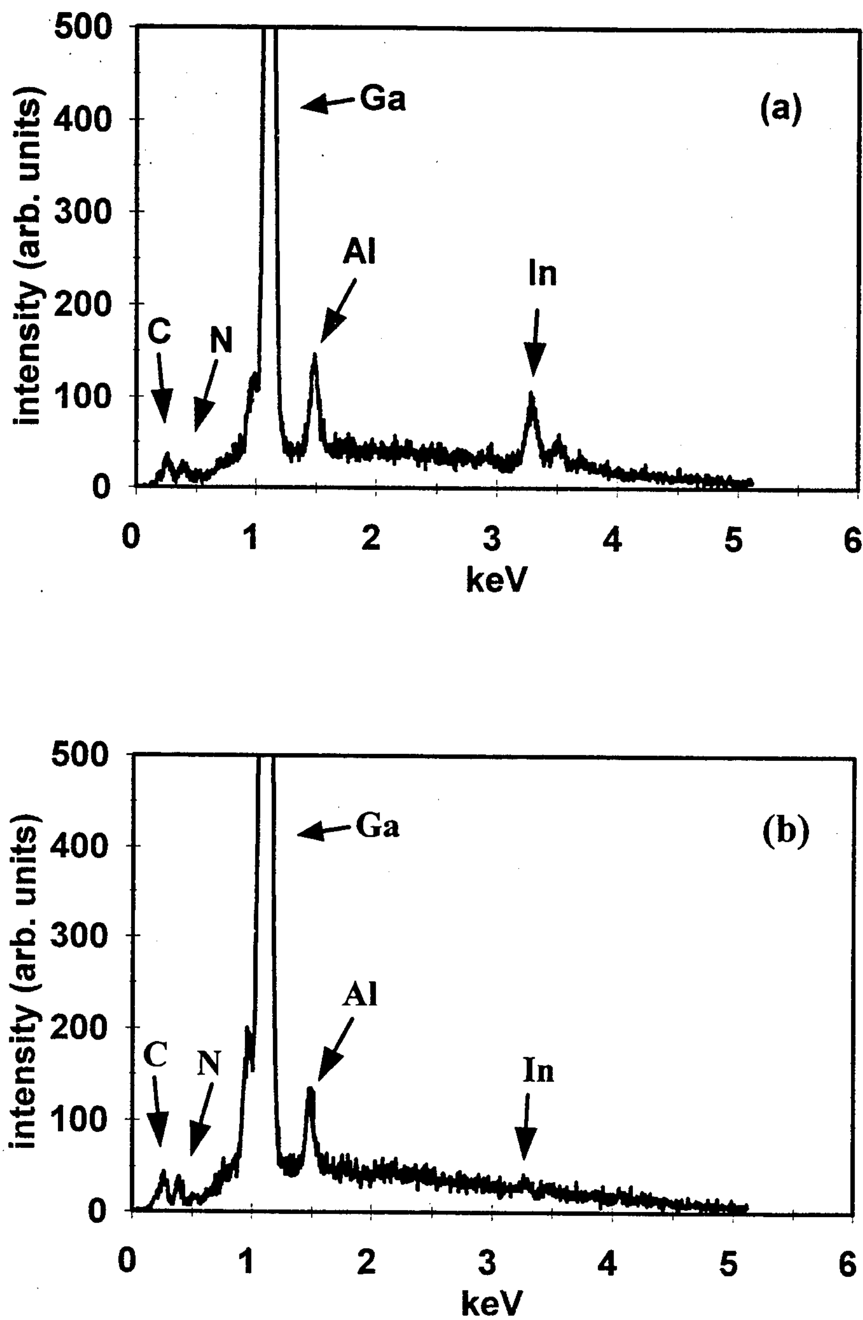

Figure 1. EDS spectra of $Al_yIn_xGa_{1-x-y}N$ quaternary alloys. The approximate values of y and x are a) 10% and 14%, and b) 10% and 3%.

Figure 2 shows the DCXRD data for this film and indicates that a single crystal quaternary alloy has been deposited. The lattice constant (c-axis) of these quaternaries, as deduced from DCXRD data, are 5.228 Å and 5.175 Å as shown in Figs. 2a and 2b, respectively. These values for the lattice constants (c-axis) can also be deduced from the chemical compositions using the formula [8]:

$$a[Al_yIn_xGa_{1-x-y}N] = (1 - x - y)\, a_{GaN} + x\, a_{InN} + y\, a_{AlN}$$

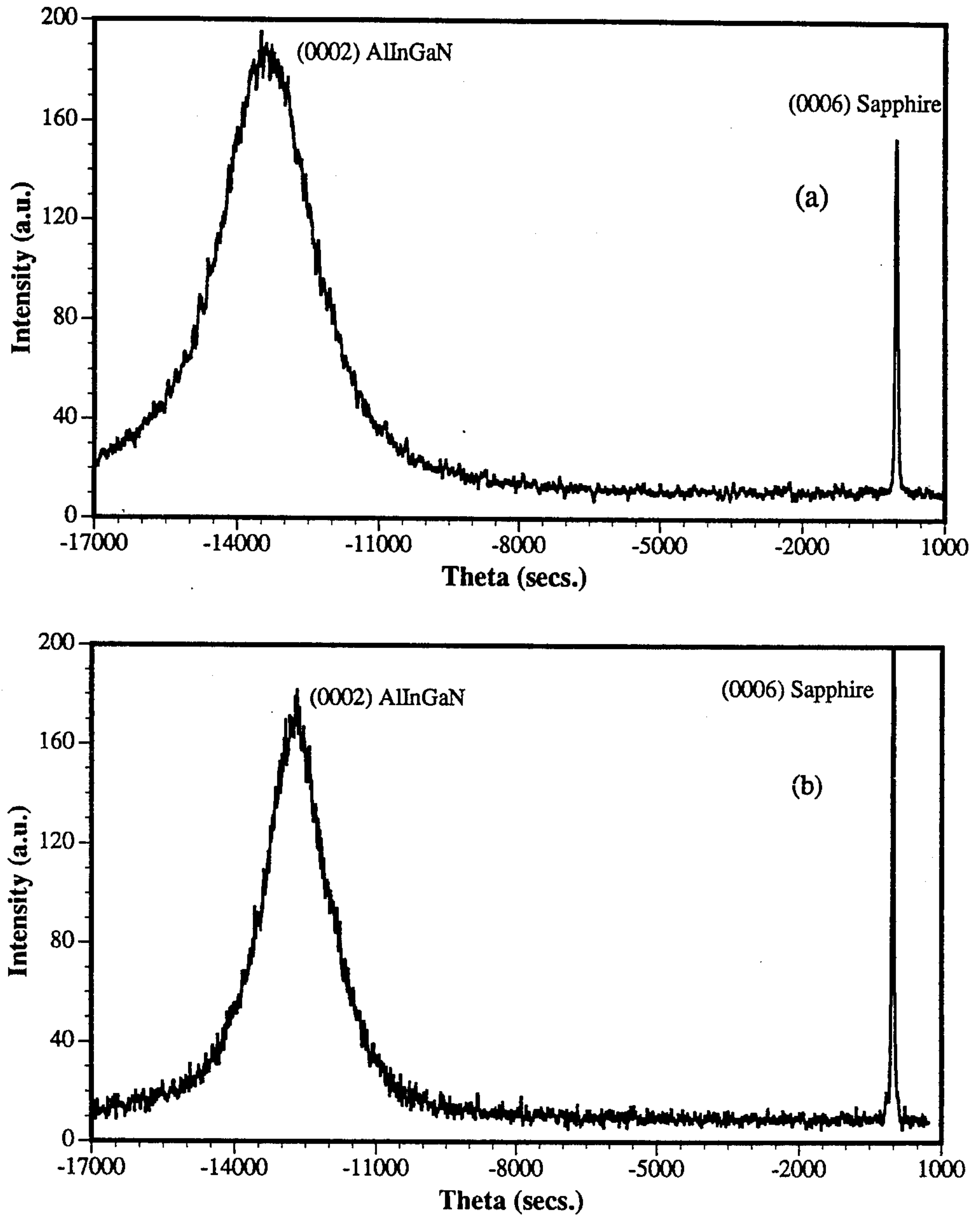

Figure 2. Double crystal X-ray diffraction of AlInGaN quaternary alloys. The corresponding lattice constants (c-axis) are a) 5.228Å and b) 5.175Å.

There is a reasonable agreement between the lattice constants measured by X-ray and the values deduced from the above equation using the chemical compositions deduced from EDS measurements. This can indicate that a solid solution of the binary constituents is present in these quaternary alloys.

Figure 3 shows the room temperature PL of the AlInGaN quaternary alloy using a He-Cd laser at an excitation level of 20 mW. The PL spectrum of $Al_{0.10}In_{0.14}Ga_{0.76}N$, shown in Fig. 3a, is dominated by band edge (BE) emission, but emissions of deep levels are also observed. These deep levels may be a result of non optimized growth conditions for this quaternary alloy. The BE emission of the quaternary at 380 nm shows a shift to a higher energy than is expected from InGaN with InN of 14%, which should be emitting at about 400 nm. This shift is presumably due to the presence of AlN in the film. Figure 3b shows the corresponding PL data for the quaternary with AlN and InN of approximately 10% and 3%, respectively. The band edge is shifted from that of AlGaN due to the presence of InN in these films. For films grown with AlN approaching 20%, BE emission was not observed and the PL spectrum was dominated by deep levels, indicating that higher growth temperatures may be needed.

At this stage it is very difficult to accurately predict the bandgap of this quaternary alloy as a function of x, y, and the lattice constant due to the limited EDS and PL data presently available and the lack of enough data to predict the bandgap of the two InGaN and AlGaN ternary alloys as a function of their compositions. Also, EDS and PL are very localized measurement techniques and can be concentrated on a small area, where as DCXRD cannot be localized to the same scale and results in the average value of the lattice constant over a larger area. In addition, we have observed variations in the values of x and y (especially x) across the wafer by several atomic percentage points, as indicated by EDS and by the PL spectra. These variations may be due to the non-uniform fluxes of the reactant gases across the wafer due to non-optimized flows, which are reflected in the broad full width at half maximum of the DCXRD rocking curves shown in Fig. 2. In our reactor, which is optimized for ALE growth, the wafer cannot rotate while under the reactant gases and so the gas flows are more critical to the uniformity. The reactant fluxes are currently being optimized to reduce or eliminate any significant variations across the wafer in order to allow a more detailed quantitative study of the quaternary alloy.

D. Conclusion

In conclusion, AlInGaN quaternary alloy films have been epitaxially grown by MOCVD which exhibit band edge emissions. EDS and X-ray diffraction results are consistent, indicating that when Vegard's law is applied, a solid solution is present. PL data indicates that this quaternary has the potential of realizing AlInGaN/InGaN lattice matched quantum well structures with sufficient differences in bandgaps (E_g) for carrier confinement. This will

release the constraints of having either ultra thin $In_xGa_{1-x}N$ quantum wells or limited values of x when AlGaN films are used as the barrier layers. Further work is needed to map the variation of the bandgap and lattice constant of this quaternary compound in order for it to be used as a viable candidate in AlInGaN/InGaN heterostructures.

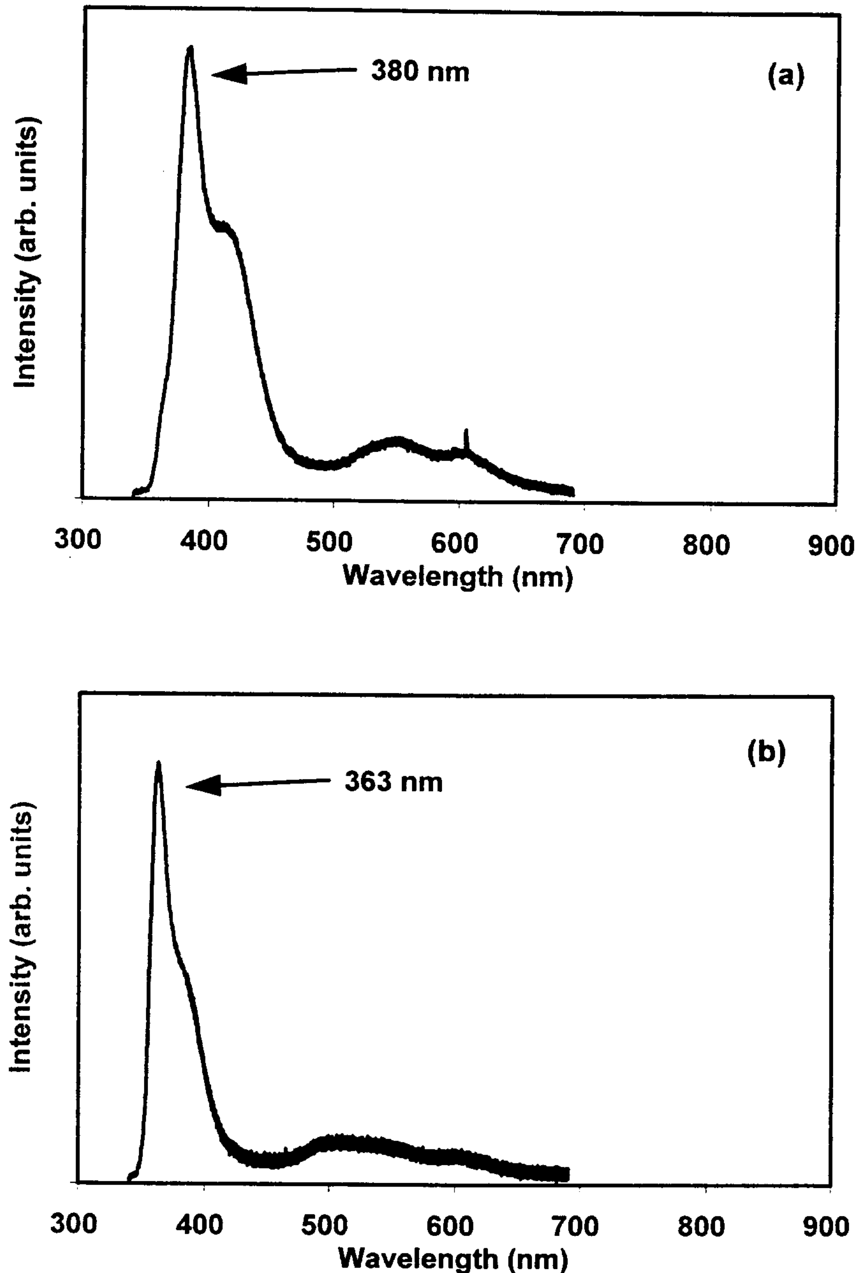

Figure 3. Room temperature photoluminescence spectra of AlInGaN quaternary alloys: (a) corresponds to the film described in Figs. 1 (a) and 2 (a) with band edge emission at 380 nm; (b) corresponds to the film described in Figs. 1 (b) and 2 (b) with band edge emission at 363 nm.

This work is supported by the Office of Naval Research, University Research Initiative project N00014-92-J-1477.

E. References

1. S. Nakamura, T. Mukai and M. Senoh, Appl. Phys. Lett. **64,** 1687 (1994).
2. S. Nakamura, T. Mukai and M. Senoh, J. Appl. Phys. **76**, 8189 (1994).
3. S. D. Lester, F. A. Ponce, M. G. Craford and D. A. Steigerwald, Appl. Phys. Lett. **66**, 1249 (1995).
4. S. Nakamura, M. Senoh, N. Iwasa and S. Nagahama, Jap. J. Appl. Phys. **84**, L797 (1995).
5. T. Matsuoka, N. Yoshimoto, T. Sasaki and A. Katsui, J. Elect. Mat. **21**, 157 (1992).
6. K. S. Boutros, F. G. McIntosh, J. C. Roberts, S. M. Bedair, E. L. Piner and N. A. El-Masry, Appl. Phys. Lett. **67**, 1797 (1995).
7. N. Karam, T. Parados, W. Rowland, J. Schetzina, N. El-Masry, and S. M. Bedair, Appl. Phys. Lett. **67**, 94 (1995).
8. C. K. Williams, T. H. Glisson, J. R. Hauser, and M. A. Littlejohn, J. Elect. Mat. **7**, 639 (1978).

XIX. Raman Spectroscopy for Characterization of Hard, Wide Band Gap Semiconductors: Diamond, GaN, GaAlN, AlN, BN

Leah Bergman and Robert J. Nemanich
Department of Physics and Department of Material Science and Engineering,
North Carolina State University, Raleigh, North Carolina 27695-8202

This paper reviews the Raman spectroscopy of diamond films, GaN, $Al_xGa_{1-x}N$ alloys, AlN, and BN. The review focuses on the influence of various physical aspects such as stress, temperature, and microstructure on the Raman active modes, as manifested by the Raman lineshape. The phonon-plasmon interaction in GaN due to the characteristic unintentional n-type doping of this material is also discussed. Furthermore, a short summary of the behavior of the optical modes of mixed alloys is presented followed by a discussion of the Raman characteristics of $Al_xGa_{1-x}N$ alloy.

To appear in Annual Reviews of Materials Science.

Introduction

Diamond, gallium nitride, aluminum nitride, and cubic boron nitride are of great potential in the development of novel opto-electronic devices due to their wide bandgap and superior mechanical and thermal properties [1-6]. Recent advances in the crystal growth techniques of diamond films [7-12] and the Group III nitride materials [1, 3, 6, 13, 14] have enabled numerous studies via Raman spectroscopy.

This paper reviews the Raman spectroscopy of diamond films, GaN, GaAlN alloys, AlN, and BN. In particular, this review focuses on the influence of various physical aspects such as stress [15], temperature [16], and microstructure [17] on the Raman active modes. The phonon-plasmon interaction in GaN due to the characteristic unintentional doping of this material is also discussed [18-21].

The remainder of this chapter is organized as follows. The second section presents a review of the applications of Raman spectroscopy to diamond films. The issue of the identification of the coexisting diamond and graphitic phases in diamond films is discussed, as well as that of the Raman lineshape of the diamond and the physical mechanisms affecting it. In the third section the Raman modes of the hexagonal wurtzite (WZ) and the cubic zinc-blend polytype structures of GaN are summarized. The effect of pressure and free carriers on Raman frequency of the WZ structure is examined. Furthermore, a review of the Raman characteristics of $Al_xGa_{1-x}N$ alloy is presented. The fourth section presents a review of the Raman active modes of the wurtzite AlN and the effect of applied pressure on the Raman frequencies. The effect of oxygen impurity on the Raman characteristics is also considered. In the last section the bonding-anisotropy of the h-BN and the effect of the crystalline size on the Raman modes is discussed. A review of the effect of high pressure and temperature on the Raman frequencies of h-BN and c-BN is also presented.

Raman Spectroscopy of Diamond Films

This section presents a review of the applications of Raman spectroscopy to diamond films. The issues considered are the identification of the coexisting diamond and graphitic phases in diamond films and the effect of the graphitic phase on the film quality. Moreover, the issue of the Raman lineshape of the diamond and the physical mechanisms affecting it is addressed.

Identification of Bonding Configurations.

Important applications of Raman spectroscopy to diamond films are the identification of the diamond structure and the amorphous structure of the sp^2 carbon (graphitic phase) that coexist in many of the diamond films [22-24]. Shroder *et al.* [23] have developed a model in which the concentrations of diamond and graphitic components in diamond films may be obtained from the Raman intensities. The following section outlines the principal results.

The Raman intensity from a material (in a backscattering geometry), I, has been shown by Loudon [25] to follow the relation:

$$I = \frac{I_0 S}{S + \alpha_1 + \alpha_2}\left\{1 - \exp\left[-\left(S + \alpha_1 + \alpha_2\right)L\right]\right\}$$

where S is the scattering efficiency, I_0 is the incident intensity, L is the sample thickness in the direction of the incident laser light, and α_1 and α_2 are the absorption coefficients at the frequencies of the incident and scattered light respectively. Wada & Solin [26] showed that the equation could be modified to give the ratio of the Raman intensities of two different materials:

$$\frac{I_D}{I} = \frac{I_{0D}}{I_0}\left[\frac{A_D}{A}\right]\left[\frac{L_D\left(\alpha_1 + \alpha_2\right)}{1}\right]\left[\frac{\Delta\Omega_D}{\Delta\Omega}\right]\left[\frac{1 - R_D}{1 - R}\right]^2\left[\frac{\left\{\sum_j\left(\hat{\mathbf{e}}_2 \bullet \mathbf{R}_j \bullet \hat{\mathbf{e}}_1\right)^2\right\}_D}{\left\{\sum_j\left(\hat{\mathbf{e}}_2 \bullet \mathbf{R}_j \bullet \hat{\mathbf{e}}_1\right)^2\right\}}\right] \quad (1)$$

where S has been redefined in terms of a scattering efficiency (A), and a summation over the inner product of the Raman tensor ($\mathbf{R}_j$) and the polarization unit vectors of the incident and scattered light, $\hat{\mathbf{e}}_1$ and $\hat{\mathbf{e}}_2$. I is the scattering intensity of the material being compared; I_D represents the scattered intensity from the diamond, and I_0 is the incident intensity. $\Delta\Omega$ is the solid angle into which light is scattered, and the term involving R is a correction term for reflection of the scattered light at the sample surface and multiple reflections within the sample. Here, α_1 and α_2 are the previously defined absorption coefficients of the material to be compared to diamond since it has been assumed that diamond is transparent to the visible laser radiation.

In order to investigate the Raman intensity from a composite, Shroder *et al.* [23] prepared samples consisting of compressed powder of ~1 μm diamond and ~ 40 μm graphite particles for which the concentrations in each sample were known. In order to apply Eq. 1 to the diamond-graphite composite samples several approximations relevant to the experimental conditions had to be made. The first approximation was that the values of L_D and $\Delta\Omega$ were the same for both materials since the Raman signal was being collected from a region of discrete particles. Moreover, the reflection losses due to light scattering between the graphite and diamond particles were assumed to be minimal and thus were disregarded. Finally, due to the random orientations of the particles, an angle-average value of the summation over all possible polarization directions was taken.

In light of these approximations, the ratio of the Raman scattering intensities of diamond to graphite may be given as:

$$\frac{I_D}{I_G} = \frac{4A'_D N_D V_D}{3A'_G N_G V'_G} = \frac{4A'_D N_D V_D}{3A'_G N_G V_G}\left[\frac{V_G}{V'_G}\right] \quad (2)$$

where A' is the angle- and polarization- averaged scattering efficiency per nearest-neighbor bond, N is the atomic density and V_D is the volume of the diamond particle which is sampled by the Raman scattering. The absorption factor of graphite is accounted for in the V'_G/V_G term which represents the fraction of each graphite particle sampled in the Raman process. Such a discriminating proportionment of volume is not applicable to diamond since it is essentially transparent to the laser light, so the entire volume of diamond is sampled by the Raman scattering. The factor of 4/3 accounts for diamond having four nearest neighbors and graphite having three nearest neighbors at each site. Equation 2 can be written in terms of the percentage of diamond in the composites, P_D, as follows:

$$\frac{I_D}{I_G} \sim \frac{4A'_D}{3A'_G}\left[\frac{P_D}{1-P_D}\right]\left[\frac{V_G}{V'_G}\right] \quad (3)$$

The absorption factor is accounted for in the V'_G/V_G term. At 514.5 nm laser excitation, graphite has an absorption depth of ~30 nm [26]. However, because the scattered light must also exit the absorption region, an absorption length of ~15 nm was considered instead (see Fig. 1a). The ratio of the scattering efficiencies, A'_D/A'_G, was taken to be ~1/75 [26].

Equation 3 states that for a given composite the relative Raman intensities are modulated not only by the relative Raman scattering efficiency but also by the volume of the absorbing component, which is actually sampled by Raman scattering. The effect of the absorption on the Raman spectra can be seen qualitatively in the spectra presented in Fig. 1b. In the figure, the spectra of diamond-graphite composites (of ~1μm diamond and ~40 μm graphite particles) is shown for which the relative concentration of diamond in the samples ranges from ~1% up to 60%. An interesting aspect of these spectra is that the ~1% diamond composite displays a 1:1 ratio between the peak intensities of diamond and graphite. At 50% diamond concentration, it can be seen that the peak due to graphite has practically disappeared even though the Raman cross section is 75 times larger in graphite than in diamond. Thus the absorption of graphite has a significant effect on the Raman spectra of the composites, as is shown in the large disparity of the measured intensities of the samples.

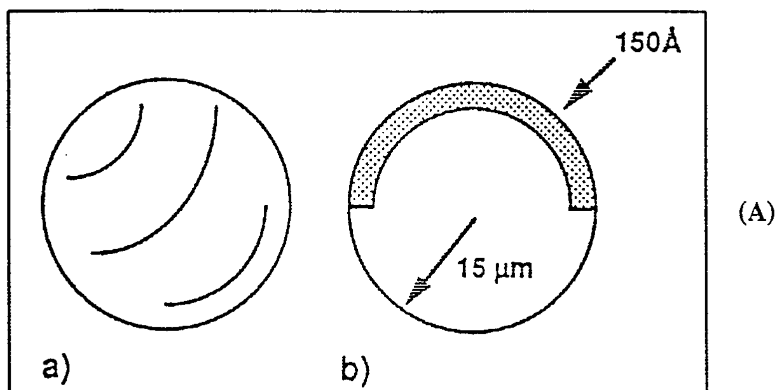

(A)

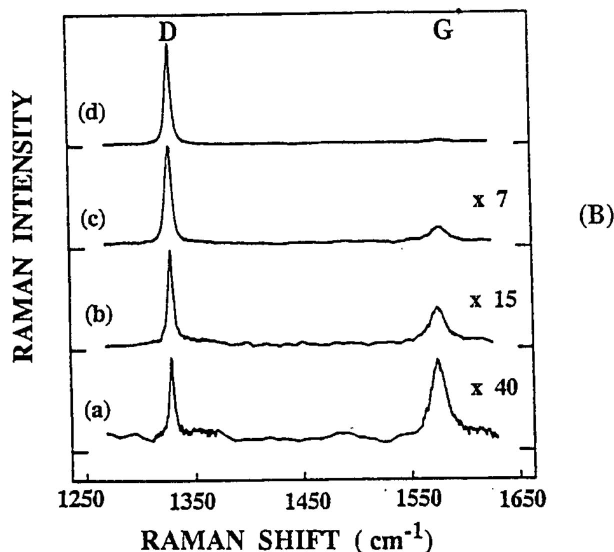

(B)

Figure 1. (A) Model of the unit volumes in the Raman scattering from composites. (a) fully illuminated diamond particle of ~ 30 µm size and (b) graphite particle ~ 30 µm size, partially illuminated in a 15 nm surface layer. (B) The Raman spectra of the composites of diamond and graphite powders. The relative concentrations of diamond in the samples are (a) 1.3%, (b) 6.6%. (c) 21.5%, and (d) 50%. The diamond band (D) is at 1332 cm^{-1} and the graphite band (G) is at 1580 cm^{-1}. From [23].

The quantitative predictions of the model, as given in Eq. 3, are evidenced in Fig. 2, where the ratio of the two peaks versus concentration of diamond is plotted for various particle sizes of graphite. It can be seen in the figure that when the particle size was taken to be 42 µm, the model and the experimental data are in agreement. Within the model, when the graphite domains are smaller than the absorption length, the value of V'_G/V_G becomes 1, and the effect

of absorption can be ignored. The only intensity-modulation factor in that case is the relative Raman scattering efficiency. In high-quality diamond film, the graphitic domains are very small, so in applying the model in most cases the absorption effect may similarly be ignored.

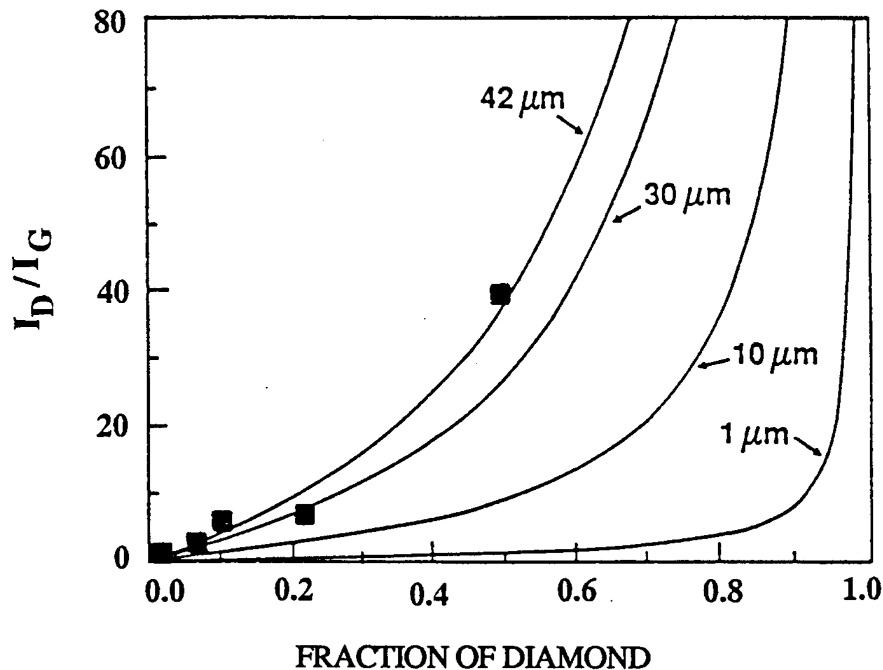

Figure 2. Ratio of peak intensities (I_D/I_G) vs relative concentration of diamond in the composite samples. The solid lines are derived from Eq. 3 assuming an average graphite particle size of 42, 30, 10, and 1 µm, respectively. From [23].

Recent investigations of photoluminescence and Raman scattering in diamond thin films have shown that the graphitic phase affects the optical as well as the mechanical properties of the diamond [27-29]. In many diamond films a strong broadband luminescence extending from approximately 1.5 to 2.5 eV and centered at ~2 eV has been observed [30]. The photoluminescence has been shown to result from transitions of an in-gap state-distribution which has been attributed to the graphitic disordered phase in the diamond films [28]. Moreover, it has been determined that the internal compressive stress in diamond thin films is due to various impurities and defects present in the film, in particular due to the graphitic phase [29, 31].

The Diamond Raman Lineshape of Diamond Films

The Raman frequency of a high quality material yields information about the vibrational energy of the phonons whereas the Raman linewidth is a measure of the phonon-lifetime. When the quality of a material is degraded due to the presence of defects, the resulting Raman lineshape reflects the effect of the defects on the phonon-characteristics. The focus of this section is recent investigations of Raman lineshape as it relates to the various defects which are present in diamond thin films.

The Raman linewidth in general can be broadened via several mechanisms: the main mechanisms applicable to the diamond line are homogeneous broadening [32] and broadening due to the size effect of the crystal, a theory which has been developed to explain the lineshape of boron-nitride material [17]. Homogeneous broadening arises from a decrease of the lifetime of the crystal phonons. The theory of homogeneous spectral lineshape predicts that the linewidth is inversely proportional to the phonon lifetime and that the lineshape is expected to be a Lorentzian [33]. The other possible mechanism which results in Raman line broadening is phonon confinement in a small domain size [17].

The well-established confinement model is based on the uncertainty principle, $\Delta k \sim 2\pi/d$, which states that the smaller the domain size d, the larger the range of different phonons that are allowed to participate in the Raman process. Hence the broadening of the Raman line in this case is due to the spread in phonon energy, and the lineshape reflects the shape of the phonon-dispersion curve. The Raman lineshape in the phonon-confinement model is given by

$$I(w) \cong \int_0^1 \frac{dq \exp(-q^2 L^2 / 4) 4\pi q^2}{[\omega - \omega(q)]^2 + (W_0 / 2)^2} \tag{4}$$

where L is the confinement size, W_0 is the diamond natural linewidth (~2 cm^{-1}), and $\omega(q)$ is the phonon-dispersion curve of the form A+B*cos($q\pi$) [17, 34-36]. In general the width, shape, and peak position are dependent on the specific character of the phonon dispersion curves. In particular for silicon, the above model predicts that as the crystalline domain size decreases, the peak of the Raman line shifts to a lower frequency and the lineshape becomes asymmetric [35].

Ager *et al.* [34] have investigated the application of the confinement model to the Raman lineshape of diamond thin films. For each of the relevant phonon-dispersion relations, Ager *et al.* modeled the expected lineshape using the confinement model (Eq. 4) and compared the results to the Raman lineshape of diamond films. The study of the expected Raman line involved three sets of lineshape calculations in which different one-dimensional dispersion curves were used. First, in case (a), a dispersion relation was used for which the phonon frequency decreases away from the Γ point. The dispersion relation has the form $\omega(q)=A+B\cos(q\pi)$, where A=1241.25 cm^{-1} and B=91.25 cm^{-1}; the shape of this curve is similar to that used in Si and GaAs phonon-confinement calculations. For case (b) the Δ_2 (O) dispersion curve was used; this curve in diamond has a shallow maximum which is farther from the Γ point. Figure 3 depicts the characteristics of the first two dispersion relations [37]. Lastly, in case (c) the weighted averaged 3D dispersion curve was used in the calculations (see [34] for a more detailed analysis).

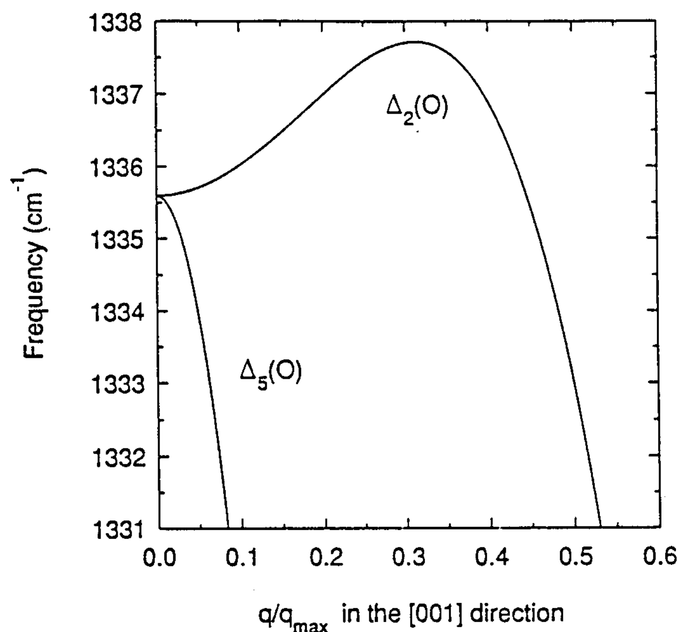

Figure 3. Detail of the (001) phonon-dispersion curves for diamond. The $\Delta_5(O)$ has a maximum at Γ point. The $\Delta_2(O)$ curve exhibits a shallow maximum away from the Γ point. From [34, 37].

Figure 4 presents the Raman linewidth vs. the Raman frequency, as obtained from Eq. 4, for the three cases of dispersion relations. Also presented in the figure is the correlation of the Raman linewidth vs. frequency which was obtained from diamond films. Figure 5 shows the

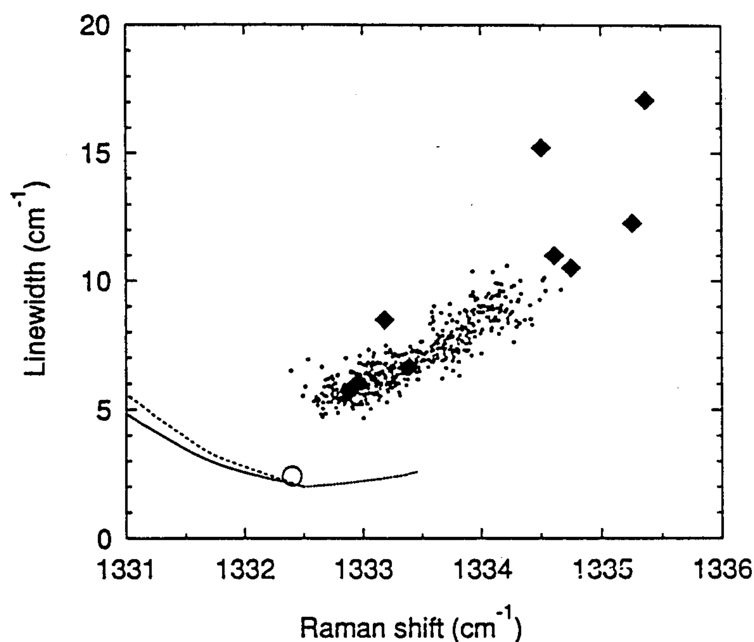

Figure 4. Raman linewidth vs Raman frequency for diamond: (circle) single-crystal; (diamonds) single-point measurements from ten diamond films; (dots) 500 spatially resolved measurements from one sample; (solid lines) phonon-confinement theory as predicted from case (a); (dotted line) the predicted model case (b), and (long dashes) of case (c). From [34].

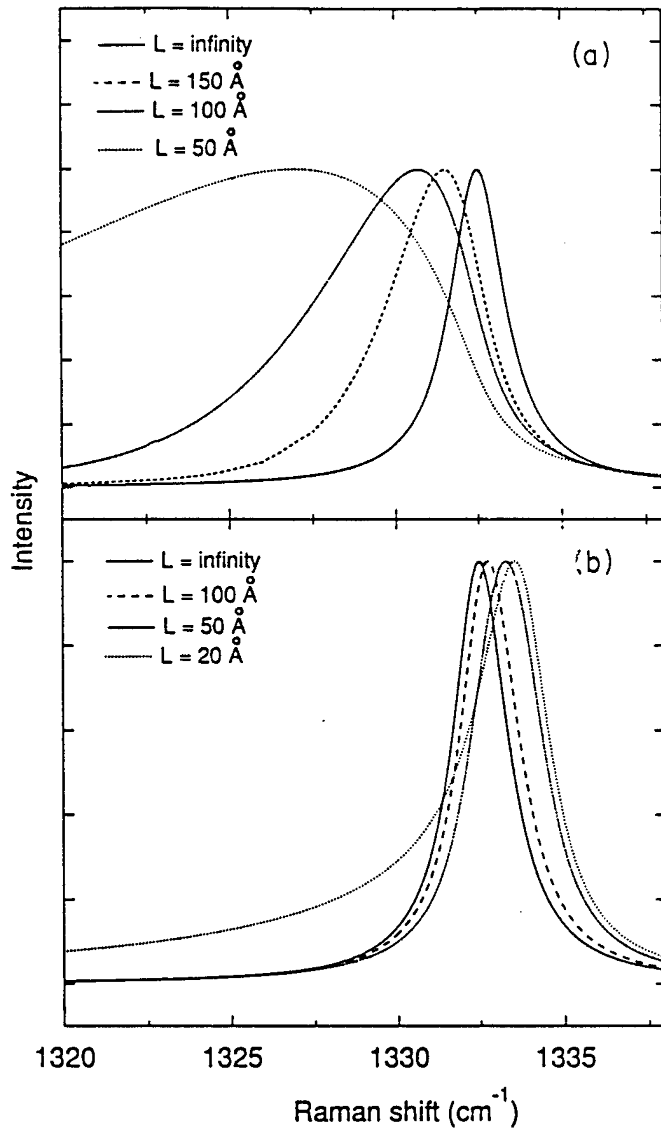

Figure 5. Calculated Raman lineshapes from the phonon confinement theory for different values of domain size L. (a) results when using dispersion relation described in case (a), (b) the results of case (b). From [34].

predicted Raman lineshapes as calculated from the phonon confinement theory for various values of domain size, L, and for dispersion relations (a) and (b). In Fig. 6 the Raman spectra of diamond films and crystal are presented. As is shown in the figures there is significant disagreement between the Raman diamond lineshapes obtained from diamond films (which are symmetric) and those predicted from the confinement model (which are asymmetric). Moreover, the confinement model predicts a red shift of the Raman frequency as the line gets broader, which is opposite in behavior to the observed diamond peak frequencies.

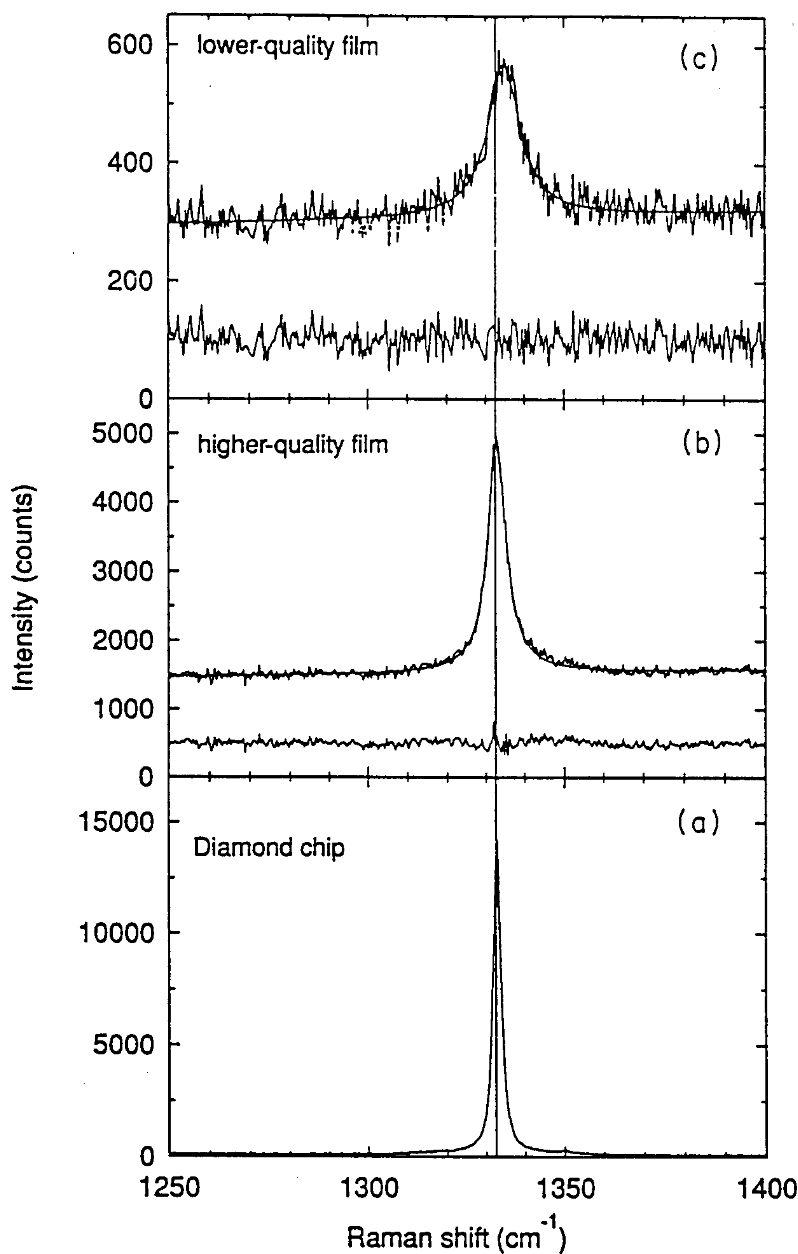

Figure 6. Raman spectra of diamonds. (a) Type IIa synthetic diamond. (b) High quality diamond film, and (c) lower-quality diamond film. The lines exhibit a Lorentzian lineshape. From [34].

From these results Ager *et al.* have concluded that the size effect in diamond films is not a dominant factor in determining the lineshape characteristics of diamond films. They suggested that the internal compressive stress in diamond is a more likely mechanism in determining the Raman line shape. Results similar to those obtained by Ager *et al.* also have been reported by Bergman & Nemanich [29]; moreover, in the latter study the Raman lineshape was found to be correlated to the internal compressive stress imposed, for the most part, by the graphitic phase present in the diamond thin films.

Recently a study of the Raman lineshape of nanometer-sized diamond particles was conducted by Yoshikawa *et al.* [38]. The diamond particles, referred to as cluster diamond, are produced via detonation of explosives, and have promising potential in a variety of mechanical applications [38]. The observed Raman spectrum of the cluster diamond has been found to agree with that calculated by the phonon confinement model. A Raman spectrum and the calculated lineshape are presented in Fig. 7. As is depicted in the figure the Raman frequency is 1320 cm^{-1} (which is a decrease from the 1332 cm^{-1} frequency of crystalline diamond or high quality film); moreover, the lineshape of the cluster diamond is asymmetric. The particle size which has been calculated via the confinement model, L=55 Å, agrees with that estimated from X-ray measurements [38].

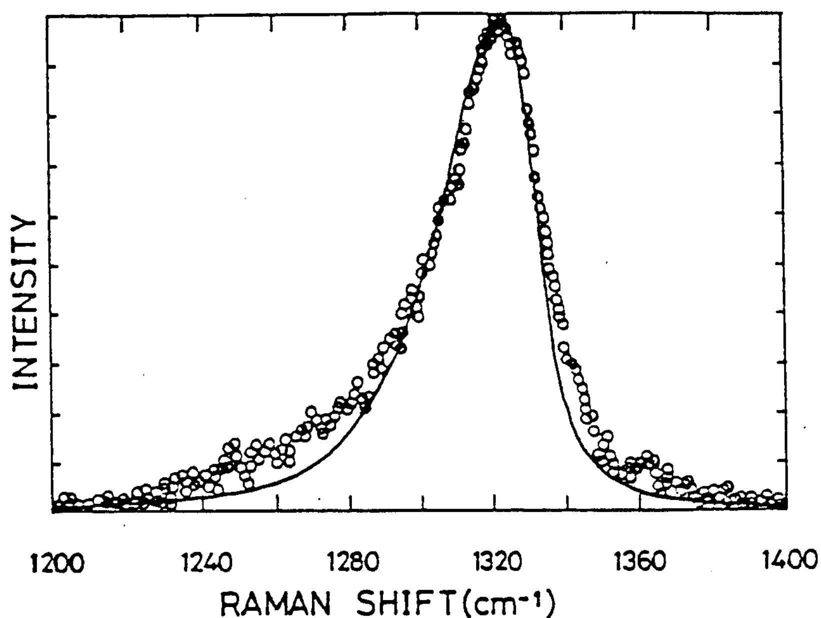

Figure 7. The Raman lineshape of cluster diamond; experimental data (circles) calculated line (solid line). From [38].

Gallium Nitride

In this section the Raman modes of the hexagonal wurtzite (WZ) and the cubic zinc-blend polytype structures of GaN are summarized. The effect of pressure and free carriers on Raman frequency and lineshape of the WZ structure is discussed. Lastly, a short summary of the behavior of the optical modes of mixed alloys is presented followed by a discussion of the Raman characteristics of $Al_xGa_{1-x}N$ alloy.

Gallium nitride in the stable state has a wurtzite crystal structure and belongs to the space group C_{6v}^4. The group theory predicts that there are six Raman active modes represented by

[39] $A_1+E_1+2E_2$. The A_1 mode splits into longitudinal (LO) and transverse (TO) components, as does the E_1 mode; the two E_2 modes are non-polar modes. Table I lists the observed Raman frequencies which have been reported in [40-42].

Table I. The Frequencies in Units of cm^{-1} of the WZ Gallium Nitride Raman Modes

A_1(LO)	A_1(TO)	E_1(LO)	E_1(TO)	$E_2^{(1)}$	$E_2^{(2)}$	Reference
—	533	—	559	145	568	[40]
710	—	741	—	—	—	[41]
738	—	—	—	—	570	[42]

The GaN samples that have been investigated by Manchon *et al.* [40] were in a crystalline form that was prepared by heating a pre-purified GaN powder at 1200°C. The A_1(LO) and the E_1(LO) modes reported in [41] were obtained from a crystalline sample and from an epitaxial GaN film grown on sapphire substrate, respectively. The samples reported in [42] were all grown on c-plane (0001) sapphire substrates. The frequency of the A_1 (LO) mode reported by the latter group is blue shifted by 28 cm^{-1} from the A_1 (LO) at 710 cm^{-1} reported in [2]. The blue shift has been tentatively ascribed to effects due to stress in the film [42].

A detailed study of the effect of pressure on the crystalline GaN Raman lines has been reported in [43]. The applied pressure was hydrostatic in the range 0 to ~50 GPa. The pressure dependence of the Raman frequencies of the A_1 (TO), E_1 (TO), $E_2^{(2)}$, and $E_2^{(1)}$ modes has been shown to follow the quadratic relation:

$$\omega(cm^{-1}) = \omega_0 + \sigma_1 P + \sigma_2 P^2 \tag{5}$$

where P is the applied pressure in units of GPa, ω_0 is the Raman frequency at zero applied pressure, and σ_1 and σ_2 are the first and second pressure coefficients. Table II presents the set of parameters that describe all the observed mode characteristics under the applied pressure. Figure 8 depicts the pressure dependence of the Raman frequencies which were generated by applying Eq. 5 to the data presented in Table II.

An interesting phenomenon of a phase transition at high pressure conditions has been observed by the researches in [43]. When the applied pressure exceeded 45 GPa the GaN crystal became dark and the Raman signal disappeared. The researchers suggested that at a pressure of ~48 GPa a phase transition might be taking place from the WZ stable structure to the NaCl structure.

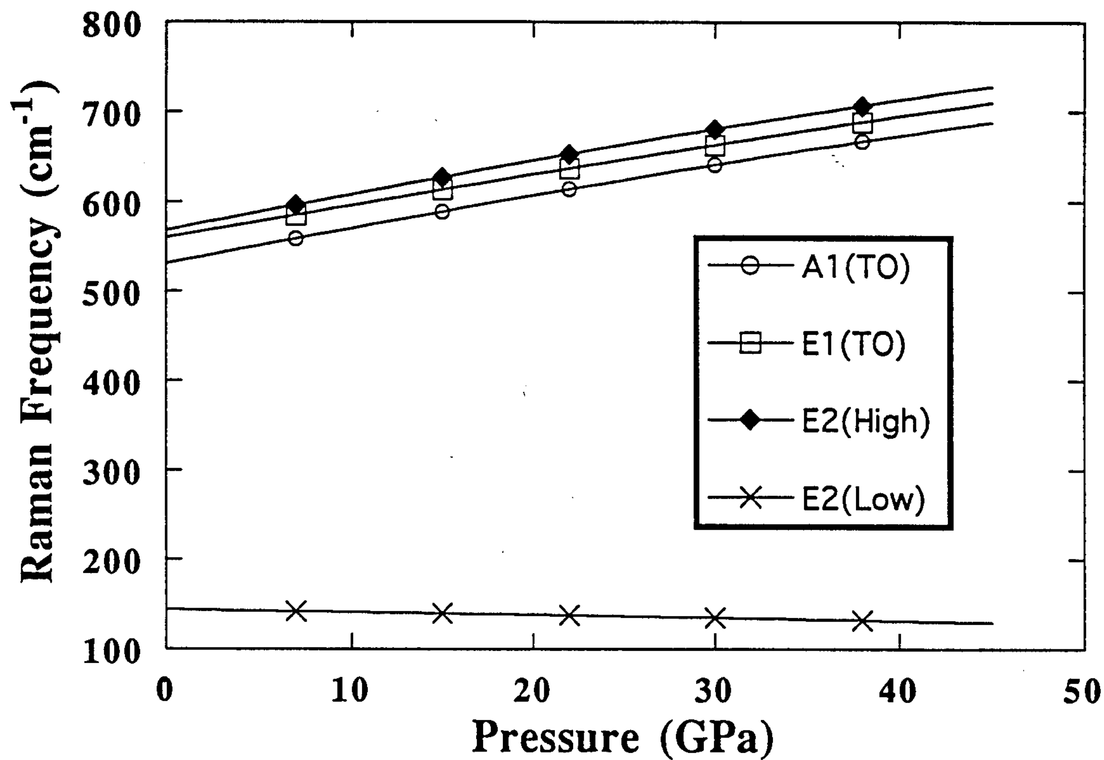

Figure 8. The pressure dependence of the Raman frequencies of WZ GaN. From data [43].

Table II. The Parameters of the Pressure Relation for the Raman Modes [43]

mode	ω_0 cm^{-1}	σ_1 cm^{-1}/GPa	σ_2 cm^{-1}/GPa^2
A_1 (TO)	531	4.06	- 0.0127
E_1 (TO)	560	3.68	- 0.0078
$E_2^{(2)}$	568	4.17	- 0.0136
$E_2^{(1)}$	144	- 0.25	- 0.0017

Another mechanism which affects the Raman lineshape in GaN is the coupling of the phonons to the plasma oscillations of the free carriers (plasmons). Klein *et al.* have developed a model which predicts the Raman lineshape for the case of phonon-plasmon interactions [44]. According to the model, when a material contains free carriers in an appreciable concentration, the Raman cross section may be modulated by two mechanisms. The first mechanism is the modulation of the Raman polarizability by the atomic displacement (deformation-potential-

mechanism), and the modulation via the longitudinal electric field of the carriers (electro-optic mechanism). The second mechanism is that of direct scattering events caused by the electronic-charge-density fluctuations. In SiC [44], GaP [45], and in GaN [19] the scattering events due to the electronic-charge-density fluctuations are found to have a much smaller effect than the deformation-potential and the electro-optic mechanisms. Thus the electronic-charge-density fluctuations mechanism may be neglected. The equation of the Raman lineshape based on this model is rather complex and has been used to fit the data [46]. However the curve fit of the experimental data to the equation yields, among other physical parameters, the plasmon frequency ω_p, from which the value of the concentration of free carriers, n, can be determined:

$$n = \frac{\omega_p^2 \varepsilon_\infty m^*}{4\pi e^2} \tag{6}$$

where for a given material e is the electron charge, m* the electronic effective mass, and ε_∞ the high frequency dielectric constant.

The determination of the concentration of free carriers via Raman spectroscopy is often more advantageous than that via electrical measurements since no contacts are required. The former technique has been proven to be effective in the determination of the free carriers concentration in doped SiC [47] and doped GaP [46]. Recently Kozawa *et al.* investigated the LO phonon-plasmon coupled modes in GaN [19]. Figure 9 shows the Raman spectra of the A_1(LO) mode at several doping levels; in the figure the Raman band shifts towards the high-frequency side and broadens with an increase in the carrier concentration. The spectra of the A_1(LO) coupled mode as well as the model-predicted lineshape are presented Fig. 10. The inset to the figure lists the values of the fitting parameters among which is the plasmon frequency ω_p, from which the carrier concentration may be evaluated (via Eq. 6 as described previously). Figure 11 shows the carrier concentration, n, calculated from the Raman data versus those obtained from the Hall measurements. As is shown in the figure, the values of the concentrations obtained in both techniques agree.

In contrast to the more well-researched hexagonal GaN, due to the difficulty in achieving high-quality cubic GaN samples little information is available on the Raman characteristics of the cubic phases. However, a few recent results have been reported in this area. Miyoshi *et al.* have managed to grow high-quality cubic zinc blend GaN films on (100) GaAs substrates [48]. The researchers observed the LO mode at 730 cm^{-1} and the TO mode at around 550 cm^{-1}. Humphreys *et al.* have achieved both cubic and WZ GaN epitaxial films which have been grown on (0001) sapphire substrates [49]. The difference between growth temperatures of the substrates was suggested to give rise to the different observed phases. A Raman peak at ~ 740 cm^{-1} was also observed in the spectra and was attributed to the cubic phase of GaN.

Lastly, recent calculations [50] predict the frequency of the Raman TO mode of the cubic zinc-blend structure to be 558 cm^{-1}.

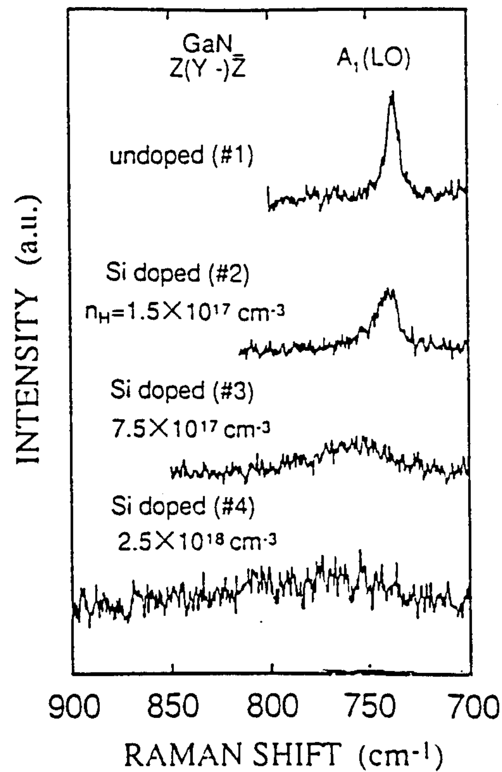

Figure 9. Raman Spectra of the A_1(LO) mode of GaN at several doping levels. From [19].

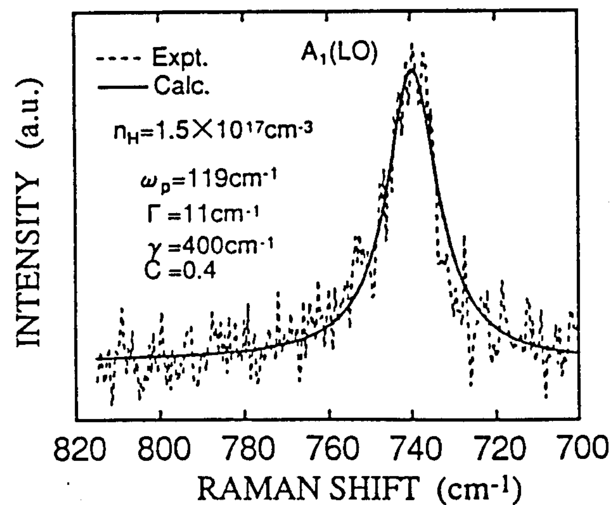

Figure 10. The experimental data and the calculated Raman lineshape of the A_1(LO) mode of GaN. From [19].

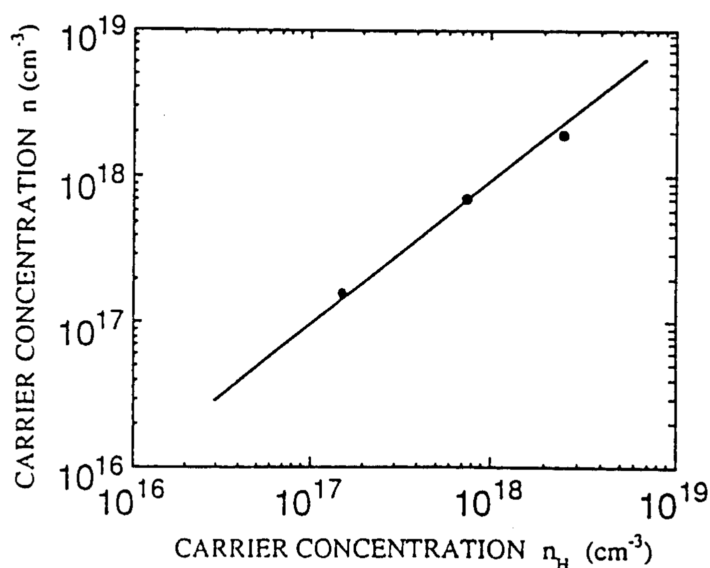

Figure 11. The free carrier concentration calculated from the Raman data vs the concentration n_H obtained from the Hall measurements. From [19].

In the remainder of this section the issue of mixed alloys is addressed. One of the most promising materials for the fabrication of opto-electronic devices is the $Al_xGa_{1-x}N$ alloy series [51-54]. The optical properties of the $Al_xGa_{1-x}N$ alloys are, to a large extent, unknown at the present time. The lack of information is mainly due to the difficulty of growing the material. The first to report the Raman characteristics of $Al_xGa_{1-x}N$ alloys were Hayashi *et al.* [55]. Their analysis was based on previous investigations of the optical phonons in other families of mixed crystals [56]. A brief review of these fundamental antecedent results is outlined next, followed by a discussion of the application to $Al_xGa_{1-x}N$.

It has been established that mixed crystals of the form $AB_{1-x}C_x$ may be classified into two main classes according to the behavior of the **k**~0 optical phonons [56]. Figure 12 depicts the two classes which are referred to as the one-mode and two-mode material respectively. In general, if the frequencies of the AB and AC components are greatly different, a two-mode behavior is expected; if the frequencies of both components have proximate values a one-mode behavior results. As can be seen in Fig. 12a, for an intermediate composition x, in the two-mode class of materials two sets of frequencies have usually been observed in the spectra. One set of frequencies is due to the LO and TO modes of the lighter AB component, and the other set is due to the LO and TO modes of the heavier AC component. The frequencies of the two-mode material are not linear with x; moreover, the modes are degenerate at x~0 and x~1. The degenerate mode at x~1 has been attributed to a local mode which arises from a residual concentration of the B component present in the AC component. On the other hand, the degenerate mode at x~0, which occurs in the composition region where AB is almost pure, has been regarded as a resonance gap-mode arising from residuals of C defects in the AB component.

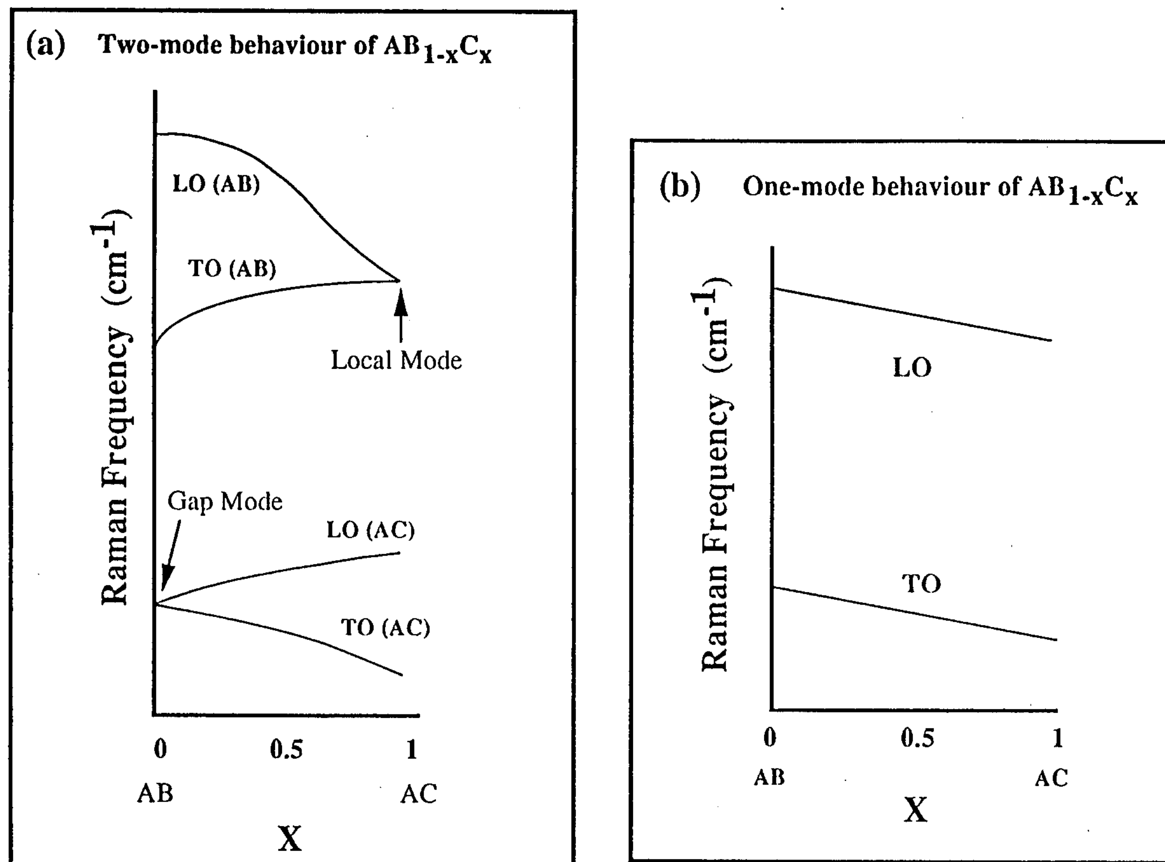

Figure 12. The two classes of mixed crystals: (a) two-mode type and (b) one-mode type material.

The phonons of the one-mode class of materials exhibit fundamentally different behavior than that of the two-mode materials. It can be seen in Fig. 12b that only one set of LO and TO frequencies is present and that the frequencies vary linearly with the composition from the AB component to the AC component. In addition to the one-mode and two-mode classes of materials there exists an intermediate class which exhibits two-mode behavior over a certain composition range and one-mode behavior over the rest of the range. The intermediate type of behavior has been observed in some of the III-V crystals [57] including $AsGa_{1-x}In_x$, $GaAs_{1-x}Sb_x$, $SbGa_{1-x}In_x$, and $InAs_{1-x}Sb_x$.

Raman studies of $Al_xGa_{1-x}N$ films in the composition range $0<x<0.15$ have been recently described [55]. Figures 13 and 14 present the Raman spectra and the frequencies as a function of composition respectively. The 0.15 composition range studied in [55] corresponds to the range in Fig. 12 where the AC (GaN) component is in an almost pure state. Therefore, if the $Al_xGa_{1-x}N$ film in this composition range is one-mode then a linear dependence of the LO and TO modes on the composition is expected. Moreover, the slopes of the two lines should have the same sign. If the film is of a two-mode type then the LO and TO dependence on composition is expected to be nonlinear and the slopes to be of opposite sign. Also a local mode, due to residual concentration of Al atoms in the GaN matrix, should exist.

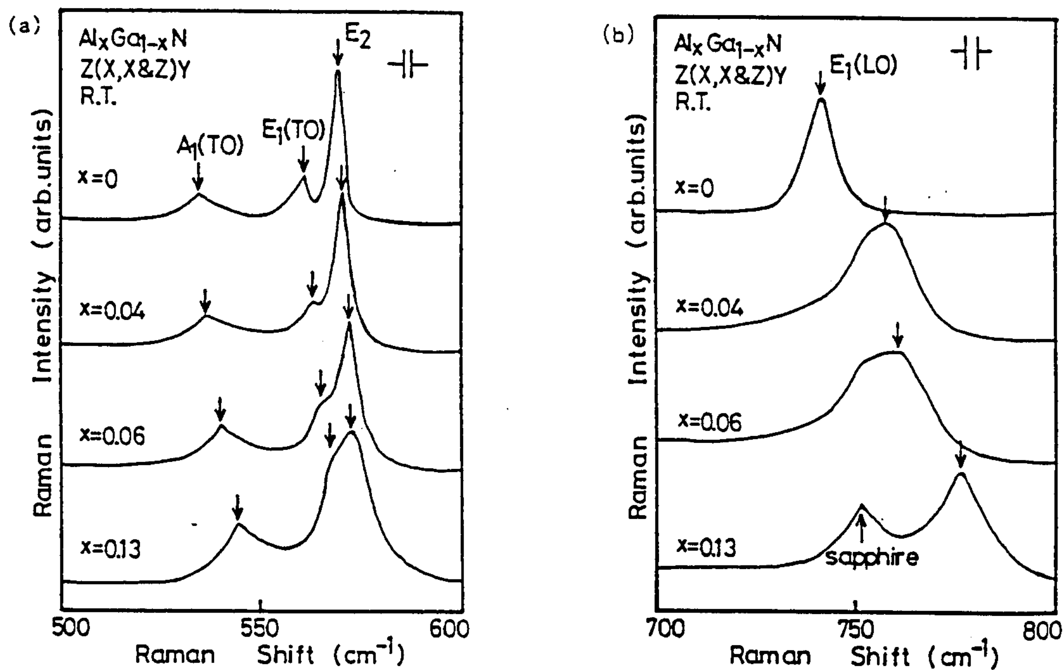

Figure 13. Raman spectra of (a) A_1(TO), E_1(TO), and E_2 modes and (b) E_1(LO) of $Al_xGa_{1-x}N$ at various compositions x. From [55].

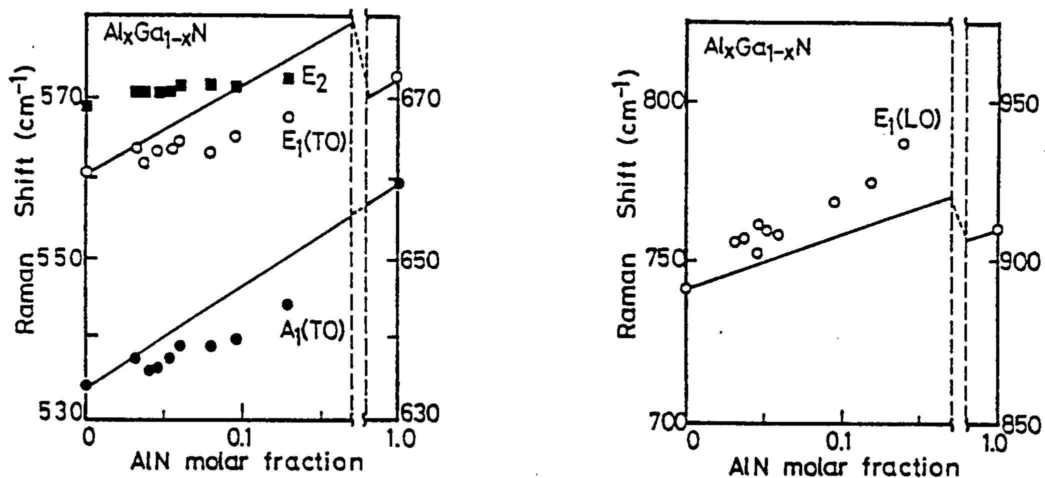

Figure 14. Compositional dependence of E_2, E_1(TO), A_1(TO), and E_1(LO) modes of $Al_xGa_{1-x}N$. From [55].

The E_1(TO) and E_1(LO) Raman frequencies which have been investigated by Hayashi *et al.* have been shown to comply, according to the above criteria, with the one-mode behavior [55]. As can be seen in Fig. 14, both E_1(TO) and E_1(LO) frequencies exhibit a linear increase (with a small deviation of unknown origin) with the Al composition and no local mode due to Al was observed.

Aluminum Nitride

In the following a review of the Raman active modes of the wurtzite AlN is presented and the effect of applied pressure on the Raman frequencies as well as the effect of oxygen impurity on the Raman characteristics is discussed.

AlN, like GaN, in the stable state has a wurtzite crystal structure and belongs to the space group C^4_{6v}. The group theory prediction are essentially the same as described above [39]. Table III lists the observed Raman frequencies of AlN single crystals reported in [15, 58-60]. As is shown in the table, there is a large variance in the reported frequencies for a given mode. This variance may be attributed to the crystalline quality of the AlN samples [58].

Table III. The Raman Frequencies in Units of cm^{-1} of the WZ Aluminum Nitride Modes

A_1(TO)	A_1(LO)	E_1(TO)	E_1(LO)	$E_2^{(1)}$	$E_2^{(2)}$	reference
614	893	673	916	252	660	[58]
607	—	—	924	241	660	[15]
659	888	671	895	—	—	[59]
667	910	667	910	—	655	[60]

Raman scattering studies of AlN crystals under pressure have been conducted by Perlin *et al.* [15] and by Sanjurjo *et al.* [59]. The applied pressure was hydrostatic in the range of 0-14 GPA. Both groups observed that the Raman frequencies of the AlN modes increase almost linearly with applied pressure. The pressure dependence of the Raman frequency ω reported by Perlin *et al.* [15] is of the form

$$\omega(cm^{-1}) = \omega_0 + \sigma_1 P + \sigma_2 P^2 \qquad (7)$$

where P is the applied pressure in units of GPa, ω_0 is the Raman frequency in no-pressure conditions, and σ_1 and σ_2 are the pressure coefficients. A slightly different pressure dependence of the form

$$\omega(cm^{-1}) = \omega_0 + \sigma_1 P \qquad (8)$$

was reported by Sanjurjo *et al.* [59]. Table IV presents the set of parameters for Eq. 7 and 8 describing the observed mode characteristics for both studies.

Table IV. The Parameters of the Pressure Relation for the AlN Raman Modes

Mode	ω_0 cm^{-1}	σ_1 cm^{-1}/GPa	σ_2 cm^{-1}/GPa^2	Reference
A_1 (TO)	607	4.63	- 0.01	[15]
E_1 (LO)	924	1.67	0.27	[15]
$E_2^{(2)}$	660	3.99	0.035	[15]
A_1 (TO)	659	4.97	—	[59]
A_1 (LO)	888	3.8	—	[59]
E_1 (TO)	671	4.84	—	[59]
E_1 (LO)	895	4.0	—	[59]

The high solubility of oxygen impurities in AlN has been shown to degrade the optical and thermal properties of the material [61-63]. Moreover, it has been observed that a critical oxygen concentration exists past which the photoluminescence, thermal conductivity, and the unit-cell volume undergo a significant change in characteristics [61]. Figure 15 shows the thermal resistance as a function of oxygen content [61-63]. As is evident from the figure, at ~ 0.8 at.% oxygen concentration, a change in the behavior of the thermal resistance occurs.

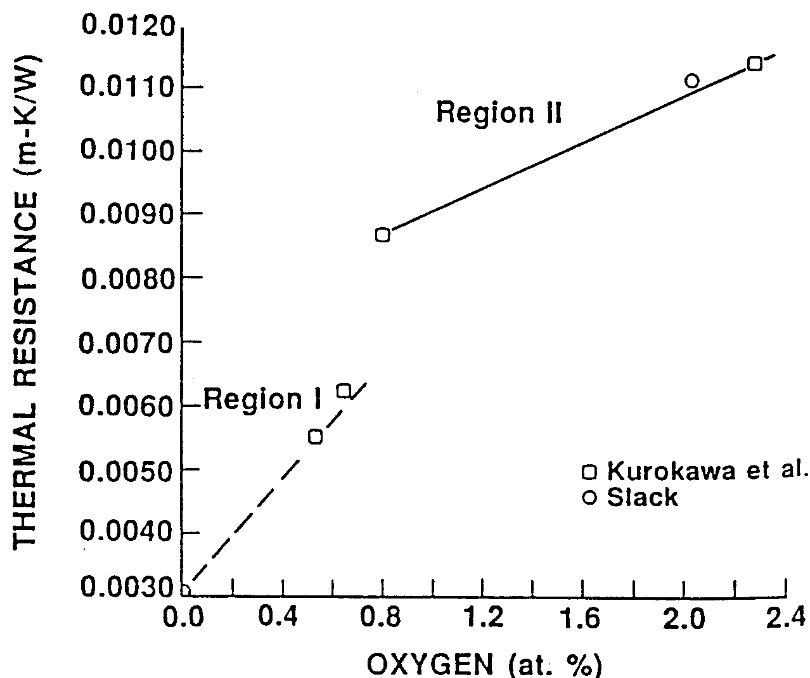

Figure 15. Thermal resistance of AlN as a function of oxygen concentration. From [61].

The influence of the oxygen impurity concentration on the Raman lineshape, as investigated by McNeil *et al.*, showed a similar trend to that above [58]. Figure 16 presents the Raman linewidth as a function of oxygen concentration: at the critical concentration of ~ 0.8 at.% a transition in the behavior of the linewidth is noted. The observed phenomenon of a critical oxygen concentration has been attributed to a change in the structure of the oxygen defect; up to 0.8 at.% the oxygen impurity is a point-like defect and above that concentration the oxygen is in the form of an extended defect [58, 61].

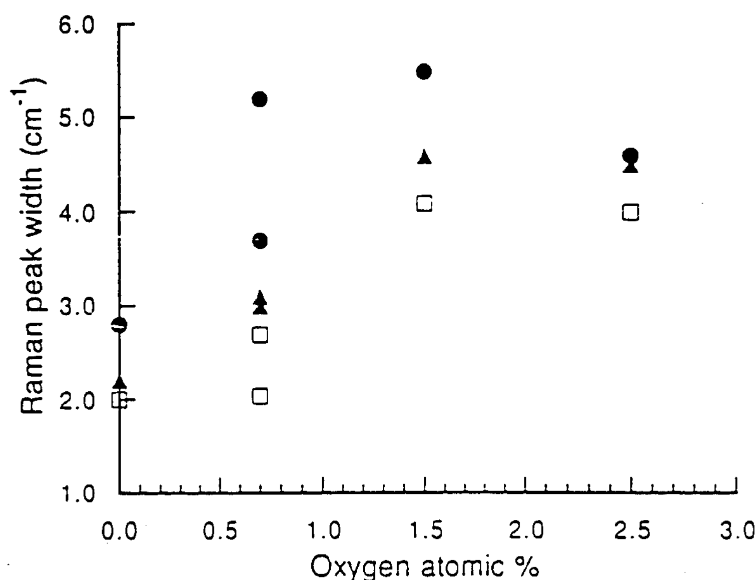

Figure 16. Raman linewidth of AlN vs oxygen concentration for E_1 mode (square), A_1 mode (circle), and E_2 mode (triangle). From [58].

Boron Nitride

Boron nitride can have the cubic, hexagonal, wurtzite, rhombohedral, or turbostratic structure [13]. Among these various structures only the zinc-blend cubic BN (c-BN) and the hexagonal BN (h-BN) have been investigated via Raman spectroscopy; this is due to the high quality crystals which have been achieved for these structures.

The following presents a review of Raman investigations of c-BN and h-BN. The bonding-anisotropy of the h-BN as well as the effect of the crystalline size on the Raman modes is discussed. Lastly, a review of the effect of high pressure and temperature on the Raman frequencies of h-BN and c-BN is presented.

The c-BN belongs to the T_d^2 space group and has LO and TO Raman active modes [60]. The h-BN on the other hand belongs to the D_{4h}^6 space group and has two E_{2g} Raman active modes [64]. Table V lists the Raman frequencies of the two structures [60, 65].

Table V. The Raman Frequencies of the h-BN and the c-BN

Frequency (cm^{-1}) of h-BN		Frequency (cm^{-1}) of c-BN	
Low frequency:	52.5 [65]	LO:	1304.0 [60]
High frequency:	1366.0 [65]	TO:	1056.0 [60]

The large variance in the Raman frequencies of h-BN (52 cm^{-1} and 1366 cm^{-1}) is due to the large anisotropy of the bonding configurations of this material. Figure 17 shows the crystal structure of h-BN: the structure consists of hexagonal planes of boron atoms bonded to nitrogen atoms. Within any plane there is a strong sp^2 bonding between the boron and the nitrogen atoms; however, only a weak Van der Waals bonding exists between planes. The low-frequency mode at 52 cm^{-1} is due to vibrations originating from adjacent planes sliding against each other (rigid-layer shear mode) while the high-frequency mode at 1366 cm^{-1} is due to in-plane vibrations between the boron and nitrogen atoms.

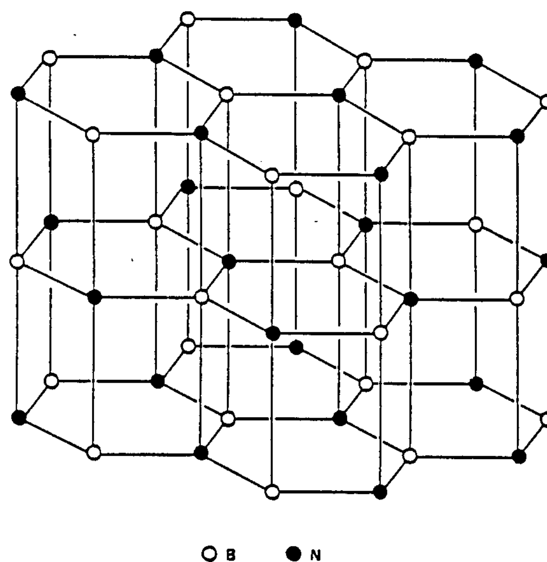

Figure 17. The crystal structure of the h-BN. From [17].

The effect of the crystallite domain size on the high-frequency 1366 cm^{-1} Raman mode of h-BN has been previously investigated [17]. The Raman measurements indicated that the Raman line shifted to higher frequency, broadened, and became asymmetric as the crystallite size decreased. It was shown in [17] that the observed Raman characteristics can be explained

via the phonon confinement model (see Eq. 4). Figure 18 depicts the experimental and calculated dependence of the Raman peak position on the crystallite size L. It is shown in the figure that the experimental data agrees with the model.

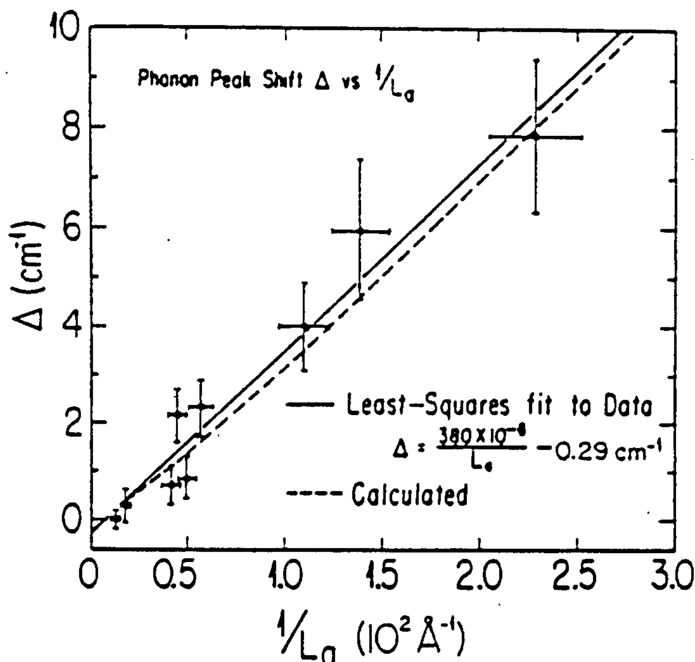

Figure 18. The dependence of the peak position of the high-frequency E_{2g} mode of h-BN vs 1/L. The solid line represents the Raman data while the dashed line represents the calculated peak position using the phonon confinement model. From [17].

The shift of the h-BN Raman line to higher frequency with decreasing confinement size is a manifestation of the unusual dispersion curves which h-BN is predicted to have; the phonon frequency of the highest branch is not a maximum at the Γ point [17]. For most crystalline solids the reverse is true; a decrease in the Raman shift (of the highest-frequency nonpolar mode) with decreasing crystallite size is expected as occurs in the case of silicon [36] and cluster diamond [38].

The effect of applied pressure (in the range 0-11 GPa) on the Raman modes of h-BN has been studied by Kuzuba *et al.* [66]. The researchers investigated the dependence of the high-frequency 1366 cm^{-1} and low-frequency 52 cm^{-1} modes on the pressure in order to study the anisotropy of the force constants. In the study it was observed that the high- as well as the low-frequency of the Raman modes increase with the applied pressure. However, the mode frequencies were found to increase with different rates, implying different pressure coefficients of 5 cm^{-1}/GPa for the low-frequency and 4 cm^{-1}/GPa for the high-frequency mode. Furthermore, the change in force constant (from the atmospheric value to the value at 11 GPa)

of both modes was calculated. It was found that the force constant of the low-frequency mode increased by a factor of four while that of the high-frequency mode increased only by 6%. The results of Kuzuba reflect the strong anisotropy of the force constants in h-BN.

Recently the pressure dependence of the LO and TO Raman modes of c-BN have been investigated [59]. The pressure coefficient for the LO and TO was found to be 3.45 cm^{-1}/GPa and 3.39 cm^{-1}/GPa respectively. In this pressure range, the pressure dependence, P, of the Raman frequency, ω, has been determined to follow the linear relation [59].

$$\omega_{LO} = 1305 + 3.45P$$
$$\omega_{TO} = 1054 + 3.39P$$

The results of the pressure dependence studies indicate that the pressure coefficients of c-BN are smaller than that of h-BN, implying that the Raman modes of c-BN comply less to stress than those of h-BN.

In addition to yielding information about the stress state, Raman spectroscopy is also a powerful tool in the study of the thermal properties of solids [67-69]. Recently the temperature dependence (in the range 300K-1830K) of the TO and LO Raman modes of c-BN has been investigated by Herchen & Cappelli [16]. The study indicated that the Raman frequency, ω, of both modes decrease with increasing temperature:

$$\omega = \omega_0 - a_1T - a_2T^2$$

where ω_0=1060.6 cm^{-1}, a_1=0.010 cm^{-1}/K, and a_2=1.42x10^{-5} cm^{-1}/K^2 for the TO mode, and ω_0=1307.6 cm^{-1}, a_1=0.003 cm^{-1}/K, and a_2=1.46x10^{-5} cm^{-1}/K^2 for the LO mode. Figure 19 presents the temperature dependence of the Raman frequencies of c-BN. The temperature behavior of the Raman frequency of crystalline diamond is also shown in the figure; it is evident that the temperature dependence of both materials is similar. The frequency change between room-temperature and 1800K was calculated for c-BN to be 5.6% and 3.8% for the TO and LO modes respectively, and 3.4% for diamond [16]. The similar temperature dependence of both materials implies that c-BN has thermal properties comparable to that of diamond.

To date no temperature dependence studies have been conducted on the anisotropy of the Raman frequencies of h-BN. However, the temperature response (in the range 300K-2325K) of the high-frequency E_{2g} Raman mode of h-BN has been studied by Exarhos & Schaaf [70]. The temperature dependence of the Raman frequency, ω, and the linewidth, $\Delta\omega$, were shown to follow the relations:

$$\omega^2 = 1372^2 - 71.98T - 1.197\times10^{-2}T^2$$
$$\Delta\omega = 7.67 + 3.62\times10^{-3}T + 5.22\times10^{-6}T^2$$

In addition, Exarhos & Schaaf outlined a method to calculate the intralamellar thermal expansion coefficient from the Raman analysis; the value was calculated to be 3.5×10^{-6} deg^{-1} [70].

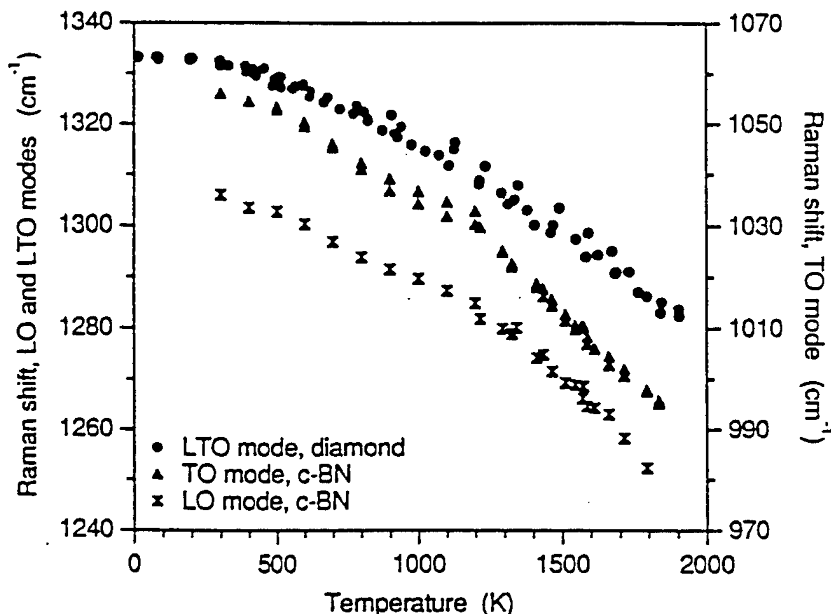

Figure 19. The temperature dependence of the Raman frequency of diamond and c-BN. From [16].

Concluding Remarks

The Raman effect arises from the interaction of light with matter; as such Raman spectroscopy is a nondestructive and powerful tool in the study of lattice dynamics. The various investigations reviewed here demonstrate the utility of Raman spectroscopy in characterizing the bond configuration, stress state, and thermal stability of wide-bandgap semiconductors. Moreover, through Raman spectroscopy valuable information may be obtained about the impurities and structural defects present in a crystal matrix. While significant progress has been made in understanding the crystal dynamics of the stable structure of GaN, AlN, and BN as well as diamond films, the investigation of the phonon characteristics of the unstable states and novel mixed alloys are still at the initial stages.

Literature Cited

1. Davis RF. 1991. Proc. of the IEEE. 79:702-12
2. Edgar JH. 1992. J. Mater. Res. 7:235-52
3. Kubota K, Kobayashi Y, Fujimoto K. 1989. J. Appl. Phys. 66:2984-88
4. Nemanich RJ. 1991. Annu. Rev. Mater. Sci. 21:535-58
5. Ravi KV. 1993. Materials Science and Engineering B. 19:203-27

6. Morkoc H, Strite S, Gao GB, Lin ME, Sverdlov B, Burns M. 1994. J. Appl. Phys. 76:1363-98
7. Badzian AR, Badzian T, Roy R, Messier R, Spear KE. 1988. Mat. Res. Bull. 23:531-48
8. Collins AT, Kamo M, Sato Y. 1990. J. Mater. Res. 5:2507-13
9. Ruan J, Choyke WJ, Partlow WD. 1991. J. Appl. Phys. 69:6632-36
10. Robins LH, Cook LP, Farabaugh EN, Feldman A. 1989. Phys. Rev. B. 39:13367-77
11. Zhu W, Badzian AR, Messier R. 1989. J. Mater. Res. 4:659-63
12. Williams BE, Glass JT, Davis RF, Kobashi K, Horiuchi T. 1988. J. Vac. Sci. Technol. A. 6:1819-20
13. Edgar JH, ed. 1994. Properties of Group III Nitrides. London: INSPEC
14. Matsuoka T. 1992. J. of Crystal Growth. 124:433-8
15. Perlin P, Polian A, Suski T. 1993. Phys. Rev. B. 47:2874-77
16. Herchen H, Cappelli MA. 1993. Phys. Rev. B. 47:14193-99
17. Nemanich RJ, Solin SA, Martin RM. 1981. Phys. Rev. B. 23:6348-56
18. Berenholc J, Chervin JC, Moustakas TD. 1995. Phys. Rev. Lett. 75:296
19. Kozawa T, Kachi T, Kano H, Taga Y, Hashimoto M, *et al.* 1994. J. Appl. Phys. 75:1098-101
20. Neugebauer J, Walle CGVd. 1994. Phys. Rev. B. 50:8067-70
21. Pankove JI, Hutchby JA. 1976. J. Appl. Phys. 47:5387-90
22. Nemanich RJ, Solin SJ. 1979. Phys. Rev. B. 20:392-401
23. Shroder RE, Nemanich RJ, Glass JT. 1990. Phys. Rev. B. 41:3738-45
24. Nemanich RJ, Glass JT, Lucovsky G, Shroder RE. 1988. J. Vac. Sci. Technol. A. 6:1783
25. Loudon R. 1964. J. Phys. 26:677
26. Wada N, Solin SA. 1981. Physica B. 105:353-356
27. Bergman L, Stoner BR, Turner KF, Glass JT, Nemanich RJ. 1993. J. Appl. Phys. 73:3951-57
28. Bergman L, McClure MT, Glass JT, Nemanich RJ. 1994. J. Appl. Phys. 76:3020-27
29. Bergman L, Nemanich RJ. 1995. J. Appl. Phys. 78:6709-19
30. Freitas JA, Butler JE, Strom U. 1990. J. Mater. Res. 5:2502-06
31. Windischmann H, Epps GF, Cong Y, Collins RW. 1991. J. Appl. Phys. 69:2231-37
32. Borer WJ, Mitra SS, Namjoshi KV. 1971. Solid State Comm. 9:1377
33. Di Bartolo B. 1969. Optical Interactions in Solids. New York: J. Wiley & Sons, Inc.
34. Ager JW, Veirs DK, Rosenblatt GM. 1991. Phys. Rev. B. 43:6491-99
35. Campbell IH, Fauchet PM. 1986. Solid State Comm. 58:739
36. Fauchet PM, Campbell IH. 1988. Critical Reviews in Solid State and Materials Sciences. 14:S79-101
37. Tubino R, Birman JL. 1977. Phys. Rev. B. 15:5843
38. Yoshikawa M, Mori Y, Obata H, Maegawa M, Katagiri G, *et al.* 1995. Appl. Phys. Lett. 67:694-6
39. Arguello CA, Rousseau DL, Porto SPS. 1969. Phys. Rev. 181:1351-63
40. Manchon DD, Barker AS, Dean PJ, Zetterstrom RB. 1970. Solid State Comm. 8:1227-31
41. Cingolani A, Ferrara M, Lugara M, Scamarcio G. 1986. Solid State Comm. 58:823-4
42. Murugkar S, Merlin R, Botchkarev A, Salvador A, Morkoc H. 1995. J. Appl. Phys. 77:6042-3
43. Perlin P, Carillon CJ, Itie JP, Miguel AS, Grzegory I, Polian A. 1992. Phys. Rev. B. 45:83-9
44. Klein MV, Ganguly BN, Colwell PJ. 1972. Phys. Rev. B. 6:2380-88
45. Hon DT, Faust WL. 1973. Appl. Phys. 1:241-56
46. Irmer G, Toporov VV, Bairamov BH, Monecke J. 1983. Phys. Stat. Sol. B. 119:595-603
47. Yugami H, Nakashima S, Mitsuishi A, Uemoto A, Shigeta M, *et al.* 1987. J. Appl. Phys. 61:354-8

48. Miyoshi S, Onabe K, Ohkouchi N, Yaguchi H, Ito R, *et al.* 1992. J. Cryst. Grow. 124:439-42
49. Humphreys TP, Sukow CA, Nemanich RJ, Posthill JB, Rudder RA, *et al.* 1990. MRS Proc. 162:531-563
50. Miwa K, Fukumoto A. 1993. Phys. Rev. B. 48:7897-902
51. Hagen J, Metcalfe RD, Wickenden D, Clark W. 1978. J. Phys. C: Solid State Phys. 11:L143-6
52. Murakami H, Asahi T, Amano H, Hiramatsu K, Sawaki N, Akasaki I. 1991. J. Crys. Grow. 115:648-51
53. Khan MA, Skogman RA, Schulze RG, Gershenzon M. 1983. Appl. Phys. Lett. 43:492-4
54. Yoshida S, Misawa S, Gonda S. 1982. J. Appl. Phys. 53:6844-8
55. Hayashi K, Itoh K, Sawaki N, Akasaki I. 1991. Solid State Comm. 77:115-8
56. Chang IF, Mitra SS. 1968. Phys. Rev. 172:924-33
57. Lucovsky G, Chen MF. 1970. Solid State Comm. 8:1397
58. McNeil LE, Grimsditch M, French RH. 1993. J. Am. Ceram. Soc. 76:1132-6
59. Sanjurjo JA, Cruz EL, Vogl P, Cardona M. 1983. Phys. Rev. B. 28:4579-84
60. Brafman O, Lengyel G, Mitra SS, Gielisse PJ, Plendl JN, Mansur LC. 1968. Solid State Comm. 6:523-6
61. Harris JH, Youngman RA, Teller RG. 1990. J. Mater. Res. 5:1763-73
62. Slack GA. 1973. J. Phys. Chem. Solids. 34:321
63. Kurokawa Y, Utsumi K, Takamizawa H. 1988. J. Am. Ceram.Soc. 71:588
64. Geick R, Perry CH, Rupprecht G. 1966. Phys. Rev. 146:543-7
65. Kuzuba T, Era K, Ishii T, Sato T. 1978. Solid State Comm. 25:863-5
66. Kuzuba T, Sato Y, Yamaoka S, Era K. 1978. Phys. Rev. B. 18:4440-43
67. Balkanski M, Wallis RF, Haro E. 1983. Phys. Rev. B. 28:1928-34
68. Hart TR, Aggarwal RL, Lax B. 1970. Phys. Rev. B. 1:638-42
69. Zouboulis ES, Grimsditch M. 1991. Phys. Rev. B. 43:12490-93
70. Exarhos GJ, Schaaf JW. 1991. J. Appl. Phys. 69:2543-8

XX. Synthesis Routes and Characterization of High Purity, Single Phase GaN Powders

A. Introduction

The recent fabrication of p-n junctions [1], heterostructures [2] and quantum wells [3] in thin film structures containing GaN and the subsequent commercial realization of blue and green light emitting diodes based on these structures have generated considerable interest and a growing number of research programs devoted to the III-V nitrides. In the wurtzite form, GaN has a band gap of 3.45 eV (near UV region) at room temperature. It also forms a continuous range of solid solutions with AlN (6.28 eV) and InN (1.95 eV). Thus optoelectronic devices having specifically engineered band gaps with energies from the visible to the deep UV are theoretically possible with these materials. The wide band gaps of these materials and their strong atomic bonding also make them candidates for high-power, high-frequency and high-temperature devices. At present, GaN films are almost universally grown on foreign substrates, e.g., sapphire and SiC. The mismatches in lattice parameters result in significant densities ($\geq 10^8$ cm/cm^{-3}) of dislocations in thefilms [4]. As such, the availability of GaN bulk single crystals and wafers for homoepitaxial film growth has gained considerable importance. Crystal growth process routes applicable to GaN, e. g., sublimation and high pressure solution methods demand the availability of a high purity, single phase, well characterized powder source.

The demand for GaN powder has always been very small, and research and development regarding production routes for this material have been non-existent. The amount, purity and cost of the commercially available GaN powder are, at present, limited, poor and extreme, respectively. The available X-ray and crystallographic data for GaN shown on PDF 2-1078 are also limited and date to 1938 [5]. This early data has a figure of merit of 14 which corresponds to an unassigned quality rating. As such, the objectives of the research reported below have been the development of viable, thermodynamically based process routes for the synthesis of very high purity GaN powder and the characterization of the resulting materials.

B. Selection of Synthesis Routes

The first reported synthesis of GaN powder was achieved by Johnson *et al.* [6] by flowing NH_3 over molten Ga heated between 900-1000°C. Subsequent research by Pichugin and Yas'kov [7] substantiated the efficiency of this process route. Lorenz [8] produced GaN powder by reacting Ga_2O_3 with NH_3 in the range of 600-1100°C. Addamiano [9] obtained GaN powder by heating fine particles of GaP and GaAs in a stream of hot NH_3 at 1000-1100 °C. Conversion of crushed single crystal GaAs into GaN was investigated by Wickenden and Isherwood [10].

In selecting methods for economically producing semiconductor purity GaN powder the instability of GaN to sublimation and the very low reactivity between Ga and N_2 (ΔG_f = 7.4 Kcal/mol; K_p= 0.004 at 900°C and ΔG_f = -4.4 Kcal/mol; K_p = 17 at 500°C) must be considered. As the first step, the oxidation state of the sublimed or evaporated specie from candidate condensed phases was determined from the free energy differences of the solid and the evaporated or sublimed specie. Subsequently, the thermodynamic data for these specie were used in the free energy calculations for the process routes which was considered to produce GaN. The results of this procedure are summarized in Table I.

Table I. Free Energy of Reaction Values for Possible Reactions to Produce GaN

Reaction	T (°C)	$\Delta G_{reaction}$ (Kcal/mol)	
$GaBr(g)+NH_3(g) = GaN(s)+HBr(g)+H_2(g)$	300-1000	-4 – +6	(1)
$GaI(g) + NH_3(g) = GaN(s)+HI(g)+H_2(g)$	300-1000	-2 – +8	(2)
$GaCl_3 (g)+ NH_3 (g) = GaN(s) + 3HCl (g)$	300-1000	+13 – +1	(3)
$GaF_3(s)+NH_3(g) = GaN(s)+3HF(g)$	300-1000	+33 – -6	(4)
$Ga_2O_3(s)+2NH_3(g) = 2 GaN(s)+3H_2O$	300-1000	+49 – +48	(5)
$GaCl(g)+NH_3(g) = GaN(s)+HCl(g)+H_2 (g)$	300-1000	-7 – +4	(6)
$Ga (1)+NH_3 (g) = GaN (s)+3/2 H_2(g)$	300-1000	-13 – -12	(7)
$Ga_2O(s)+2NH_3(g)= 2GaN(s)+H_2O(g)+H_2(g)$	300-1000	- 8 – 0	(8)
$Ga_2O(g)+2NH_3(g)= 2GaN(s)+H_2O(g)+H_2(g)$	300-1000	-47 – -23	(9)

The $\Delta G_{reaction}$ values at the approximate temperatures that would be employed in GaN powder production (600-1000 °C) for reactions (1-6) are mostly positive and thus indicate that they would not occur. Therefore, with the exception of (5), these reactions were ruled out. As mentioned above, Addamiano [9] was able to obtained GaN powder from GaP and GaAs by firing these compounds in flowing dry NH_3. However, these compounds were not considered for precursor materials in the present program due to their higher price/gram relative to commercially available GaN powder. Furthermore, the conversion of GaAs requires an intermediate conversion to Ga_2O_3, since a thin layer of GaN formed on the surface of GaAs prevents complete conversion of GaAs into GaN [11]. This additional step increases the possibility of contamination. The same problem was not reported for GaP, however, the evaporation of P has been a major problem [5] in this conversion process.

When the thermodynamic, kinetic and economic criteria are considered, reactions (7), (8) and (9) are shown to be the most suitable reaction for the synthesis of pure GaN. Among these

candidate routes, reaction (7) offers a viable method whereby the resulting GaN can be as pure as the starting reactants. The availability of ultra pure Ga metal coupled with the recent advances in the reduction of both water and oxygen in the NH_3 to <1 ppm allow the achievement of very high purity, single phase GaN powder at reasonable costs.

Reaction (7) was employed in this research with several modifications to the experimental procedures used by the earlier investigators. An important product of these studies was a marked refinement of the existing crystallographic and XRD data, as well as related microstructural information for the GaN powder as discussed below.

Reaction (5) was also investigated experimentally as an alternative synthesis route. This route, has been used by many researchers to describe the conversion of Ga_2O_3 (i.e. β-Ga_2O_3) into GaN. However, thermodynamic calculations from available data show that this reaction will not occur temperatures where GaN production is feasible. It is only favorable if reaction (8) is embedded in this process.

The reactant phase of $Ga_2O(g)$, in reaction (9), is not commercially available but may be formed from a mixture of Ga and Ga_2O_3 via the reaction

$$Ga_2O_3 + 4\ Ga = 3\ Ga_20\ (g). \qquad (10)$$

A 4:1 molar mixture of Ga and Ga_2O_3 reportedly [12] has a Ga_2O vapor pressure of 0.2 Torr at 800°C and 10 Torr at 1000°C. However this production scheme was not considered due to the difficulty of capturing the ultra-fine GaN powder that forms in the gas phase. Furthermore, this two step process involving reaction (10) increases the possibility of contamination of the GaN powder by oxygen and other elements.

C. Experimental Procedure

To produce GaN powder via reaction #7 in Table I, precursor materials of 99.999% pure molten Ga metal, contained in pure quartz reaction boats, and 99.9999% pure NH_3 gas were reacted in a 1.5" dia., 36" long horizontal tube furnace having a quartz liner. A schematic of system is shown in Fig. 1. A three-dimensional matrix of boat position (2" intervals from the NH_3 inlet), NH_3 flow rate (200-500 sccm) and boat temperature (800-1200°C) was employed to determine the optimum conditions for complete conversion of Ga to GaN. The Ga was heated to the desired temperature prior to reaction under flowing NH_3. In order to minimize GaN decomposition, upon completion of each experiment, the samples were pulled in to the cooling zone of the furnace with the stroke rod and rapidly cooled (10°C/min) to room temperature (see Fig. 1) under an increased flow of NH_3 (typically 1000 sccm.). No free Ga or other phase was observed in the X-ray diffraction (XRD) patterns of the GaN powder synthesized between 900 and 1050°C. The rapid formation of a gas permeable GaN layer was achieved within this temperature range such that the unreacted metal was continuously exposed

to NH_3. Similar studies between 1050 and 1200°C resulted in a small but X-ray detectable amount of free Ga in the powder, presumably as a result of the decomposition of the GaN. At temperatures below 900°C, a GaN crust formed on the surface of the liquid Ga regardless of the flow rate of NH_3 (400-1000 sccm) or the reaction time (1-4 hrs) and stopped the reaction. For our system, the optimum conditions of boat position, boat temperature and NH_3 flow rate, for the complete conversion of the Ga to GaN were 20" from the NH_3 inlet, 400 sccm and 975°C, respectively. This material produced under these conditions was selected for characterization via XRD and scanning electron microscopy (SEM).

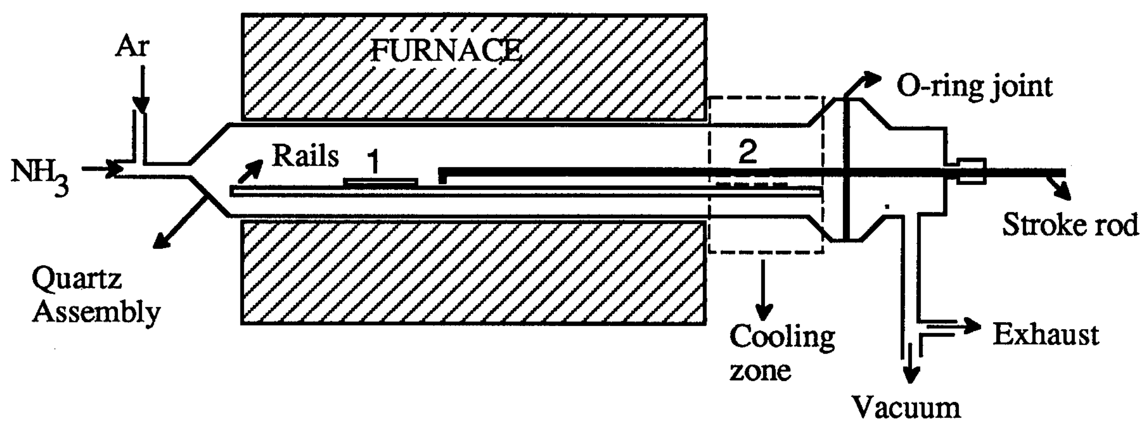

Figure 1. Schematic of the GaN powder production system.

After removal from the boats, the material was crushed and slightly ground in an Agate Mortar. The XRD patterns of the GaN powder were obtained using a Rigaku (D/MAX-IIA) powder diffractometer equipped with an incident beam monochromator to obtain Cu $K\alpha_1$ radiation. The conditions of 0.02 degrees per step $2\theta°$ scan with 4 s counting time were used for the diffraction scans. Systematic machine errors were determined using a 99.999% pure internal Si standard. Error corrections were subsequently made on the actual d-spacings obtained from the XRD data. Both Appleman and Evans [13] and TREOR [14] cell refinement methods were used to perform least squares refinements of the data. Further details of the X-ray analysis procedures are given in Ref. [15].

The conversion of Ga_2O_3 was also conducted in the system shown in Fig. 1. The precursor materials of 99.9999% NH_3 and 99.999% pure powder Ga_2O_3 were used. The Ga_2O_3 was loaded into quartz boats and heated in the range of 800-1100°C, for 1-2 hrs under an NH3 flow rate of 500 sccm. Complete conversion of Ga_2O_3 into GaN was observed at 1050°C. X-ray scans were conducted on powder taken from different locations in the boat to confirm complete conversion. Experiments in the 800 to 1000°C range yielded material which showed low intensity, broad GaN X-ray peaks.

SEM images of the crushed GaN powders produced by both methods, were obtained using a JEOL Model 6400 field emission microscope at 5 kV. The data obtained from these studies regarding the average particle size, particle size distribution and morphology are very important for the next step in the crystal growth research, namely, the consolidation of the powder into solid shapes having densities near theoretical.

All powders were analyzed by Inductively Coupled Plasma (ICP) and Secondary Ion Mass Spectroscopy (SIMS) techniques to determine the presence and concentrations of impurities.

D. Results and Discussion

The GaN produced via reaction of molten Ga with flowing NH_3 at 975°C was porous and off-white in color. No detectable interaction between the boat and the metal or the GaN was discerned; thus, the purity of the GaN was controlled by the purity of the reactants. Since the latter can now be purchased in very high purities, semiconductor quality GaN is now possible. An analysis of 30 common elements via the ICP technique revealed only 100 ppm of manganese and 50 ppm of magnesium, as detectable impurities. These impurities are assumed to have come from the precursor Ga metal. The only disadvantage of the procedure used is that it is a batch processes which limits the quantity of material produced in a given run to the size of the furnace and the container for the metal.

An SEM image typical of the optimized GaN powder is shown in Fig. 2a. The particle size distribution of the GaN powder is narrow (1 to 5μm) with a majority of particles being ≈1 μm. The morphology of the particles is a mixture of various polyhedrons and rounded particles.

The XRD studies of the GaN produced by this route show a marked improvement in the crystallographic quality relative to existing data. The unit cell data and the data from a representative X-ray diffraction pattern of single phase GaN powder are presented in Tables II and III, respectively. The PDF file # 2-1078 reports a figure of merit of F_{19}=14, with 19 planes being indexed. The diffraction data determined in this research and presented in Table III has a figure of merit of F_{23}=175 where all observed planes were indexed in the interval of 30° - 130°.

In the second synthesis process, complete conversion of the Ga_2O_3 into GaN was achieved in flowing NH_3. No other phases were observed in the X-ray spectra. As before, no visible interaction between the quartz boat and the Ga_2O_3 or the GaN powder was detected. ICP analysis revealed no detectable impurities in the GaN.

The SEM studies of the GaN showed mainly submicron particles having various polyhedral shapes as well as a small percentage of rod-like 5-10 micron long forms (Fig 2b). Similar rod-like morphologies were also observed in the Ga_2O_3 powder. A close examination of these SEM images revealed that both the sizes and morphologies of the GaN particles were determined mainly by of the Ga_2O_3 precursor.

Table II. Unit Vell Data for GaN

a = 3.18907 (8) Å   b = 3.18907 (8) Å   c = 5.1855 (2) Å

α = 90° β= 90° γ= 120°

V = 45.672 (2) $(Å)^3$ D_x = 6.0886 gr cm^{-3} Z = 2   Formula wt: 83.7297

Crystal System: Hexagonal

Figure of merit type F_N, Werner [14] M_{23} =374 Werner [14]

Value : F_{23} = 174 (0.004579, 29)

Table III. XRD Data for GaN

2θ exp (°)	I/Io	d_{exp} (å)	*hkl*	Δ2θ (°)
32.3904	56	2.762	100	-0.002
34.5702	45	2.593	002	-0.002
36.8465	100	2.437	101	0.000
48.0902	19	1.891	102	-0.001
57.7758	31	1.5945	110	+0.002
63.4492	27	1.4649	103	+0.019
67.8117	4	1.3809	200	+0.001
69.1040	22	1.3582	112	+0.005
70.5114	12	1.3345	201	-0.004
72.9062	3	1.2964	004	+0.003
78.3940	3	1.2186	202	+0.000
82.0349	2	1.1737	104	-0.009
91.1101	7	1.0790	203	-0.005
95.1200	3	1.0438	210	+0.010
97.6528	8	1.0234	211	-0.002
99.9511	5	1.0059	114	+0.004
105.0019	6	0.9709	105	+0.008
105.4025	5	0.9683	212	+0.001
109.1648	1	0.9452	204	-0.003
113.5807	4	0.9207	300	-0.011
119.0945	8	0.8936	213	+0.003
125.2224	4	0.8676	302	+0.000
126.0445	2	0.8644	006	-0.009

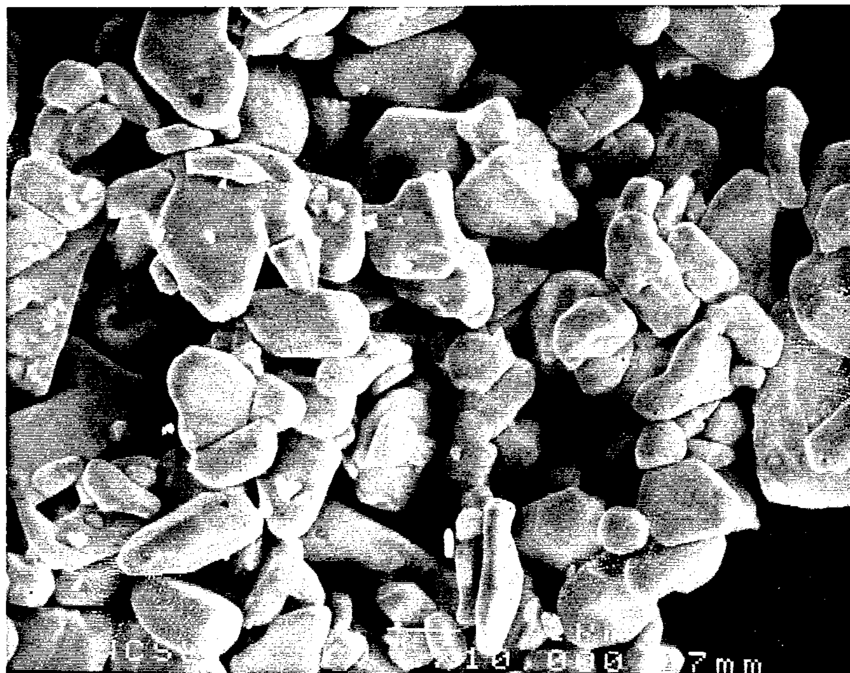

Fig. 2a. SEM image of GaN obtained from $Ga+NH_3$

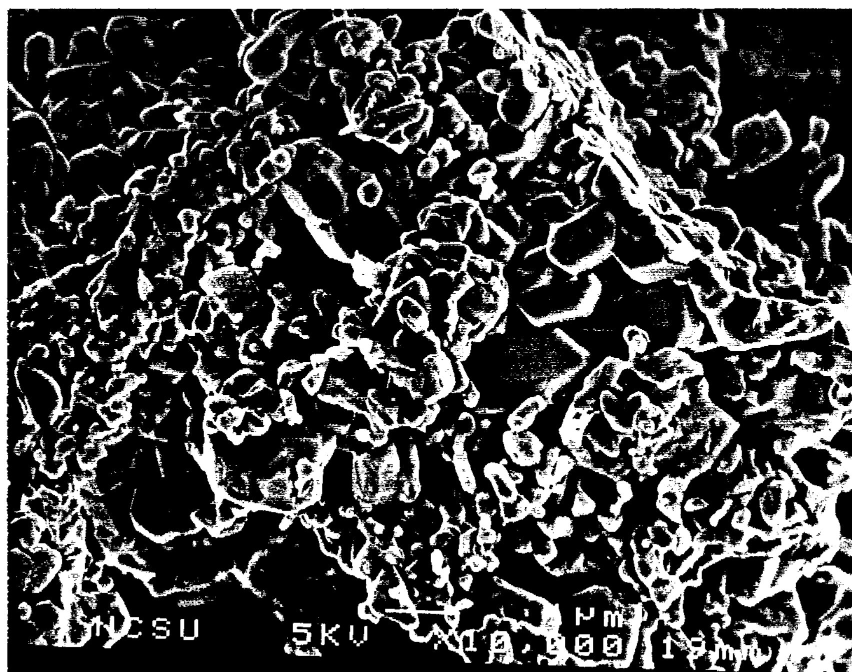

Fig. 2b. SEM image of GaN obtained by conversion of Ga_2O_3

As noted earlier, reaction (5) has a positive ΔG_{rx}^f value for all temperatures used in this research. Thermodynamic calculations of several intermediate reactions were made in order to explain the inconsistency between the experimental results and positive ΔG_{rx} of reaction (5). The species of NH, NH_2, NH_3, H_2 and N_2 can be assumed to be present in our system at 1000°C due to the combustion of NH_3 gas. Thermodynamic data show that Ga_2O_3, in the presence of H_2, NH or NH_2 will be reduced to Ga_2O. Free energy calculations show that reactions between NH, NH_2 or NH_3 and Ga_2O results in the synthesis of GaN. It is not possible to determine the exact specie(es) which is (are) responsible for the conversion of Ga_2O_3 into GaN. The lifetimes of NH and NH_2 are extremely short in comparison to H_2 and NH_3; thus, it is very likely the these latter gases control the reduction and nitridization reactions, respectively.

It was thought that the GaN particles produced via oxide conversion could have unreacted cores containing high amount of oxygen. However, a comparison of the SIMS data taken from GaN obtained by both routes did not show any significant difference in oxygen concentrations. A conservative estimate was made from the single crystal sputtering rate of GaN to ensure that cores of the GaN particles were analyzed.

E. Summary

An economically viable process route has been established to produce high purity single phase GaN powder via reaction of liquid Ga metal with flowing NH_3. An alternative method of producing GaN from Ga_2O_3 was also achieved. For the first route the optimum temperature, NH_3 flow rate and boat position in the hot wall tube furnace relative to the NH_3 inlet for the complete reaction were 975°C, 400 sccm and 20" respectively. As for the second route the experimental parameters, in the same order, were 1050°C, 500 sccm and 20", respectively. Results from the SEM, SIMS and ICP techniques revealed that, although material purity and quality are suitable for our needs, the latter approach will necessitate conditioning of the precursor oxide since particle morphology of the resulting GaN is not suitable for consolidation processes. X-ray diffraction (XRD) data obtained from the powder produced via the first route, revealed the GaN to be single phase with a=3.1891 Å, c=5.1855 Å, space group=$P6_3mc$, Z = 2 and D_x =6.0886 gr. cm^{-3}.

F. Acknowledgements

The authors express their appreciation to Dr. A. Cuneyt Tas of the Middle East Technical University, Metallurgical Engineering Department, Ankara, Turkey and C. Basceri of North Carolina State University, Materials Science and Engineering Department, Raleigh, North Carolina, for their valuable support in the XRD characterization studies and to the Office of Naval Research for monetary support for this research under contract N00014-92-J-1477.

G. References

1. R. J. Molnar, R. Singh and Moustakas, Appl. Phys. Lett. **62**, 268 (1995).
2. Nichia Chemical Industries, Ltd., 491 Oka, Kaminaka, Anan, Tokushima 774, Japan.
3. S. Krishnankutty, R. M. Kolbas, M. A. Khan, J. N. Kuznia, J. M. Van Hove and D. T. Olson, J. Electron. Mater. **21**, 437(1992).
4. T. W. Weeks Jr., M. D. Bremser, K. S. Ailey, E. Carlson, W. G. Perry and R. F. Davis, Appl. Phys. Lett. **67**(3), 401 (1995).
5. H. Juza, Z. Anorg. Chem. **239**, 285 (1938).
6. W. C. Johnson and J. B. Parsons and M. C. Crew, J. Phys. Chem. **36**, 2651 (1932).
7. I. G. Pichugin, and D. A. Yaskov, Inorg. Mat. **6**, 1732 (1972).
8. M. R. Lorenz and B. B. Binkowski, J. Electrochem. Soc. **109**, 24 (1962).
9. A. Addamiano, J. Electrochem. Soc. **108**, 1072 (1972).
10. B. J. Isherwood and D. K. Wickenden, J. Mater Sci. **5**, 869 (1970).
11. Faulkner, K. R., *et al.*, J. Mater Sci. **5**, 308 (1970).
12. C. J. Frosh and C. D. Thurmond, J. Phys. Chem. **66**, 877 (1962).
13. D. E. Appleman and Evans, H. T., U.S. Geological Survey, Computer Contribution 20, U.S. National Technical Information Service, Document No. PB-216188, (1973).
14. Werner, P. E. (1984). Trial and Error Program for Indexing of Unknown Powder Patterns, TREOR, University of Stockholm, Stockholm, Sweden.
15. C. M. Balkas, C. Basceri, R. F. Davis, J. Powder Diffraction, December, (1995).

XXI. Hot Pressing of III-V Nitrides

A. Introduction

Considerable research is being pursued in the III-V nitrides and the importance of producing high purity bulk material for use in film growth techniques such as sublimation has become apparent. Aluminum nitride (AlN) has been successfully hot pressed which leads to the assumption gallium nitride (GaN) can be hot pressed, as well [1]. But gallium nitride (GaN) has proven to be less readily pressed in initial trials and research into the morphology affecting pressing has been conducted.

B. Experimental Procedure

A tube furnace was used to produce gallium nitride from gallium (Ga) metal and ammonia (NH_3) gas as described by Balkas *et al.* [2]. The GaN was ground in a zirconia mortar and pestle to deagglomerate the material. Scanning Electron Microscopy (SEM) was performed on this material using a JEOL 6400 FE with an accelerating voltage of 5kV. To compare particle size and shape, SEM was performed on commercial AlN powder, Tokuyama Grade F.

A sample of the GaN powder was jet milled, under a nitrogen atmosphere, using a Fluid Energy Aljet Model 00 Jet-O-Mizer Grinding System. A Microtrac analysis to determine particle size distribution was run on the original and milled powder. SEM was also performed on the jet milled powder to determine particle size and shape.

C. Results

Figures 1 and 2 are SEM micrographs representative of the GaN and AlN powder, respectively. The GaN has a wide particle size range, from approximately 0.1mm to submicron in size. Most of the GaN particles appear irregular, but some exhibit the expected hexagonal character. In comparison, the AlN is monosized and spherical with a smaller particle size, approximately 0.5 μm.

The jet milled GaN, shown in Fig. 3, still shows a wide particle size range but with smaller particles from approximately 10 μm to submicron size. The particle shape is irregular, with no evidence of hexagonal character. The Microtrac Analysis of the GaN powder corroborates the findings of the SEM for the feed and jet milled material. The original powder ranged in size from 124.5 to 0.375 μm, as compared to 5.5 to 0.187 μm for the feed material.

D. Discussion

The comparison of the AlN and GaN powders indicated that the GaN had a much broader particle size range, more irregular shape and larger particle size. Since AlN has been successfully hot pressed the goal was to create a GaN morphology similar to that of AlN. Jet

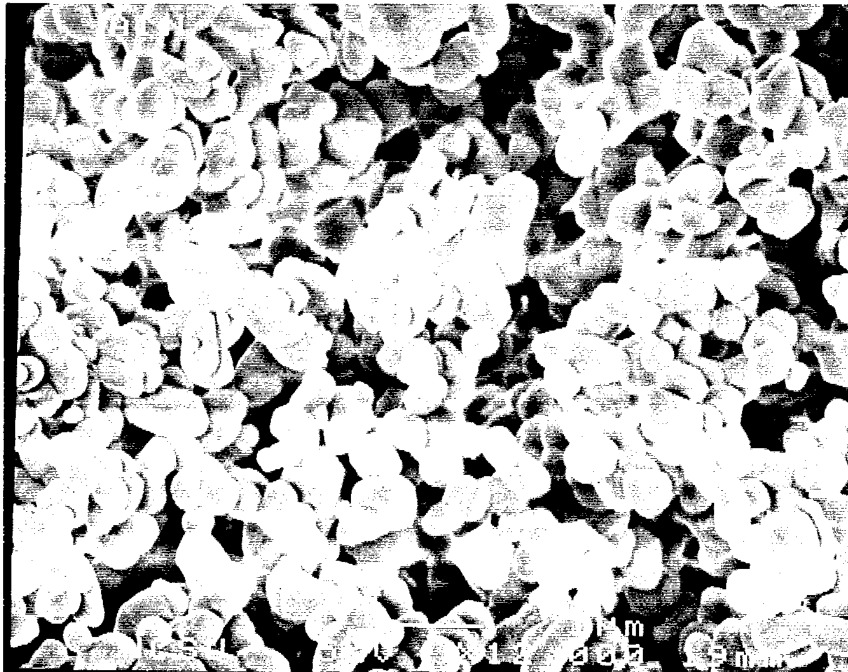

Figure 1. SEM micrograph of commercial AlN powder.

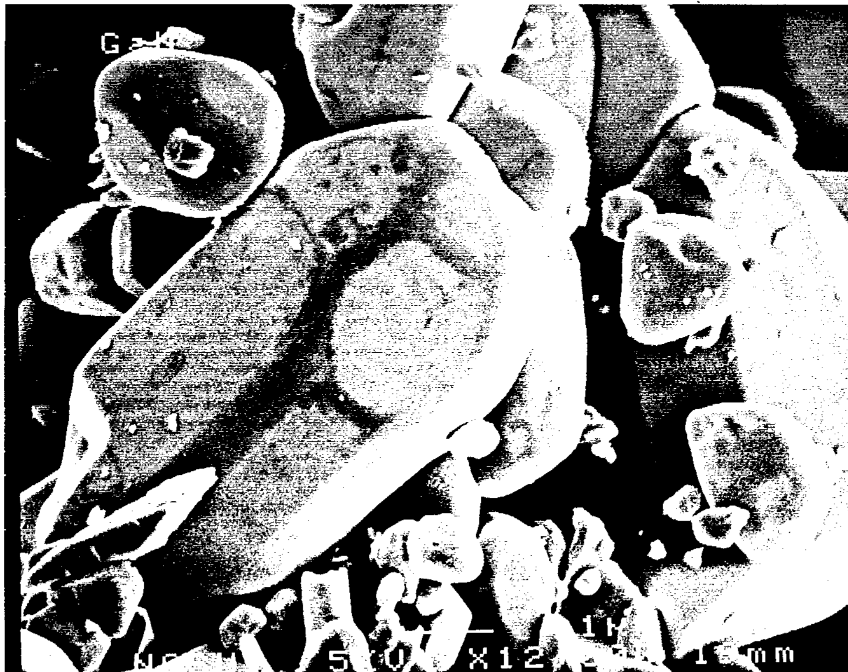

Figure 2. SEM Micrograph of GaN powder.

Figure 3. SEM micrograph of jet milled GaN.

milling was selected to condition the GaN powder over more conventional milling procedures for two reasons. Currently the GaN can be produced in only small quantities, no more than 20 grams per run. A jet mill can process samples as small as 10 grams, a parameter that cannot be matched by conventional grinding methods. Jet milling is also capable of achieving particle sizes into the submicron range, which is a size range comparable to that of AlN powder. The jet milling procedure was successful in reducing the particle size and size range of the GaN powder, but the shape gained no spherical nature. As observed in the SEM micrographs, the jet milled GaN powder is not identical to the AlN, but does more closely resembles its powder shape and size.

E. Conclusions

As success in pressing AlN has been demonstrated, its powder morphology (particle size, shape, and size range) were used as guidelines to produce a more readily pressed powder form of GaN. The particle size and size range of AlN were successfully approximated in GaN.

F. Future Research Plans and Goals

Preliminary hot pressing of the jet milled GaN produced limited success. A pressed density high enough for handling was achieved, but several parameters in the pressing operation must be modified. First, the GaN is pressed in graphite dies with SiC coated sleeves to protect the

powder from contamination. The sleeves frequently break during pressing. A new sleeve design will be considered to avoid this failure. The strength of the sleeve material and the tolerance between the die and the sleeve may be contributing factors. In previous experiments GaN has converted back to its components at temperatures above 1000°C. GaN conversion to Ga metal destroys the pressing process and has been encountered in some pressing trials. Careful control of the temperature must be investigated so the optimum temperature for pressing can be reached without conversion. Another obvious factor that will be experimented with is the pressure schedule to achieve maximum density.

AlN powder has the benefit of being produced in an easily pressed morphology. The commercial AlN used in this research is produced by carbothermal reduction, a process that has the advantage of producing fine spherical powder [1]. This process is not viable for producing GaN because of problems with carbon contamination. New production methods for GaN will be investigated that produce pressable powder without conditioning. One possible production route is freeze drying. The procedure is relatively simple; typically, a solution of gallium and nitride salts would be atomized into a freezing bath, where the droplets freeze on contact. The ice and the solution will separate on freezing. These droplets would then be charged to a freeze dryer where the solvent would sublime and perfectly homogenous and spherical granules would be produced. This procedure has some documented success for other electronic ceramic materials and will be considered as an alternative production route [3,4].

G. References

1. L. M. Sheppard. Cer. Bull. **69** (11), 1801 (1990).
2. C. M. Balkas, C. Basceri, R. F. Davis. Powder Diffr. **10** (3), 1 (1995).
3. T. Tachiwaki, M. Suzuki, H. Okajima, S. Koizumi, T. Ito, A. Hiraki. Appl. Surf. Sci. **70/71**, 751 (1993).
4. L. G. Mamsurova, V. P. Shabatin, A. V. Shlyakhtina, L. G. Shcherbakova. Inorg. Matls. **25** (4), 550 (1989).

XXII. Towards the Identification of the Dominant Donor in GaN

P. Perlin,[1] T. Suski,[1] H. Teisseyre,[1] M. Leszczynski,[1] I. Grzegory,[1] J. Jun,[1] S. Porowski,[1]

P. Bogusławski,[2,3] J. Bernholc,[3] J. C. Chervin,[4] A. Polian,[4] T. D. Moustakas[5]

1. UNIPRESS, High Pressure Research Center, Polish Academy of Sciences, 01-142 Warsaw, Poland

2. Institute of Physics, Polish Academy of Sciences, 02-668 Warsaw, Poland

3. Department of Physics, North Carolina State University, Raleigh, NC 27695-8202

4. Physique Des Milieux Condenses, Universite Pierre et Marie Curie, 75252 Paris CEDEX 05, France

5. Department of Electrical, Computer and System Engineering, Boston University, Boston, MA 02215

Abstract

We analyze optical absorption, transmission, luminescence, and Raman scattering in n-type GaN at hydrostatic pressures up to 30 GPa. The results show a freeze-out of free carriers at the pressure of about 20 GPa. This effect is explained by trapping of electrons in a level that is a resonance at ambient pressure, but becomes a gap state at high pressures. *Ab initio* calculations indicate that the nitrogen vacancy has an appropriate electronic structure and is the best candidate to be the dominant native donor responsible for the autodoping of GaN.

71.55.Eq, 61.72.Ji, 78.30.Fs, 78.55.Cr

Gallium nitride is considered to be one of the most promising materials for the construction of short-wavelength light emitting devices, such as blue diodes and lasers [1]. In spite of impressive technological achievements of a last few years (*e.g.*, the production of the first commercially available blue diode), there are still substantial gaps in our knowledge of the basic physical properties of this material. One of them concerns the origin of n-type conductivity in undoped GaN crystals. Experimentally, room temperature concentrations of conduction electrons range from 10^{17} to 10^{20} cm^{-3} independently of the method of growth, *i.e.,* they have been observed in both bulk crystals and in MBE- or OMCVD-grown epitaxial films. Maruska and Tietjan [2] and Ilegems and Montgomery [3] proposed that the autodoping is due to native defects, since concentrations of contaminants are lower by a few orders of magnitude than the highest concentrations of conduction electrons. Furthermore, the electron concentration is sensitive to the growth parameters (temperature and growth rate), which is easier to explain by a varying rate of creation of defects than by a varying incorporation of contaminants. The residual donor was tentatively identified with the nitrogen vacancy [2–5]. Technologically, it is very likely that V_N appears during the growth because of the very high nitrogen equilibrium pressure at the growth temperatures; this implies that the growth occurs under Ga-rich conditions. So far, however, the dominant donor was not positively identified with the nitrogen vacancy.

Recently, *ab initio* calculations of electronic structure of native defects in GaN were performed by Bogusławski *et al.* [6] and Neugebauer and Van de Walle [7]. They have shown that V_N introduces a resonant level inside the conduction bands at about 0.8 eV above the band minimum. In the neutral charge state, the one electron that should occupy this resonance autoionizes to bottom of the conduction bands and becomes bound by the Coulomb tail of the vacancy potential, forming a shallow level. Thus, at atmospheric pressure, the vacancy behaves like a shallow effective-mass donor. When the concentration of vacancies exceeds the critical Mott value, which is about 10^{18} cm^{-3} for GaN, the sample should become metallic.

In order to confirm the presence of a resonant level predicted by the theory we have

performed experiments under high hydrostatic pressures. Our method is based on the fact that the pressure coefficient of the bottom of the conduction band is usually higher than that of the resonance. Consequently, at sufficiently high pressures a crossover should occur between the two levels, and the resonance should become a genuine gap state that may trap electrons. After the crossover, free electrons would disappear from the conduction band and would occupy the deep-defect-induced state. To induce the crossover, the conduction band minimum should rise by at least 0.8 eV, assuming that the resonance does not move. Since the pressure coefficient of the gap is about 40 meV/GPa [8], one has to apply a pressure of about 20 GPa. Such high pressures necessitate the usage of diamond anvils, which practically excludes transport measurements. In this Letter we discuss the results of four optical experiments under pressure, which both probe for the existence of the resonant-deep transition and shed light on the origin of the so-called yellow luminescence at about 2.3 eV [10], which acts as a lifetime killer and suppresses the important blue luminescence. The first experiment measures the absorption due to free electrons in the infrared (IR) region of the spectrum (0.9-1.6 μm). The second, complementary experiment measures the far-infrared (2-20 μm) transmission. The third one investigates the variation with pressure of the yellow photoluminescence. Finally, we analyze our earlier Raman experiments on bulk samples [11].

We have used two types of GaN samples. The first samples were bulk GaN crystals grown at the nitrogen pressure of about 1.5 GPa and temperature of 1500 °C [12]. These samples are characterized by free electron concentration of about 5×10^{19} cm^{-3}. The second type was a 2.5 μm epitaxial film grown by MBE on a sapphire substrate. The Hall concentration of electrons was 4×10^{17} cm^{-3}. For the purpose of high pressure measurements, the substrate was thinned to about 20 μm. The experiments were performed in diamond anvil cells (Mao-Bell–like [13] or Letoullec-Pinceaux [14] designs were used). We have employed a 4:1 methanol-ethanol mixture as a pressure-transmitting medium. A small piece of ruby was placed in the cell to monitor the pressure. Linear ruby scale (3.65 Å/GPa) was used to determine the pressure from the energy of ruby luminescence.

To measure the absorption, the light beam from a 150 W halogen lamp was focused on a 100 μm pinhole, whose image was projected on the sample. The outcoming light was dispersed by a Spex 500M spectrometer and detected by a Peltier-cooled PbS detector. This experimental setup limited the available spectral range to $\lambda \leq 1.6$ μm. Since this represents only a very small part of the free carrier absorption, we have decided to expand the examined spectral range by measuring the transmission. In this experiment we used a Perkin-Elmer 1600 Series Fourier spectrometer equipped with an IR microscope. The microscoping system allowed us to determine very accurately the ratio of the light intensity transmitted through the sample to that passing through the pressure-transmitting medium close to the sample. We measured the total IR transmission of the sample, *i.e.*, the ratio of intensities of the "white" light in the spectral range limited by the sensitivity of our IR detector (2-20μm). The yellow luminescence was excited either by the 333-363 nm UV light of an argon laser or, at higher pressures, by the 325 nm line of a He-Cd laser. The Raman scattering measurements were performed with the use of a triple Dilor-XY spectrometer. The details of this experiment are given elsewhere [11].

Free-carrier absorption in the near IR region was measured in a bulk single crystal with $n \simeq 5\times 10^{19}$ cm^{-3}. Figure 1 shows the absorption spectra at various pressures. For pressures lower than 15 GPa there is no substantial change in the shape of the absorption. However, between 15 GPa and 20 GPa the intensity of the absorption decreases and practically disappears above 20 GPa.

Figure 2 shows the pressure dependence of the total transmission of a thin (15 μm) bulk single crystal. For pressures lower than about 20 GPa, the transmission is practically constant and close to 15%. The transmission increases rapidly starting at 20 GPa. At the highest pressures the transmission exceeds 100%, which simply means that the absorption of the pressure-transmitting medium is higher than that of the sample.

The pressure dependence of the "yellow" luminescence is shown in Fig. 3. In this experiment we have used both an epitaxial film and a bulk sample. The mechanism of this luminescence will be discussed below. ¿From Fig. 3 it follows that the energy of

the luminescence band changes linearly with pressure up to about 18 GPa. (Thus, at the highest pressures, the "yellow" luminescence becomes blue). Its pressure coefficient, about 30 meV/GPa, is very close to the pressure coefficient of the band gap [8]. At about 20 GPa, the slope changes and the peak position does not change with pressure.

Figure 4 compares the Raman spectra of GaN at low (2 GPa) and very high (32.2 GPa) pressures [11] for a sample with electron concentration exceeding 10^{19} cm^{-3}. It shows that new phonon peaks appear in the high pressure spectrum. Here we are interested in the peak labeled L_5 with wavenumber of about 850 cm^{-1} at 32.2 GPa. By extrapolating its position to the ambient pressure we obtain an energy of 740 cm^{-1}, see inset. Since this energy is very close to the 738-741 cm^{-1} energy of the LO phonon in GaN recently measured in epitaxial samples [15], we assign the L_5 peak to the LO phonon. The presence of this peak was detected only for pressures higher than 22 GPa, as shown in the inset of Fig. 4.

The experimental results can be consistently explained by the presence of a resonant state in the conduction band. Hydrostatic pressure induces a crossover of the resonance with the bottom of the conduction band at about 20 GPa. After the crossover, conduction electrons become trapped in the resonance-derived gap level. Consequently, since practically all electrons disappear from the conduction band, the concentration of defects giving rise to the resonance must be equal or higher than the concentration of dominant native donors. We propose here that it is the native donor that induces the resonance and we identify it with the nitrogen vacancy.

We will now discuss each case in more detail. Both absorption and transmission measurements show that at pressures higher than about 20 GPa the IR absorption in the 0.9-1.5 μm range abruptly decreases. There are two main mechanisms of absorption in the IR region, phonon absorption and free carrier absorption. The former mechanism is important only in the far IR region (*i.e.*, for $\lambda \geq 0.18$ μm), and should not change substantially with pressure. In contrast, free carrier absorption can change considerably when the concentration of free electrons changes. Therefore, we interpret the quenching of the IR absorption as due to a freeze-out of electrons from the conduction band. More precisely, we estimate from our data

that the electron concentration decreases by at least two orders of magnitude.

This picture explains also the Raman experiment. Our interpretation is based on the work of Mooradian and Wright [16], who observed and discussed the plasmon-phonon coupling in GaAs. They show that the plasmon-phonon coupling shifts the LO mode to higher energies and reduces its oscillator strength. This occurs at low pressures, when the concentration of free carriers is higher than 10^{18} cm^{-3} [17]. The pressure-induced freezout of electrons leads to a reappearance of the LO mode.

We now turn to the luminescence data. Two mechanisms of the "yellow" luminescence have been proposed in the literature. In the first one, the luminescence is due to a transition from the conduction band or a shallow donor state to a deep localized state [10]. The second mechanism [18] assumes a transition from a deep gap state to a shallow acceptor. The agreement of the pressure coefficient of the yellow luminescence reported here with that of the band gap supports the former mechanism. Note that this interpretation implies that the pressure coefficient of the deep final state is very small, which is indeed plausible for deep states. For example, this is the case for the zinc-related luminescence in GaN [19]. In contrast, it is difficult to explain the observed pressure dependence of the this luminescence in the framework of the second mechanism.

Accordingly, at low pressures the pressure coefficient of the luminescence is equal to the pressure coefficient of the band gap. After the emergence of the resonance from the conduction band into the gap, the luminescence is due to a transition from the resonance-derived deep state to the same final gap state. This explains the change of slope occurring at about 20 GPa.

To confirm the proposed interpretation we have calculated the electronic structure of the nitrogen vacancy under hydrostatic pressure. The calculations were performed by quantum molecular dynamics, in large unit cells corresponding to 72 atoms in the perfect crystal. We used norm-conserving pseudopotentials, plane-wave basis, and Γ-point sampling of the Brillouin zone. The calculated pressure coefficient of the band gap is 43 meV/GPa, in good agreement with the experimental value [8]. Our results show that the vacancy-induced

resonance, located at 0.8 eV above the bottom of the conduction band at zero pressure, moves down with pressure at a rate of 5 meV/GPa. The resonance crosses the bottom of the conduction band at a pressure of about 18 GPa.

We have considered two other explanations of our data. First, we have found that the interstitial Ga also introduces a resonance which crosses the bottom of the conduction band at about 20 GPa. However, the calculated concentrations of Ga(I) in undoped samples are lower than those of V_N by a few orders of magnitude [6]. A second possibility is a pressure-induced crossover of the conduction band minimum at Γ with one of the secondary minima at the edge of the Brillouin zone. According to our results, this crossover occurs at about 60 GPa, which is too high.

In summary, our high pressure optical experiments show that a freeze-out of electrons from the conduction band occurs at about 20 GPa. We propose that this effect is due to an emergence of a conduction band resonance into the forbidden gap. The resonance-derived deep state captures free electrons, leading to the freeze-out of free carriers. *Ab initio* calculations show that the nitrogen vacancy is a shallow donor at ambient pressures, and introduces a resonance that crosses the bottom of the conduction band at $\sim$ 20 GPa. The good agreement between experiment and theory strongly supports both the proposed interpretation and the hypothesis that the nitrogen vacancy is the residual donor responsible for the observed n-type character of bulk GaN samples.

This work was supported in part by grants KBN 2-P302-064-07 and 2-P302-124-07, NSF DMR-9408437, and ONR N00014-92-J-1477.

REFERENCES

[1] R. F. Davis, Physica B **185**, 1 (1993); S. Strite and H. Morkoc, J. Vac. Sci. Technol. B **10**, 1237 (1992).

[2] H. P. Maruska and J. J. Tietjen, Appl. Phys. Lett. **15**, 327 (1969).

[3] M. Ilegems and M. C. Montgomery, J. Phys. Chem. Solids **34**, 885 (1973).

[4] B. Monemar and O. Lagerstedt, J. Appl. Phys. **50**, 6480 (1979).

[5] T. L. Tansley and R. J. Egan, Phys. Rev. B **45**, 10942 (1992), and the references therein.

[6] P. Bogusławski, E. Briggs, T.A. White, M.G. Wensell, and J. Bernholc, Mat. Res. Soc. Symp. Proc. **339**, 693 (1994); P. Bogusławski, E. Briggs, and J. Bernholc, to be published.

[7] J. Neugebauer and C. G. Van de Walle, Phys. Rev. B **50**, 8067 (1994).

[8] The linear pressure coefficient of the band gap, 47 meV/GPa, has been determined in Ref. [9] by fitting the gap with a quadratic function of pressure. A linear fit the same data gives a value of 36 meV/GPa.

[9] P. Perlin, I. Gorczyca, N.E. Christensen, I. Grzegory, H. Teisseyre, and T. Suski, Phys. Rev. B **45**, 13307 (1992).

[10] T. Ogino and M. Aoki, Jpn. J. Appl. Phys. **19**, 2395 (1980).

[11] P. Perlin, C. Jauberthie-Carillon, J.P. Itie, A. San Miguel, and I. Grzegory, A. Polian, Phys. Rev. B **45**, 83 (1992).

[12] I. Grzegory and S. Krukowski, Physica Scripta **T39**, 242 (1991).

[13] H.K. Mao and P.M. Bell, Carnegie Inst. Washington Yearbook **77**, 904 (1978).

[14] R. Letoullec, J.P. Pinceaux and P. Loubeyre, High Pressure Research **1**, 77 (1988).

[15] H. Sobotta, H. Neuman, R. Franzheld, and W. Seifert, Phys. Stat. Solidi (b) **174**, K57 (1992).

[16] A.A. Mooradian and G.B. Wright, Phys. Rev. Lett. **16**, 999 (1967).

[17] T. Kozawa *et al.*, J. Appl. Phys. **75**, 1098 (1994).

[18] E. R. Glaser *el al.*, Appl. Phys. Lett. **63**, 2673 (1993); and to appear in Phys. Rev. B.

[19] H. Teisseyre, P. Perlin, T. Suski, I. Grzegory, J. Jun, and S. Porowski, J. Phys. Chem. Solids, in press.

FIGURES

FIG. 1. Free carrier absorption spectra of single crystal bulk GaN at T=300 K for various pressures.

FIG. 2. Pressure dependence of the total infrared transmission of a bulk GaN single crystal at T=300 K.

FIG. 3. Pressure dependence of the energy of the "yellow" luminescence for a bulk sample and an epitaxial film of GaN.

FIG. 4. Raman spectra of a bulk single crystal at low (2 GPa) and high (32.2 GPa) pressures. The peaks labeled A_1(TO), E_1(TO), and E_2 reflect the phonon modes of GaN. Their appearence results from depolarization of the laser light due to strain in the diamond anvils [11]. The peak L_5 appears above about 20 GPa. Insert: pressure dependence of the L_5 peak energy. The solid line represents a linear extrapolation of the peak energy to ambient pressure.

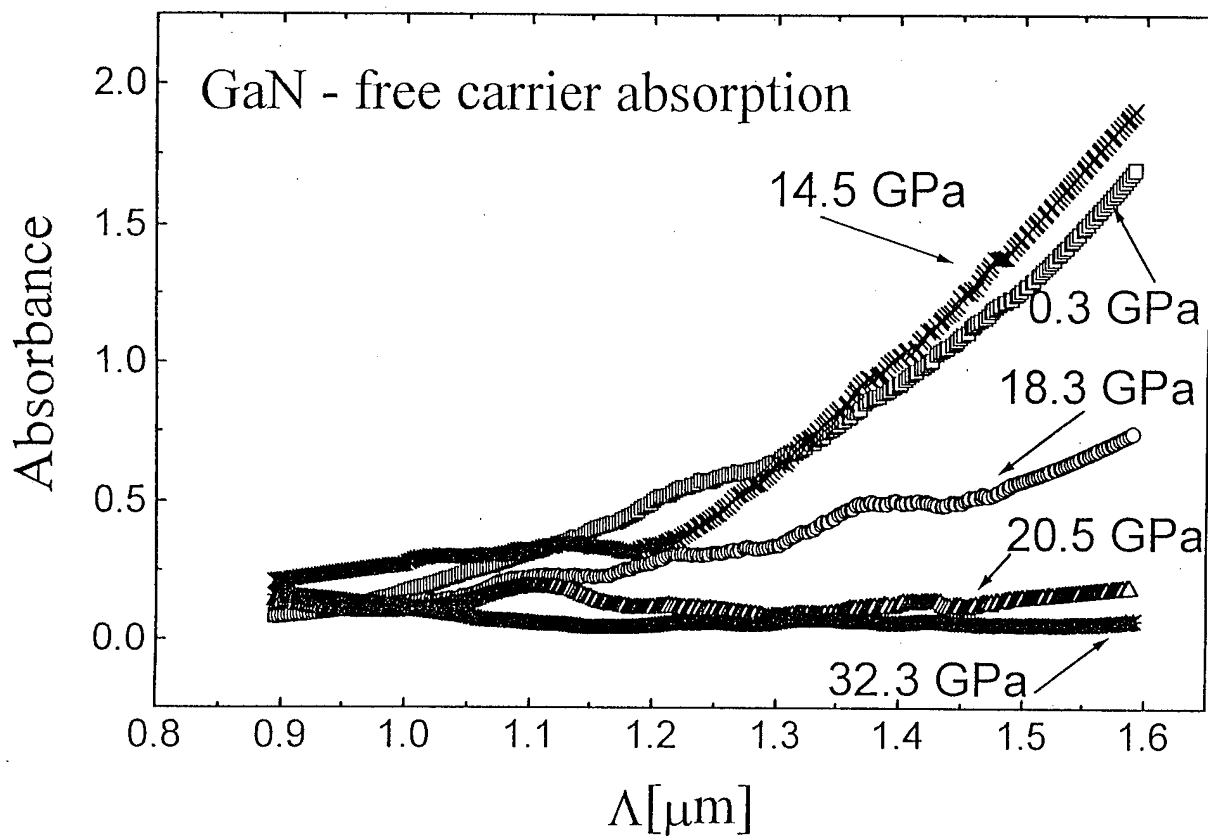

Figure 1

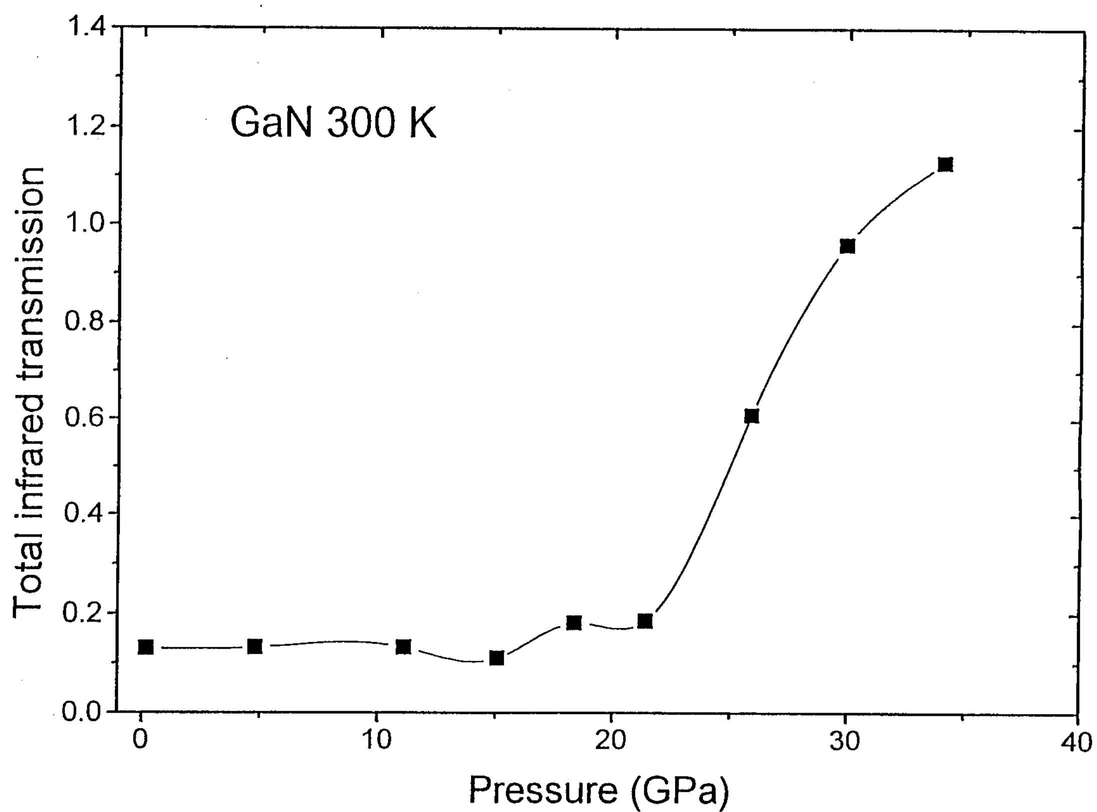

Figure 2

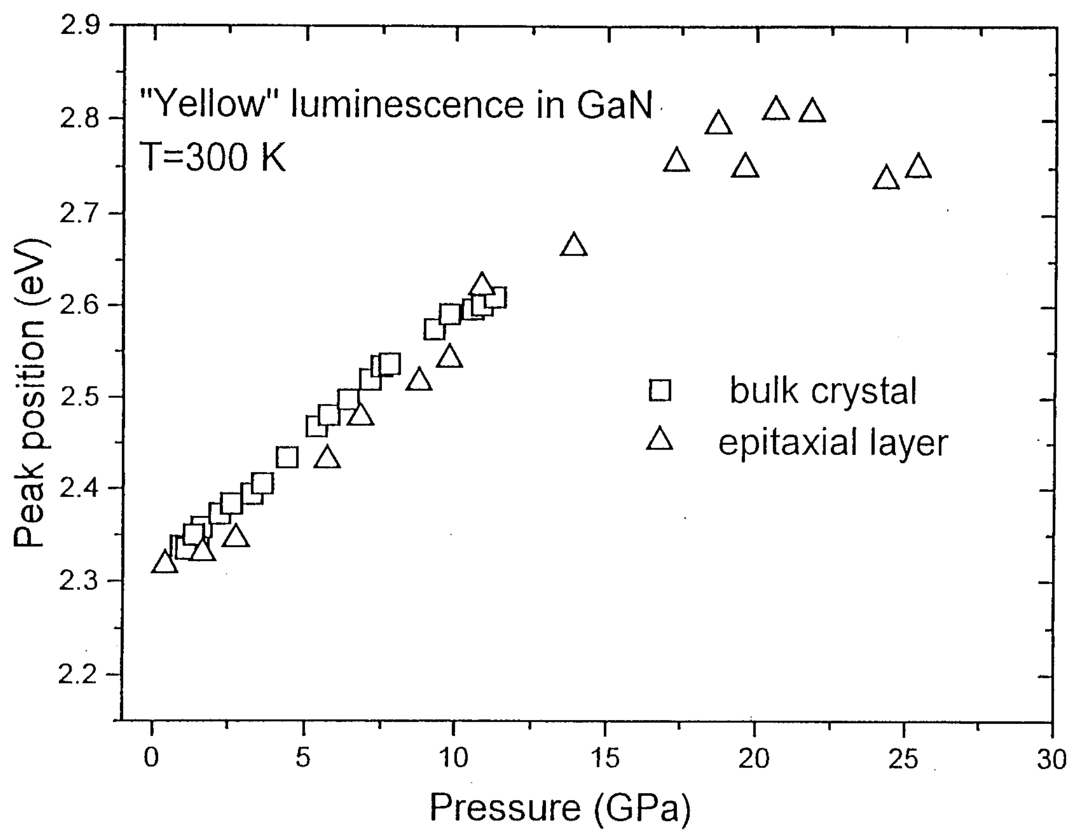

Figure 3

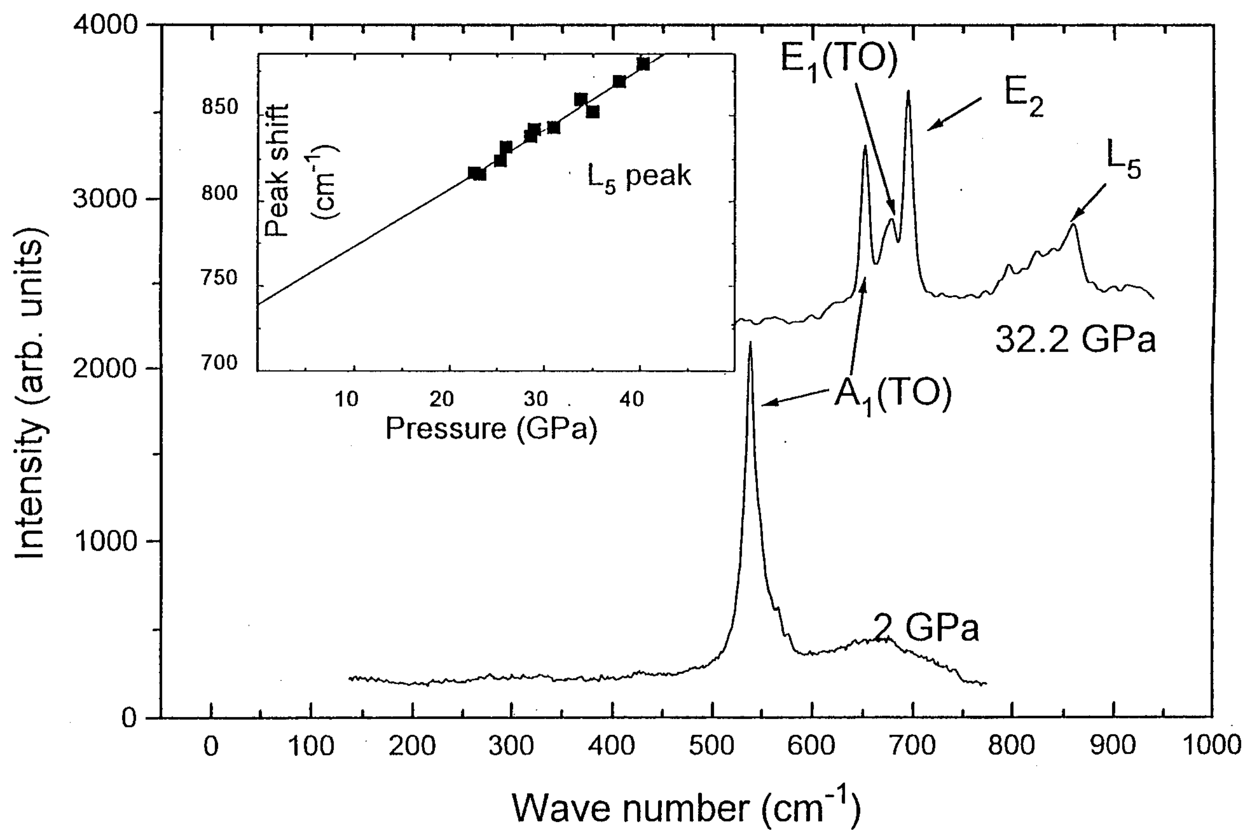

Figure 4

XXIII. Dry Etching of Gallium Nitride

A. Introduction

Gallium Nitride (GaN) is a wide bandgap semiconductor which has applications such as short wavelength light emitters and detectors, high temperature electronics, and high power electronics [1,2]. A crucial step in creating these devices is to etch anisotropic features in the GaN. Wet etching has been employed in many semiconductor processes. Thus far, wet etching has produced poor results on GaN, such as slow etch rate and isotropic etch profiles [3]. Both of these characteristics are undesirable for commercial applications. As technology advances, the need for anisotropic etch profiles increases to accommodate a smaller, more densely packed network of devices. Dry etching is an attractive alternative to wet etching. Varying degrees of anisotropy along with high etch rates can be achieved using different dry etch techniques.

There are three primary dry etch techniques that have been employed on GaN. They are Reactive Ion Etching (RIE), Electron Cyclotron Resonance Etching (ECR) and Magnetron Enhanced Reactive Ion Etching (MIE). GaN has been etched via RIE at NCSU, as well as other III-V Nitride groups [4-6]. Out of the three techniques, RIE produces the slowest etch rates and lowest degree of anisotropy. ECR, which has had much attention from Pearton *et al.* [1,3,7-8], produces significantly better results than RIE. MIE, which is the least used technique, was employed by McLane *et al.* [2], and produced results comparable to that of ECR etching.

B. Etching Overview

As previously stated, each of the three primary dry etch techniques will be discussed. They will be presented individually, and then compared at the end of this section.

Reactive Ion Etching. As the III-V Nitride technology advances, the need for commercially viable processes is getting more important. In this case, a commercially viable etching process would be one that produces the fastest controllable etch rate along with etch profiles that are suitable for the desired electronic device. RIE is lacking in both of these areas. The reason for these shortcomings are the parameters that are involved in the process. RIE is generally performed at pressures between 10 and 100 mtorr [4-6]; at these pressures the mean free path of the bombarding ions is between 5 and .5 mm respectively. With mean free paths this small, the bombarding ions will hit other ions and scatter. This scattering will result in the ions not hitting the GaN surface at 90° angles, resulting in a lesser degree of anisotropy than is usually desired. There are some cases where isotropic etch profiles are desired, but for the most part, anisotropic etch profiles are desired.

Etch rate is another area where RIE has fallen behind the other two methods. Lin *et al.* [4] have reported the highest etch rate to date via RIE of 105 nm/min in a BCl_3 plasma. This is

actually a fairly high etch rate, but at what cost? The parameters were 15 sccm BCl_3, 10 mtorr pressure, 150 w RF power, and -600 v dc bias. The etch rate is in part a function of the dc self bias and the energy of the bombarding ions is also a function of the dc self bias. As the ion energy increases, there is a better the chance of etch induced damage to the surface of the material. There have been no etch induced surface damage studies on GaN reported to date. Murtagh *et al.* [9] showed via Photo reflectance Spectroscopy that the larger the dc self bias, the greater the surface damage to GaAs. Even though GaN is a much stronger material than GaAs, it could still undergo the same damage as GaAs, just to a lesser extent.

Electron Cyclotron Resonance Etching. Out of the major types of etching GaN, ECR has the most widespread use in the research field. Shul *et al.* [10] have recently reported etch rates of 285 nm/min in a $Cl_2/H_2/CH_4/Ar$ plasma using ECR etching. One of the reasons for the high etch rates is that ECR produces a high density plasma, which results in higher etch rates as compared to RIE. The plasma in an RIE is everywhere in the chamber between the source and ground. In and ECR etcher, the plasma is magnetically confined by permanent magnets on the outside of the chamber.

The potential for surface damage to the material is reduced in an ECR etcher. ECR etching uses a microwave source instead of a RF source which lowers the energies of the ions bombarding the surface of the material. This in turn reduces the risk of producing etch induced surface damage.

Magnetically Enhanced Reactive Ion Etching. The major difference between RIE and MIE is that the plasma is magnetically confined in an MIE etcher. The magnetic field confines the plasma around the cathode that the sample is on. This in turn increases the etch rate and lowers the dc bias. Along with other things, the dc bias is a function of the surface area of the ground. Since the plasma is confined, the surface area of the ground that the plasma is exposed to is significantly reduced. McLane *et al.* [2] have reported etch rates of 350 nm/min using a BCl_3 plasma which is the highest reported to date.

The above has been a brief description of the three primary dry etch techniques for GaN. Both the MIE and ECR are basically enhancements, some more drastic than others, to a typical RIE setup. They improve upon three major faults of RIE; namely the slow etch rate, surface damage, and isotropic etch profiles. Table I is a summary of the 3 different etching methods and some typical etching parameters along with the corresponding etch rates.

C. Experimental Procedure

Experimental Apparatus. Figure 1 shows the basic etching setup. It consists of a Reactive Ion Etcher, gas handling/storage, gas scrubber, and mass spectrometer. The etcher is a Technics 85 series RIE which consists of an anodized aluminum chamber with a water cooler

Table I. Etch Rate Parameters for Dry Etching of GaN

Maximum Etch Rate (nm/min)	Plasma Gasses	Pressure (mtorr)	Power (watts)	DC Bias (- volts)	Reference
285	$Cl_2/H_2/CH_4/Ar$	2	275	NM#	[10] ECR
110	Cl_2/H_2	1	1000	150	[1] ECR
110	$HI/H_2/Ar$	1	1000	150	[8] ECR
90	$HBr/H_2/Ar$	1	1000	150	[8] ECR
350	BCl_3	7	NM#	100	[2] MIE
105	BCl_3	10	150	231	[4] RIE
60	HBr/Ar	50	NM#	350	[6] RIE
50	$SiCl_4/Ar$	20	NM#	400	[5] RIE

NM# designates a parameter that was not mentioned in the reference.

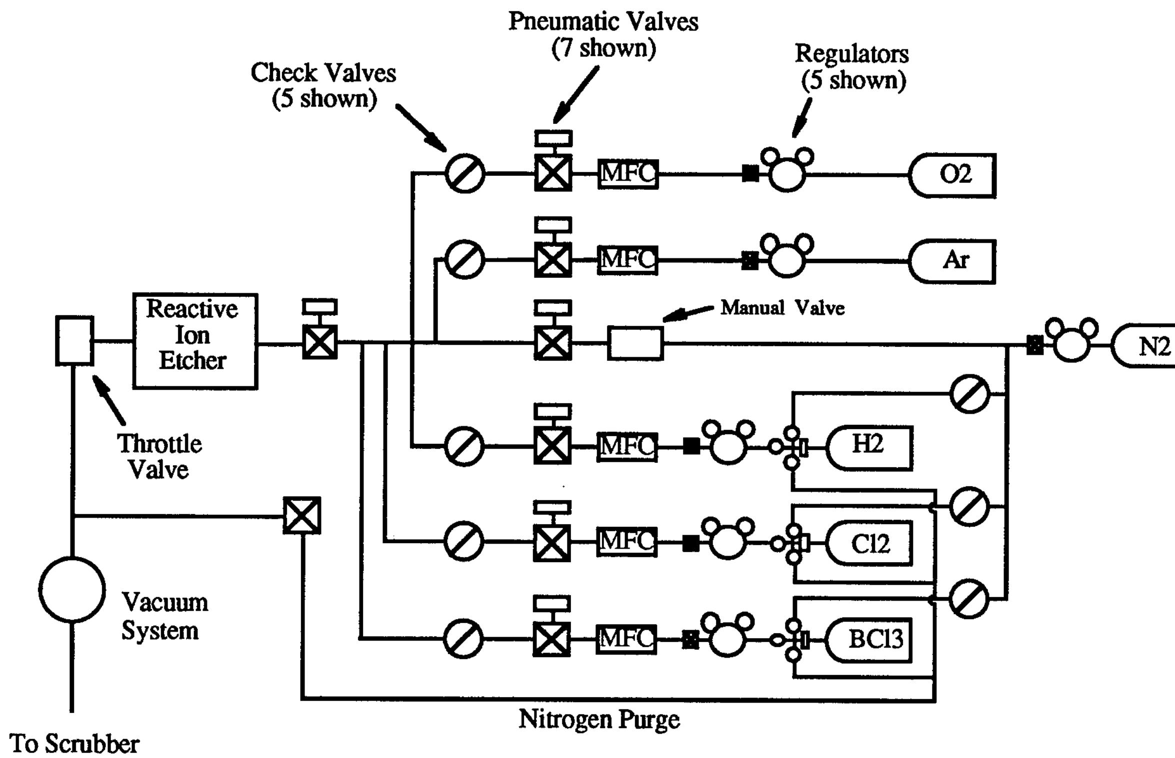

Figure 1. RIE Schematic Diagram.

anodized aluminum cathode. Connected to the cathode is a 13.56 MHz RF generator with an auto impedance matching network. The generator and the matching network produce and maintain the power to sustain a plasma discharge in the chamber. Pressure in the chamber is monitored by an MKS 627A Capacitance Manometer. A Leybold mechanical pump and an Alcatel turbomolecular pump maintain the proper level of vacuum required for processing.

To etch GaN more practically, some modifications had to be made to the chamber of the etcher. Prior to modification, the cathode was a flat, featureless disk of anodized aluminum. To make the system etch GaN more effectively, a magnetic array was designed and connected to the existing cathode. Figure 2 is a top view of the new cathode design. It consists of 2 SmCo magnets, 2 pole pieces, 3 pieces of cold rolled steel to be a return path for the magnetic flux, and an 'I' shaped piece of aluminum. The aluminum is going to be the new cathode. The aluminum is connected to the old cathode, while the remainder of the old cathode will be covered with a piece of quartz to act as a dielectric. This array will confine much of the plasma between the two pole pieces to make it as dense as possible around the GaN sample. Figure 3 illustrates this effect.

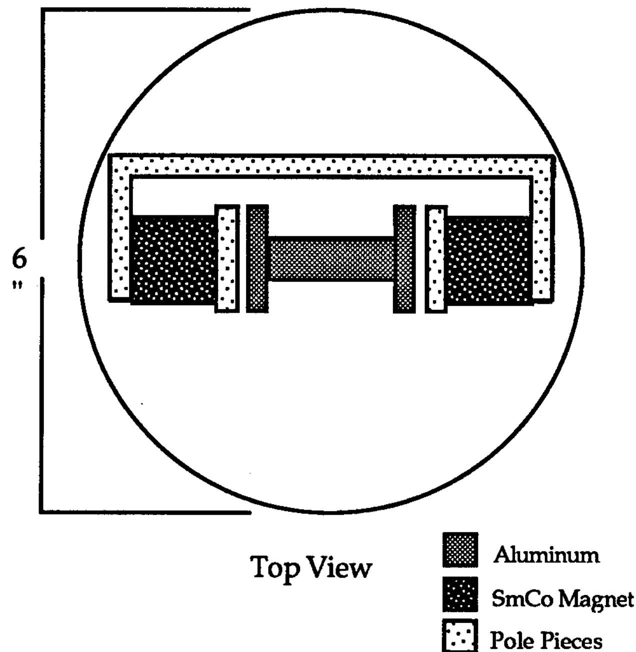

Figure 2. Magnet array placement on cathode.

Choice of Process Gasses. The gasses that the etching system is now capable of using are BCl_3, Cl_2, H_2, O_2, and Ar. Chlorides have proven to be effective gasses to etch GaN [1,2,4,8,10].

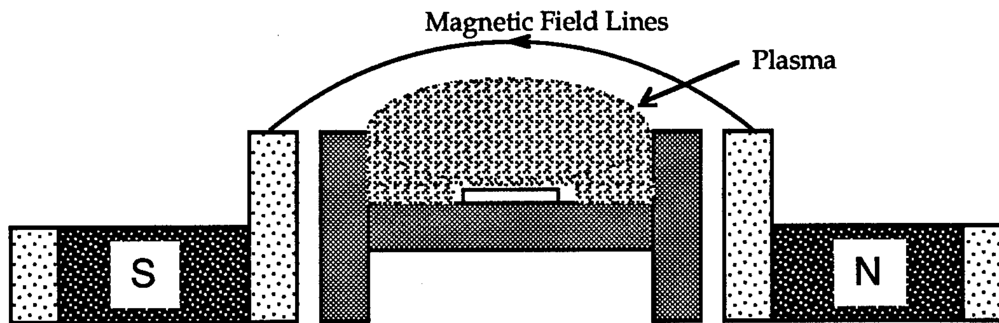

Figure 3. Side view of magnet array showing confined plasma.

Etching Procedure. The first step in the etching process is to deposit a mask material on to the sample. Ni and SiO_2 are the masks of choice for this process. Their etch rates are nominal when compared to the etch rate of the GaN. The sample must then be patterned via photolithography. Once the exposed mask material is etched away all that is left is finely patterned features in the mask material.

Once the mask is finished on the sample, the sample is briefly exposed to an argon plasma to clean off any residue from the masking procedure that may be on the sample. After the argon plasma, the sample is etched in the RIE until the desired amount of material is removed. The mask material is then removed with diluted HNO_3 for Ni and buffered oxide etch for the SiO_2.

The analytical tools that are used to characterize the etch are a profilometer for the step height, an SEM for the slope of the step, AFM for the surface roughness, and AES to observe the residual gas species on the sample surface. Schottky contacts are also going to be deposited to see how etching affects the barrier height and ideality factor [11].

D. Results and Discussion

The RIE has been modified in the following ways: the cathode has been altered as described in part C and a turbomolecular pump has been added to the system. After reading the comparison of the three etch procedures in part B, the reason for the magnet array should be apparent. Prior to adding the new vacuum pump, the lowest the system could pump down to while flowing process gasses was 20 mtorr. According to McLane *et al.* [2], the etch rate in an MIE system decreases above 7 mtorr. Now the chamber can pump down to 1 mtorr while flowing the process gasses. Etches have not yet been performed with this new configuration.

Prior to these modifications, etching was performed in the system. Etch rates of 20 nm/min were achieved using Cl_2/Ar gas, 275 w RF, -320 v dc, 3 sccm gas flow, and 50 mtorr pressure. This etch rate is considerably less that what is possible today using MIE or ECR etching.

E. Future Research

In the future, parametric studies will be done varying the process gas and flow rates, power, and pressure to determine which combination yields the fastest etch rates and least surface damage/contamination. The primary gasses are going to be chlorides, but the use of other gasses may be explored. Surface analysis techniques will be employed to determine the roughness of the surface, etch profiles, step height, and surface contamination. Since the end product of the III-N research is electronic devices and optoelectronic devices, knowing the effects of etch induced surface damage is very important. If an etched surface is highly contaminated or very rough, it may not be good for electronic and optoelectronic devices. Therefore, determining the surface effects is equally important as determining the etch rates. Other effects, such as heating the sample, may also be explored. The ultimate goal of this research is to etch anisotropic features with etch rates suitable for industry, and damage/contamination free etch surfaces.

F. References

1. S. J. Pearton, C. R. Abernathy, F. Ren, Appl. Phys. Lett. **64**, 2294 (1994).
2. G. F. McLane, L. Casas, S. J. Pearton, C. R. Abernathy, Appl. Phys. Lett. **66**, 3328 (1995).
3. S.J. Pearton, C.R. Abernathy, F. Ren, J. R. Lothian, P. W. Wisk, A. Katz, J. Vac. Sci. Technol. A **11**, 1772 (1993).
4. M.E. Lin, Z. F. Fan, Z. Ma, L. H. Allen, H. Morkoc, Appl. Phys. Lett. **64**, 887 (1994).
5. I. Adesida, A. Mahajan, E. Andideh, Appl. Phys. Lett. **63**, 2777 (1993).
6. A. T. Ping, I. Adesida, M. Asif Khan, J. N. Kuznia, Electronics Letters **30**, 1895 (1994).
7. S.J. Pearton, C. R. Abernathy, F. Ren, J. R. Lothian, P. W. Wisk, A. Katz, C. Constantine, Semicond. Sci. Technol. **8**, 310 (1993).
8. S.J. Pearton, C. R. Abernathy, C. B. Vartuli, Electronics Letters **30**, 1985 (1994).
9. M. Mortagh, P. V. Kelly, P. Herbert, M. O'Connor, G. Duffy, G. M. Crean, Applied Surface Science **63**, 158 (1993).
10. R. J. Shul, A. J. Howard, S. J. Pearton, C. R. Abernathy, C. B Vortuli, P. A. Barnes, M. J. Bozack, J. Vac. Sci. Technol. B **13**, 2016 (1995).
11. G. F. McLane, W. R. Buchwald, Mat. Res. Soc. Symp. Proc. **340**, 221 (1994).

XXIV. Photoassisted Dry Etching of GaN

R. T. Leonard
Department of Materials Science and Engineering, North Carolina State University, Raleigh, North Carolina 27695

S. M. Bedair
Department of Electrical and Computer Engineering, North Carolina State University, Raleigh, North Carolina 27695

Photoassisted etching of GaN in HCl by 193 nm ArF excimer laser is reported. A directed stream of HCl etchant with background pressure of $\sim 5 \times 10^{-4}$ Torr, sample temperature between 200-400°C, and 1400 mJ/cm^2 laser fluence combined to produce etching. Smooth etch features and distinct sidewalls were observed. For the HCl/ GaN system, photoassisted etching occurred only when both HCl and laser energy were present.

Submitted for publication in Applied Physics Letters.

A. Introduction

Successful realization of devices made from GaN depends on the ability to have controlled etching and processing of this wide band gap material. The ineffectiveness of wet etches has forced research into more advanced measures for device processing [1,2]. Recently, ion beam techniques such as chemically assisted ion beam etching (CAIBE) [3-6] and plasma based techniques [7-17] including reactive ion etching (RIE) and electron cyclotron resonance discharge etching have shown promise as effective tools for etching GaN. These processes use an ionized reactant, typically a halogen species, that impinges the surface resulting in either chemically or mechanically removed material. HCl has recently been used in CAIBE to produce vertical sidewall etch features [6]. To eliminate ion damage produced by these techniques, low biased electron cyclotron resonance discharges [11] have been used; however, a different etching process is needed which should include etch profile control, etch selectivity, as well as masking compatibility with existing patterning techniques.

Photoassisted etching appears to be a promising alternative process in overcoming current problems inherent in etching GaN. Photoassisted etching combines simultaneous exposure of reactive gas and ultraviolet laser radiation in contrast with the biased reactive plasma of RIE or the energetic ion beam of CAIBE. Laser interaction with the surface, bulk material, and chemical reactants results in excitations which are electronic and vibrational in nature, leading to the breaking of bonds and desorption of reactant products [18]. The energy input into the sample during photoassisted etching results in heat and/ or photoassisted fragmentation of chemical bonds at the surface, thus it is expected that damage free etched surfaces can be achieved. Successful photoassisted etching has already been shown for GaAs, resulting in a controlled etch profile [19]. Furthermore, projected patterning of GaAs for photoassisted etching has also been demonstrated [20].

In this paper, we will report preliminary results and demonstrate photoassisted etching of GaN using HCl with an ArF (193 nm) excimer laser. Results will show that distinct features with smooth surfaces and little damage are possible using photoassisted etching.

B. Experimental Procedure

Figure 1 shows a schematic of the vacuum system main chamber along with the gas delivery and laser introduction. The vacuum system was comprised of a load lock, intermediate chamber and main growth/ etching chamber. The main chamber was ion pumped maintaining a base pressure of $\sim 3.0\times10^{-9}$ Torr when the system was not in use. A 500 l/ s Balzers TPU 510 corrosive series turbomolecular process pump maintained a base pressure of around 1×10^{-8} Torr before introducing reactant gas. HCl (99.999% purity) was directed at the substrate via a mass flow controller switched doser. The laser source was a Lambda Physik EMG-103-MSC ArF excimer (193 nm) focused at the substrate with an incident angle of 30° normal to the

sample. Metalorganic chemical vapor deposition GaN grown on (0001) sapphire substrate (~0.3 μm thick) was solvent cleaned and mounted on a sample holder. Stainless steel clips served both to hold the GaN to the sample holder and as a physically overlaid mask, blocking exposure to the excimer radiation. The sample, laser, and gas doser were aligned to achieve a physically masked etch feature.

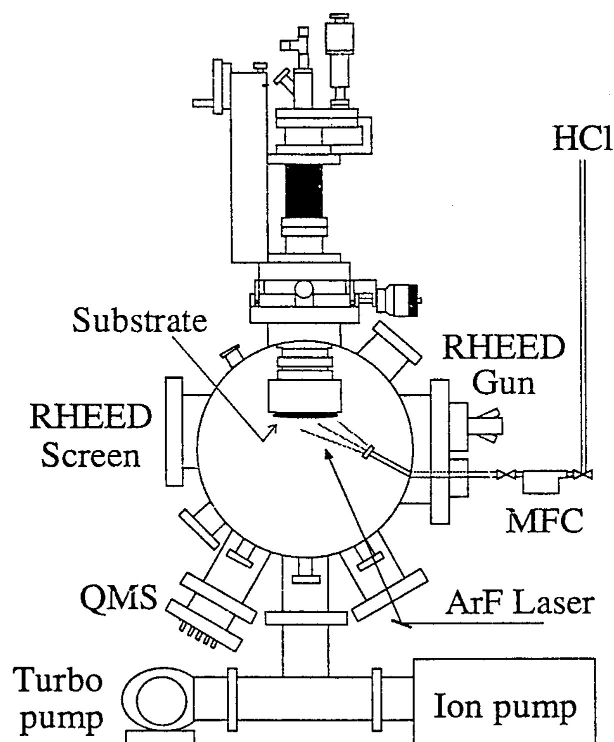

Figure 1. Schematic of main etching chamber.

The experimental laser characteristics are as follows: 30 Hz repetition rate; ~18 ns pulse; 703 mm lens (@193 nm) focusing the laser down to 30% of its original size of 0.4×2.5 cm beam dimensions; and output energy of 110-160 mJ/ pulse measured at the exit window of the excimer. The total number of pulses was typically 60,000 to 80,000. The HCl was directed onto the sample at an estimated flux of ~10^{18} molecules/cm^2-s, and the background pressure rose to near 5×10^{-4} Torr. Photoassisted etching was conducted in the 200-400°C temperature range determined by a calibrated thermocouple. The samples were characterized by photoluminescence, profilometry (Tencor Alpha-Step 200), scanning electron microscopy (SEM: Hitachi S-530, Jeol field emission JSM-6400F), and were observed both before and after etching with differential interference contrast optical microscopy.

C. Results and Discussion

Prior to etching, the sample had uniform thickness fringes; afterwards, an etched region interrupted the initial fringe pattern which was easily seen by the unaided eye. The etched feature was bounded by new fringes indicating that the etch depth was non-uniform across the feature, probably due to non-uniform laser intensity. Photoluminescence revealed there was little or no GaN emission peak ~365 nm in the etch region compared to just outside the etch region. Photoluminescence does not show that all of the GaN was etched, but suggests that a significant amount of GaN was removed.

Smoothness of the etched surfaces observed by SEM confirms that photoassisted chemical etching occurred instead of physical ablation. Figure 2 is a representative SEM micrograph of the etched region of a sample etched under the described heating, HCl flux, and laser conditions. The laser power (at exit of the excimer) was 110-120 mJ focused producing power densities of 1300-1400 mJ/ cm^2 at the sample. Ablative etching would produce roughened features due to explosive melting of the material. These features were not observed in any etched sample by optical microscopy or SEM. Other samples continuously heated at ~650°C with the same laser conditions did not yield any etch features without HCl flux. Preliminary results show no etching characteristics for the combination of HCl and temperatures near 650°C with no laser irradiation. Although the exact nature of the photoassisted etching reaction is not clear, it is thought that a laser enhanced reaction between HCl and GaN forms chlorides of gallium which are thermally desorbed, and that nitrogen leaves the surface either as molecular or NH_x species. The combination of both HCl and ArF laser energy is a necessary condition to produce photoassisted etching for this system.

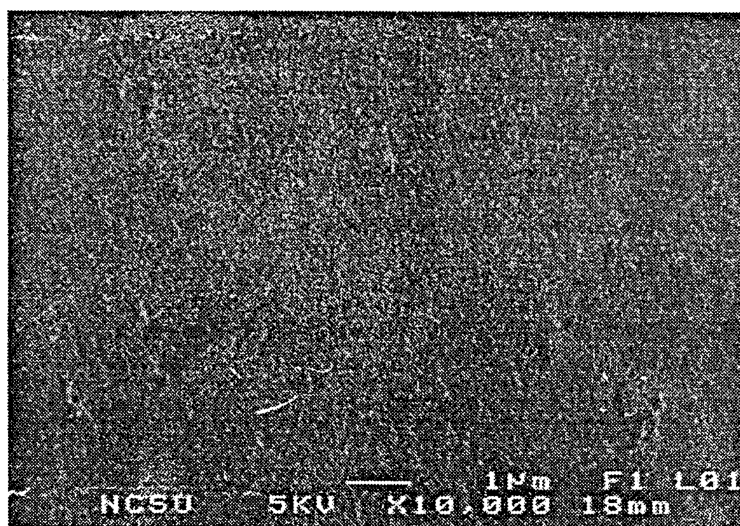

Figure. 2. Field emission SEM micrograph of GaN etched surface.

With part of the sample physically masked, profilometry shows several features in Fig. 3. The masked material in region (a) has the same appearance as before etching, indicating that no etching reaction occurs without laser exposure. Physical masking produced a distinct etched sidewall feature ~135 nm deep at (b). The feature in the etched region at (c) is smooth within the resolution of the stylus, confirming the SEM results of Fig. 2. Other photoassisted etched samples have these same characteristic smooth features as described.

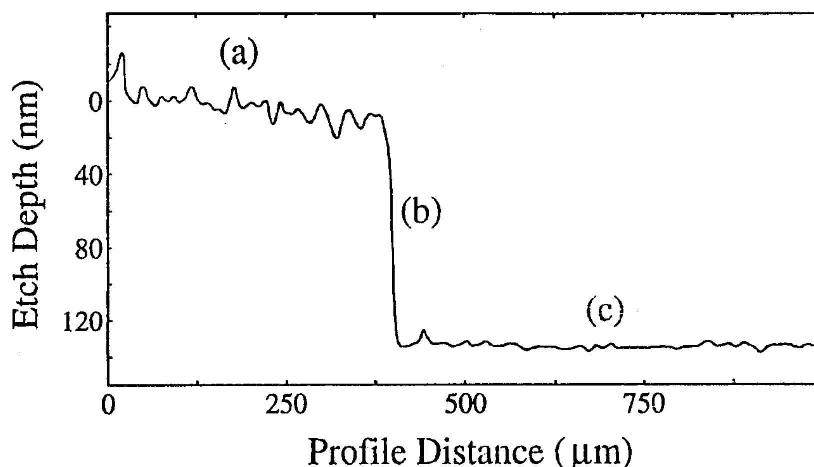

Figure 3. Three surface features of etched GaN: (a) physically masked region; (b) etched sidewall; (c) laser irradiated area.

Experiments to date have not been designed to precisely determine etch rate—only that photoassisted etching of GaN is indeed possible. Epitaxial material used for these studies has been thin (<300 nm). Direct determination of etch rate has not been possible, since in some cases the film was etched too long, through to the substrate. Assuming the etch depth as measured from profilometry and the run time/ pulses, simple calculation of etch depth/ time yields about 8 nm/min (~0.04 Å/ pulse). Higher etching rates are expected by increasing the laser pulse rate, and optimizing etching temperature, laser energy density and HCl flux.

D. Conclusion

In conclusion, we report the photoassisted HCl dry etching of GaN. Smooth etch features have been produced indicating that ablation of the substrate does not occur. Physical masking produced distinct features by this method suggesting that projected patterning of III-V nitrides can possibly be achieved in the future. By combining techniques such as molecular beam epitaxy and projected patterning, the material could be etched and have a regrowth step immediately following etching, thereby reducing the number of processing steps (and possible errors) in device fabrication. Due to the pulsed nature of this process, coupled with the result

that both laser and HCl must be present to etch the GaN, the ability to provide a self limited surface reaction could lead to controlled, atomic layer etching.

The authors would like to acknowledge the help of T. M. Rosier, Dr. F. G. McIntosh, M. Moussa, and Dr. N. E. El-Masry, and thank the Office of Naval Research University Research Initiative for their continued support of this research.

E. References

1. S. Strite, M. E. Lin, and H. Morkoç, Thin Solid Films **231**, 197 (1993).
2. H. Morkoç, S. Strite, G. B. Gao, M. E. Lin, B. Sverdlov, and M. Burns, J. Appl. Phys. **76**, 1363 (1994).
3. H. Tanaka, F. Shimokawa, T. Sasaki, and T. Matsuoka, Optoelect. Dev. Tech. **6**, 150 (1991).
4. A. T. Ping, C. Youtsey, and I. Adesida, J. Elect. Mater. **24**, 229 (1995).
5. I. Adesida, A. T. Ping, C. Youtsey, T. Dow, M. Asif Khan, D. T. Olson, and J. N. Kuznia, Appl. Phys. Lett. **65**, 889 (1994).
6. A. T. Ping, I. Adesida, and M. Asif Khan, Appl. Phys. Lett. **67**, 1250 (1995).
7. S. J. Pearton, C. R. Abernathy, F. Ren, J. R. Lothian, P. W. Wisk, A. Katz, and C. Constatine, Semicond. Sci. Technol. **8**, 310 (1993).
8. I. Adesida, A. Mahajan, E. Andideh, M. Asif Khan, D. T. Olson, and J. N. Kuznia, Appl. Phys. Lett. **63**, 2777 (1993).
9. S. J. Pearton, C. R. Abernathy, F. Ren, J. R. Lothian, P. W. Wisk, and A. Katz, J. Vac. Sci. Technol. A **11**, 1772 (1993).
10. S. J. Pearton, C. R. Abernathy, and C. B. Vartuli, Elect. Lett. **30**, 1985 (1994).
11. S. J. Pearton, C. R. Abernathy, and F. Ren, Appl. Phys. Lett. **64**, 2294 (1994).
12. A. T. Ping, I. Adesida, and M. Asif Khan, and J. N. Kuznia, Elect. Lett. **30**, 1895 (1994).
13. M. E. Lin, Z. F. Fan, Z. Ma, L. H. Allen, and H. Morkoç, Appl. Phys. Lett. **64**, 887 (1994).
14. R. J. Shul, S. P. Kilcoyne, M. Hagerott Crawford, J. E. Parmeter, C. B. Vartuli, C. R. Abernathy, and S. J. Pearton, Appl. Phys. Lett. **66**, 1761 (1995).
15. S. J. Pearton, C. B. Vartuli, R. J. Shul, and J. C. Zolper, Mat. Sci. and Eng. **B31**, 309 (1995).
16. S. J. Pearton, F. Ren, T. R. Fullowan, A. Katz, W. S. Hobson, U. K. Chakrabarti, and C. R. Abernathy, Mater. Chem. and Phys. **32**, 215 (1992).
17. S. J. Pearton, Mat. Sci. and Eng. **B27**, 61 (1995).
18. T. J. Chuang in *Laser Microfabrication: Thin Film Processes and Lithography*, D. J. Ehrlich and J. Y. Tsao, eds., Academic Press, Inc., San Diego, 1989, p. 87.
19. P. Tejedor and F. Briones, in Mat. Res. Soc. Symp. Proc. **201**, 141 (1991).
20. P. D. Brewer, D. McClure, and R. M. Osgood, Jr., Appl. Phys. Lett. **49**, 803 (1986).

XXV. Contact Formation on n-type and p-type GaN

A. Introduction

The formation of ohmic contacts with semiconductor materials and devices is a fundamental component of solid state device architecture. As device size has diminished and the scale of integration has increased, the quality of these interfaces has become an increasingly important concern. In addition, the presence of parasitic resistances and capacitances, such as those existing at contact interfaces, becomes more detrimental at higher operating powers and higher oscillation frequencies. For many devices, the losses that occur at the contact interfaces account for a large fraction of the total losses and, as such, are responsible for significant impact on device performance.

The development of adequate and reliable ohmic contacts to the compound semiconductors, particularly those with wider bandgaps, has met a number of challenges. The subject of ohmic contacts to p- and n-type III-V compounds, mostly GaAs, AlGaAs, and InP, has received a great deal of attention over the past decade and significant advances have been made [1-12]. By comparison, the III-V nitrides have received little attention in this regard. However, interest in these materials has been renewed in recent years as great strides have been made in the successful, commercial implementation of bright blue GaN LED devices.

GaN Surface Cleaning. Over the course of the development of semiconductor device technology, surface cleaning procedures have been devised to 1) degrease and remove gross contamination, 2) remove particulates and metal atom contamination, and 3) remove surface oxides to provide surfaces as atomically clean as possible. In practice, surface cleaning is as much of an art form or craft as it is a science; understanding of the surface composition and structure often lags well behind the successful application of processing steps. Procedures are frequently derived empirically with little detailed understanding of the chemistry or physics involved. Often, the meaning of the word "clean" varies depending on the surface conditions required for success with different processing steps, though surface impurity concentrations may vary by orders of magnitude. Given that the sensitivity of surface analytical techniques for detection of submonolayer coverage is limited, there are inherent limits on the ability to show conclusively that a surface is truly atomically clean [13].

As stated above, there are indications in the literature that cleanliness and preparation of the semiconductor surface prior to contact deposition play significant role in the performance of the interface. The goal of the surface cleaning studies described in this report is to determine the most effective choices of wet chemical cleaning and thermal desorption cleaning to use prior to metallization.

Metallization Strategies. The majority of successful ohmic contact systems that have so far been implemented with the more conventional compound semiconductors have relied upon alloying (liquid-phase reaction) or sintering (solid-phase reaction) via post-deposition annealing treatments, and/or the presence of high carrier concentrations near the interface [1,2,6,12]. However, many otherwise successful ohmic contact systems have only limited thermal stability and are subject to degradation—usually in the form of extensive interdiffusion, interfacial reaction, and interphase growth, accompanied by increase in contact resistivity—under subsequent thermal processing steps. It is reasonable to suppose that the cleanliness and preparation of the semiconductor surface prior to contact deposition plays a significant role in the behavior of the interface, and there are indications in the recent literature that support this [2,11,12,14]. Thorough oxide removal is especially important, though it may well prove to be a persistent challenge with Al-containing compounds in particular.

In this study, two main approaches are being taken in the development of ohmic contacts to GaN and AlN. The first approach is similar to that which has resulted in the majority of successful ohmic contacts to the more conventional compound semiconductors such as GaAs: the creation of high carrier concentrations in the semiconductor at the metal interface by means of alloying, sintering, or implantation of dopant species. The so-called pinning of the Fermi level at this surface, particularly with GaAs, results in a more or less fixed potential barrier at the metal interface. In the case of the pinned Fermi level of GaAs, the approach has generally been to shrink the width of the depletion layer by means of increasing the carrier concentration to the point where carriers tunnel readily through the barrier. Even with optimization of contact composition and annealing times and temperatures, the lowest contact resistivities (ρ_c) have been obtained only on the most heavily doped materials. Though there are indications that high doping levels and extensive interfacial reactions through alloying and sintering are not essential for ohmic contact formation in all cases, these processes have proven useful for minimizing ρ_c [2,11,12,14].

The other approach toward ohmic contact formation to be taken in this study involves the Schottky-Mott-Bardeen (SMB) model of semiconductor interfaces [15,16]. In this model the relative values of work function of the materials involved determine the band structure of the interface and thus the nature of any potential barriers present. The presence of interfacial states at the semiconductor surface can interfere with the alignment of the Fermi level across the interface and overshadow the effect of the inherent difference in work function between the two materials. The III-V nitride compounds are more ionically bonded than their phosphide and arsenide counterparts, as a result of larger electronegativity differences between the component elements. According to the observations of Kurtin *et al.* [17], this fact indicates that the nitrides should experience less Fermi level stabilization or "pinning" at the surface than do the more covalent compounds. Thus, the barrier heights of contacts to the nitrides should be more

dependent on the contact material than is the case with the more conventional and more covalent semiconductors such as Si, GaAs, InP, SiC, etc. With the work of Foresi and Moustakas [18,19], M.E. Lin *et al.* [20], Binari *et al.* [21], and the present authors, investigation of this concept is now underway. The SMB model also indicates that the cleanliness of the interface plays an important role in its electrical behavior, particularly in the minimization or elimination of any insulating layers at the interface.

One area of contacts development that has received a significant amount of attention is that of the metal silicide compounds. Silicide thin films have been extensively studied and applied as contacts and interconnects, mostly for silicon-based technology [22-27]. In comparison, the properties of the metal germanides are not well documented. As a general rule, germanides have been found to be more resistive than silicides and their chemistry with Si-based materials more complex. However, in a series of studies, M. O. Aboelfotoh *et al.* have shown that a particular phase of copper germanide, specifically the ordered monoclinic phase ε_1-Cu_3Ge, is an exception to these rules [28-31]. Thin films of Cu_3Ge exhibit remarkably low resistivities, unlike Cu_3Si and, unlike both Cu and Cu_3Si, are surprisingly stable with respect to oxygen and air exposure. As such, Cu_3Ge presents itself as a potentially useful contact metal. Indeed, preliminary experimentation with Cu_3Ge contacts on GaAs and GaN, primarily on n-type and heavily-doped p-type material, has produced some favorable results in terms of ohmic contact formation. For these reasons, copper-germanium contacts were investigated during this reporting period as possible candidates for high-quality, low-resistivity ohmic contacts.

B. Experimental Procedure

GaN Film Deposition. The substrates used for III-nitride film growth were 6H-SiC wafers supplied by Cree Research, Inc. The III-N films used in these contacts studies were grown by means of metalorganic vapor phase epitaxy (MOVPE). The growth reactor used for the nitride film deposition is described in other sections of this report. Magnesium incorporated into the films during growth as the p-type dopant, Ge, was used to grow n-type material via MBE and Si was used as the more effective donor impurity for the MOVPE-grown films.

Surface Analysis. Auger electron spectroscopy (AES) was used to characterize the presence of chemical impurities on the cleaned GaN surfaces. This technique involves the energy analysis of characteristic electron emission from the surface of a sample in response to an incident electron beam. Like the related technique x-ray photoelectron spectroscopy (XPS), which uses incident x-ray radiation as the primary energy source, AES allows the detection of atoms in the first few atomic layers of a surface (1-5 nm) to a sensitivity of approximately 0.5-1%. This sensitivity corresponds under most conditions to submonolayer coverage and thus, is usefully applied to studying the contamination of surfaces by oxide and hydrocarbon deposition.

Auger electron spectroscopy was performed at the NCSU Surface Science Laboratory, using an AES analysis system manufactured by VG Instruments Ltd. Incident beam energy was 3 kV with a spot size of 1 m. Spectra were acquired over the energy range 30-1230 eV, with an energy resolution of 1 eV/step.

Contact Deposition. Prior to metals deposition, the GaN/SiC films were cleaned with a 1:1 HCl:DI H_2O dip and carefully pulled dry from the solution. Any remaining cleaning solution was blown dry with N_2. The UHV system used for the Ti, TiN, and Cu_3Ge depositions provided the means for heating the samples in vacuum. In these cases, the GaN samples were thermally desorbed at 700°C for 15 min for further cleaning of the surfaces. Titanium and TiN were grown on Si-doped GaN (MOVPE-grown, $n=1.2\times10^{18}$ cm^{-3} and $n=7.4\times10^{18}$ cm^{-3}) using electron beam evaporation of Ti; for TiN deposition, purified N_2 activated by a Kaufman-type ion gun was added. Both the Ti and TiN growth were performed at a substrate temperature of 350°C and a deposition rate of 10-15 Å/min. Total thickness for both metal films was 1000 Å. Auger depth-profiling analysis of TiN films grown under these conditions have revealed them to be stoichiometric TiN and uniform through the thickness even when variations in pressure and deposition rate occurred during growth. In addition, the metallic gold-like appearance of the TiN compound is a reliable indicator of stoichiometry. Film thicknesses were monitored using a quartz crystal oscillator. The Cu_3Ge contacts on n-type GaN (MOVPE, Si-doped) were deposited at NCSU in a UHV electron beam evaporation system. The Cu and Ge components of this contact system were deposited sequentially, 800 Å layers of Cu followed by 1200 Å of Ge; these film thicknesses place Cu and Ge on the GaN surface with a Cu:Ge atomic ratio of 3:1. The alloying of the layers was accomplished by heating at 400°C for 15 minutes while in vacuum after the metal evaporation, as described by Aboelfotoh *et al.* [27-30]. The TLM patterns for the Ti, TiN, and Cu_3Ge contacts were defined using photolithography. On p-GaN:Mg, Pt films were deposited by means of Ar ion sputtering using a shadow mask to define the test pattern. No thickness monitor was available in the sputtering system; but from the sputter time, voltage, and current, the deposition was expected to result in a film approximately 600 Å thick.

Contact Characterization. After deposition, I-V measurements were taken between separate pads of the TLM patterns using tungsten probe tips and an HP 4145C Semiconductor Parameter Analyzer. Annealing treatments for the Ti, TiN, and Pt contacts were performed in a flowing Ar atmosphere (ultra-pure carrier grade from Air Products, Inc.) at a series of temperatures (600, 700, 800 and 900°C for 30 s each step) using a Heatpulse 410 rapid thermal annealing (RTA) furnace. The Cu_3Ge contacts were annealed under UHV conditions at 600, 700, and 800°C for 15 min at each step. TLM measurements were taken by measuring the total resistance between identical contact pads as a function of separation distance l. The contact resistivity was obtained from the plot of R(l) vs. l, as described by Reeves and Harrison [32].

The mathematical assumptions and pattern geometry inherent in this model yield values for ρ_c that represent an upper limit; thus, the measured values are conservative assessments of performance. In addition, for every test pattern geometry there is a lower limit of ρ_c below which it is not possible to obtain precise ρ_c calculations. This is due to the fact that the linear R(l) plot becomes very steep and too close to the origin with decreasing ρ_c. For the shadow-mask test geometry used in this study to date and for many of the TLM results reported by other researchers in the field, the practical lower limit for precise ρ_c calculation is about 10^{-6} $\Omega \cdot cm^2$.

C. Results

GaN Surface Cleaning. Acquired AES spectra from surfaces cleaned in a variety of wet chemical solutions are shown in Fig. 1. The label "DI" refers to deionized water; the term "solvent cleaning" refers to the conventional sequence trichloroethylene (TCE), acetone, and methanol (MeOH); all of the samples were solvent-cleaned prior to the acid dip step. The last cleaning step for each sample was followed by blowing dry with N_2, without water rinse. The as-received sample was exposed to air for at least a week prior to characterization; all of the cleaned samples were loaded into the vacuum system (base pressure 5×10^{-9} T and below) as soon as possible. Each received an unavoidable exposure to air for approximately 10 minutes during the time required to secure each sample to the sample holder.

For the purpose of graphing these data, the nitrogen peak-to-peak heights were all set to the same value so that the relative concentrations of O and C may be compared. The associated data of peak height ratios are listed in Table I. The peak-to-peak heights of the oxygen and carbon signals are related to the peak-to-peak height of the nitrogen signal and indicate the relative abundance of oxygen-based and carbon-based surface coverages. The ratios of peak heights have been used because, though the total number of counts in a given peak may vary from run to run, the *relative* peak intensities remain the same for a given surface.

Table I. Relative Auger Peak Intensities from GaN Surfaces Cleaned with Different Wet Chemical Treatments

Treatment	O/N	C/N
As-received	0.39	0.28
UV/ozone oxidized	0.98	0.31
HCl:DI (1:1)	0.21	0.24
HCl:MeOH (1:1)	0.24	0.32
HF:DI (1:20)	0.33	0.38
HF:DI (1:1)	0.26	0.18
HF:MeOH (1:1)	0.33	0.41

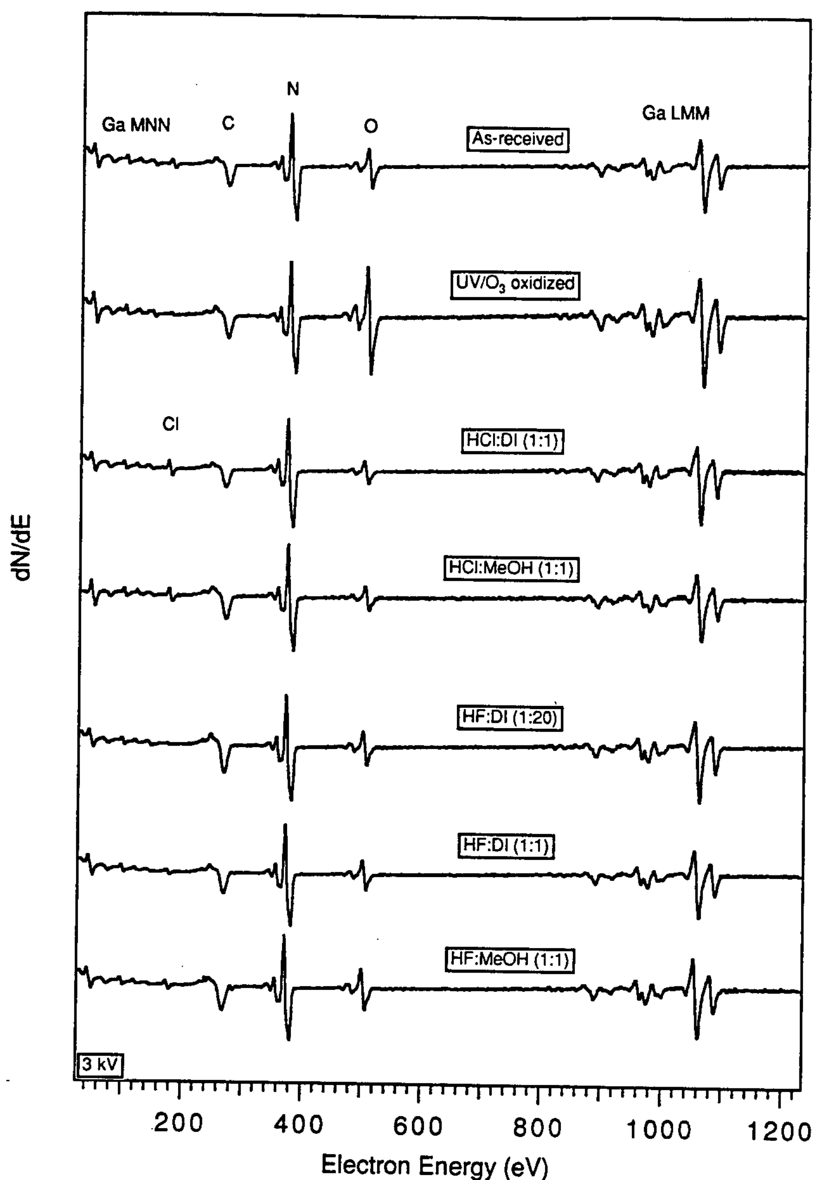

Figure 1. AES survey spectra of GaN surfaces cleaned with different chemical treatments.

Of all the wet chemical cleaning methods compared here, the HCl:DI (1:1) solution yielded the lowest relative concentration of oxygen on the air-exposed surfaces. A substantial decrease in O coverage after HCl- and HF-based cleaning treatments has been observed for both simple air-exposed and UV/ozone oxidized GaN surfaces indicating the actual removal of surface oxides. The use of methanol to dilute the HCl solution resulted in an increase of both O and C, presumably due to the physisorption of methanol, though both HCl-based solutions resulted in lower O/N ratios than did any other surface condition examined. All of the remaining cleaning treatments showed larger relative concentrations of both O and C, with the exception of HF:DI producing an as-cleaned C/N ratio of 0.18. Of all the HF cleaning treatments examined, the

HF:DI (1:1) treatment gave the lowest O and C concentrations. The highest concentrations of O and C observed were found on the HF:MeOH-treated surface, slightly higher than those on the as-received surface.

The effects of heating GaN surfaces on the presence of O and C are shown in Fig. 2. The following HCl-based and HF-based cleaning methods were compared: HCl:DI (1:1), HCl:MeOH (1:1), HF:DI(1:1), and HF:MeOH (1:1). All of the desorption series show a gradual decrease in the presence of O and C through 650°C. However, small but detectable amounts of O and C were still present on the GaN surfaces even after heating to 800°C. During the 800°C heating steps, residual gas analysis in the UHV heating chamber revealed the presence of small amounts of gas-phase Ga released by the samples, indicating the beginnings of GaN decomposition. The relative proportions of O and C that remained on each surface after the desorption series were different for the HCl-cleaned and HF-cleaned samples: after the 800°C desorption step, the HCl-cleaned surfaces showed the lowest O levels, while the HF-cleaned surfaces showed the lowest C levels.

Table II. Relative AES Peak Intensities for GaN Surfaces as a Function of Temperature and Surface Treatment.

	HCl:DI (1:1)		HCl:MeOH (1:1)		HF:DI (1:1)		HF:MeOH (1:1)	
Desorption Temperature	O/N	C/N	O/N	C/N	O/N	C/N	O/N	C/N
RT	0.21	0.24	0.23	0.31	0.26	0.18	0.41	0.33
500°C	0.18	0.17	0.16	0.27	0.16	0.16	0.18	0.32
625°C	0.14	0.14	0.16	0.25	0.17	0.13	0.16	0.24
800°C	0.39	0.17	0.15	0.21	0.19	0.08	0.17	0.29

Ti and TiN Contacts on n-GaN:Si. The as-deposited Ti contacts on Si-doped, MOVPE-grown n-GaN exhibited rectifying behavior and high resistance. The TiN contacts were deposited on GaN of two different carrier concentrations ($n=1.2\times10^{18}$ cm^{-3} and $n=7.4\times10^{18}$ cm^{-3}); in both cases the TiN contacts were ohmic in the as-deposited condition, though the higher-doped samples showed substantially lower resistance in current-voltage measurements. For the lower-doped n-GaN, TLM measurements of TiN/n-GaN yielded as-deposited ρ_c values of 650 $\Omega\cdot$cm^2. The specific contact resistivities and high series resistance in the as-deposited Ti/n-GaN and TiN/n-GaN ($n=1.2\times10^{18}$ cm^{-3}) contacts decreased sharply in response to annealing, as shown in Figs. 3 and 4, respectively. After the 600°C

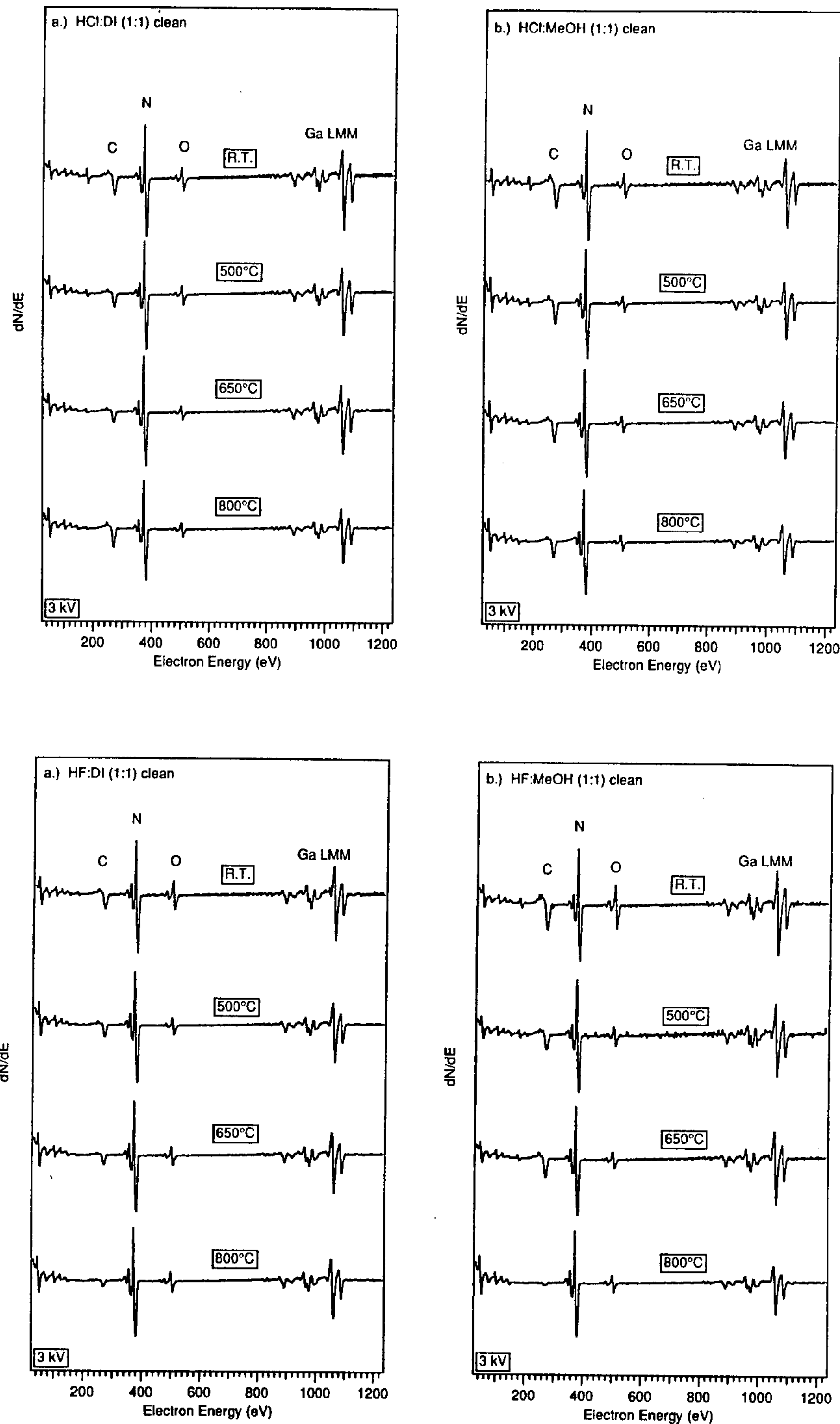

Figure 2. AES survey spectra of GaN surfaces as a function of temperature.

anneal, the Ti contacts lost most of their rectifying character and the overall resistance decreased markedly. With subsequent anneal steps through 900°C, the ρ_c of both contacts dropped substantially; the TiN contacts reached 1.1×10^{-2} $\Omega\cdot cm^2$ and the Ti contacts reached

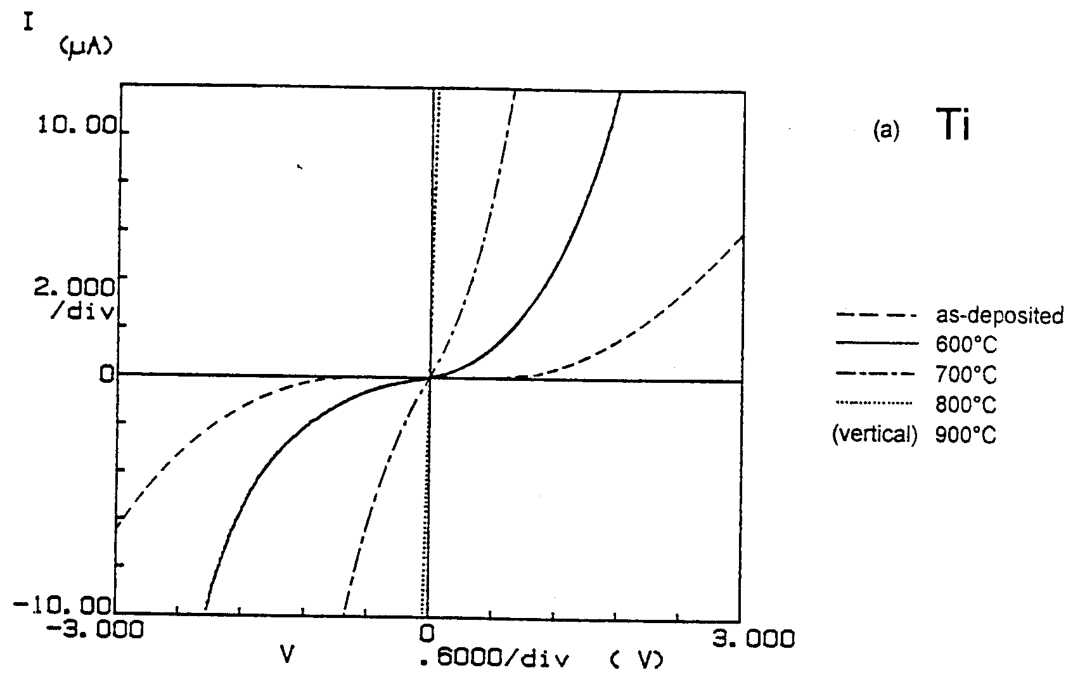

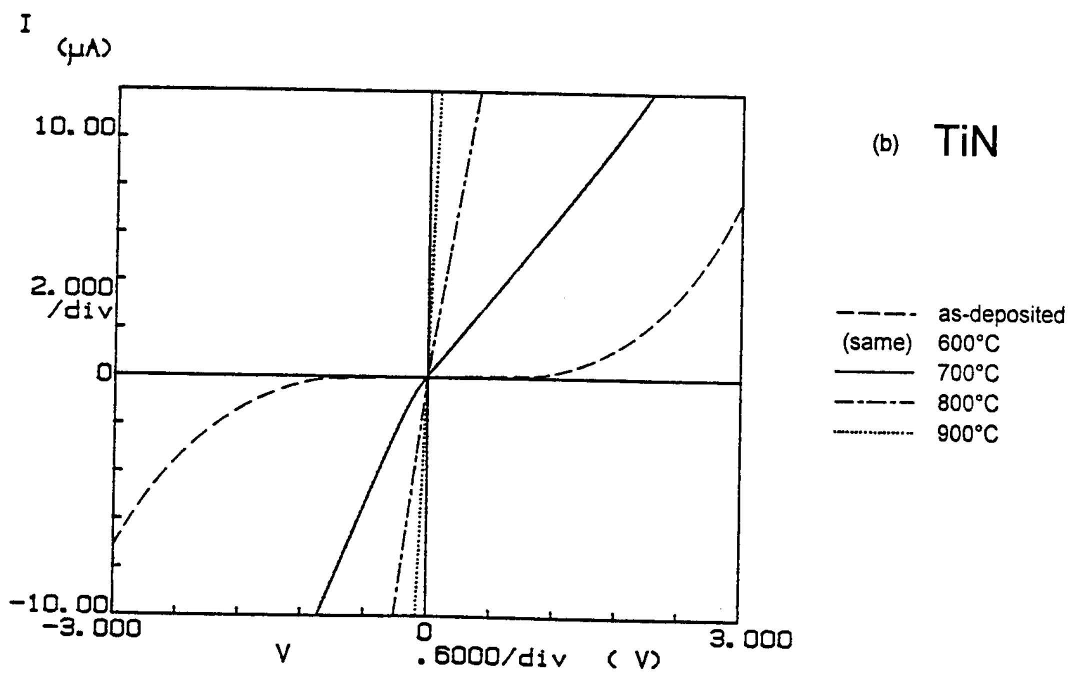

Figure 3. Evolution of I-V behavior for (a) Ti and (b) TiN metal contacts on n-GaN as a function of annealing temperature.

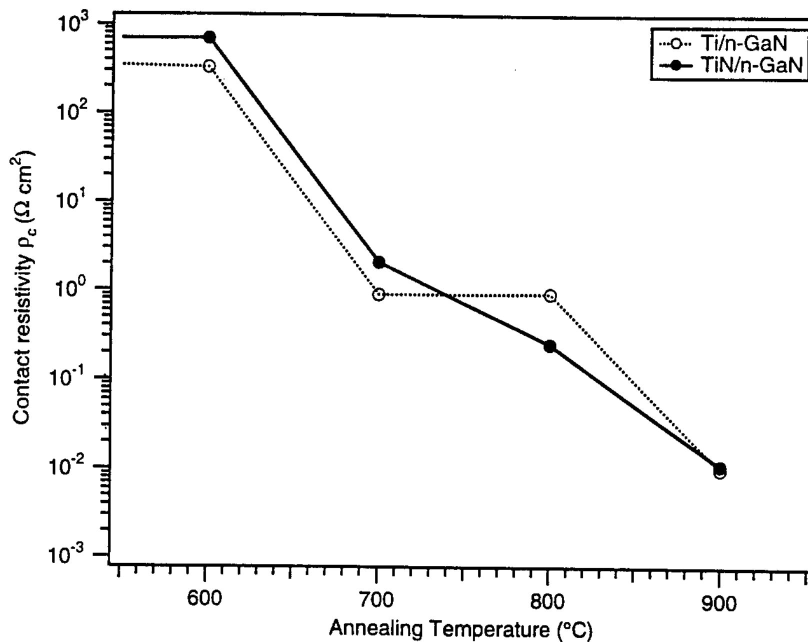

Figure 4. Specific contact resistivity ρ_c for Ti and TiN contacts on n-GaN ($n=1.2\times10^{18}$ cm^{-3}) as a function of annealing temperature.

9.9×10^{-3} $\Omega\cdot$cm^2. The TiN contacts on the more highly doped GaN ($n= 7.4\times10^{18}$ cm^{-3}) exhibited low-ρ_c behavior is the as-deposited condition; TLM measurements revealed a low room temperature specific contact resistivity of 2.5×10^{-5} $\Omega\cdot$cm^2. In contrast to the TiN contacts on the lower-doped GaN, the already low-ρ_c behavior did not change as a result of annealing treatment.

Room temperature TLM measurements showed that the ρ_c for both the Ti and TiN contacts decreased with increasing temperature, from 10^2 to the 10^{-2} Ω cm^2 range. These results are plotted in Fig. 4, showing ρ_c as a function of annealing temperature. Neither the Ti nor the TiN contacts changed substantially with respect to contact resistivity until the 700°C anneal. A large drop in ρ_c, of over two orders of magnitude, occurred after 700 °C and followed by smaller drops in ρ_c at higher temperatures.

Cu_3Ge Contacts on n-GaN:Si. Current-voltage measurements of the Cu_3Ge contacts on GaN:Si ($n=7.4\times10^{18}$ cm^{-3}) revealed nearly-linear ohmic behavior with low overall resistance; TLM measurements showed the ρ_c to be 4.9×10^{-3} $\Omega\cdot$cm^2. The same contact system deposited on lower-doped GaN ($n=4.5\times10^{17}$ cm^{-3}) was much more resistive and showed more non-linearity in the I-V measurements; a ρ_c of 18 $\Omega\cdot$cm^2 was obtained. In both cases, the as-alloyed contacts had a shiny, smooth surface, indicative of little or no roughening or reaction at the interface. Subsequent annealing of the samples under UHV conditions resulted in little change in ρ_c for both doping levels, until the samples were heated at 800°C. However, after the 600°C anneal, the I-V measurements of the contacts on the lightly-doped GaN

($n=4.5\times10^{17}$ cm^{-3}) became substantially more linear. After the 800°C annealing step, the Cu_3Ge ρ_c for both GaN doping levels increased sharply, as shown in Fig. 5. For the $n=7.4\times10^{18}$ cm^{-3} contacts, the ρ_c rose to 1.0 $\Omega\cdot cm^2$, and on the $n=4.5\times10^{17}$ cm^{-3} contacts the ρ_c reached 69 $\Omega\cdot cm^2$. In addition, the metal contact surfaces appeared somewhat dulled after the 800°C anneal, indicating that some roughening had taken place. Current-voltage measurements of the Cu_3Ge metal layers themselves revealed that the metal layers had become much more resistive as a result of the 800°C anneal. This increased series resistance in the measurement circuit was responsible for the increase in calculated ρ_c values.

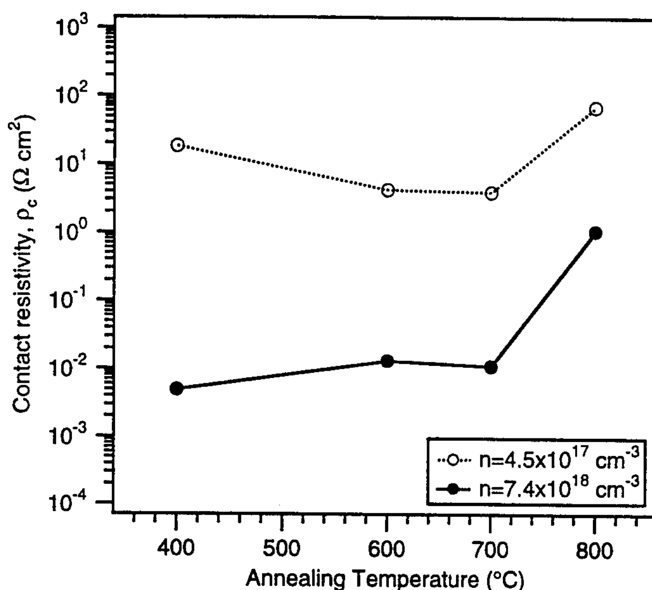

Figure 5. Specific contact resistivity for Cu_3Ge/n-GaN:Si contacts as a function of annealing temperature.

Pt Contacts on p-GaN:Mg. These contacts were found to be quasi-ohmic and highly resistive in the as-deposited condition, as shown in Fig. 6. Upon annealing at temperatures up through 800°C, the I-V behavior of the Pt contacts became more linear and ohmic and resistances dropped. After the 900°C step, however, the contacts began to turn more resistive again. Associated with this increase in resistance was an increasingly dull appearance of the Pt metal surface, indicative of possible interfacial reaction.

D. Discussion

GaN Surface Cleaning. The presence of measurable amounts of O and C on all of the air-exposed surfaces is not surprising, given the fact that at atmospheric pressure, the time required to adsorb 1 monolayer is less than 10^{-9} s. Also, the use of UV/ozone oxidation on the

as-received surface resulted, not surprisingly, in a very large increase in O and a slight increase in C coverage. A very small Cl peak was observed as well. Trace amounts of possible Cl appear in the spectra from other samples as well, due perhaps to earlier cleaning treatments (>1 month prior to this study), from HCl or TCE, and/or chloride present as the predominant impurity in even high-purity HF solutions.

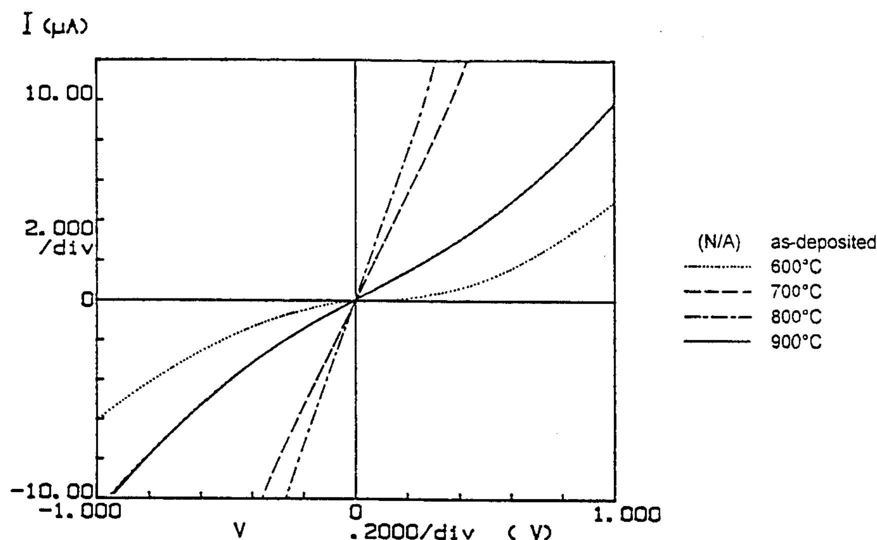

Figure 6. Evolution of I-V behavior for Pt contacts on Mg-doped GaN as a function of annealing temperature.

Though the acid:MeOH-treated surfaces naturally exhibited higher C peak intensities before the thermal desorption, both the HCl:MeOH- and HF:MeOH-treated samples showed lower C peak intensities than the HCl:DI- and HF:DI-treated samples after the 800°C heating step. This observation is consistent with the expectation that the methanol is primarily physisorbed, and its occupation of many available surface sites protects the surface from coverage with more strongly bound C-containing species. This effect is much more pronounced with the HF cleaning than with the HCl; for both the HF:DI and HF:MeOH-cleaned surfaces, the C/N peak height ratios had diminished drastically after the 800°C heating step. This substantial difference in thermal desorption behavior supports the expectation that HF is more effective than HCl at passivating active sites on the surface—or at least sites active with respect to carbon bonding. On all of the samples heated to 800°C, a certain amount of the initial oxide coverage stubbornly refused to desorb. Approximately similar O/N signal intensities remained after the 800°C desorption, with the HF:DI-treated samples retaining somewhat more oxygen than the others.

The results of other recent thermal desorption experiments performed in vacuum on similar GaN films have so far shown that O and C do not completely disappear, even up to temperatures where GaN decomposition occurs (>800-900°C), unless an active species is

present to assist in surface removal, i.e., hydrogen plasma, ion bombardment, etc. Ingrey *et al.* reported the same phenomenon for InGaAs [33]. An important consideration in this regard is the current concern with the role of H and its compensation of acceptor impurities. The search for a method of obtaining surfaces as atomically "pristine" as possible must necessarily include the characterization of any surface damage or other property degradation that may occur in connection with surface cleaning procedures. The use of ionized, accelerated gas-phase species in cleaning methods is likely to cause some surface damage, depending on the kinetic energy and mass of the ionized species. In addition, there are indications that even short-term exposure to aqueous acid cleaning solutions can cause micro roughening of GaAs surfaces, which increases with time of exposure [34].

The relative increases of O and C before the 800°C analysis were different for the two cleaning treatments. While the C concentration on the HCl:DI surface remained approximately the same, the relative O signal more than doubled. On the HF:MeOH surface, the C signal increased while the O signal remained the same. In addition, there is some evidence that the C on the HCl:DI surface changed state prior to the 800°C analysis: it shows a different peak shape in that spectrum, while all the other spectra in this study exhibit the typical "aliphatic" C contamination peak shape. Assuming that the suspected contamination of the samples involved both O and C, the differences between the samples may reflect different types of surface passivation or protection against further surface coverage. The larger amount of C-containing surface coverage on the HF:MeOH-treated GaN may have served to protect against subsequent oxidation, as described in Ingrey's work on III-V surface cleaning [13], while the essentially cleaner HCl:DI-treated surface lacked such protection. Overall, the HCl:DI treatment produces the cleanest surfaces observed to date, both with and without subsequent thermal desorption. The possible additional protection offered by the HF:MeOH treatment may be useful for longer-term storage of GaN films, depending on the methods used for further cleaning.

Ti and TiN Contacts on n-GaN:Si. TiN is metallic in electrical behavior, in contrast to the insulating nitride formed by Al. Both AlN and TiN have highly negative free energies of formation and are therefore thermodynamically favored. As described in the preceding section, the nitridation of Al at the contact interface results in increasing resistivity. By comparison, the formation of metallic TiN at the contact interface is expected to improve contact characteristics; a substantial decrease in ρ_c as a function of annealing was indeed observed. The role of Ti nitridation in the formation of low-resistivity Ti-containing contacts to n-GaN has been discussed by Lin *et al.* [20]. The results of the present study indicate that high-temperature annealing benefits both Ti and TiN contacts. The roles played by microstructural changes and loss of N from the GaN at high temperatures are being investigated by means of cross-sectional, high-resolution TEM analysis that is currently underway.

Both Ti and TiN are low work function metals with TiN having the lower value (ϕ_{Ti}=4.1 eV, ϕ_{TiN}=3.74 eV), and thus according to the Schottky-Mott-Bardeen model should be more likely to form ohmic contacts to n-type semiconductors. In addition, there are reasons to expect that both Ti and TiN might deposit epitaxially on GaN and AlN, as they both do on 6H-SiC [35,36]. Titanium has a hexagonal structure and a basal-plane lattice parameter (a_{Ti}=2.951 Å, a_{Hf}=3.195 Å) similar to that of SiC, GaN and AlN (a_{SiC}=3.08 Å; a_{GaN}=3.189 Å; a_{AlN}=3.112 Å). TiN has the NaCl structure and has a reasonably close lattice match to hexagonal GaN (-5.9 %) and AlN (-3.6 %) in the close-packed (111) planes. TiN is thermally very stable and highly resistant to oxidation, forming only a thin passive oxide film on the surface. Though Ti oxidizes readily, it too forms only a thin passive film on the surface under normal conditions, and has a high melting point.

The Ti and TiN were deposited at the same temperature to the same thickness (1000 Å) on similar GaN:Si films. The primary difference between the two metal depositions is the presence of extra available N during TiN growth to fully bond with the Ti. In TiN the Ti becomes stoichiometrically nitrided and strongly bound to N, whereas in the case of Ti alone, any Ti nitride formation that takes place must derive its nitrogen from the GaN. The nitridation of Ti is thermodynamically favored with respect to GaN: the Gibbs free energy of formation ΔG_f^0 for TiN at 298 K is -6309.2 kJ/mol, while ΔG_f^0 for GaN is only -77.8 kJ/mol. The difference in ΔG_f^0 between the two does not change appreciably through 1000 K. The removal of Ti from the GaN would result in N vacancies, which are widely believed to function as shallow donors in GaN. M.E. Lin and H. Morkoç *et al.* have estimated that 2 monolayers of TiN formation at a contact interface is sufficient to form a 10 nm surface layer of GaN having an electron density of 10^{20} cm^{-3} through which electrons could efficiently tunnel, thus greatly increasing the current-carrying capacity of the contact interface [20,37].

The TiN contacts deposited on these GaN:Si films (n=1.2×10^{18} cm^{-3}) did not show the low-resistance behavior exhibited by the as-deposited TiN contacts on more highly doped GaN:Si (n=9.4×10^{18} cm^{-3}) described in the preceding 1994 Annual Report (December 1994). This difference in GaN carrier concentration may account for much of the difference in ρ_c behavior. Overall, the Ti and TiN contacts in this experiment behaved similarly with respect to annealing treatment—possibly for different reasons. The TiN has a lower work function and thus may produce a lower barrier than Ti on GaN, but the un-nitrided Ti is able to create N vacancies in the GaN interfacial region, which would also result in improved contact behavior. More detailed study of this contact system, especially high-resolution microstructural characterization via X-TEM to look for epitaxial relationships and any compositional changes that take place, is planned to help understand the current transport mechanisms and establish the utility of this contact system for high-temperature device applications.

CuGe Contacts on n-GaN:Si. As described above, the Cu_3Ge contacts exhibited ohmic behavior on both lightly-doped ($n=4.5\times10^{17}$ cm^{-3}) and heavily-doped ($n=7.4\times10^{18}$ cm^{-3}) n-GaN:Si films. This behavior was observed in both the as-alloyed contacts, alloyed in vacuum at 400°C, and contacts annealed in vacuum through 800°C. The annealing treatments were intended to increase the donor concentration at the contact interface by means of Ge diffusion into the GaN. A reduction of ρ_c was not seen as a result of the annealing treatments up through 700°C, indicating that little transport of Ge into the GaN took place at these temperatures. The increase in ρ_c that occurred after the 800°C anneal was a result of degradation of the metal layer itself. In the as-alloyed state, the metal layer exhibited low-resistivity properties; after the 800°C anneal the probe-to-probe resistance of the metal layer had increased dramatically and overwhelmed all other electrical effects contributing to the I-V measurements used for TLM calculations.

Since the Cu_3Ge ε_1 phase melts completely at 747°C, the changes in metal properties are most likely due to its melting and cooling. The reason for heating the metal contact layer above its melting point is drawn from the industry's experience with the familiar Au-Ge ohmic contacts on n-GaAs, which are annealed at temperatures above the Au-Ge alloy melting point to achieve ohmic behavior. However, the best results with Au-Ge contacts are achieved when the Au-Ge alloy is capped with a thin layer of Ni and then a thick low-resistivity overlayer of Au. Also, it is now known that the Ni layer, originally added to keep the liquid Au-Ge metal from "balling up" on the GaAs surface during alloying, actually participates in the contact alloying process in an extensive and complex way. Far from being a neutral, refractory capping layer, the Ni has been found to alloy extensively and to enhance the interdiffusion of the interface constituents, even at the relatively low temperatures used for this contact system (~425°C) [2]. In an analogous way, it may be possible to obtain better performance from the Cu_3Ge/n-GaN contact system if capping layers or other processing parameters can be adjusted to protect the metal from degradation at high temperatures. Also, it may be possible to enhance the GaN contact interface with Ge and thus improve ρ_c by annealing the contacts at longer times at temperatures below the melting point.

Pt Contacts on p-GaN:Mg. Platinum is a very high work function metal ($\phi_{Pt}=5.65$ eV) and thus provides a favorable band offset for minimizing the Schottky barrier to a p-type semiconductor. In addition, Pt is thermally very stable and highly resistant to oxidation. In the preceding annual report for this project (December 1994), linear ohmic behavior and very low ρ_c was observed for as-deposited Pt contacts to Mg-doped GaN. Investigation of Pt as an ohmic contact candidate for p-type GaN was conducted earlier in this study, as described in the semiannual report for June 1993, but the results were not as promising at that time. Substantial improvements in GaN film quality and electrical properties have been made since then. The newer GaN:Mg described here were grown by MOVPE instead of MBE, as was the case when

the earlier study was conducted. The measurement of carrier concentration and mobility via Hall measurements has been difficult for p-type GaN so far, due to inconsistent and high-resistance ohmic contact behavior.

The work of Sands *et al.* [38,39] has shown that extensive interfacial reaction can occur between Pt and GaAs, due to metallurgical reactions involving both Ga and As. Though lacking the mobile and reactive As species, GaN nevertheless has shown the ability to react with noble metals when annealed at high temperature, as described in the preceding annual report in connection with Au contacts on p-GaN. Thus, changing behavior of the Pt contacts as a function of annealing temperature is not surprising. The increasing resistance seen for the 900°C anneal is likely due to a progression of interfacial phase formation. Upcoming cross-sectional microstructural characterization will provide additional information and aid in the understanding of the behavior of this contact system.

E. Conclusions

The results of surface cleaning experiments conducted in this study so far has shown that HCL:DI (1:1) solution cleaning produces the cleanest surfaces of all the wet chemical cleaning methods yet examined on GaN films, particularly if the wet cleaning is followed by a thermal desorption to at least 625°C. All of the cleaning methods examined that involved HF were found to leave more O and C on the surface in general, though there was some evidence that the HF:MeOH treatment might protect a GaN surface from further oxygen coverage. As yet, complete removal of O and C from air-exposed GaN surfaces has not been seen, even up to temperatures where GaN decomposition occurs (>800-900°C), unless an active species is present to assist in surface removal, i.e., hydrogen plasma, ion bombardment, etc.

The comparison of Ti and TiN contacts on similarly-doped n-GaN has shown them to behave similarly with respect to the effects of annealing on the specific contact resistivity. In both cases, the ρ_c dropped significantly as a result of annealing through 900°C. It is likely that the improvement in the behavior of the Ti contact system is due to the formation of TiN at the GaN interface, accompanied by loss of N in the form of N vacancies in the GaN. In the case of TiN, the improvement in behavior as a result of annealing may also be due to the loss of N from the interfacial region of the GaN. The TiN compound can exist over a range of stoichiometry and can thus accommodate a certain amount of additional N lost from the GaN at the high annealing temperatures, which would again increase the donor concentration at the contact interface. More detailed study of this contact system, especially high-resolution microstructural characterization via X-TEM to look for epitaxial relationships and any compositional changes that take place, is planned to help understand the current transport mechanisms and establish the utility of this contact system for high-temperature device applications.

As was the case with the TiN/n-GaN contacts, the ρ_c varied dramatically with the carrier concentration of the GaN studied. There was no significant improvement in ρ_c as a result of post-deposition annealing, though in the case of Cu_3Ge contacts on lightly-doped GaN the I-V behavior became substantially more linear after annealing at 600°C. The Cu_3Ge metal layers deteriorated as a result of annealing them at temperatures above the metal's melting point. High temperatures (above 700°C) may be necessary to drive Ge diffusion into the GaN to provide increased donor concentrations at the contact interface, but the melting of the Cu_3Ge metal and consequent degradation of its properties may make this difficult. Annealing the contacts for longer times at temperatures below the melting point may improve their performance. It may also be possible to preserve the integrity of the Cu_3Ge metal during high-temperature annealing through the use of capping layers or other adjustments of processing parameters.

Annealing studies of sputtered Pt contacts on Mg-doped GaN have shown an improvement in current-carrying behavior as a result of annealing, though a deterioration in performance was observed for the highest annealing temperature (900°C). The achievement of low-resistivity ohmic contacts to p-GaN is a necessary component for the development and application of many types of GaN-based devices. Further characterization of contact candidates for p-type material, including microstructural information obtained from X-TEM analysis, will yield greater understanding of the chemical and structural contributions to contact behavior and will allow more rapid and knowledgeable development of improved contact schemes and their capabilities.

F. References

1. T. C. Shen, G. B. Gao, H. Morkoç, J. Vac. Sci. Technol. B **10** (5) 2113 (1992).
2. R. Williams, *Modern GaAs Processing Techniques* (Artech House, Norwood, MA, 1990).
3. M. Murakami, Materials Science Reports (5) 273 (1990).
4. A. Piotrowska and E. Kaminska, Thin Solid Films **193/194** 511 (1990).
5. A. Piotrowska, A. Guivarc'h and G. Pelous, Solid-St. Electron. **26** (3) 179 (1983).
6. V. L. Rideout, Solid-St. Electron. **18** 541 (1975).
7. K. Tanahashi, H. J. Takata, A. Otsuki and M. Murakami, J. Appl. Phys. **72** (9) 4183 (1992).
8. H. C. Hugon, B. Agius, F. Varniere, M. Froment and F. Pillier, J. Appl. Phys. **72** (8) 3570 (1992).
9. H. J. Takata, K. Tanahashi, A. Otsuki, H. Inui and M. Murakami, J.Appl. Phys. **72**(9) 4191 (1992).
10. W. O. Barnard, G. Myburg and F. D. Auret, Appl. Phys. Lett. **61** (16) 1933 (1992).
11. G. Stareev, Appl. Phys. Lett. **62** (22) 2801 (1993).
12. E. D. Marshall and M. Murakami, in *Contacts to Semiconductors,* edited by L. J. Brillson (Noyes, Park Ridge, NJ, 1993).
13. S. Ingrey, J. Vac. Sci. Technol. A **10** (4) 829 (1992).
14. F. W. Ragay, M. R. Leys and J. H. Wolter, Appl. Phys. Lett. **63** (9) 1234 (1993).
15. H. K. Henisch, *Semiconductor Contacts.* (Clarendon Press, Oxford, 1984).
16. E. H. Rhoderick and R. H. Williams, *Metal-Semiconductor Contacts* (Oxford University Press, New York, 1988).

17. S. Kurtin, T. C. McGill and C. A. Mead, Phys. Rev. Lett. **22** (26) 1433 (1969).
18. J. S. Foresi, *Ohmic Contacts and Schottky Barriers on GaN,* M.S. Thesis, Boston University (1992).
19. J. S. Foresi and T. D. Moustakas, Appl. Phys. Lett. **62** (22) 2859 (1993).
20. M. E. Lin, Z. Ma, F. Y. Huang, Z. F. Fan, L. H. Allen, and H. Morkoç, Appl. Phys. Lett. **64** (8) 1003 (1994).
21. B. L. Crowder and S. Zirinski, IEEE Trans. Electron Devices **ED-26**, 369 (1979).
22. S. C. Binari, H.B. Dietrich, and G. Kelner, Electronics Lett. **30**(11) 909 (1994).
23. S. P. Murarka, *Silicides for VLSI Applications,* Academic Press, New York (1983).
24. L. Krusin-Elbaum, J. Y.-C. Sun, and C.-Y. Ting, IEEE Trans. Electron Devices **ED-34**, 58 (1987).
25. J. C. Hensel, R. T. Tung, J. M. Poate, and F. C. Unterwald, Appl. Phys. Lett. **44**, 913 (1984); Phys. Rev. Lett. **54**, 1840 (1985).
26. P. H. Woerlee, P. M. Th.M . van Attekum, A. A. M. Hoeben, G. A. M. Hurkx, and R. A. M. Wolters, Appl. Phys. Lett. **44**, 876 (1984).
27. M. T. Huang, T. L. Martin, V. Malhotra, and J. E. Mahan, J. Vac. Sci. Technol. B **3**, 836 (1985).
28. L. Krusin-Elbaum and M. O. Aboelfotoh, Appl Phys. Lett. **58**(12) 1341 (1991).
29. M. O. Aboelfotoh, H. M. Tawancy, and L. Krusin-Elbaum, Appl. Phys. Lett. **63**(12) 1622 (1993).
30. M. O. Aboelfotoh, K. N. Tu, F. Nava, and M. Michelini, J. Appl. Phys. **75**(1) (1994).
31. M. O. Aboelfotoh, H. M. Tawancy, J. Appl. Phys. **75**(4) (1994).
32. G. K. Reeves and H. B. Harrison, IEEE Electron Device Lett. **EDL-3** 111 (1982).
33. S. Ingrey, W. Lau, and R. Sodhi, J. Vac. Sci. Technol. A **7**, 1554 (1989).
34. D. E. Aspnes and A. A. Studna, Appl. Phys. Lett. **46** (11) 1071 (1985).
35. L. M. Porter, R. F. Davis, J. S. Bow, M. J. Kim, R. W. Carpenter, and R. C. Glass, J. Mater. Res., **10** (3) 668 (1995).
36. R. C. Glass, Ph.D. thesis, North Carolina State University, June 1993.
37. H. Morkoç, S. Strite, G. B. Gao, M. E. Lin, B. Sverdlov, and M. Burns, J. Appl. Phys. **76** (3) 1363 (1994).
38. T. Sands, V. G. Keramidas, A.J. Yu, K-M. Yu, R. Gronsky, and J. Washburn, J. Mater. Res. **2** (2) 262 (1987).
39. T. Sands, V. G. Keramidas, K-M. Yu, J. Washburn, and K Krishnan, J. Appl. Phys. **62** (5) 2070 (1987).

XXVI. III-V Nitrides for Use in Semiconductor Microelectronic Device Applications

A. Introduction

The distinct combination of physical and electronic properties make III-V nitrides promising materials for optoelectronic and microelectronic applications. AlN, GaN, and InN have direct band gaps of 6.2, 3.2, and 1.9eV, respectively. In conjunction with their continuous solid solubility, one has the ability to engineer band gaps within the range of 1.9 to 6.2 eV, which can be used to construct blue LEDs and deep UV lasers.

The III-V nitrides have advantageous physical properties such as high thermal stability, high physical hardness, and high chemical stability, as well as their wide band gaps. In combining these properties, the III-V nitrides lend themselves as excellent candidates for high power and high temperature devices [1].

There is one significant drawback to the use of the III-V nitrides: the lack of a homoepitaxial substrate. In order to achieve monocrystalline thin films, heteroepitaxy has been employed using a number of different substrates. This method has allowed the production of single crystal films, but the films have had poor crystal quality and high unintentional doping levels [2].

Recent developments have shown that good single crystal thin films of AlN and GaN can be grown using techniques such as Metal Organic Chemical Vapor Deposition (MOCVD) and Molecular Beam Epitaxy (MBE) [3-7]. The most successful of these films, which exhibit high resistivity and low unintentional doping, have been grown on Al_2O_3 (sapphire) and α-SiC. Conductive n and p-type GaN films have also been produced using the appropriate doping impurities.

With the production of device-quality material, successful attempts have been made to produce microelectronic devices using the III-V nitrides [8-15]. Khan *et al.* have made many strides in this area, including being the first to fabricate a MESFET device from the nitrides. Binari *et al.* have also fabricated MESFET devices along with MISFET devices. Binari fabricated an depletion mode device using Si_3N_4 as the gate insulator, see Fig. 1. For a gate length of 0.9 mm, the transconductance was 16 mS/mm at 30°C and 11 mS/mm at 200°C. The frequency response of these devices were measured, resulting in an f_T and f_{max} of 5 and 9 GHz, respectively [15].

Currently much of the research concerning MISFET devices is directed towards depletion mode devices. This can be attributed primarily to the inability to successfully process the material. Many strides have been made in the areas of implantation and etching [16-18]. Other areas of research which are beginning to be addressed include the investigation of insulator materials. Some initial work has been done by Casey *et al.* on SiO_2-GaN MOS capacitors [19].

His results indicate that SiO_2 grown on GaN by a remote plasma method yielded a structure with low interface trap density.

It is the plan of this project to complete the steps needed to construct a MISFET structure. The steps will be discussed further in the following section.

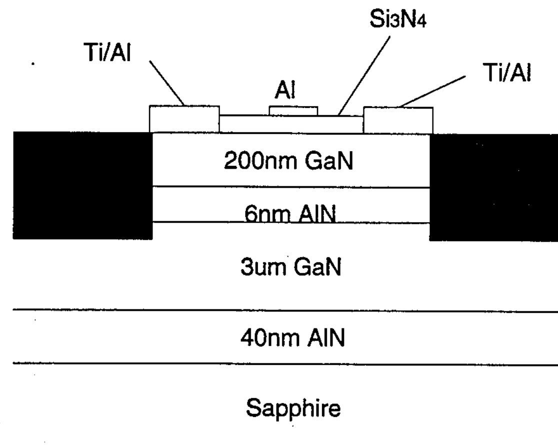

Figure 1. MISFET cross section.

B. Future Research Plans and Goals

This research group has demonstrated the ability to grow high-quality single crystal thin films of GaN and AlN with high resistivity and low levels of unintentional doping. These films have been grown by MBE and MOCVD on α-SiC, utilizing a high temperature monocrystalline AlN buffer layer. Both n and p type doping of the GaN films have been achieved through these methods.

The goal of this project is to develop and fabricate a MISFET device. Using a inversion layer for conduction, these devices have a higher breakdown than the depletion mode device, thus they are better suited for the hi power applications. With the growth of device quality material, a number of steps must be taken in order to obtain a device. Some of these tasks include contacts, etching, and implantation. These areas of research are all currently being addressed within this group.

To further develop the device, a insulator must be found for the gate. Some materials such as SiO_2, Al_2O_3, and Si_3N_4 are being investigated currently. Capacitance-voltage measurements will be employed to determine the most suitable material. There are limitations with GaN in the device development. A backside contact for device purposes is not feasible due to the insulating AlN buffer layer. To conduct the measurements, all contacts must be made on the GaN surface. This will introduce series resistance into the equation, thus introducing some error.

Once a suitable insulator is found, a further study into the electronic capabilities of the material will be required. Determination of whether GaN has the ability to invert will be sought. This will determine the route which must be taken in the design of the final device. These factors are the challenges that lie ahead in the development of MISFET devices.

C. Conclusion

With their combination of thermal and electrical properties, the III-V nitrides have the potential to be excellent materials for use in high power and high temperature applications. With the production of device quality material, the time has arrived to develop these devices. There are a number of factors that will determine when fabrication will be realized. It is the goal of this project to complete the work needed to achieve a working device.

D. References

1. R. F. Davis, Proc. IEEE **79**, 702 (1991).
2. S. Strite and H. Morkoç, J. Vacuum Sci. Technol. B **10**, 1237 (1992).
3. M. Asif Khan, J. N. Kuznia, J. M. Van Hove, D. T. Olson, S. Krishnankutty, and R. M. Kolbas, Appl. Phys. Lett. **58**, 526 (1991).
4. H Amano, T. Asahi, and I. Akasaki, Jpn J. Appl. Phys. **29**, L205 (1990).
5. S. Yoshida, S.Gonda, and S. Misawa, J. Appl. Phys. **53**, 6844 (1982).
6. M. Hegems and H. C. Montgomery, J Phys. Chem Solids **34**, 885 (1973).
7. C. Wang and R. F. Davis, Appl. Phys. Lett. **63**, 990 (1993).

   M. Asif Khan, J. N. Kuznia, A. R. Bhattarai, and D. T. Olson, Appl. Phys. Lett. **62**, 1786 (1993).

9. M. Asif Khan, J. M. Van Hove, J. N. Kuznia, and D. T. Olson, Appl. Phys. Lett. **58**, 2408 (1991).
10. M. Asif Khan, J. N. Kuznia, J. M. Van Hove, N. Pan, and J. Carter, Appl. Phys. Lett. **60**, 3027 (1992).
11. M. Asif Khan, A. R. Bhattarai, J. N. Kuznia, and D. T. Olson, Appl. Phys. Lett. **63**, 1214 (1993).
12. M. Asif Khan, J. N. Kuznia, D. T. Olson, W. J. Schaff, J. W. Burm, and M. S. Shur, Appl. Phys. Lett. **65**, 1121 (1994).
13. M. Asif Khan, M. S. Shur, J. N. Kuznia, Q. Chen, J. W. Burm, and W.J. Schaff, Appl. Phys. Lett. **66**, 1083 (1995).
14. S. C. Binari, L. B. Rowland, W. Kruppa, G. Kelner, K. Doverspike, and D.K. Gaskill, Electronics Lett. **30**, 1248 (1994).
15. S. C. Binari, L. B. Rowland, G. Kelner, W. Kruppa, H. B. Dietrich, K. Doverspike, and D. K. Gaskill, Proc. 21st Int. Symp. on Compound Semiconductors, September 1994, San Diego.
16. R. J. Shul, A. J. Howard, S. J. Pearton, C. R. Abernathy, C. B. Vartuli, P. A. Barnes, and M. J. Bozack, J. Vac. Sci. Technol. B 13, 2016 (1995).
17. G. F. McLane, L. Casas, S. J. Pearton, and C. R. Abernathy, Appl. Phys. Lett.66, 3328 (1995).
18. S. J. Pearton, C. B. Vartuli, J. C. Zolper, C. Yuan, and R. A. Stall, Appl. Phys. Lett. 67, 1435 (1995).
19. H. C. Casey, Dept. of Electrical Engineering, Duke University.

XXVII. Distribution List

Mr. Max Yoder Office of Naval Research Electronics Division, Code: 312 Ballston Tower One 800 N. Quincy Street Arlington, VA 22217-5660	3
Administrative Contracting Officer Office of Naval Research Regional Office Atlanta 101 Marietta Tower, Suite 2805 101 Marietta Street Atlanta, GA 30323-0008	1
Director, Naval Research Laboratory ATTN: Code 2627 Washington, DC 20375	1
Defense Technical Information Center Bldg. 5, Cameron Station Alexandria, VA 22304-6145	2